

Controlling Peptide Structure and Function

A thesis submitted in total fulfilment of the requirements for the
degree of Doctor of Philosophy

by

Yuan Qi Yeoh



September 2020

School of Physical Sciences

Department of Chemistry

Table of Contents

| | |
|---|-----------|
| Abstract..... | I |
| Declaration..... | III |
| Acknowledgements..... | IV |
| Publications..... | V |
| Abbreviations..... | VI |
| | |
| CHAPTER 1..... | 1 |
| 1.1 Importance of secondary structure in proteins / peptides..... | 2 |
| 1.1.1 α -helix, β -strand, β -sheet, and β -turn secondary structures..... | 3 |
| 1.1.2 Antibacterial peptide gramicidin S..... | 7 |
| 1.1.3 Controlling peptide secondary structure and antibacterial activity through photopharmacology and hypoxia activation..... | 10 |
| 1.2 Dynamic behavior of proteins / peptides | 17 |
| 1.2.1 Probing the structural dynamic behavior of peptides through single-molecule junctions | 18 |
| 1.3 Work presented in this thesis | 22 |
| 1.3.1 Photoswitchable antibacterial peptides..... | 22 |
| 1.3.2 Hypoxia-activated antibacterial prodrug..... | 23 |
| 1.3.3 Unravelling the structural dynamic properties within a photoswitchable peptide ... | 23 |
| 1.4 References | 24 |
| | |
| CHAPTER 2..... | 36 |
| Foreword | 37 |
| Statement of Authorship | 38 |
| 2.1 Abstract | 41 |
| 2.2 Introduction..... | 42 |
| 2.3 Results and Discussion..... | 44 |
| 2.3.1 Design and Synthesis of Peptides 1-3 | 44 |
| 2.3.2 Spectroscopic Analysis for Peptides 1-3 | 45 |
| 2.3.3 Molecular Modelling for Peptides 1-3 | 47 |

| | |
|---|-----------|
| 2.3.4 Biological Assay for Peptides 1-3 | 50 |
| 2.4 Conclusion | 52 |
| 2.5 Acknowledgements | 52 |
| 2.6 References | 53 |
| 2.7 Supplementary Information | 58 |
| 2.7.1 Materials | 58 |
| 2.7.2 Methods | 58 |
| 2.7.3 Experimental..... | 60 |
| 2.7.4 UV-Vis Spectrum for Peptides 1-3..... | 66 |
| 2.7.5 ¹ H NMR Spectroscopy | 67 |
| 2.7.6 Half-life Analysis | 74 |
| 2.7.7 Molecular Modelling..... | 75 |
| 2.7.8 References | 81 |
| CHAPTER 3..... | 82 |
| Foreword | 83 |
| Statement of Authorship | 84 |
| 3.1 Abstract | 87 |
| 3.2 Introduction | 88 |
| 3.3 Results and Discussion..... | 89 |
| 3.4 Conclusion | 93 |
| 3.5 Acknowledgements | 94 |
| 3.6 References | 95 |
| 3.7 Supplementary Information | 98 |
| 3.7.1 Materials | 98 |
| 3.7.2 Methods | 98 |
| 3.7.3 Experimental..... | 100 |
| 3.7.4 HPLC Chromatograms | 107 |
| 3.7.5 UV-Vis Spectra | 109 |
| 3.7.6 Half-Life Analysis | 111 |
| 3.7.7 Molecular Modelling..... | 112 |
| 3.7.8. ¹ H NMR Spectroscopy | 114 |
| 3.7.9 References | 120 |

| | |
|--|----------------|
| CHAPTER 4 | 121 |
| Foreword | 122 |
| Statement of Authorship | 123 |
| 4.1 Abstract | 126 |
| 4.2 Introduction | 127 |
| 4.3 Results and Discussion..... | 129 |
| 4.4 Conclusion | 132 |
| 4.5 Acknowledgements | 132 |
| 4.6 References | 133 |
| 4.7 Supplementary Information | 136 |
| 4.7.1 Materials | 136 |
| 4.7.2 Methods | 136 |
| 4.7.3 Experimental..... | 138 |
| 4.7.4 Spectroscopic Analysis..... | 142 |
| 4.7.5 HPLC Chromatograms | 143 |
| 4.7.6 ¹ H NMR Spectra..... | 144 |
| CHAPTER 5 | 148 |
| Foreword | 149 |
| Statement of Authorship | 150 |
| 5.1 Abstract | 153 |
| 5.2 Introduction | 154 |
| 5.3 Results and Discussion..... | 156 |
| 5.3.1 Peptide Design and Device Fabrication | 156 |
| 5.3.2 Real-time conductance measurements for <i>cis</i> and <i>trans</i> isomers of cyclic peptide 1 | 158 |
| 5.3.3 Molecular dynamics (MD) simulations of GMG-SMJ | 164 |
| 5.4 Conclusion | 170 |
| 5.5 Acknowledgements | 171 |
| 5.6 References | 172 |
| 5.7 Supplementary Information | 175 |
| 5.7.1 Device fabrication and molecular connection | 175 |
| 5.7.2 Probability analysis of single-molecule connection | 176 |

| | |
|---|------------|
| 5.7.3 Experimental Results..... | 177 |
| 5.7.4 Electrical measurements of control experiments..... | 182 |
| 5.7.5 Kinetic Analysis | 183 |
| 5.7.6 Molecular Dynamics (MD) Simulations of GMG-SMJs | 184 |
| 5.7.7 Computational Results..... | 190 |
| 5.7.8 References | 196 |
| CHAPTER 6..... | 198 |
| 6.1 Conclusion | 199 |
| 6.2 Further studies..... | 199 |
| 6.3 References | 200 |

Abstract

The function of a protein or peptide is governed by its unique secondary structure and intrinsic dynamic properties. Hence, an ability to control secondary structure and an understanding of its dynamic behavior would allow for the regulation of protein function. However, proteins exhibit conformational complexity, which impedes a thorough investigation of the relationship between structure and function. Thus, model peptides present as ideal candidates for this purpose. Research undertaken in this thesis aims to control the secondary structure and hence, peptide activity, in addition to probing the intrinsic dynamic properties corresponding to specific structural changes within peptides. This research deepens our understanding of the secondary structure and the underlying dynamic properties of peptides, with these fundamental behaviors potentially transcending to proteins, which may provide important insights into their functions.

Chapter one provides an overall introduction to the importance of secondary structure in proteins/peptides, and the structural dynamic behavior that governs protein function. Various strategies are introduced to control the secondary structure and antibacterial activity of peptides, along with the single-molecule junction technique used to probe the structural dynamic properties of peptides.

Chapter two presents the photopharmacological approach to regulate secondary structure, and hence, antibacterial activity of a series of gramicidin S peptide mimetics through the photochemical control of a component azobenzene photoswitch. Detailed ^1H NMR spectroscopy and density functional theory (DFT) calculations were used to define the secondary structure in the *cis* and *trans* configurations of the peptides, and both isomers of all peptide mimetics were assayed against *S. aureus*. Notably, peptides **2a** and **2b** were found to exhibit a four-fold difference between the *cis*-enriched and *trans*-enriched photostationary states. This study revealed a clear relationship between well-defined secondary structure, amphiphilicity, and optimal antibacterial activity.

Chapter three describes the design and synthesis of three short photoswitchable tetrapeptides based on a known synthetic antibacterial. Each peptide contains an azobenzene photoswitch incorporated into either the N-terminal side chain, C-terminal side chain, or the C-terminus, to allow reversible switching between the *cis* and *trans* configurations. The C-terminus azobenzene (**3**) exhibited the most potent antibacterial activity against *S. aureus*, with an MIC of 1 µg/mL. A net positive charge, hydrophobicity, position of the azobenzene, secondary structure, and amphiphilicity were all found to be crucial to antibacterial activity.

Chapter four reports a prodrug based on a known antibacterial compound to target *S. aureus* and *E. coli* under reductive conditions. The prodrug was synthesized by masking the N-terminus and side chain amines of a component lysine residue as 4-nitrobenzyl carbamates, while activation of the prodrug was achieved by removing the protecting groups under conditions that mimic hypoxia. Antibacterial susceptibility assays confirmed the liberation of the active antibacterial agent from the inactive prodrug to kill *S. aureus* and *E. coli*.

Chapter five investigates the structural dynamic properties of a single-peptide using the single-molecule junction technique characterized by electrical conductance. The nanodevice was fabricated using a photoswitchable peptide containing an azobenzene photoswitch to provide both a well-defined secondary structure, and an intrinsically disordered structure. Real-time conductance measurements revealed three distinct states for each isomer, with molecular dynamics simulations showing each state corresponds to a specific range of hydrogen bond lengths within the *cis* isomer, and specific dihedral angles in the *trans* isomer. This study provides previously undisclosed insights into the structural dynamic behavior of peptides, which may well be applicable to proteins.

Declaration

I certify that this work contains no material which has been accepted for the award of any other degree or diploma in my name, in any university or other tertiary institution and, to the best of my knowledge and belief, contains no material previously published or written by another person, except where due reference has been made in the text. In addition, I certify that no part of this work will, in the future, be used in a submission in my name, for any other degree or diploma in any university or other tertiary institution without the prior approval of the University of Adelaide and where applicable, any partner institution responsible for the joint-award of this degree.

I acknowledge that copyright of published works contained within this thesis resides with the copyright holder(s) of those works.

I also give permission for the digital version of my thesis to be made available on the web, via the University's digital research repository, the Library Search and also through web search engines, unless permission has been granted by the University to restrict access for a period of time.

.....
Yuan Qi Yeoh

18/9/2020
.....
Date

Acknowledgements

I would like to express my gratitude to my supervisor, Prof. Andrew Abell, for his supervision and guidance. I am grateful for his insightful advice on research and support throughout my candidature. I would also like to offer my sincere appreciation to my co-supervisor, Dr. Jingxian Yu, for his valuable advice, insight, and aspiring guidance throughout the research. To Dr. John Horsley, thank you for your kind assistance in research, especially in revising manuscripts. You have taught me to write better. It is a true pleasure to work with all of you.

Thank you to my collaborators, Dr. Steven Polyak and Dr. Blagojce Jovcevski, for their kind assistance in the antimicrobial susceptibility tests. Thank you to Prof. Xuefeng Guo and his group at Peking University to collaborate in an exciting and impactful research project. To all past and present members of the Abell group, thank you for your helpful discussions and suggestions on chemistry. Thanks also to all technical staff in the Department of Chemistry at The University of Adelaide.

To my family, especially my parents, my heartfelt gratitude for your upbringing and continued support that led me to pursue this journey. Thank you to my sisters, Yuan Yi and Yuan Xin, for the laughter and joy to maintain my sanity. To Douglas, thank you for your support that keeps me going through difficult times. Also, to my church friends and family, both at Albert Park and St. Stephen's, thank you for the countless encouragement and prayers. It is indeed a blessing to know you guys.

Above all, praise and thanks be to God for the wonderful grace and providence in everyday life. To God be the glory.

Publications

Yeoh, Y. Q.; Yu, J.; Polyak, S. W.; Horsley, J. R.; Abell, A. D., Photopharmacological control of cyclic antimicrobial peptides. *ChemBioChem* **2018**, *19* (24), 2591–2597.

Yeoh, Y. Q.; Horsley, J. R.; Polyak, S. W.; Abell, A. D., A hypoxia-activated antibacterial prodrug. *Bioorg. Med. Chem. Lett.* **2020**, *30* (11), 127140.

Yeoh, Y. Q.; Horsley, J. R.; Yu, J.; Polyak, S. W.; Jovcevski, B.; Abell, A. D., Short photoswitchable antibacterial peptides. *ChemMedChem* **2020**, *15* (16), 1505–1508.

Chen, X.; Yeoh, Y. Q.; He, Y.; Zhou, C.; Horsley, J. R.; Abell, A. D.; Yu, J.; Guo, X., Unravelling structural dynamics within a photoswitchable single-peptide: A step towards multi-modal bio-inspired nanodevices. *Angew. Chem. Int. Ed.* **2020**, 10.1002/anie.202004701.

Abbreviations

| | |
|---------------------|--|
| ^{13}C NMR | carbon nuclear magnetic resonance |
| ^1H NMR | proton nuclear magnetic resonance |
| ACN | acetonitrile |
| AFM | atomic force microscopy |
| Boc | <i>tert</i> -Butyloxycarbonyl |
| CDCl_3 | deuterated chloroform |
| COSY | correlation spectroscopy |
| CVD | chemical vapor deposition |
| DFT | density functional theory |
| DIPEA | <i>N,N</i> -Diisopropylethylamine |
| DMF | <i>N,N</i> -Dimethylformamide |
| DMSO | dimethylsulfoxide |
| DMSO-d_6 | deuterated dimethylsulfoxide |
| EBL | electron beam lithography |
| <i>E. coli</i> | <i>Escherichia coli</i> |
| EDC.HCl | <i>N</i> -(3-dimethylaminopropyl)- <i>N'</i> -ethylcarbodiimide hydrochloride |
| equiv | equivalents |
| FET | field-effect transistor |
| Fmoc | fluorenylmethyloxycarbonyl |
| GMG-SMJ | graphene-molecule-graphene single-molecule junction |
| GPCR | G protein-coupled receptors |
| HATU | 1-[Bis(dimethylamino)methylene]-1 <i>H</i> -1,2,3-triazolo[4,5- <i>b</i>]pyridinium 3-oxid hexafluorophosphate |
| HBTU | <i>N,N,N',N'</i> -Tetramethyl- <i>O</i> -(1 <i>H</i> -benzotriazol-1-yl)uronium hexafluorophosphate |
| HOBt | hydroxybenzotriazole |
| HOMO | highest occupied molecular orbital |
| HRMS | high resolution mass spectrometry |
| LUMO | lowest unoccupied molecular orbital |
| MCBJ | mechanically controllable break junction |

| | |
|------------------|--|
| MD | molecular dynamics |
| MeOH | methanol |
| MIC | minimum inhibitory concentration |
| MPSH | molecular projected self-consistent Hamiltonian |
| MRSA | methicillin-resistant <i>Staphylococcus aureus</i> |
| NEGF | non-equilibrium Green's function |
| nNOS | neuronal nitric oxide synthase |
| Pbf | 2,2,4,6,7-Pentamethyldihydrobenzofuran-5-sulfonyl |
| PET | photoinduced electron transfer |
| PSS | photostationary state |
| RMS | root-mean-square |
| ROESY | rotating-frame Overhauser effect spectroscopy |
| RP-HPLC | reverse phase high performance liquid chromatography |
| rt | room temperature |
| <i>S. aureus</i> | <i>Staphylococcus aureus</i> |
| SEM | Scanning Electron Microscope |
| SPPS | solid phase peptide synthesis |
| STM-BJ | scanning tunnelling microscopy break junction |
| T3P | 1-Propanephosphonic anhydride solution |
| tBu | <i>tert</i> -Butyl |
| TFA | trifluoroacetic acid |
| TIPS | triisopropylsilane |
| TLR | toll-like receptors |
| TMS | tetramethylsilane |
| TOCSY | total correlated spectroscopy |
| UV | ultraviolet |
| UV-Vis | ultraviolet to visible absorption spectroscopy |
| v/v | volume per unit volume |
| Vis | visible light |
| λ_{\max} | maximum absorption wavelength |



CHAPTER 1

Introduction



1.1 Importance of secondary structure in proteins / peptides

Peptides consist of a short chain of amino acids, with the most fundamental being dipeptides, tripeptides, and tetrapeptides. Long linear chains of amino acid residues are known as polypeptides, which can fold to give a well-defined and functional three-dimensional structure. Proteins can adopt four levels of structure, namely primary, secondary, tertiary, and quaternary. The primary structure of a protein is defined by the unique amino acid sequence, which then folds into secondary structures that are stabilized by hydrogen bonds between the amide CO and NH groups of the repeating constituents on the polypeptide backbone.¹ The two main types of secondary structures for peptides/proteins are α -helices and β -strands. These secondary structures can aggregate into a three-dimensional tertiary structure, stabilized by interactions between the side chains of amino acid residues that constitute the polypeptide. These side chain interactions include hydrogen bonding, ionic bonding, dipole-dipole interactions, hydrophobic interactions, and disulfide bonds.² Two or more polypeptide chains, known as subunits, can then assemble to form a protein with a quaternary structure. A well-defined secondary structure in the hierarchical classification of protein structure is of significant interest as it provides a basis for fold recognition.³ The protein fold is the unique geometric arrangement of structural motifs in space, and its identification is essential in determining protein structure and function.⁴ For example, enzymes are proteins containing secondary structures that fold into a globular conformation for catalytic activity, while the structural protein collagen possesses an extended helical conformation to maintain cell rigidity.⁵ These protein structures highlight the importance of secondary structure as fundamental structural elements that define the overall protein architecture and function. Thus, an ability to control the secondary structure of a protein would allow modulation of protein function. Since the structure and conformation of proteins is incredibly complex, alternative means such as model peptides are commonly used to study the relationship between structure and function.⁶

1.1.1 α -helix, β -strand, β -sheet, and β -turn secondary structures

An α -helix is formed when the linear sequence of amino acids is tightly coiled around the long axis of the peptide, with the side chains of component amino acid residues projecting outward from the helical backbone (Figure 1.1a).² The α -helix is the most abundant form of secondary structure in proteins.⁷ A right-handed helix consists of 3.6 residues per turn, which is stabilized by intramolecular hydrogen bonds between each amide CO (i) and NH ($i + 4$) on the peptide backbone (Figure 1.1b).⁸ The ideal dihedral angles for an α -helix are, $\Phi = -60^\circ$ and $\Psi = -45^\circ$ (Figure 1.1c).⁸

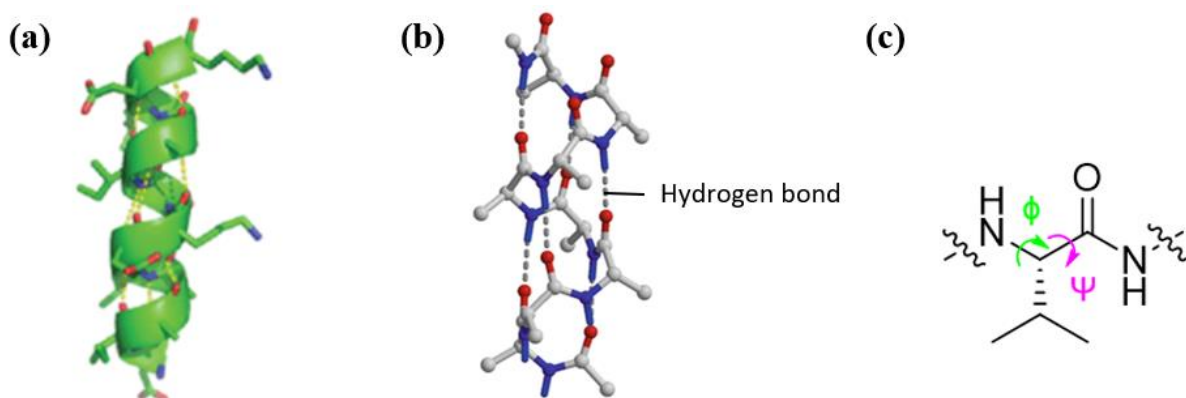


Figure 1.1. The α -helix secondary structure. (a) Side view of an α -helix model, showing the side chains of the amino acid residues projecting outward from the peptide backbone.⁸ (b) The α -helix is stabilized by intramolecular hydrogen bonds between the amide CO (i) and NH ($i + 4$) groups on the peptide backbone.⁹ (c) Schematic diagram of dihedral angles in a peptide backbone. Phi (Φ) indicates the rotation between the N-C α bond, while psi (Ψ) indicates the rotation between the C α -CO bond.

Work in this thesis is primarily concerned with peptides containing a β -strand, which is an extended arrangement of amino acids folded to form a pleated structure, with the distance between adjacent amino acid residues along the strand approximately 3.5 Å.¹⁰ A β -sheet, formed by two or more β -strands connected via hydrogen bonding (Figure 1.2a), comprises more than 30 % of all protein structures.¹¹ It is described as parallel when both strands are running in the same direction, while two aligned strands running in the opposite direction are termed antiparallel. The amide CO and NH groups in a β -strand are situated orthogonal to the backbone,

thus reducing steric hindrance between the side chains (Figure 1.2b). Ideal dihedral angles for the peptide backbone are $\Phi = -119^\circ$, $\Psi = 113^\circ$ for a parallel β -sheet, and $\Phi = -139^\circ$, $\Psi = 135^\circ$ for an antiparallel β -sheet.¹¹ A β -turn secondary structure is produced when a peptide chain reverses its overall direction, folding into a β -hairpin motif that is stabilized by intramolecular hydrogen bonds (Figure 1.2c).¹² The β -turn is the third most important secondary structure after α -helices and β -strands, comprising 25-30 % of all protein structures.¹³ There are eight different types of β -turns, each of which are defined by the values of Φ and Ψ dihedral angles of the corner residues, $i + 1$ and $i + 2$.¹³ The amino acids with a strong turn-forming propensity, such as ^DPro-Gly, ^DPhe-Pro, and Aib-^DPro, are known to promote the formation of β -turn and β -hairpin secondary structures that are commonly found in cyclic peptides.¹⁴

The β -strand, β -sheet, and β -turn secondary structures provide key recognition motifs for protein-protein interactions to mediate various biological processes.¹⁵ For example, the regulation of signal transduction by G protein-coupled receptors (GPCR) requires heterodimerization between rhodopsin and arrestin through β -strand domains, forming an extended network of antiparallel β -sheets to modulate downstream signaling effectors.¹⁶ Figure 1.3 shows the crystal structure of the rhodopsin-arrestin complex, which is stabilized by electrostatic interactions, hydrogen bonding, and disulfide cross-linkages. Moreover, immune system regulation by toll-like receptors (TLR)¹⁷ and binding interactions between cell adhesion molecules, CD2 and CD58,¹⁸ also require β -strand, β -sheet, or β -turn/hairpin secondary structures, highlighting their importance for protein-protein interactions. This thesis presents the synthesis of a series of peptides that adopt a β -strand geometry, and then an investigation into associated biological activity and structural dynamic properties as described in each chapter. For example, the cyclic peptide gramicidin S contains a β -sheet comprising two antiparallel β -strands, linked by two β -turns, which are crucial to its antibacterial property. This antibacterial peptide is considered further in the following section, and also in chapter 2.

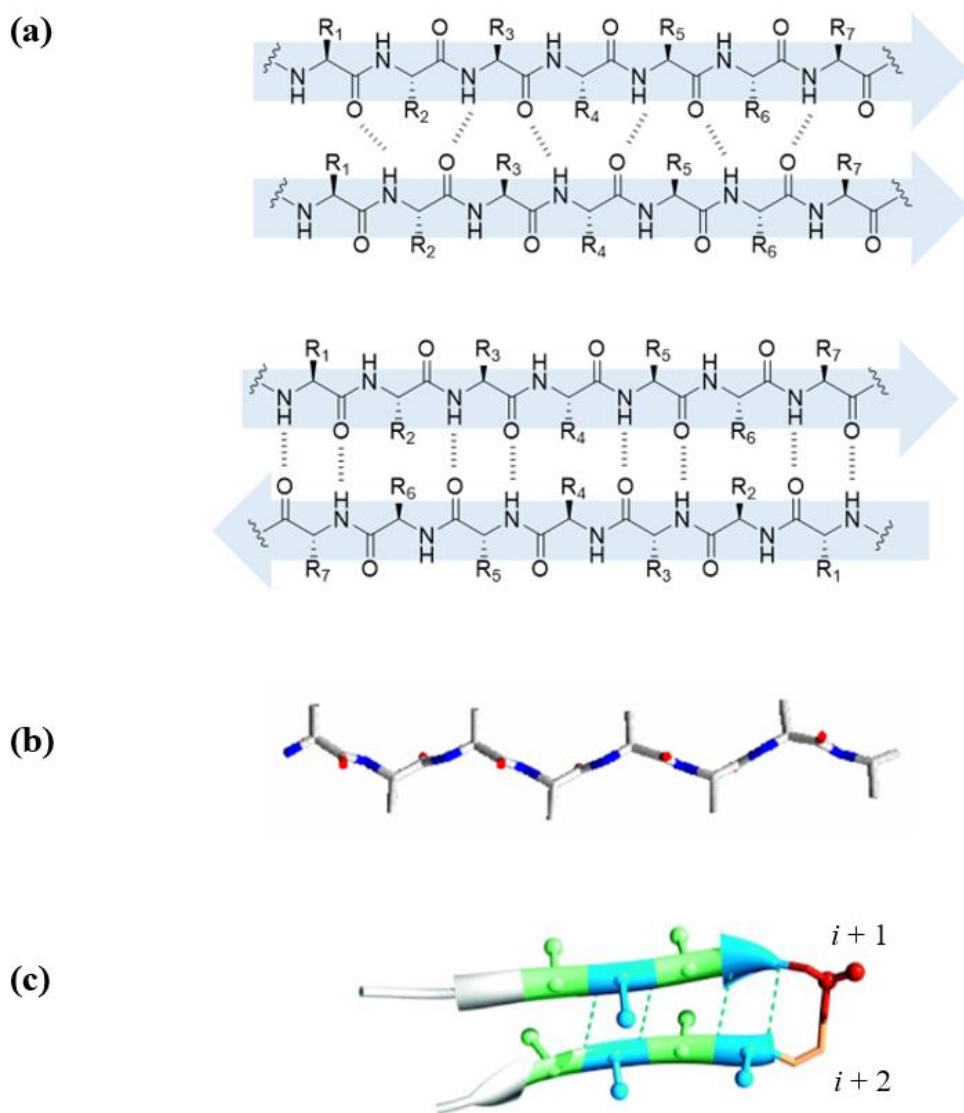


Figure 1.2. β -strand, β -sheet, and β -turn secondary structures. (a) Schematic diagram of a parallel (top) and an antiparallel (bottom) β -sheet, consisting of two β -strands linked by intermolecular hydrogen bonds, indicated by dashed lines. Arrows represent the direction from N- to C-terminus. (b) A β -strand showing the amide CO (red) and NH groups (blue) situated orthogonal to the peptide backbone, thus minimizing steric hindrance between the side chains. (c) Ribbon representation of a β -turn induced by the corner residues, $i + 1$ and $i + 2$, folding into a β -hairpin motif that is stabilized by intramolecular hydrogen bonds, indicated by dashed lines.¹⁴

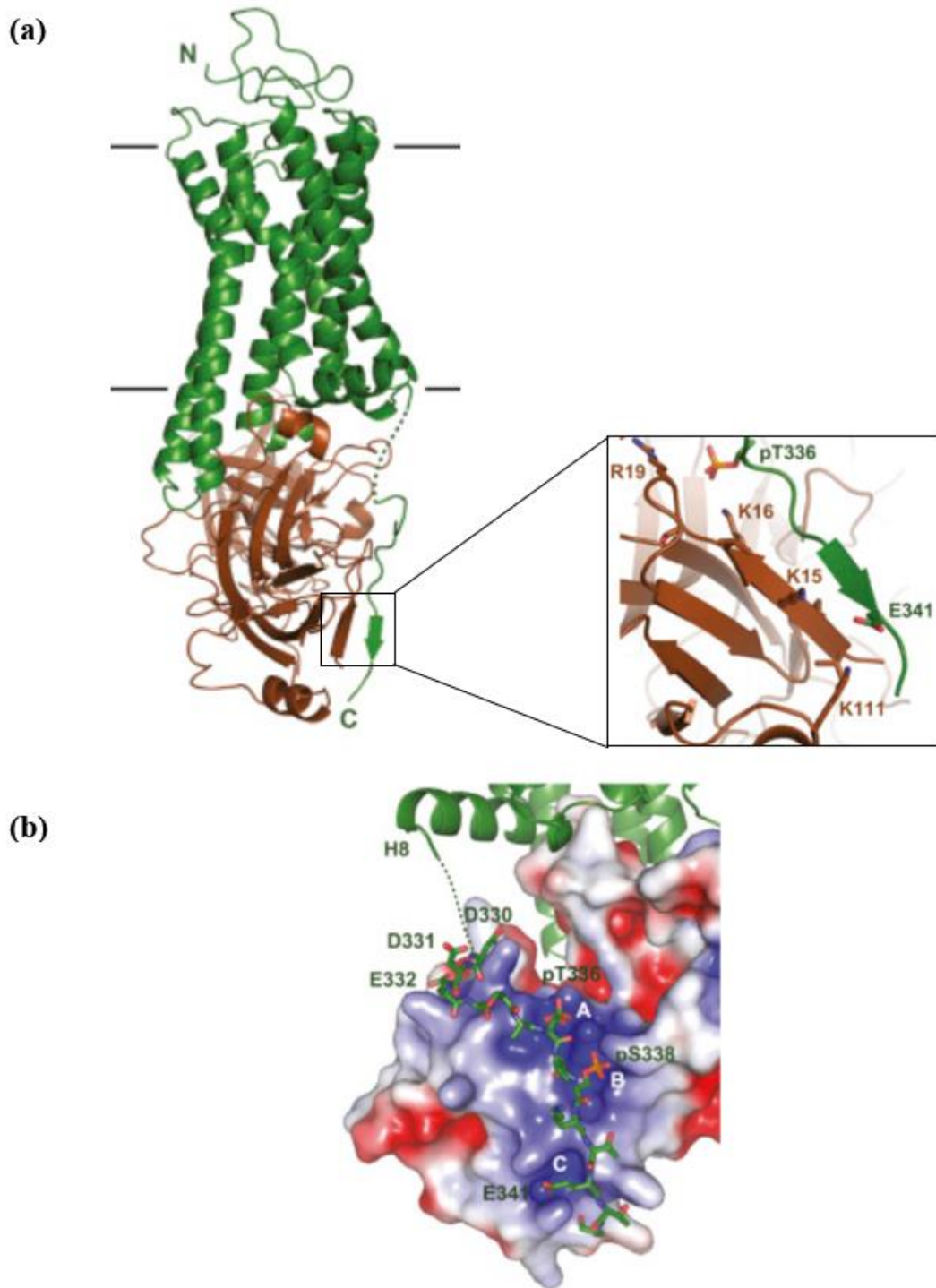


Figure 1.3. Crystal structure of the rhodopsin-arrestin complex. (a) The C-terminus tail of rhodopsin (green) dimerizes with the N-terminus of arrestin (brown) through the β -strand domains, forming an extended network of antiparallel β -sheets to mediate specific cell signaling pathways. Inset shows the enlarged section of the antiparallel β -sheet. (b) Docking structure of the rhodopsin-arrestin complex, showing the electrostatic interactions between the β -strand domains of rhodopsin and arrestin.¹⁶

1.1.2 Antibacterial peptide gramicidin S

Gramicidin S, a natural antibiotic isolated from soil bacterium *Bacillus brevis*,¹⁹ is a cyclic decapeptide [cyclo(^DFPVOL)₂, where ^DF=D-phenylalanine, O=ornithine] with a symmetrical antiparallel β -sheet conformation, linked by two type-II' β -turns (Figure 1.4).²⁰ The β -sheet secondary structure in gramicidin S is stabilized by four strong intramolecular hydrogen bonds between the two β -strands, with bond lengths ranging between 2.0-2.2 Å.²⁰ The antibacterial properties of gramicidin S have been attributed to its well-defined secondary structure and its overall amphiphilic nature.²¹ Specifically, the side chain amines of the ornithine residues can be protonated to carry positive charges, while the remaining amino acid residues form a surface with a hydrophobic membrane core.²² This amphiphilic nature allows gramicidin S to establish electrostatic interactions for binding onto negatively charged bacterial outer membranes, and induces further disruption on inner lipid membranes.²³ The bacterial membrane is essential for many metabolic functions, including transport, osmoregulation and respiration processes, biosynthesis and cross-linking of peptidoglycan, and synthesis of lipids.²⁴ Thus, any disruption of the bacterial membrane will trigger metabolic dysfunction and ultimately lead to cell death.²⁴ The detailed mechanism of action for gramicidin S is not clearly understood, and it remains controversial. Previous studies have proposed that following binding, gramicidin S induces pore formation in a detergent-like manner, leading to the disintegration of the bacterial membrane.²⁴ However, more recent studies revealed a more multifaceted and complex mechanism, where gramicidin S destabilizes the bacterial membrane by regulating certain membrane proteins.²⁵⁻²⁶ Gramicidin S displays superior activity against a broad spectrum of Gram-positive and Gram-negative bacteria,²⁷ and is less susceptible to resistance due to its preferential disruption of the bacterial membrane,²⁸ and multiple modes of antibacterial action.²⁵⁻²⁶ Thus, gramicidin S presents as a promising alternative to treat multidrug-resistant bacteria that pose a worldwide threat to public health. Although gramicidin S serves as a potent antibiotic, it also exhibits hemolytic effects, bringing with it unknown safety and toxicity concerns for oral administration. Hence, in its natural form, it has limited therapeutic value apart from topical application.^{27, 29}

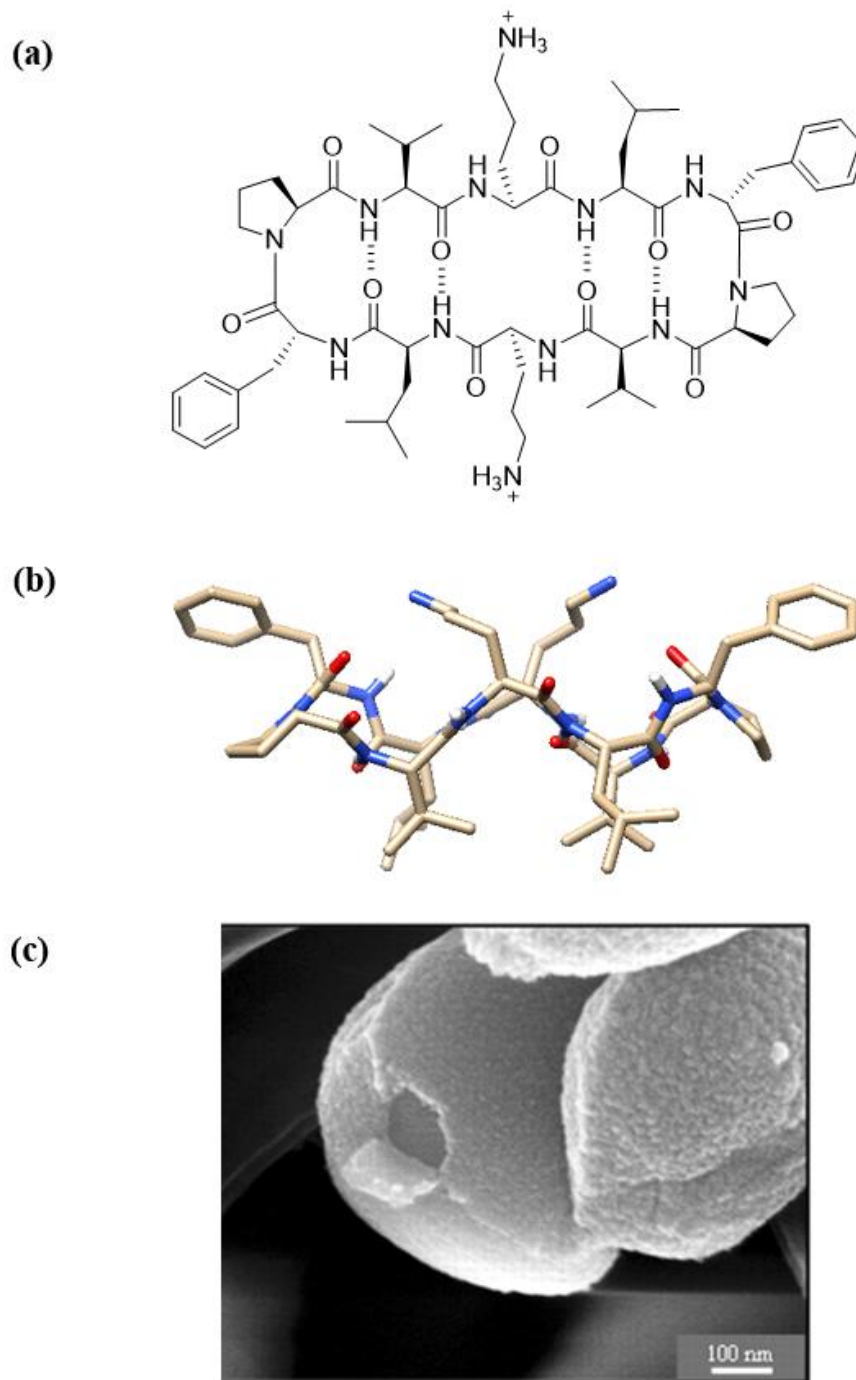


Figure 1.4. The natural antibacterial peptide gramicidin S. (a) Chemical structure of gramicidin S, stabilized by four intramolecular hydrogen bonds (dashed lines). (b) Model structure of gramicidin S (side view), highlighting the β -sheet conformation. (c) Scanning Electron Microscope (SEM) image showing the disruption of *S. aureus* bacterial membrane by gramicidin S.²⁴

Inspired by the promising antibacterial properties of the naturally occurring gramicidin S peptide, a number of studies have been conducted to design and develop gramicidin S peptide mimetics with reduced side effects. The Hodges, Overhand, and Tamaki research groups each modified the ring size of gramicidin S, which had an impact on the β -sheet content, amphiphilicity, hydrophobicity, and thus, antibacterial activity of the peptide mimetics.³⁰⁻³² Moreover, several other groups modified the β -turn region of gramicidin S by replacing the corner residues (^DPhe-Pro) with dipeptide surrogates.^{27, 33} A recent study by the Valérie group reported the design and synthesis of a diastereomeric pair of gramicidin S peptide mimetics using β,γ -diamino acids to mimic the β -turns (Figure 1.5), which exhibited moderate antibacterial property, with significantly diminished hemolytic activity.³⁴ Other basic design principles for gramicidin S peptide mimetics include changing the overall charge of the peptide, inducing secondary structure, altering the ratio of hydrophobic and hydrophilic residues, and improving the peptide amphiphilicity.³⁵⁻³⁶ Furthermore, numerous synthetic peptides have been reported to target specific bacteria based on combinatorial library approaches.³⁷⁻³⁸ Despite the superior activity of many gramicidin S peptide mimetics and related synthetic peptides, their clinical application remains limited due to high toxicity *in vivo* and lability toward proteases.³⁹ Hence, other strategies are required to enhance bioavailability as developed further in this thesis.

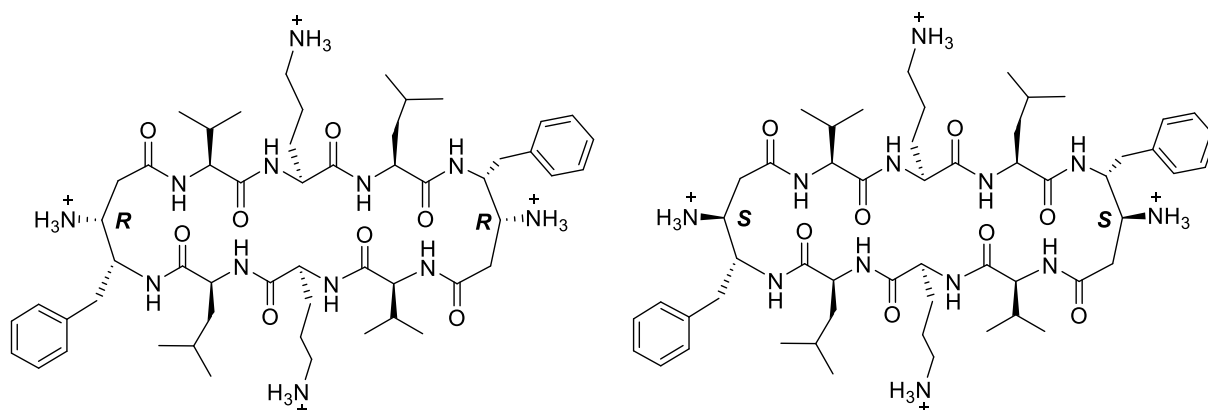


Figure 1.5. Chemical structures for the diastereomeric pair of gramicidin S peptide mimetics developed by the Valérie group using β,γ -diamino acids to mimic the β -turns.³⁴

1.1.3 Controlling peptide secondary structure and antibacterial activity through photopharmacology and hypoxia activation

Photopharmacology is an emerging strategy to modulate the bioactivity of a compound using light of a specific wavelength (Figure 1.6).⁴⁰⁻⁴¹ In the case of an antibacterial peptide, this would allow reversible control of its secondary structure to modulate antibacterial activity. Light provides an ideal means to regulate bioactivity as the timing, location, and intensity of irradiation can be fine-tuned to allow localized treatment of an associated disease.⁴²⁻⁴⁴ This approach also offers an opportunity to mitigate off-target side effects, and in the context of an antibiotic, the development of resistance.⁴⁵⁻⁴⁶ Photocontrol is achieved by incorporating a reversible molecular switch (photoswitch) into the compound, which is interconverted between two isomeric forms upon photoisomerization using light of a specific wavelength.⁴⁷ Photoisomerization induces changes in both physical and chemical properties, thus enabling reversible ‘on’ and ‘off’ regulation of activity. Previous studies have demonstrated the use of various photoswitches, such as azobenzene,⁴⁸⁻⁴⁹ stilbene,⁵⁰⁻⁵¹ thioxylyated amide,⁵² fumaramide,⁵³ hemithioindigo,⁵⁴⁻⁵⁵ diarylethene,⁵⁶⁻⁵⁷ spiropyran,⁵⁸⁻⁵⁹ and overcrowded alkene⁶⁰ to control the secondary structure and hence, activity of peptides (Figure 1.7). The most well-known of these is the azobenzene photoswitch.

The discovery of azo compounds ($-N=N-$) in the mid-1800s instigated the development of synthetic coloring agents in the dye and pigment industry.⁶¹ An example of azo derivatives is the azobenzene molecule, with its photochromic properties revealed upon exposure to light.⁶² Extensive studies have been performed on azobenzene, making it among the best characterized photoswitch.⁶³⁻⁶⁴ Azobenzene can be reversibly interconverted between the *cis* and *trans* configurations using light of specific wavelengths,⁶⁵ which produces significant structural changes.⁶⁶⁻⁶⁸ The *trans* isomer adopts an extended near planar structure, and is thermodynamically more stable than its ‘bent’ counterpart, the *cis* isomer, by approximately 50 kJ/mol.^{65, 67} The distances between two specific carbon atoms located at the *para* position of each phenyl ring of an unsubstituted azobenzene are ~ 9.0 Å and ~ 5.5 Å for the *trans* and *cis* isomers respectively.⁶⁹ This large difference in spatial arrangement gives rise to the distinctive physical and chemical properties of each isomer. The *trans* isomer of an unsubstituted azobenzene has no dipole moment, while its *cis* counterpart possesses a dipole moment of 3

Debye.⁷⁰ The absorbance spectra for each isomer are distinct, yet display some slight overlap. Specifically, the *trans* isomer exhibits an intense absorbance band around 320 nm due to the $\pi \rightarrow \pi^*$ transition.⁷¹⁻⁷⁴ In contrast, the *cis* isomer shows a significantly less intense absorbance around 320 nm, with a weak absorbance around 420 nm due to the forbidden $n \rightarrow \pi^*$ transition.⁷¹⁻⁷⁴ Conversion of the *trans* to *cis* isomer using UV light (320 nm) provides a photoisomerization yield of approximately 80%, whereas ~99% conversion of the *cis* to *trans* isomer is attainable through visible light or heat.^{70, 75} The photoswitching of azobenzene using highly ionizing UV light limits the application of azobenzene in biological systems. Thus, numerous studies have been conducted in an attempt to shift the photoswitchable wavelength of azobenzene into the visible light or infrared regions that are more compatible with biological systems.⁷⁶⁻⁷⁸ Nevertheless, azobenzene is the most commonly used class of photoswitch for the photocontrol of biomolecules⁷⁹ due to its many advantages such as high quantum yield,⁷⁰ fast isomerization,^{70, 80} low rate of photobleaching,⁷⁴ and relative ease of synthesis.^{70, 80} The Abell group has demonstrated the incorporation of an azobenzene photoswitch into peptides to control the activity of antibiotics,⁸¹ biosensors,⁸² protease inhibitors,⁸³⁻⁸⁵ and smart membranes.⁸⁶ Figure 1.8 shows the photoswitchable peptide-based biosensor containing an azobenzene photoswitch, modelled on the neuronal nitric oxide synthase (nNOS) β -hairpin ligand to detect and control its interaction with α -syntrophin protein. The azobenzene photoswitch allows photochemical control of the secondary structure, enabling switching between a random configuration (*trans*) and a well-defined β -strand geometry (*cis*) that mimics the β -hairpin motif of native nNOS, to facilitate binding to the PDZ domain of α -syntrophin.⁸²

An alternative method to control the activity of antibacterial peptides is a hypoxia-activated prodrug strategy. Tissue hypoxia is a common microenvironmental hallmark associated with bacterial infection, with low levels of oxygen caused by reduced blood supply to the infected tissue.⁸⁷ Hence, hypoxia-activated prodrugs present as an attractive strategy to regulate the activity of an antibiotic, such that the active agent is only released under conditions of low oxygen, as found in specific bacterial-infected tissues.⁸⁸⁻⁸⁹ These prodrugs are designed by masking the warhead with a protecting group, which is reduced under hypoxic conditions to produce the corresponding active form for a directed therapeutic effect.⁹⁰ This particular approach limits general exposure to the active agent, thereby mitigating possible undesirable side effects. Importantly, it improves the selectivity of drug delivery as the antibacterial is only

activated at the site of infection, which can potentially lead to the suppression of antibiotic resistance. Figure 1.9 illustrates the mechanism of reductive activation for a particular hypoxia-activated prodrug, Evofosfamide (TH 302), which contains a 2-nitroimidazole protecting group. The reductase mediates one-electron reduction of the prodrug to produce a radical anion.⁹⁰ In the presence of oxygen, the unpaired electron in the radical anion is rapidly scavenged by molecular oxygen to regenerate the prodrug, resulting in a futile cycle.⁹⁰ Conversely, in a hypoxic environment, the radical anion will be reduced further, inducing fragmentation to release the active drug for, in this case, anticancer activity.⁹⁰ This concept has been widely employed in cancer research to design and synthesize hypoxia-activated prodrugs,⁹¹⁻⁹³ and a number of these prodrugs are currently undergoing clinical studies as they have demonstrated great promise for targeted therapy.⁹⁴ However, hypoxia-activated prodrug strategies for bacterial-infected tissue are in their infancy, thereby signifying the need for future fundamental research in this area.

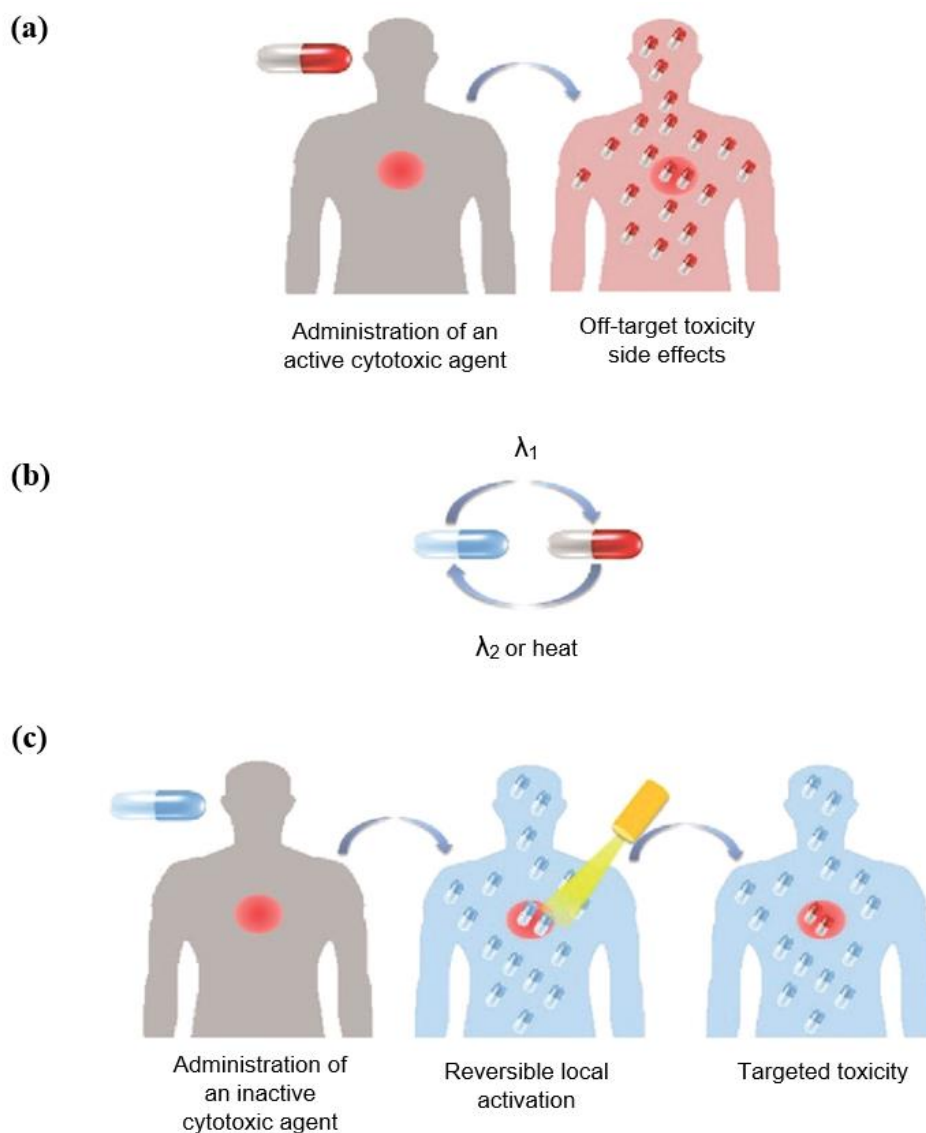


Figure 1.6. Differences between conventional delivery of a bioactive compound and photopharmacology. (a) Conventional delivery of a bioactive compound causes off-target side effects due to the non-selective toxicity. (b) Reversible switching between the inactive (blue) and active (red) compound using light of a specific wavelength. (c) The photopharmacological approach reversibly activates the inactive compound to allow localized treatment and targeted toxicity upon irradiation using light of a specific wavelength. (Figure adapted from Szymanski et al.⁴³)

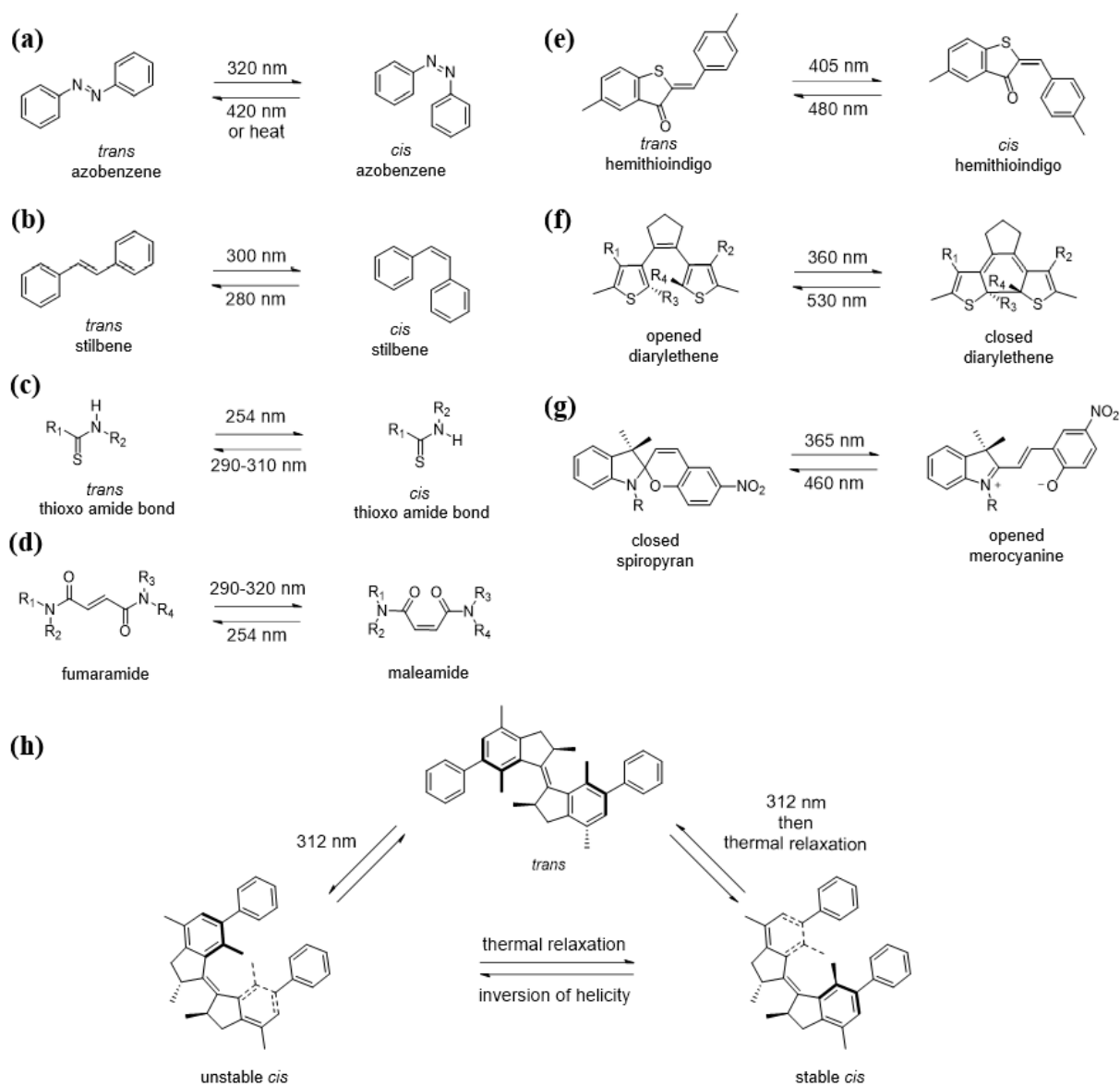


Figure 1.7. Chemical structures of various photoswitches used in photopharmacology, showing photoisomerization using light of a specific wavelength. **(a)** Azobenzene. **(b)** Stilbene. **(c)** Thioxylated amide. **(d)** Fumaramide-maleamide. **(e)** Hemithioindigo. **(f)** Diarylethene. **(g)** Spiropyran-merocyanine. **(h)** Overcrowded alkene.

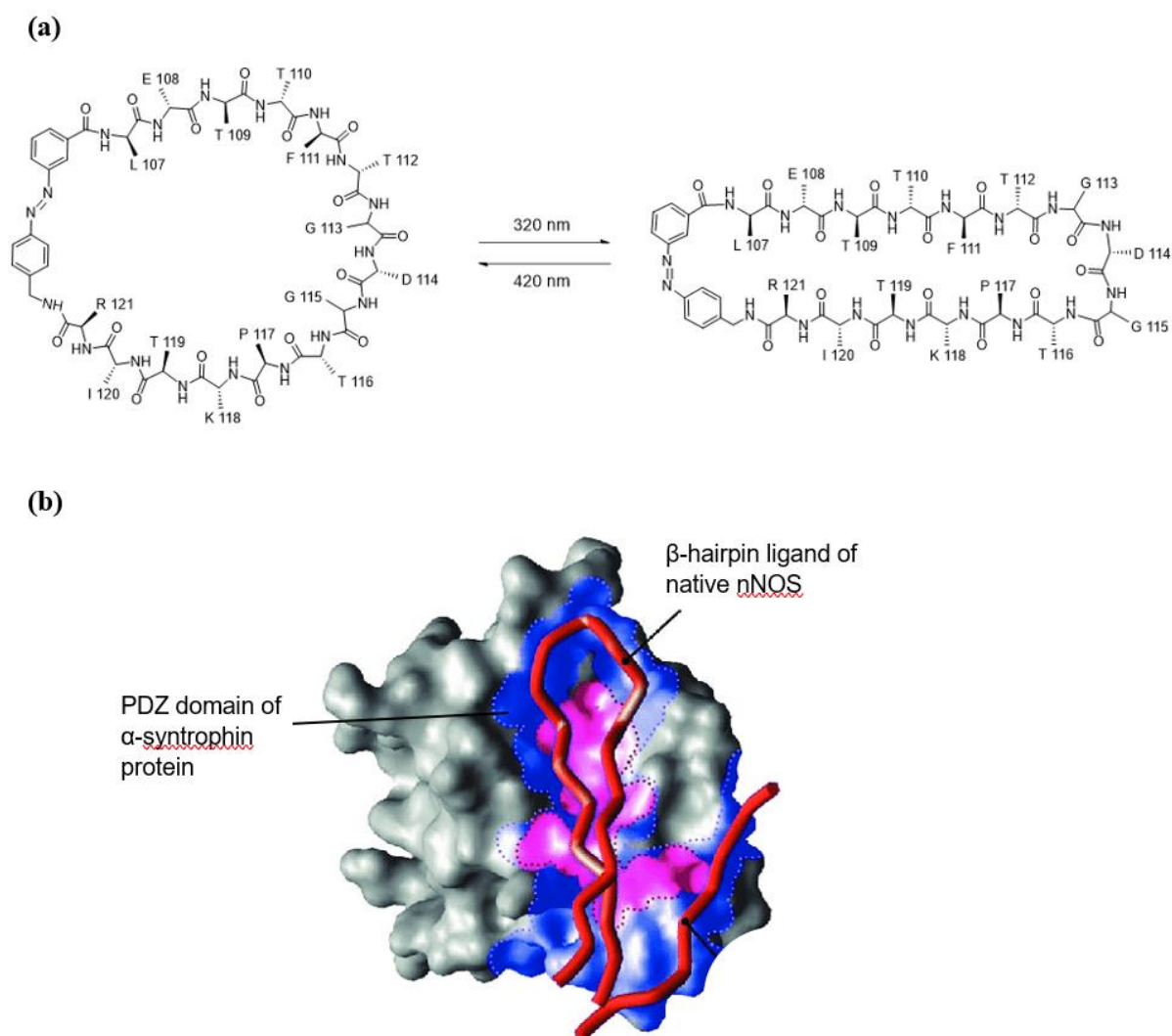


Figure 1.8. Photoswitchable peptide-based biosensor containing an azobenzene photoswitch, modelled on the β -hairpin region of neuronal nitric oxide synthase (nNOS).⁸² **(a)** The large spatial dissimilarity between the *trans* (left) and *cis* (right) configurations. The azobenzene in its *cis* configuration mimics the β -hairpin motif of nNOS, producing a cyclic peptide with a well-defined β -strand geometry for binding to the PDZ domain of the α -syntrophin protein. In contrast, the ill-defined *trans* configuration does not allow binding to α -syntrophin. **(b)** Crystal structure showing the well-defined β -strand and β -hairpin secondary structures of native nNOS for binding to the PDZ domain of the α -syntrophin protein.⁹⁵

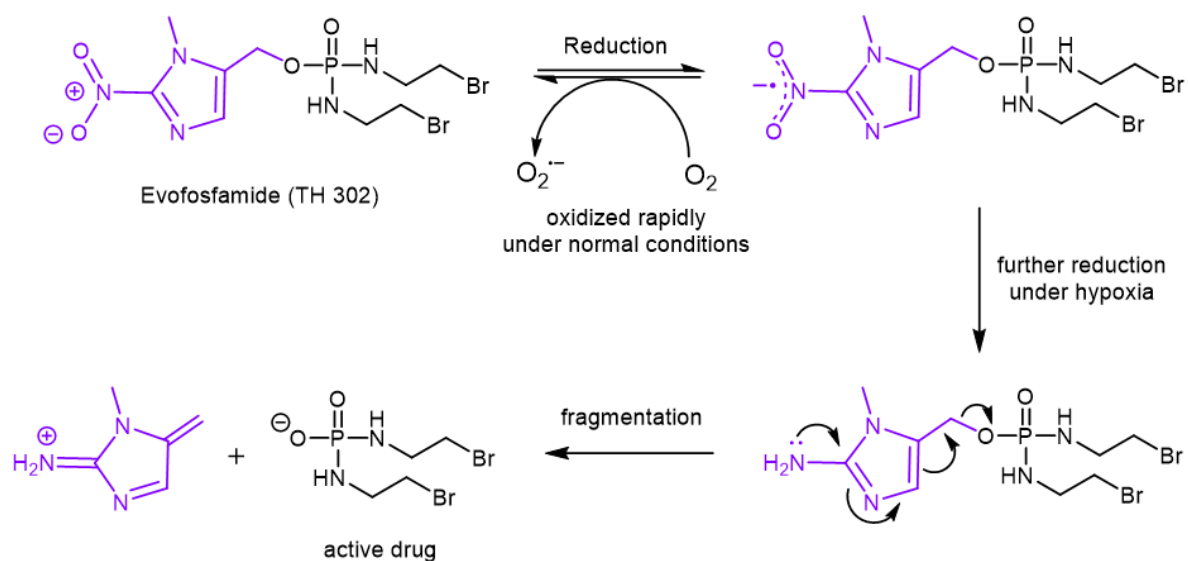


Figure 1.9. Reductive activation of a hypoxia-activated prodrug, Evofosfamide (TH 302), which contains a 2-nitroimidazole protecting group (purple). The reductase mediates one-electron reduction of the prodrug to form a radical anion. In well-oxygenated tissue, the unpaired electron of the radical anion will be rapidly scavenged by molecular oxygen to regenerate the prodrug, resulting in a futile cycle. In contrast, the prodrug radical anion will be reduced further and fragmented to trigger an anticancer effect under a hypoxic environment.⁹⁰

1.2 Dynamic behavior of proteins / peptides

All proteins are dynamic structures⁹⁶ that undergo random thermal fluctuations and conformational changes to regulate a complex network of molecular recognition and interaction for a multitude of biological processes.^{15,97} The dynamic nature of proteins indicates that merely probing the secondary structural elements does not adequately provide all crucial information needed to understand protein function, as protein behavior and properties stem from protein dynamics.⁹⁸⁻⁹⁹ Indeed, in a growing number of cases, cellular functions are defined by intrinsically disordered proteins, which can fold into well-defined complexes upon binding to their ligands to perform a specific function.¹⁰⁰⁻¹⁰⁴ The functional role of such intrinsically disordered proteins is acknowledged in areas such as transcriptional regulation,¹⁰⁵ translational regulation,¹⁰⁶ and cellular signal transduction,¹⁰⁷ thus demonstrating the importance of flexibility for such transient interactions. Moreover, structural plasticity also enables these intrinsically disordered proteins to interact with multiple binding partners to optimize function.¹⁰⁸ Hence, understanding protein function requires comprehensive studies on the structural and dynamic properties (structural dynamics) of proteins. However, the structural dynamic properties of proteins cannot be fully elucidated under equilibrium conditions,⁹⁹ such as X-ray crystallography, as this approach only provides a snapshot of the peptide frozen in crystal structures.⁹⁸ To further our understanding of structured/unstructured proteins in motion, sophisticated biophysical instrumentation is required to measure the physical properties from which their structural dynamic behavior can be inferred. Moreover, it is extremely challenging to probe the intrinsic structural dynamic properties of proteins due to their conformational complexity.¹⁰⁹ Thus, a model peptide containing a well-defined secondary structure, able to be controlled by such strategies as those discussed in section 1.1.3, presents as an ideal candidate to probe the structural dynamic behavior of peptides. Exercising control over the secondary structure allows for detection and measurement of the physical properties that are specific to each peptide conformation, providing insights into the structural dynamic behavior that governs protein/peptide function.

1.2.1 Probing the structural dynamic behavior of peptides through single-molecule junctions

The single-molecule junction method provides an ideal platform to probe the structural dynamic behavior of peptides, as it allows ultrasensitive detection and measurement of the structural dynamic properties of peptides in real-time, with single-bond resolution (Figure 1.10). A typical single-molecule junction comprises a molecule bridged between a pair of nanogapped metal or graphene electrodes. The single-molecule contains anchoring groups, for example, amine ($-NH_2$), thiols ($-SH$), and fullerenes on its termini or side chains, to allow coupling to functionalized electrodes via donor-acceptor (dative) interactions, or through covalent bonding.¹¹⁰⁻¹¹¹ In general, covalent linkages are more stable than dative bonding due to greater bond strength.¹¹² The working concept of a single-molecule junction involves detecting the biophysical changes induced by an external stimulus such as light, temperature, magnetic field, biological interaction, and chemical stimulus, which are then transduced into measurable signals.¹¹³ These signals can be characterized using microscopic, electrical, optical, or optoelectronic techniques,¹¹⁴ which allow direct observation of novel phenomena such as the Kondo effect, negative differential resistance, and Coulomb blockade.¹¹⁵ Moreover, the single-molecule junction enables the discovery of intrinsic physical properties of materials (e.g., structural dynamics) that are not accessible in bulk molecular crystals using conventional means.¹¹⁶⁻¹¹⁷ Hence, several experimental techniques have been developed to fabricate and study single-molecule junctions, including mechanically controllable break junctions (MCBJs),¹¹⁸⁻¹²⁰ atomic force microscopy (AFM),¹²¹⁻¹²² electromigration,¹²³⁻¹²⁴ scanning tunneling microscopy break junctions (STM-BJ),^{121, 125-126} and oxidative lithography (Figure 1.11). The Guo group demonstrated the establishment of a graphene-molecule-graphene single-molecule junction (GMG-SMJ) (Figure 1.12) to study a range of fundamental chemical processes including hydrogen bond dynamics,¹²⁷ nucleophilic substitution reaction,¹²⁸ conductance switching,¹²⁹⁻¹³¹ and charge transport,¹³²⁻¹³³ thus highlighting the robustness and versatility of this technique. The fabrication of a GMG-SMJ begins with the growth of single-layered graphene on copper foils via chemical vapor deposition (CVD). The graphene films are then transferred onto the SiO_2/Si wafers, and the gold electrodes are patterned by lithography and thermal evaporation. Next, the nanogapped graphene electrode arrays are constructed by electron beam lithography (EBL), followed by oxygen plasma etching to functionalize the

graphene point contacts with carboxylic acid groups. Lastly, the target molecule is coupled onto the carboxylic acid groups on the graphene point contacts via amide bonds to form a GMG-SMJ, where the successful formation of a GMG-SMJ is confirmed by a typical I - V curve. The GMG-SMJ nanodevice is characterized using electrical detection, which transduces molecular information into quantized changes in conductance.¹³⁴⁻¹³⁵ This label-free technique is ideal for investigating the structural dynamic behavior of a photoswitchable peptide, whereas the alternative optical and mechanical detection methods can themselves induce undesirable structural changes within the molecule.¹³⁶⁻¹³⁷ Real-time conductance measurements on the GMG-SMJ platform enable the structural dynamic behavior of both well-defined *cis* and intrinsically disordered *trans* peptides to be revealed and compared from within the one single-peptide, thus elucidating important fundamental insights into this dynamic phenomenon.

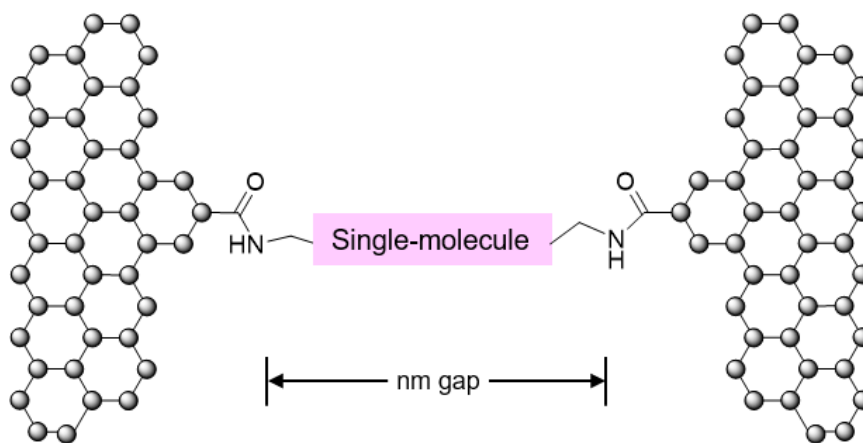


Figure 1.10. Schematic representation of a single-molecule junction containing a molecule bridged between a pair of nanogapped graphene electrodes, anchored via amide bonds.

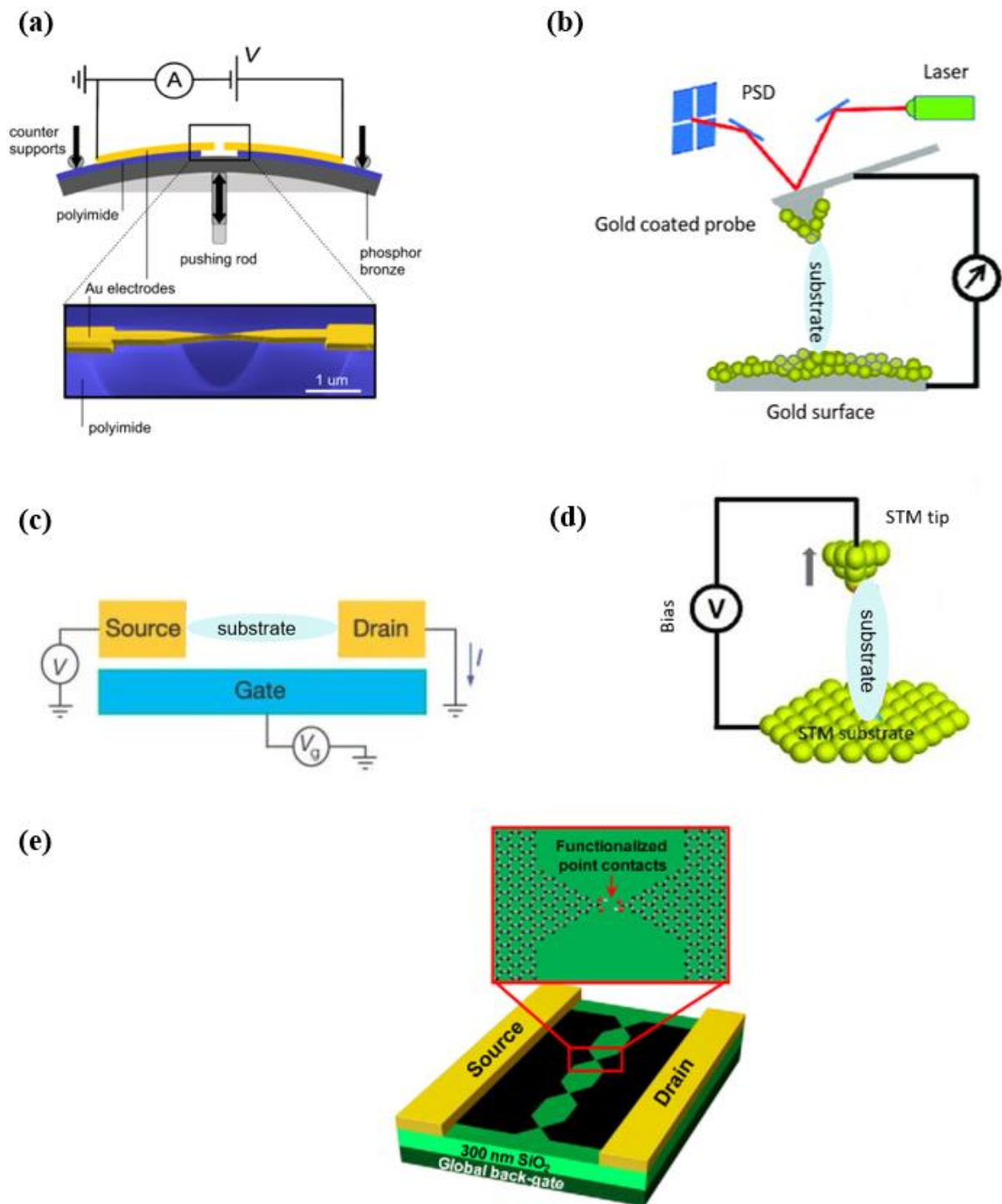


Figure 1.11. Schematic representations of experimental techniques used to fabricate and study single-molecule junctions. **(a)** Mechanically controllable break junctions (MCBJs).¹¹⁸ **(b)** Atomic force microscopy (AFM).¹²² **(c)** Electromigration.¹²⁴ **(d)** Scanning tunneling microscopy break junctions (STM-BJ).¹²¹ **(e)** Oxidative lithography.¹³⁸

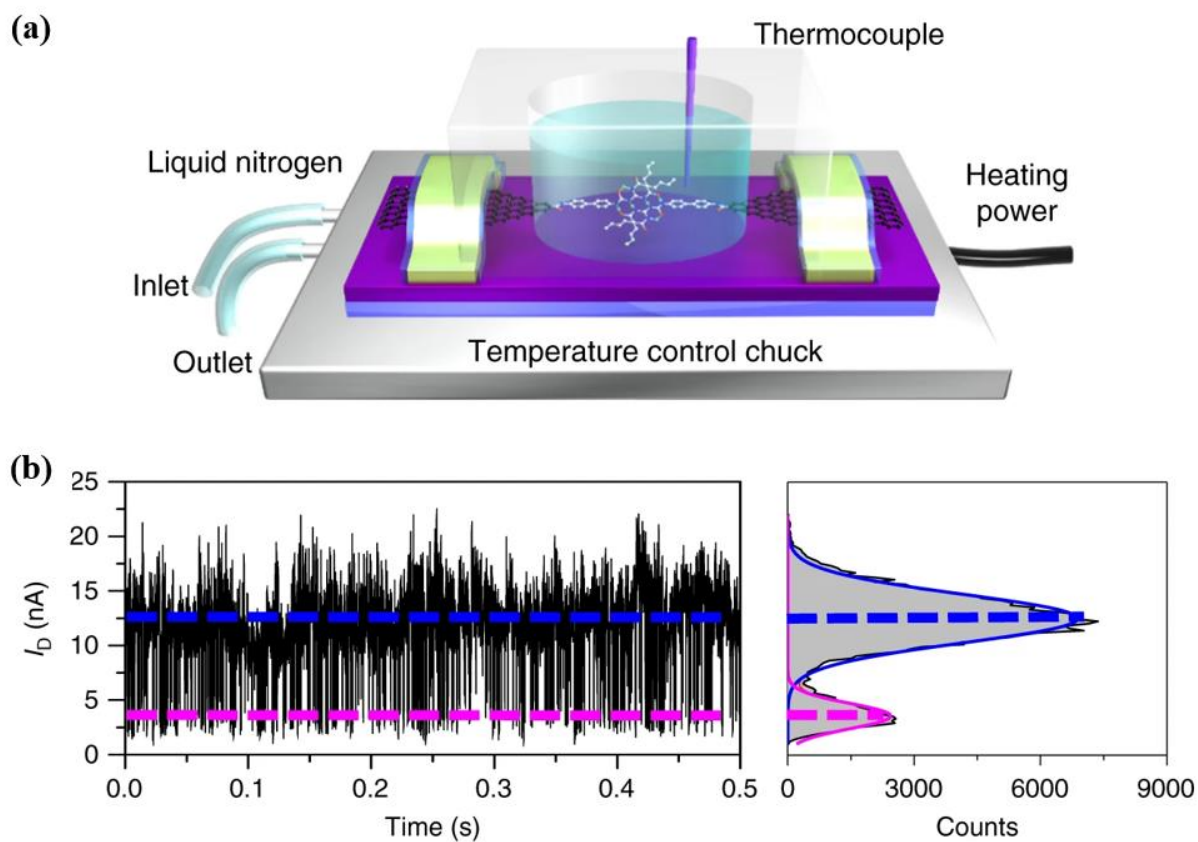


Figure 1.12. Experimental setup and real-time conductance measurements of a single-molecule junction developed by the Guo group.¹³⁹ **(a)** Schematic illustration of the experimental setup of a graphene-molecule-graphene single-molecule junction (GMG-SMJ) characterized by electrical conductance. **(b)** Real-time conductance measurements to elucidate the dynamic behavior of the single-molecule. The right-hand panel shows the corresponding histogram of conductance levels, exhibiting a bimodal distribution. $V_{\text{bias}} = 300$ mV.

1.3 Work presented in this thesis

1.3.1 Photoswitchable antibacterial peptides

Photopharmacology has been used to modulate the antibacterial activity of cyclic gramicidin S peptide mimetics. An azobenzene photoswitch is incorporated into the backbone of gramicidin S to allow control of the peptide secondary structure upon photoisomerization. The two corner amino acid residues, D-phenylalanine and proline, were chosen for replacement as *cis* azobenzene mimics the β -turn in a cyclic peptide to give a well-defined β -sheet secondary structure. In contrast, the *trans* azobenzene moiety separates both β -strands to totally disrupt the secondary structure, resulting in an ill-defined, random configuration. Hence, the *cis* isomer of each peptide mimetic is expected to retain the antibacterial activity of the natural gramicidin S, while the *trans* isomer is not. Moreover, the effects of the positive charges and amphiphilicity of the peptide mimetics were also investigated, by substituting the ornithine residues of gramicidin S with either arginine (positively charged) or glutamic acid (negatively charged). In this thesis, a series of gramicidin S peptide mimetics were rationally designed and synthesized to demonstrate the relationship between secondary structure/charge/amphiphilicity and antibacterial activity. The peptides are assayed against *Staphylococcus aureus* (*S. aureus*) to assess their respective antibacterial properties. This study is described in detail in Chapter 2.

In addition to the aforementioned gramicidin S peptide mimetics, this photopharmacological approach was used to modulate the antibacterial activity of three tetrapeptides, based on a known synthetic peptide that possesses a rapid bactericidal activity against methicillin-resistant *S. aureus* (MRSA).¹⁴⁰ Similarly, an azobenzene photoswitch is integrated into either the N-terminal side chain, C-terminal side chain, or the C-terminus, to allow reversible switching between the *cis*-enriched and *trans*-enriched photostationary states (PSS). This study reveals the importance of numerous factors influencing antibacterial peptide activity against *S. aureus* such as net positive charge, hydrophobicity, position of the azobenzene photoswitch, secondary structure, and amphiphilicity. The study is detailed in Chapter 3.

1.3.2 Hypoxia-activated antibacterial prodrug

A hypoxia-activated prodrug approach offers a possible alternative to photopharmacology to control the activity of antibacterial drugs for localized treatment. In this thesis, a hypoxia-activated antibacterial prodrug based on a broad spectrum antibacterial compound,¹⁴¹ was designed and synthesized to contain a protecting group able to be activated under conditions that mimic hypoxia, to target both Gram-positive bacteria, *S. aureus*, and Gram-negative bacteria, *E. coli*. Significantly, the active antibacterial compound is known to be nontoxic towards mammalian cells,¹⁴¹ and possesses a lysine residue with free amines at both the N-terminus and side chain that are essential for its bioactivity. These amines were masked with 4-nitrobenzylcarbonyl protecting groups to neutralize the cationic charges of the compound, thereby abolishing electrostatic interactions that allow binding to the bacteria. Subsequent removal of the protecting groups under reductive conditions that mimic hypoxia is proposed to restore the binding interaction and hence, antibacterial activity. The full details of this study are reported in Chapter 4.

1.3.3 Unravelling the structural dynamic properties within a photoswitchable peptide

Due to the intrinsic complexity of proteins, model peptides present as ideal alternatives to unravel inherent structural dynamic properties.¹⁰⁹ Peptide **2a** (Figure 2.1, Chapter 2) was chosen here as it contains an in-built azobenzene photoswitch to allow reversible interconversion between two isomers. We have previously demonstrated that photoisomerization of this peptide induces a significant geometric change between a well-defined β -strand geometry of the *cis* isomer and a random, disordered structure for the *trans* isomer.⁸¹ By having both isomers within the one simple model, it is possible to study their respective structural dynamic behavior in a controlled setting at the most fundamental level. To fabricate this nanodevice, cyclic peptide **2a** was covalently attached to nanogapped graphene electrodes to form a graphene-molecule-graphene single-molecule junction (GMG-SMJ), characterized by electrical detection. When the peptide is tethered between the nanogapped electrodes, photoisomerization of the

azobenzene photoswitch is expected to result in a significant difference in electrical conductance between the two isomers due to their distinctive structures. Real-time conductance measurements on the GMG-SMJ platform reveal fundamental structural dynamic behavior of both well-defined and intrinsically disordered peptides, thus elucidating important insights into this dynamic phenomenon which may potentially extend to proteins. This study is presented in Chapter 5.

1.4 References

1. Adler, M. J.; Jamieson, A. G.; Hamilton, A. D., Hydrogen-Bonded Synthetic Mimics of Protein Secondary Structure as Disruptors of Protein-Protein Interactions. In *Small-Molecule Inhibitors of Protein-Protein Interactions*, Vassilev, L.; Fry, D., Eds. Springer: Berlin, 2011; pp 1–23.
2. Gromiha, M. M., Proteins. In *Protein Bioinformatics: From Sequence to Function*, Elsevier: New Delhi, 2010; pp 1–27.
3. Ji, Y.-Y.; Li, Y.-Q., The role of secondary structure in protein structure selection. *Eur. Phys. J. E* **2010**, *32* (1), 103–107.
4. Feng, Z.; Hu, X.; Jiang, Z.; Song, H.; Ashraf, M. A., The recognition of multi-class protein folds by adding average chemical shifts of secondary structure elements. *Saudi J. Biol. Sci.* **2016**, *23* (2), 189–197.
5. Alberts, B.; Johnson, A.; Lewis, J.; Raff, M.; Roberts, K.; Walter, P., *Molecular Biology of the Cell, 4th edition*. Garland Science: New York, 2002.
6. Yu, J.; Horsley, J. R.; Abell, A. D., Peptides as Bio-Inspired Electronic Materials: An Electrochemical and First-Principles Perspective. *Acc. Chem. Res.* **2018**, *51* (9), 2237–2246.
7. Haimov, B.; Srebnik, S., A closer look into the α -helix basin. *Sci. Rep.* **2016**, *6* (1), 38341.
8. Boyle, A. L.; Woolfson, D. N., *De novo* designed peptides for biological applications. *Chem. Soc. Rev.* **2011**, *40* (8), 4295–4306.
9. Turk, D., Boxes of Model Building and Visualization. In *Protein Crystallography: Methods and Protocols*, Wlodawer, A.; Dauter, Z.; Jaskolski, M., Eds. Springer New York: New York, NY, 2017; pp 491–548.

10. Cheng, P.-N.; Pham, J. D.; Nowick, J. S., The supramolecular chemistry of β -sheets. *J. Am. Chem. Soc.* **2013**, *135* (15), 5477–5492.
11. Loughlin, W. A.; Tyndall, J. D. A.; Glenn, M. P.; Hill, T. A.; Fairlie, D. P., Update 1 of: Beta-Strand Mimetics. *Chem. Rev.* **2010**, *110* (6), PR32–PR69.
12. Thorat, V. H.; Ingole, T. S.; Vijayadas, K. N.; Nair, R. V.; Kale, S. S.; Ramesh, V. V. E.; Davis, H. C.; Prabhakaran, P.; Gonnade, R. G.; Gawade, R. L.; Puranik, V. G.; Rajamohanam, P. R.; Sanjayan, G. J., The Ant-Pro Reverse-Turn Motif. Structural Features and Conformational Characteristics. *Eur. J. Org. Chem.* **2013**, *2013* (17), 3529–3542.
13. de Brevern, A. G., Extension of the classical classification of β -turns. *Sci. Rep.* **2016**, *6* (1), 33191.
14. Obrecht, D.; Chevalier, E.; Moehle, K.; Robinson, J. A., β -Hairpin protein epitope mimetic technology in drug discovery. *Drug Discov. Today Technol.* **2012**, *9* (1), e63–e69.
15. Laxio Arenas, J.; Kaffy, J.; Onger, S., Peptides and peptidomimetics as inhibitors of protein–protein interactions involving β -sheet secondary structures. *Curr. Opin. Chem. Biol.* **2019**, *52*, 157–167.
16. Zhou, X. E.; He, Y.; de Waal, P. W.; Gao, X.; Kang, Y.; Van Eps, N.; Yin, Y.; Pal, K.; Goswami, D.; White, T. A.; Barty, A.; Latorraca, N. R.; Chapman, H. N.; Hubbell, W. L.; Dror, R. O.; Stevens, R. C.; Cherezov, V.; Gurevich, V. V.; Griffin, P. R.; Ernst, O. P.; Melcher, K.; Xu, H. E., Identification of Phosphorylation Codes for Arrestin Recruitment by G Protein-Coupled Receptors. *Cell* **2017**, *170* (3), 457–469.
17. Lauenstein, J. U.; Scherm, M. J.; Udgate, A.; Moncrieffe, M. C.; Fisher, D. I.; Gay, N. J., Negative Regulation of TLR Signaling by BCAP Requires Dimerization of Its DBB Domain. *J. Immunol.* **2020**, *204* (8), 2269.
18. Gokhale, A.; Weldeghiorghis, T. K.; Taneja, V.; Satyanarayanajois, S. D., Conformationally Constrained Peptides from CD2 To Modulate Protein–Protein Interactions between CD2 and CD58. *J. Med. Chem.* **2011**, *54* (15), 5307–5319.
19. Cause, G. F.; Brazhnikova, M. G., Gramicidin S Origin and Mode of Action. *Lancet* **1944**, *244* (6327), 715–716.
20. Llamas-Saiz, A. L.; Grotenbreg, G. M.; Overhand, M.; van Raaij, M. J., Double-stranded helical twisted β -sheet channels in crystals of gramicidin S grown in the presence of trifluoroacetic and hydrochloric acids. *Acta Crystallogr. D* **2007**, *63* (3), 401–407.
21. Prenner, E. J.; Kiricsi, M.; Jelokhani-Niaraki, M.; Lewis, R. N. A. H.; Hodges, R. S.; McElhaney, R. N., Structure-activity relationships of diastereomeric lysine ring size analogs of

- the antimicrobial peptide gramicidin S: mechanism of action and discrimination between bacterial and animal cell membranes. *J. Biol. Chem.* **2005**, *280* (3), 2002–2011.
22. Jelokhani-Niaraki, M.; Hodges, R. S.; Meissner, J. E.; Hassenstein, U. E.; Wheaton, L., Interaction of gramicidin S and its aromatic amino-acid analog with phospholipid membranes. *Biophys. J.* **2008**, *95* (7), 3306–3321.
23. Tennessen, J. A., Molecular evolution of animal antimicrobial peptides: widespread moderate positive selection. *J. Evol. Biol.* **2005**, *18* (6), 1387–1394.
24. Hartmann, M.; Berditsch, M.; Hawecker, J.; Ardakani, M. F.; Gerthsen, D.; Ulrich, A. S., Damage of the bacterial cell envelope by antimicrobial peptides gramicidin S and PGLa as revealed by transmission and scanning electron microscopy. *Antimicrob. Agents Chemother.* **2010**, *54* (8), 3132–3142.
25. Berditsch, M.; Afonin, S.; Reuster, J.; Lux, H.; Schkolin, K.; Babii, O.; Radchenko, D. S.; Abdullah, I.; William, N.; Middel, V.; Strähle, U.; Nelson, A.; Valko, K.; Ulrich, A. S., Supreme activity of gramicidin S against resistant, persistent and biofilm cells of *Staphylococci* and *Enterococci*. *Sci. Rep.* **2019**, *9* (1), 17938.
26. Wenzel, M.; Rautenbach, M.; Vosloo, J. A.; Siersma, T.; Aisenbrey, C. H. M.; Zaitseva, E.; Laubscher, W. E.; van Rensburg, W.; Behrends, J. C.; Bechinger, B.; Hamoen, L. W., The Multifaceted Antibacterial Mechanisms of the Pioneering Peptide Antibiotics Tyrocidine and Gramicidin S. *mBio* **2018**, *9* (5), e00802-18.
27. Kawai, M.; Yamamura, H.; Tanaka, R.; Umemoto, H.; Ohmizo, C.; Higuchi, S.; Katsu, T., Proline residue-modified polycationic analogs of gramicidin S with high antibacterial activity against both Gram-positive and Gram-negative bacteria and low hemolytic activity. *J. Pept. Res.* **2005**, *65* (1), 98–104.
28. Bechinger, B.; Gorr, S. U., Antimicrobial Peptides: Mechanisms of Action and Resistance. *J. Dent. Res.* **2017**, *96* (3), 254–260.
29. Wallis, R. S.; Hafner, R., Advancing host-directed therapy for tuberculosis. *Nat. Rev. Immunol.* **2015**, *15* (4), 255–263.
30. Jelokhani-Niaraki, M.; Kondejewski, L. H.; Wheaton, L. C.; Hodges, R. S., Effect of ring size on conformation and biological activity of cyclic cationic antimicrobial peptides. *J. Med. Chem.* **2009**, *52* (7), 2090–2097.
31. Swierstra, J.; Kapoerchan, V.; Knijnenburg, A.; van Belkum, A.; Overhand, M., Structure, toxicity and antibiotic activity of gramicidin S and derivatives. *Eur. J. Clin. Microbiol. Infect. Dis.* **2016**, *35* (5), 763–769.

32. Tamaki, M.; Takanashi, K.; Harada, T.; Fujinuma, K.; Shindo, M.; Kimura, M.; Uchida, Y., Novel Cycloundecapeptides Related to Gramicidin S with Both High Antibiotic Activity and Low Hemolytic Activity. *Chem. Pharm. Bull.* **2011**, *59* (12), 1481–1484.
33. Legrand, B.; Mathieu, L.; Lebrun, A.; Andriamanarivo, S.; Lisowski, V.; Masurier, N.; Zirah, S.; Kang, Y. K.; Martinez, J.; Maillard, L. T., Thiazole-Based γ -Building Blocks as Reverse-Turn Mimetic to Design a Gramicidin S Analogue: Conformational and Biological Evaluation. *Chem. Eur. J.* **2014**, *20* (22), 6713–6720.
34. Wan, Y.; Stanovych, A.; Gori, D.; Zirah, S.; Kouklovsky, C.; Alezra, V., β,γ -diamino acids as building blocks for new analogues of Gramicidin S: Synthesis and biological activity. *Eur. J. Med. Chem.* **2018**, *149*, 122–128.
35. Torres, M. D. T.; Sothiselvam, S.; Lu, T. K.; de la Fuente-Nunez, C., Peptide Design Principles for Antimicrobial Applications. *J. Mol. Biol.* **2019**, *431* (18), 3547–3567.
36. Guan, Q.; Huang, S.; Jin, Y.; Campagne, R.; Alezra, V.; Wan, Y., Recent Advances in the Exploration of Therapeutic Analogues of Gramicidin S, an Old but Still Potent Antimicrobial Peptide. *J. Med. Chem.* **2019**, *62* (17), 7603–7617.
37. Hilpert, K.; Volkmer-Engert, R.; Walter, T.; Hancock, R. E. W., High-throughput generation of small antibacterial peptides with improved activity. *Nat. Biotechnol.* **2005**, *23* (8), 1008–1012.
38. Lee, P.-C.; Chu, C.-C.; Tsai, Y.-J.; Chuang, Y.-C.; Lung, F.-D., Design, synthesis, and antimicrobial activities of novel functional peptides against Gram-positive and Gram-negative bacteria. *Chem. Biol. Drug Des.* **2019**, *94* (2), 1537–1544.
39. Pfalzgraff, A.; Brandenburg, K.; Weindl, G., Antimicrobial Peptides and Their Therapeutic Potential for Bacterial Skin Infections and Wounds. *Front. Pharmacol.* **2018**, *9*, 281.
40. Broichhagen, J.; Frank, J. A.; Trauner, D., A Roadmap to Success in Photopharmacology. *Acc. Chem. Res.* **2015**, *48* (7), 1947–1960.
41. Hüll, K.; Morstein, J.; Trauner, D., *In Vivo* Photopharmacology. *Chem. Rev.* **2018**, *118* (21), 10710–10747.
42. Peddie, V.; Abell, A. D., Photocontrol of peptide secondary structure through non-azobenzene photoswitches. *J. Photochem. Photobiol. C* **2019**, *40*, 1–20.
43. Szymanski, W.; Ourailidou, M. E.; Velema, W. A.; Dekker, F. J.; Feringa, B. L., Light-Controlled Histone Deacetylase (HDAC) Inhibitors: Towards Photopharmacological Chemotherapy. *Chem. Eur. J.* **2015**, *21* (46), 16517–16524.

44. Velema, W. A.; van der Berg, J. P.; Hansen, M. J.; Szymanski, W.; Driessen, A. J. M.; Feringa, B. L., Optical control of antibacterial activity. *Nat. Chem.* **2013**, *5* (11), 924–928.
45. Lerch, M. M.; Hansen, M. J.; van Dam, G. M.; Szymanski, W.; Feringa, B. L., Emerging Targets in Photopharmacology. *Angew. Chem. Int. Ed.* **2016**, *55* (37), 10978–10999.
46. Velema, W. A.; Szymanski, W.; Feringa, B. L., Photopharmacology: Beyond Proof of Principle. *J. Am. Chem. Soc.* **2014**, *136* (6), 2178–2191.
47. Feliciano, M.; Vytla, D.; Medeiros, K. A.; Chambers, J. J., The GABA(A) receptor as a target for photochromic molecules. *Bioorg. Med. Chem.* **2010**, *18* (22), 7731–7738.
48. Renner, C.; Moroder, L., Azobenzene as Conformational Switch in Model Peptides. *ChemBioChem* **2006**, *7* (6), 869–878.
49. Samanta, S.; Qin, C.; Lough, A. J.; Woolley, G. A., Bidirectional Photocontrol of Peptide Conformation with a Bridged Azobenzene Derivative. *Angew. Chem. Int. Ed.* **2012**, *51* (26), 6452–6455.
50. Erdélyi, M.; Karlén, A.; Gogoll, A., A New Tool in Peptide Engineering: A Photoswitchable Stilbene-type β -Hairpin Mimetic. *Chem. Eur. J.* **2006**, *12* (2), 403–412.
51. Karlsson, C.; Blom, M.; Johansson, M.; Jansson, A. M.; Scifo, E.; Karlén, A.; Govender, T.; Gogoll, A., Phototriggerable peptidomimetics for the inhibition of *Mycobacterium tuberculosis* ribonucleotide reductase by targeting protein–protein binding. *Org. Biomol. Chem.* **2015**, *13* (9), 2612–2621.
52. Satzger, H.; Root, C.; Gilch, P.; Zinth, W.; Wildemann, D.; Fischer, G., Photoswitchable Elements within a Peptide Backbone Ultrafast Spectroscopy of Thioxylated Amides. *J. Phys. Chem. B* **2005**, *109* (10), 4770–4775.
53. Mazzier, D.; Crisma, M.; De Poli, M.; Marafon, G.; Peggion, C.; Clayden, J.; Moretto, A., Helical Foldamers Incorporating Photoswitchable Residues for Light-Mediated Modulation of Conformational Preference. *J. Am. Chem. Soc.* **2016**, *138* (25), 8007–8018.
54. Petermayer, C.; Dube, H., Indigoid Photoswitches: Visible Light Responsive Molecular Tools. *Acc. Chem. Res.* **2018**, *51* (5), 1153–1163.
55. Kitzig, S.; Rück-Braun, K., Synthesis of hemithioindigo-based chromopeptides by using the Tmb auxiliary in native chemical ligation studies. *J. Pept. Sci.* **2017**, *23* (7-8), 567–573.
56. Babii, O.; Afonin, S.; Ishchenko, A. Y.; Schober, T.; Negelia, A. O.; Tolstanova, G. M.; Garmanchuk, L. V.; Ostapchenko, L. I.; Komarov, I. V.; Ulrich, A. S., Structure–Activity Relationships of Photoswitchable Diarylethene-Based β -Hairpin Peptides as Membranolytic Antimicrobial and Anticancer Agents. *J. Med. Chem.* **2018**, *61* (23), 10793–10813.

57. Reisinger, B.; Kuzmanovic, N.; Löffler, P.; Merkl, R.; König, B.; Sterner, R., Exploiting Protein Symmetry To Design Light-Controllable Enzyme Inhibitors. *Angew. Chem. Int. Ed.* **2014**, *53* (2), 595–598.
58. Zhang, X.; Heng, S.; Abell, A. D., Photoregulation of α -Chymotrypsin Activity by Spiropyran-Based Inhibitors in Solution and Attached to an Optical Fiber. *Chem. Eur. J.* **2015**, *21* (30), 10703–10713.
59. Fujimoto, K.; Amano, M.; Horibe, Y.; Inouye, M., Reversible Photoregulation of Helical Structures in Short Peptides under Indoor Lighting/Dark Conditions. *Org. Lett.* **2006**, *8* (2), 285–287.
60. Poloni, C.; Stuart, M. C. A.; van der Meulen, P.; Szymanski, W.; Feringa, B. L., Light and heat control over secondary structure and amyloid-like fiber formation in an overcrowded-alkene-modified Trp zipper. *Chem. Sci.* **2015**, *6* (12), 7311–7318.
61. Griffiths, J., II. Photochemistry of azobenzene and its derivatives. *Chem. Soc. Rev.* **1972**, *1* (4), 481–493.
62. Hartley, G. S., The *Cis*-form of Azobenzene. *Nature* **1937**, *140* (3537), 281–281.
63. Bandara, H. M. D.; Burdette, S. C., Photoisomerization in different classes of azobenzene. *Chem. Soc. Rev.* **2012**, *41* (5), 1809–1825.
64. Lednev, I. K.; Ye, T. Q.; Matousek, P.; Towrie, M.; Foggi, P.; Neuwahl, F. V. R.; Umapathy, S.; Hester, R. E.; Moore, J. N., Femtosecond time-resolved UV-visible absorption spectroscopy of *trans*-azobenzene: dependence on excitation wavelength. *Chem. Phys. Lett.* **1998**, *290* (1), 68–74.
65. Qin, C.-G.; Lu, C.-X.; Ouyang, G.-W.; Qin, K.; Zhang, F.; Shi, H.-T.; Wang, X.-H., Progress of Azobenzene-based Photoswitchable Molecular Probes and Sensory Chips for Chemical and Biological Analysis. *Chinese J. Anal. Chem.* **2015**, *43* (3), 433–443.
66. Goulet-Hanssens, A.; Barrett, C. J., Photo-control of biological systems with azobenzene polymers. *J. Polym. Sci. Pol. Chem.* **2013**, *51* (14), 3058–3070.
67. Hamon, F.; Djedaini-Pilard, F.; Barbot, F.; Len, C., Azobenzenes-synthesis and carbohydrate applications. *Tetrahedron* **2009**, *65* (49), 10105–10123.
68. Sadovski, O.; Beharry, A. A.; Zhang, F.; Woolley, G. A., Spectral Tuning of Azobenzene Photoswitches for Biological Applications. *Angew. Chem. Int. Ed.* **2009**, *48* (8), 1484–1486.
69. Merino, E.; Ribagorda, M., Control over molecular motion using the *cis-trans* photoisomerization of the azo group. *Beilstein J. Org. Chem.* **2012**, *8*, 1071–1090.

70. Lubbe, A. S.; Szymanski, W.; Feringa, B. L., Recent developments in reversible photoregulation of oligonucleotide structure and function. *Chem. Soc. Rev.* **2017**, *46* (4), 1052–1079.
71. Freyer, W.; Brete, D.; Schmidt, R.; Gahl, C.; Carley, R.; Weinelt, M., Switching behavior and optical absorbance of azobenzene-functionalized alkanethiols in different environments. *J. Photochem. Photobiol. A* **2009**, *204* (2), 102–109.
72. Fujino, T.; Arzhantsev, S. Y.; Tahara, T., Femtosecond Time-Resolved Fluorescence Study of Photoisomerization of trans-Azobenzene. *J. Phys. Chem. A* **2001**, *105* (35), 8123–8129.
73. Kumar, G. S.; Neckers, D. C., Photochemistry of azobenzene-containing polymers. *Chem. Rev.* **1989**, *89* (8), 1915–1925.
74. Szymański, W.; Beierle, J. M.; Kistemaker, H. A. V.; Velema, W. A.; Feringa, B. L., Reversible Photocontrol of Biological Systems by the Incorporation of Molecular Photoswitches. *Chem. Rev.* **2013**, *113* (8), 6114–6178.
75. Schütt, M.; Krupka, S. S.; Milbradt, A. G.; Deindl, S.; Sinner, E.-K.; Oesterhelt, D.; Renner, C.; Moroder, L., Photocontrol of Cell Adhesion Processes: Model Studies with Cyclic Azobenzene-RGD Peptides. *Chem. Biol.* **2003**, *10* (6), 487–490.
76. Dong, M.; Babalhavaeji, A.; Samanta, S.; Beharry, A. A.; Woolley, G. A., Red-Shifting Azobenzene Photoswitches for *in Vivo* Use. *Acc. Chem. Res.* **2015**, *48* (10), 2662–2670.
77. Hansen, M. J.; Lerch, M. M.; Szymanski, W.; Feringa, B. L., Direct and Versatile Synthesis of Red-Shifted Azobenzenes. *Angew. Chem. Int. Ed.* **2016**, *55* (43), 13514–13518.
78. Wegener, M.; Hansen, M. J.; Driessen, A. J. M.; Szymanski, W.; Feringa, B. L., Photocontrol of Antibacterial Activity: Shifting from UV to Red Light Activation. *J. Am. Chem. Soc.* **2017**, *139* (49), 17979–17986.
79. Beharry, A. A.; Woolley, G. A., Azobenzene photoswitches for biomolecules. *Chem. Soc. Rev.* **2011**, *40* (8), 4422–4437.
80. Mahimwalla, Z.; Yager, K. G.; Mamiya, J.-i.; Shishido, A.; Priimagi, A.; Barrett, C. J., Azobenzene photomechanics: prospects and potential applications. *Polym. Bull.* **2012**, *69* (8), 967–1006.
81. Yeoh, Y. Q.; Yu, J.; Polyak, S. W.; Horsley, J. R.; Abell, A. D., Photopharmacological Control of Cyclic Antimicrobial Peptides. *ChemBioChem* **2018**, *19* (24), 2591–2597.
82. Horsley, J. R.; Yu, J.; Wegener, K. L.; Hoppmann, C.; Rück-Braun, K.; Abell, A. D., Photoswitchable peptide-based ‘on-off’ biosensor for electrochemical detection and control of protein-protein interactions. *Biosens. Bioelectron.* **2018**, *118*, 188–194.

83. Blanco, B.; Palasis, K. A.; Adwal, A.; Callen, D. F.; Abell, A. D., Azobenzene-containing photoswitchable proteasome inhibitors with selective activity and cellular toxicity. *Bioorg. Med. Chem.* **2017**, *25* (19), 5050–5054.
84. Pearson, D.; Abell, A. D., Structural Optimization of Photoswitch Ligands for Surface Attachment of α -Chymotrypsin and Regulation of Its Surface Binding. *Chem. Eur. J.* **2010**, *16* (23), 6983–6992.
85. Pearson, D.; Alexander, N.; Abell, A. D., Improved Photocontrol of α -Chymotrypsin Activity: Peptidomimetic Trifluoromethylketone Photoswitch Enzyme Inhibitors. *Chem. Eur. J.* **2008**, *14* (24), 7358–7365.
86. Kumeria, T.; Yu, J.; Alsawat, M.; Kurkuri, M. D.; Santos, A.; Abell, A. D.; Losic, D., Photoswitchable Membranes Based on Peptide-Modified Nanoporous Anodic Alumina: Toward Smart Membranes for On-Demand Molecular Transport. *Adv. Mater.* **2015**, *27* (19), 3019–3024.
87. Schaffer, K.; Taylor, C. T., The impact of hypoxia on bacterial infection. *FEBS J.* **2015**, *282* (12), 2260–2266.
88. Yang, H., Sha, W., Liu, Z., Tang, T., Liu, H., Qin, L., Cui, Z. Chen, J., Liu, F. Zheng, R., Huang, X., Wang, J., Feng, Y., Ge, B., Lysine acetylation of DosR regulates the hypoxia response of *Mycobacterium tuberculosis*. *Emerg. Microbes Infect.* **2018**, *7*, 34.
89. Fu, Q., Yang, Y. J., Li, C., Zeng, Q. F., Zhou, T., Li, N., Liu, Y., Liu, S. K., Liu, Z. J., The CC and CXC chemokine receptors in channel catfish (*Ictalurus punctatus*) and their involvement in disease and hypoxia responses. *Dev. Comp. Immunol.* **2017**, *77*, 241–251.
90. Wang, J.; Foehrenbacher, A.; Su, J.; Patel, R.; Hay, M. P.; Hicks, K. O.; Wilson, W. R., The 2-Nitroimidazole EF5 Is a Biomarker for Oxidoreductases That Activate the Bioreductive Prodrug CEN-209 under Hypoxia. *Clin. Cancer Res.* **2012**, *18* (6), 1684–1695.
91. Albertella, M. R.; Loadman, P. M.; Jones, P. H.; Phillips, R. M.; Rampling, R.; Burnet, N.; Alcock, C.; Anthony, A.; Vjaters, E.; Dunk, C. R.; Harris, P. A.; Wong, A.; Lalani, A. S.; Twelves, C. J., Hypoxia-Selective Targeting by the Bioreductive Prodrug AQ4N in Patients with Solid Tumors: Results of a Phase I Study. *Clin. Cancer Res.* **2008**, *14* (4), 1096–1104.
92. Jameson, M. B.; Rischin, D.; Pegram, M.; Gutheil, J.; Patterson, A. V.; Denny, W. A.; Wilson, W. R., A phase I trial of PR-104, a nitrogen mustard prodrug activated by both hypoxia and aldo-keto reductase 1C3, in patients with solid tumors. *Cancer Chemother. Pharmacol.* **2010**, *65* (4), 791–801.

93. Wang, J.; Guise, C. P.; Dachs, G. U.; Phung, Y.; Hsu, A.; Lambie, N. K.; Patterson, A. V.; Wilson, W. R., Identification of one-electron reductases that activate both the hypoxia prodrug SN30000 and diagnostic probe EF5. *Biochem. Pharmacol.* **2014**, *91* (4), 436–446.
94. Sharma, A.; Arambula, J. F.; Koo, S.; Kumar, R.; Singh, H.; Sessler, J. L.; Kim, J. S., Hypoxia-targeted drug delivery. *Chem. Soc. Rev.* **2019**, *48* (3), 771–813.
95. Hillier, B. J.; Christopherson, K. S.; Prehoda, K. E.; Brecht, D. S.; Lim, W. A., Unexpected Modes of PDZ Domain Scaffolding Revealed by Structure of nNOS-Syntrophin Complex. *Science* **1999**, *284* (5415), 812.
96. Vinson, V. J., Proteins in Motion. *Science* **2009**, *324* (5924), 197.
97. Iegre, J.; Brear, P.; Baker, D. J.; Tan, Y. S.; Atkinson, E. L.; Sore, H. F.; O' Donovan, D. H.; Verma, C. S.; Hyvönen, M.; Spring, D. R., Efficient development of stable and highly functionalised peptides targeting the CK2 α /CK2 β protein–protein interaction. *Chem. Sci.* **2019**, *10* (19), 5056–5063.
98. Henzler-Wildman, K.; Kern, D., Dynamic personalities of proteins. *Nature* **2007**, *450* (7172), 964–972.
99. Samuni, U.; Friedman, J. M., Proteins in Motion. In *Protein-Ligand Interactions: Methods and Applications*, Ulrich Nienhaus, G., Ed. Humana Press: Totowa, NJ, 2005; pp 287–300.
100. Babu, M. M.; van der Lee, R.; de Groot, N. S.; Gsponer, J., Intrinsically disordered proteins: regulation and disease. *Curr. Opin. Struct. Biol.* **2011**, *21* (3), 432–440.
101. Demarest, S. J.; Martinez-Yamout, M.; Chung, J.; Chen, H.; Xu, W.; Dyson, H. J.; Evans, R. M.; Wright, P. E., Mutual synergistic folding in recruitment of CBP/p300 by p160 nuclear receptor coactivators. *Nature* **2002**, *415* (6871), 549–553.
102. Lin, C. H.; Hare, B. J.; Wagner, G.; Harrison, S. C.; Maniatis, T.; Fraenkel, E., A Small Domain of CBP/p300 Binds Diverse Proteins: Solution Structure and Functional Studies. *Mol. Cell* **2001**, *8* (3), 581–590.
103. Nyqvist, I.; Dogan, J., Characterization of the dynamics and the conformational entropy in the binding between TAZ1 and CTAD-HIF-1 α . *Sci. Rep.* **2019**, *9* (1), 16557.
104. Dyson, H. J.; Wright, P. E., Intrinsically unstructured proteins and their functions. *Nat. Rev. Mol. Cell Bio.* **2005**, *6* (3), 197–208.
105. Kumar, A.; Kumar, P.; Kumari, S.; Uversky, V. N.; Giri, R., Folding and structural polymorphism of p53 C-terminal domain: One peptide with many conformations. *Arch. Biochem. Biophys.* **2020**, *684*, 108342.

106. Metskas, L. A.; Rhoades, E., Folding upon phosphorylation: translational regulation by a disorder-to-order transition. *Trends Biochem. Sci.* **2015**, *40* (5), 243–244.
107. Tsytlonok, M.; Sanabria, H.; Wang, Y.; Felekyan, S.; Hemmen, K.; Phillips, A. H.; Yun, M.-K.; Waddell, M. B.; Park, C.-G.; Vaithiyalingam, S.; Iconaru, L.; White, S. W.; Tompa, P.; Seidel, C. A. M.; Kriwacki, R., Dynamic anticipation by Cdk2/Cyclin A-bound p27 mediates signal integration in cell cycle regulation. *Nat. Commun.* **2019**, *10* (1), 1676.
108. Hilser, V. J.; Thompson, E. B., Intrinsic disorder as a mechanism to optimize allosteric coupling in proteins. *Proc. Natl. Acad. Sci. USA* **2007**, *104* (20), 8311.
109. Horsley, J.; Yu, J.; Yeoh, Y. Q.; Abell, A., Peptides as Bio-inspired Molecular Electronic Materials. In *Peptides and Peptide-based Biomaterials and their Biomedical Applications*, Sunna, A.; Care, A.; Bergquist, P. L., Eds. Springer International Publishing: Cham, 2017; pp 131–153.
110. Su, T. A.; Neupane, M.; Steigerwald, M. L.; Venkataraman, L.; Nuckolls, C., Chemical principles of single-molecule electronics. *Nat. Rev. Mater.* **2016**, *1* (3), 16002.
111. Sun, L.; Diaz-Fernandez, Y. A.; Gschneidner, T. A.; Westerlund, F.; Lara-Avila, S.; Moth-Poulsen, K., Single-molecule electronics: from chemical design to functional devices. *Chem. Soc. Rev.* **2014**, *43* (21), 7378–7411.
112. Xin, N.; Guan, J.; Zhou, C.; Chen, X.; Gu, C.; Li, Y.; Ratner, M. A.; Nitzan, A.; Stoddart, J. F.; Guo, X., Concepts in the design and engineering of single-molecule electronic devices. *Nat. Rev. Phys.* **2019**, *1* (3), 211–230.
113. Gu, C.; Jia, C.; Guo, X., Single-Molecule Electrical Detection with Real-Time Label-Free Capability and Ultrasensitivity. *Small Methods* **2017**, *1* (5), 1700071.
114. Xiang, D.; Wang, X.; Jia, C.; Lee, T.; Guo, X., Molecular-Scale Electronics: From Concept to Function. *Chem. Rev.* **2016**, *116* (7), 4318–4440.
115. Tsutsui, M.; Taniguchi, M., Single molecule electronics and devices. *Sensors* **2012**, *12* (6), 7259–7298.
116. Kiguchi, M.; Kaneko, S., Single molecule bridging between metal electrodes. *Phys. Chem. Chem. Phys.* **2013**, *15* (7), 2253–2267.
117. Komoto, Y.; Fujii, S.; Iwane, M.; Kiguchi, M., Single-molecule junctions for molecular electronics. *J. Mater. Chem. C* **2016**, *4* (38), 8842–8858.
118. Perrin, M. L.; Martin, C. A.; Prins, F.; Shaikh, A. J.; Eelkema, R.; van Esch, J. H.; van Ruitenbeek, J. M.; van der Zant, H. S. J.; Dulić, D., Charge transport in a zinc–porphyrin single-molecule junction. *Beilstein J. Nanotechnol.* **2011**, *2*, 714–719.


119. Tsutsui, M.; Shoji, K.; Taniguchi, M.; Kawai, T., Formation and Self-Breaking Mechanism of Stable Atom-Sized Junctions. *Nano Lett.* **2008**, *8* (1), 345–349.
120. Vrouwe, S. A. G.; van der Giessen, E.; van der Molen, S. J.; Dulic, D.; Trouwborst, M. L.; van Wees, B. J., Mechanics of lithographically defined break junctions. *Phys. Rev. B* **2005**, *71* (3), 035313.
121. Wang, K., DNA-Based Single-Molecule Electronics: From Concept to Function. *J. Funct. Biomater.* **2018**, *9* (1), 8.
122. Li, M.; Dang, D.; Liu, L.; Xi, N.; Wang, Y., Imaging and Force Recognition of Single Molecular Behaviors Using Atomic Force Microscopy. *Sensors* **2017**, *17* (1), 200.
123. Park, H.; Park, J.; Lim, A. K. L.; Anderson, E. H.; Alivisatos, A. P.; McEuen, P. L., Nanomechanical oscillations in a single-C60 transistor. *Nature* **2000**, *407* (6800), 57–60.
124. Park, J.; Pasupathy, A. N.; Goldsmith, J. I.; Chang, C.; Yaish, Y.; Petta, J. R.; Rinkoski, M.; Sethna, J. P.; Abruña, H. D.; McEuen, P. L.; Ralph, D. C., Coulomb blockade and the Kondo effect in single-atom transistors. *Nature* **2002**, *417* (6890), 722–725.
125. Kim, T.; Liu, Z.-F.; Lee, C.; Neaton, J. B.; Venkataraman, L., Charge transport and rectification in molecular junctions formed with carbon-based electrodes. *Proc. Natl. Acad. Sci. USA* **2014**, *111* (30), 10928.
126. Li, Z.; Smeu, M.; Afsari, S.; Xing, Y.; Ratner, M. A.; Borguet, E., Single-Molecule Sensing of Environmental pH—an STM Break Junction and NEGF-DFT Approach. *Angew. Chem. Int. Ed.* **2014**, *53* (4), 1098–1102.
127. Zhou, C.; Li, X. X.; Gong, Z. L.; Jia, C. C.; Lin, Y. W.; Gu, C. H.; He, G.; Zhong, Y. W.; Yang, J. L.; Guo, X. F., Direct observation of single-molecule hydrogen-bond dynamics with single-bond resolution. *Nat. Commun.* **2018**, *9*, 807.
128. Gu, C. H.; Hu, C.; Wei, Y.; Lin, D. Q.; Jia, C. C.; Li, M. Z.; Su, D. K.; Guan, J. X.; Xia, A. D.; Xie, L. H.; Nitzan, A.; Guo, H.; Guo, X. F., Label-free dynamic detection of single-molecule nucleophilic-substitution reactions. *Nano Lett.* **2018**, *18* (7), 4156–4162.
129. Jia, C. C.; Migliore, A.; Xin, N.; Huang, S. Y.; Wang, J. Y.; Yang, Q.; Wang, S. P.; Chen, H. L.; Wang, D. M.; Feng, B. Y.; Liu, Z. R.; Zhang, G. Y.; Qu, D. H.; Tian, H.; Ratner, M. A.; Xu, H. Q.; Nitzan, A.; Guo, X. F., Covalently bonded single-molecule junctions with stable and reversible photoswitched conductivity. *Science* **2016**, *352* (6292), 1443–1445.
130. Jia, C. C.; Wang, J. Y.; Yao, C. J.; Cao, Y.; Zhong, Y. W.; Liu, Z. R.; Liu, Z. F.; Guo, X. F., Conductance switching and mechanisms in single-molecule junctions. *Angew. Chem. Int. Ed.* **2013**, *52* (33), 8666–8670.

131. Xin, N.; Wang, J. Y.; Jia, C. C.; Liu, Z. T.; Zhang, X. S.; Yu, C. M.; Li, M. L.; Wang, S. P.; Gong, Y.; Sun, H. T.; Zhang, G. X.; Liu, Z. R.; Zhang, G. Y.; Liao, J. H.; Zhang, D. Q.; Guo, X. F., Stereoelectronic effect-induced conductance switching in aromatic chain single-molecule junctions. *Nano Lett.* **2017**, *17* (2), 856–861.
132. Jia, C. C.; Guo, X. F., Molecule-electrode interfaces in molecular electronic devices. *Chem. Soc. Rev.* **2013**, *42* (13), 5642–5660.
133. Xin, N.; Li, X. X.; Jia, C. C.; Gong, Y.; Li, M. L.; Wang, S. P.; Zhang, G. Y.; Yang, J. L.; Guo, X. F., Tuning charge transport in aromatic-ring single-molecule junctions via ionic-liquid gating. *Angew. Chem. Int. Ed.* **2018**, *57* (43), 14026–14031.
134. Chen, X.; Zhou, C.; Guo, X., Ultrasensitive Detection and Binding Mechanism of Cocaine in an Aptamer-based Single-molecule Device. *Chin. J. Chem.* **2019**, *37* (9), 897–902.
135. Gu, C.; Hu, C.; Wei, Y.; Lin, D.; Jia, C.; Li, M.; Su, D.; Guan, J.; Xia, A.; Xie, L.; Nitzan, A.; Guo, H.; Guo, X., Label-Free Dynamic Detection of Single-Molecule Nucleophilic-Substitution Reactions. *Nano Lett.* **2018**, *18* (7), 4156–4162.
136. Hedegaard, S. F.; Derbas, M. S.; Lind, T. K.; Kasimova, M. R.; Christensen, M. V.; Michaelsen, M. H.; Campbell, R. A.; Jorgensen, L.; Franzyk, H.; Cárdenas, M.; Nielsen, H. M., Fluorophore labeling of a cell-penetrating peptide significantly alters the mode and degree of biomembrane interaction. *Sci. Rep.* **2018**, *8* (1), 6327.
137. Liu, J.; Huang, X.; Wang, F.; Hong, W., Quantum Interference Effects in Charge Transport through Single-Molecule Junctions: Detection, Manipulation, and Application. *Acc. Chem. Res.* **2019**, *52* (1), 151–160.
138. Jia, C.; Ma, B.; Xin, N.; Guo, X., Carbon Electrode–Molecule Junctions: A Reliable Platform for Molecular Electronics. *Acc. Chem. Res.* **2015**, *48* (9), 2565–2575.
139. Zhou, C.; Li, X.; Gong, Z.; Jia, C.; Lin, Y.; Gu, C.; He, G.; Zhong, Y.; Yang, J.; Guo, X., Direct observation of single-molecule hydrogen-bond dynamics with single-bond resolution. *Nat. Commun.* **2018**, *9* (1), 807.
140. Lau, Q. Y.; Ng, F. M.; Cheong, J. W. D.; Yap, Y. Y. A.; Tan, Y. Y. F.; Jureen, R.; Hill, J.; Chia, C. S. B., Discovery of an ultra-short linear antibacterial tetrapeptide with anti-MRSA activity from a structure–activity relationship study. *Eur. J. Med. Chem.* **2015**, *105*, 138–144.
141. Ghosh, C.; Manjunath, G. B.; Akkapeddi, P.; Yarlagadda, V.; Hoque, J.; Uppu, D. S. S. M.; Konai, M. M.; Haldar, J., Small Molecular Antibacterial Peptoid Mimics: The Simpler the Better! *J. Med. Chem.* **2014**, *57* (4), 1428–1436.



CHAPTER 2

Photopharmacological control of
cyclic antibacterial peptides



Foreword

Gramicidin S is a natural antibacterial peptide that is particularly active against Gram-positive *Staphylococcus aureus* (*S. aureus*), but exhibits toxicity towards human erythrocytes. This chapter presents a photopharmacological approach to regulate a series of cyclic peptides **1-3** based on gramicidin S, using an azobenzene photoswitch to reversibly control secondary structure and, hence, antibacterial activity. Detailed ^1H NMR spectroscopy and density functional theory (DFT) calculations were performed to fully characterize the *cis*-enriched and *trans*-enriched photostationary states (PSS) for each peptide. Each PSS for peptides **1-3** was assayed against *S. aureus* to reveal a clear relationship between secondary structure, amphiphilicity, and optimal antibacterial activity.

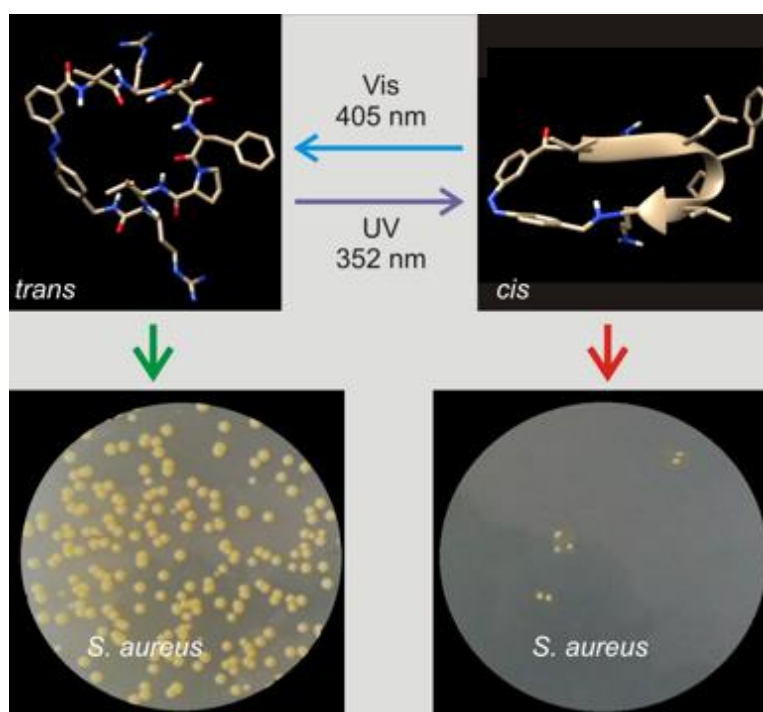


Figure 2.0. Graphical representation of the model of gramicidin S mimetic, peptide **2b**, showing a four-fold difference in the minimum inhibitory concentration (MIC) between the *cis*-enriched and *trans*-enriched PSS against *S. aureus*. This photopharmacological approach provides an opportunity to turn antibacterial activity ‘on’ and ‘off’ to allow potential future point-of-care applications.

Statement of Authorship

| | | |
|---------------------|---|---|
| Title of Paper | Photopharmacological control of cyclic antimicrobial peptides | |
| Publication Status | <input checked="" type="checkbox"/> Published | <input type="checkbox"/> Accepted for Publication |
| | <input type="checkbox"/> Submitted for Publication | <input type="checkbox"/> Unpublished and Unsubmitted work written in manuscript style |
| Publication Details | Yeoh, Y. Q.; Yu, J.; Polyak, S. W.; Horsley, J. R.; Abell, A. D., Photopharmacological control of cyclic antimicrobial peptides. <i>ChemBioChem</i> 2018, 19 (24), 2591–2597. | |

Principal Author

| | | | |
|--------------------------------------|--|------|-----------|
| Name of Principal Author (Candidate) | Yuan Qi Yeoh | | |
| Contribution to the Paper | Performed synthesis and characterization for all compounds and wrote manuscript. | | |
| Overall percentage (%) | 70 | | |
| Certification: | This paper reports on original research I conducted during the period of my Higher Degree by Research candidature and is not subject to any obligations or contractual agreements with a third party that would constrain its inclusion in this thesis. I am the primary author of this paper. | | |
| Signature | | Date | 15/6/2020 |

Co-Author Contributions

By signing the Statement of Authorship, each author certifies that:

- i. the candidate's stated contribution to the publication is accurate (as detailed above);
- ii. permission is granted for the candidate to include the publication in the thesis; and
- iii. the sum of all co-author contributions is equal to 100% less the candidate's stated contribution.

| | | | |
|---------------------------|---|------|------------|
| Name of Co-Author | Jingxian Yu | | |
| Contribution to the Paper | Supervised development of work, performed DFT calculations, and revised manuscript. | | |
| Signature | | Date | 15/06/2020 |

| | | | |
|---------------------------|--|------|-----------|
| Name of Co-Author | Steven W. Polyak | | |
| Contribution to the Paper | Performed antimicrobial assays and revised manuscript. | | |
| Signature | | Date | 15/6/2020 |

| | | | |
|---------------------------|---|------|----------|
| Name of Co-Author | John R. Horsley | | |
| Contribution to the Paper | Helped in data interpretation and revised manuscript. | | |
| Signature | | Date | 15/6/20. |

| | | | |
|---------------------------|--|------|-----------|
| Name of Co-Author | Andrew D. Abell | | |
| Contribution to the Paper | Supervised development of work and revised manuscript. A corresponding author. | | |
| Signature | | Date | 22/6/2020 |

Photopharmacological control of cyclic antibacterial peptides

Yuan Qi Yeoh^a, Jingxian Yu^a, Steven W. Polyak^{b,1}, John R. Horsley^a and Andrew D. Abell^{a*}

^a*ARC Centre of Excellence for Nanoscale BioPhotonics (CNBP), Department of Chemistry, The University of Adelaide, SA 5005, Australia.*

^b*School of Biological Sciences, Department of Molecular and Cellular Biology, The University of Adelaide, SA 5005, Australia.*

¹*Present address: School of Pharmacy and Medical Sciences, University of South Australia, City East Campus (P4-10), North Terrace, Adelaide, SA 5000, Australia.*

Publication

Yeoh, Y. Q.; Yu, J.; Polyak, S. W.; Horsley, J. R.; Abell, A. D., Photopharmacological Control of Cyclic Antimicrobial Peptides. *ChemBioChem* **2018**, *19* (24), 2591–2597.

2.1 Abstract

Gramicidin S is a naturally occurring antibacterial cyclic peptide. Herein, we present a series of cyclic peptides based on gramicidin S that contain an azobenzene photoswitch to reversibly control secondary structure and, hence, antibacterial activity. Detailed ^1H NMR spectroscopy and density functional theory (DFT) calculations revealed a β -sheet/ β -turn secondary structure for the *cis* configuration of each peptide, and an ill-defined conformation for all associated *trans* structures. The *cis*-enriched and *trans*-enriched photostationary states (PSS) for peptides **1–3** were assayed against *Staphylococcus aureus* (*S. aureus*) to reveal a clear relationship between well-defined secondary structure, amphiphilicity, and optimal antibacterial activity. Specifically, our results suggest that a synergy exists between these factors, with amphiphilicity playing a more significant role than secondary structure in this context. Most notably, peptides **2a** and **2b** exhibited a fourfold difference in antibacterial activity in the *cis*-enriched PSS over the *trans*-enriched equivalent. This photopharmacological approach allows antibacterial activity to be regulated through photochemical control of the azobenzene photoswitch, thereby opening new avenues in the design and synthesis of future antibiotics.

2.2 Introduction

Gramicidin S (Figure 2.1) is a naturally occurring cyclic peptide-based antibiotic with a symmetrical antiparallel β -sheet conformation, linked by two type-II' β -turns.¹⁻² The antibacterial properties of gramicidin S have been attributed to its well-defined β -sheet secondary structure and overall amphiphilic character.³⁻⁸ The peptide contains two basic ornithine amino acids and a series of hydrophobic amino acids that allow gramicidin S to bind to and penetrate anionic bacterial lipid membranes.⁹ Gramicidin S is particularly active against Gram-positive *S. aureus*,¹⁰⁻¹² thus making it a potentially potent antibiotic to treat a range of specific bacterial infections. Photopharmacology presents as an ideal approach to regulate the activity of gramicidin S to allow further exploitation of its desirable antibacterial properties. Specifically, the introduction of a photoswitch into its backbone allows reversible control of the secondary structure and, hence, binding affinity, aggregation, and folding properties.¹³ Antibacterial activity can then be switched 'on' or 'off' upon irradiation with light of a specific wavelength, with spatiotemporal precision. This would enhance selectivity and likely reduce toxicity and potential for the development of antibacterial resistance.¹⁴ Previous studies have illustrated the role of a photoswitch in such a photopharmacological approach to modulate the activity of membrane channels,¹⁵⁻¹⁶ enzyme inhibitors,¹⁷⁻²² anticancer drugs,²³⁻²⁴ and other antibiotics.²⁵⁻²⁶ A recent study incorporated a diarylethene photoswitch into the backbone of gramicidin S to regulate antibacterial activity.²⁷ While good antibacterial activity was observed, their gramicidin S analogues contain no discernible secondary structure. The difference in antibacterial activity between the open and closed forms of their gramicidin S analogues was directly attributed to the change in amphiphilicity. Any fundamental relationship between secondary structure and amphiphilicity remains to be fully addressed.

Accordingly, a series of photoswitchable antibacterial peptides (**1-3**, Figure 2.1) based upon gramicidin S was synthesized for an extended study, each containing a meta-/para-substituted azobenzene photoswitch incorporated into its backbone. These peptides were chosen to define the role of secondary structure and amphiphilicity on antibacterial activity, with both *cis*-enriched and *trans*-enriched PSS assayed against *S. aureus*. An azobenzene was chosen for incorporation into the peptide backbone of gramicidin S as it is known to give rise to a significant geometric change, high photoisomerization yield and fast isomerization, while

having a relative ease of synthesis.²⁸⁻³² In addition, an azobenzene in its *cis* conformation is known to mimic the β -turn in β -hairpin structures.³³ We anticipated that a suitable azobenzene in its *cis* conformation would mimic the β -turn of the native gramicidin S, allowing the peptide to adopt a β -sheet structure. This gramicidin S mimetic would be expected to be active in suppressing bacterial growth, whereas the corresponding *trans* isomer with its ill-defined random structure, would not.

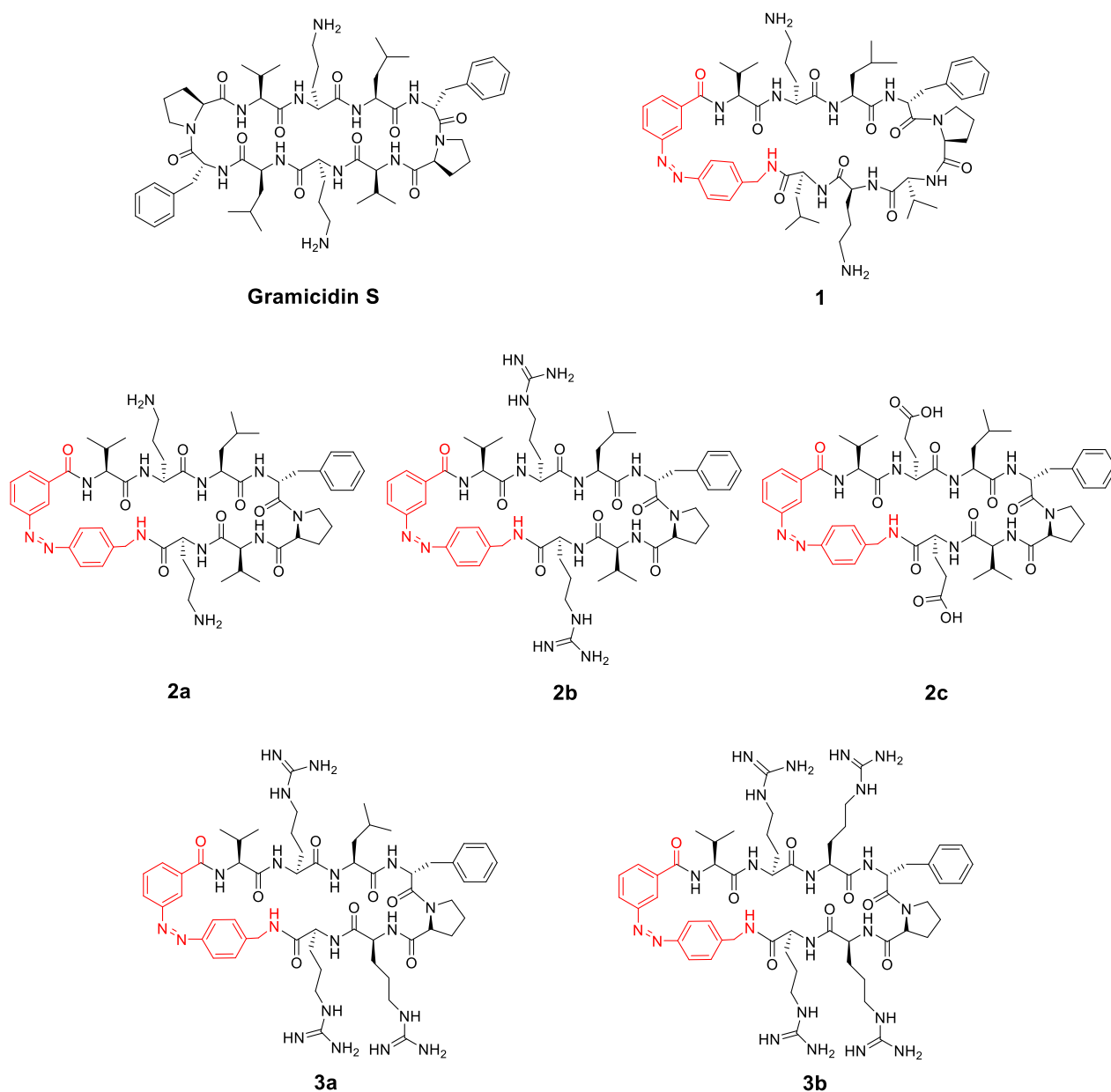


Figure 2.1. Chemical structures of gramicidin S and its mimetics, peptides **1-3** (*cis* isomers). The azobenzene photoswitch is highlighted in red in peptides **1-3**.

2.3 Results and Discussion

2.3.1 Design and Synthesis of Peptides 1-3

Cyclic peptides **1-3** (Figure 2.1) mimic the structure and conformation of natural gramicidin S, which has the amino acid sequence, cyclo(^DFPVOL)₂ (^DF=D-phenylalanine, O=ornithine). Peptide **1** has a similar amino acid sequence to gramicidin S, with proline and D-phenylalanine residues replaced by the azobenzene photoswitch. Proline and D-phenylalanine were positioned in the β-turn region of the native gramicidin S, where these residues are known to generate a well-defined turn in a cyclic structure.^{27, 34} A *meta-/para*-substituted azobenzene photoswitch (red highlighted region in peptides **1-3**, Figure 2.1) was chosen because of its propensity to mimic the desired β-turn as defined by modelling results (see 2.3.3 Molecular Modelling). The remaining amino acid residues native to gramicidin S were retained in peptide **1**, to maintain the amphiphilic side chain pattern required for biological activity.⁶ It was anticipated that, by mimicking the β-turn found in the native gramicidin S, the *cis* isomer of the azobenzene photoswitch would bring both β-strands into close proximity to preserve the well-defined secondary structure of the peptide. Thus, *cis*-peptide **1** was expected to retain antibacterial activity. Conversely, the azobenzene photoswitch in its *trans* configuration would be expected to disrupt the β-sheet/β-turn character of peptide **1** and, hence, result in diminished activity. Modelling of *cis*-peptide **1** (Figure 2.3) by DFT calculations revealed a distortion in its β-strand secondary structure due to strain exerted by the photoswitch on the peptide backbone. The leucine residue was removed from the underside strand of **1** to give peptide **2a** in order to further explore this supposition. Ensuing computational data on **2a** was consistent with a more well-defined β-strand secondary structure. Alternative basic amino acid residues (arginine) and acidic amino acid residues (glutamic acid) were incorporated into the structure to investigate the effect of positive and negative charges on antibacterial activity, as in peptides **2b** and **2c** respectively. Hence, any observed differences in antibacterial activity would then be directly attributable to the positively or negatively charged amino acid residues, as the active *cis* isomers of **2a-2c** would be expected to adopt similar secondary structures. The role of amphiphilicity on antibacterial activity was investigated by incorporating additional basic amino acid residues into the peptide backbone (**3a** and **3b**) in place of the hydrophobic amino acids leucine and valine.

All peptides and a gramicidin S control were synthesized by solid phase peptide synthesis (SPPS) as outlined in the Experimental section, and crude products were purified by RP-HPLC prior to biological testing. The component azobenzene photoswitch was synthesized using an existing methodology.³⁵

2.3.2 Spectroscopic Analysis for Peptides 1-3

For all experiments, the thermally stable *trans*-enriched PSS was isomerized to a *cis*-enriched PSS by irradiation using UV light (352 nm). Conversely, *cis* to *trans* isomerism was induced by irradiation with visible light (405 nm). The *trans*-enriched PSS of each peptide (**1-3**) exhibited a broad absorption band ($\lambda_{\text{max}} = 328\text{-}330$ nm), whereas each *cis*-enriched PSS displayed a stronger absorbance at 428 nm, and an absorbance of much lower intensity at 328-330 nm (Figure S2.1). These observed values concur with literature.³⁶ The intense absorbance at 328-330 nm is due to the symmetry allowed $\pi \rightarrow \pi^*$ transition, while the weak absorbance peak at 428 nm is the result of the symmetry forbidden $n \rightarrow \pi^*$ transition.³⁷ A far less intense absorption band at 328 nm was apparent for the *cis*-enriched PSS of peptides **1-3**, which is likely due to a small amount of *trans* isomer remaining after irradiation. Both azobenzene isomers are known to give some overlap of absorption spectra.³⁸

A more quantitative measure of each PSS was determined by the ratio of ¹H NMR integrals. Figures S2.4a and S2.5a (boxed areas) show the ratios between the *cis* and *trans* PSSs, calculated from the ¹H NMR integrals at $\delta = 7.91$ and 6.83 for peptide **1** and $\delta = 7.83$ and 6.81 for peptide **2a**. These ¹H NMR resonances correspond to hydrogens of the *para*-substituted phenyl ring in the *trans* and *cis* isomers of the azobenzene unit respectively.³⁹ It was determined that the photoisomerization yield for the *cis*-enriched PSS of peptides **1-3** was relatively high, ranging from 64%-90%, as detailed in Table 2.1. The secondary structures of the peptides **1-3** were defined by ¹H NMR, with ³*J*_{NHC α H} coupling constants in the range of 8-10 Hz⁴⁰ for a β -strand. Analysis of the *cis*-enriched PSS of **2a-2c** revealed ³*J*_{NHC α H} coupling constants of 8.0-8.8 Hz, consistent with a more well-defined β -strand structure than the *cis* isomers of **1** and **3**.

The half-lives for the *cis*-enriched PSS of each peptide (Table 2.1) were determined to be between 2-4 days, by analyzing the kinetics of the *cis-trans* thermal back isomerization. However, the *cis*-enriched PSS of peptides **2a-2c** have longer half-lives than the *cis*-enriched PSS of peptides **1** and **3**, which have less well-defined secondary structures as revealed by ¹H NMR. The half-lives for the *cis*-enriched PSS of peptides **2a-2c** range between 3.5-4 days, thus highlighting their robustness and stability. This considerable time frame is sufficient for antibacterial assaying against *S. aureus*, which in this case was 16-20 hours.

Table 2.1. Photoisomerization yields and half-lives of gramicidin S mimetics, peptides **1-3**, in their respective photostationary states (PSS).

| Peptide | Photoisomerization Yield (%) | | Half-Life (<i>cis</i> -enriched PSS) (h) |
|-----------|------------------------------|--------------|---|
| | <i>cis</i> | <i>trans</i> | |
| 1 | 90 | 84 | 74.8 |
| 2a | 90 | 88 | 84.2 |
| 2b | 71 | 75 | 99.9 |
| 2c | 90 | 85 | 97.0 |
| 3a | 84 | 66 | 87.8 |
| 3b | 64 | 67 | 48.4 |

2.3.3 Molecular Modelling for Peptides 1-3

The lowest energy structure for the *cis* isomer of peptide **1** (Figure 2.3) was determined by density functional theory (DFT). The resulting model revealed four intramolecular hydrogen bonds linking the upper and lower strands, with two of these considered strong bonds (2.0 Å and 2.2 Å), and the other two moderate to weak (2.5 Å and 3.8 Å). The *cis* isomers of peptides **2** and **3** contain three strong hydrogen bonds (1.8 Å-2.0 Å, Table S2.2). In comparison, native gramicidin S possesses four strong intramolecular hydrogen bonds (2.0 Å-2.3 Å) (Figure 2.2a) connecting the upper and lower strands of the cyclic peptide, which play an important role in defining its β -sheet structure. The *trans* isomers for each of peptides **1-3** lack intramolecular hydrogen bonding and, hence, secondary structure. The computational molecular models for both isomers of peptide **2b** are shown in Figure 2.4a to highlight this structural disparity.

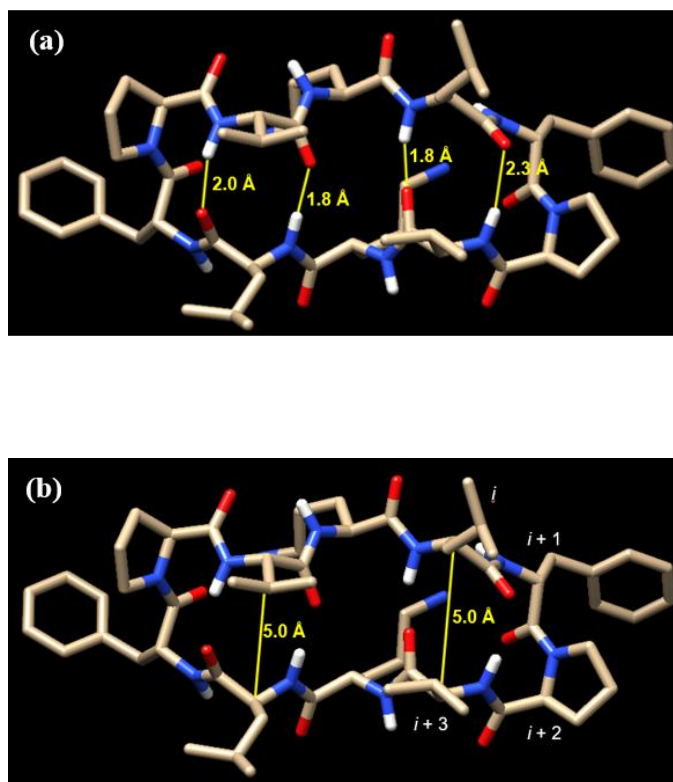


Figure 2.2. Molecular models of gramicidin S. (a) Containing four strong intramolecular hydrogen bonds, highlighted in yellow. (b) Containing two β -turns, indicated by the distances between $C\alpha(i)$ and $C\alpha(i+3) = 5.0 \text{ \AA}$ ($< 7 \text{ \AA}$), highlighted in yellow.

The calculated backbone dihedral angles for the *trans* isomers of peptides **1-3** were found to be outside the allowable ϕ , ψ , and ω angles specific to a β -strand structure.⁴¹ A standard β -sheet should contain more than 30% β -sheet content.⁴² The *cis* isomers of peptides **2a-2c** were found to contain 43% β -sheet content, while the *cis* isomers of peptides **1** and **3** contain 29%. Notably, the *cis* isomer of **1** showed a large kink on the underside of the backbone, which distorts the β -sheet structure of the peptide (Figure 2.3). A β -turn is denoted by four consecutive ‘corner’ amino acid residues i to $i+3$,³⁴ and is considered to be present if two specific criteria are fulfilled: i) a distance of less than 7 Å between the $C_{\alpha}(i)$ and $C_{\alpha}(i+3)$, and ii) the $(i+1)$ and $(i+3)$ residues are not in an α -helix.⁴³ Based on these parameters, gramicidin S possesses two β -turns (Figure 2.2b) in agreement with previous reports,¹⁻² with $C_{\alpha}(i)$ to $C_{\alpha}(i+3)$ distance of 5.0 Å. The *cis* isomer of peptides **1-3** contains a β -turn, with $C_{\alpha}(i)$ to $C_{\alpha}(i+3)$ distances ranging between 5.7 Å and 6.0 Å. The corresponding distance for each of the *trans* isomers of **1-3** exceeds 7 Å, indicating the random nature in each case. Figure 2.4b shows the molecular models for peptide **2b**, highlighting the presence of a β -turn in the *cis* isomer, whereas the *trans* isomer is devoid of a β -turn.

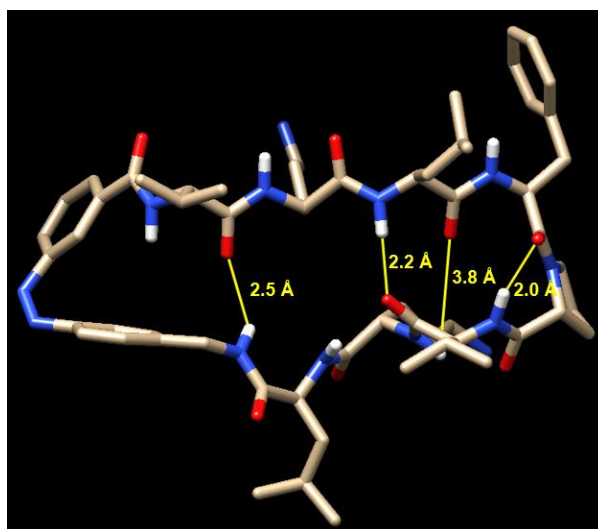


Figure 2.3. Molecular model for the *cis* isomer of peptide **1**, showing the presence of four intramolecular hydrogen bonds linking the upper and lower strands, with two of these considered strong bonds (2.0 Å and 2.2 Å), and the other two moderate to weak (2.5 Å and 3.8 Å). A large kink is evident on the underside strand of the backbone, which distorts the β -sheet structure of the peptide.

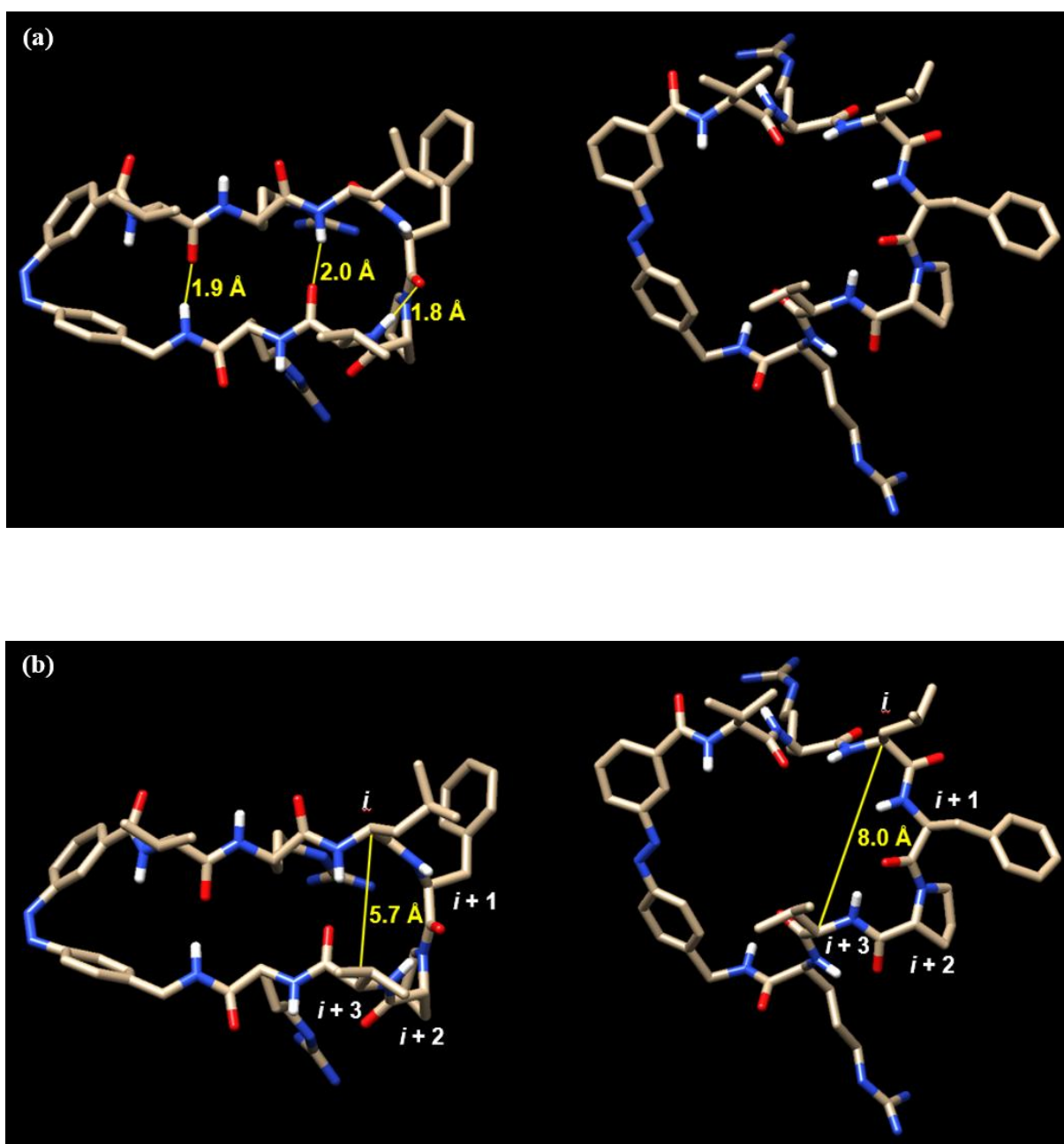


Figure 2.4. Molecular models of peptide **2b**. **(a)** The *cis* isomer (left) contains three strong intramolecular hydrogen bonds, highlighted in yellow, but no intramolecular hydrogen bond is evident for the *trans* isomer (right). **(b)** The *cis* isomer of peptide **2b** possesses a β -turn, indicated by the distance between $C_{\alpha}(i)$ and $C_{\alpha}(i+3) = 5.70 \text{ \AA}$ ($< 7 \text{ \AA}$), but the *trans* isomer is devoid of a β -turn, as the distance between $C_{\alpha}(i)$ and $C_{\alpha}(i+3) = 8.00 \text{ \AA}$ ($> 7 \text{ \AA}$).

2.3.4 Biological Assay for Peptides 1-3

Peptides **1-3** and gramicidin S were assayed for their antibacterial activity against *S. aureus* ATCC 49775, as detailed in the Experimental section. Briefly, each peptide was dissolved in DMSO at a concentration of 8 mg/mL, and irradiated separately using either UV (352 nm) or Vis (405 nm) light for 2h to obtain the respective *cis*-enriched and *trans*-enriched PSS. Two-fold serial dilutions were made for each peptide, which were then separately inoculated with *S. aureus* at 37°C for 16-20 hours. The lowest concentration that inhibited bacterial growth was reported as the minimal inhibitory concentration (MIC). The minimum inhibitory concentration (MIC) of the prototypical peptide gramicidin S was in agreement with previous reports^{27, 44} (2 µg/mL, Table 2.2). No detectable difference in bioactivity was observed between the *cis*-enriched and *trans*-enriched PSS of **1** (MIC 64 µg/mL). This result is consistent with the earlier molecular modelling study (see 2.3.3 Molecular Modelling) which showed a distorted β -strand secondary structure in peptide **1** due to the photoswitch. Peptides **2a** and **2b**, both designed to address the strain on the peptide backbone, showed differential bioactivity due to photoswitching. For **2a**, the *cis*-enriched PSS was fourfold more active than the *trans*-enriched equivalent (Table 2.2). This important finding demonstrates that the antibacterial activity of the peptide can be regulated by controlling the peptide secondary structure through photoisomerization. Consistent with this observation, the *cis*-enriched PSS of **2b** also afforded fourfold greater bioactivity over its *trans*-enriched equivalent. Indeed, *cis*-enriched **2b** provided the most potent antibacterial analogue in this series (MIC 32 µg/mL). These findings are consistent with our design principles where substitution of ornithine residues with arginine residues, as in peptide **2b**, was predicted to enhance membrane penetrating properties,⁴⁵ resulting in improved antibacterial activity. In further agreement, both PSS of the glutamic acid-containing peptide **2c** were inactive against *S. aureus* at the highest concentration tested (256 µg/mL), confirming the importance of basic amino acids for antibacterial activity. Replacement of hydrophobic residues valine and leucine with arginine residues (**3a** and **3b**) resulted in a decrease in antibacterial activity, presumably due to disruption of the amphiphilic nature of the peptides with associated decreased penetration through the bacterial membrane. As **3a** and **3b** both possess approximately 30% β -sheet character, we postulate that amphiphilicity plays a more significant role than secondary structure in this context. Together, our experimental and computational data shows that antibacterial activity in these gramicidin S peptide mimetics is

dependent on a fine balance between well-defined secondary structure and the amphiphilic nature of the amino acid side chains. Indeed, our gramicidin S analogues have indicated a synergy between these two factors, where the well-defined β -sheet framework is likely essential for stabilizing the residues responsible for maintaining amphiphilicity.

Table 2.2. Minimum inhibitory concentration (MIC) of gramicidin S and its mimetics, peptides **1-3**, in their respective photostationary states (PSS).

| Peptide | PSS | MIC ($\mu\text{g/mL}$) |
|----------------|--------------|--|
| Gramicidin S | - | 2 |
| 1 | <i>cis</i> | 64 |
| | <i>trans</i> | 64 |
| 2a | <i>cis</i> | 64 |
| | <i>trans</i> | 256 |
| 2b | <i>cis</i> | 32 |
| | <i>trans</i> | 128 |
| 2c | <i>cis</i> | >256 |
| | <i>trans</i> | >256 |
| 3a | <i>cis</i> | 256 |
| | <i>trans</i> | >256 |
| 3b | <i>cis</i> | >256 |
| | <i>trans</i> | >256 |

2.4 Conclusion

In this study, a series of photoswitchable cyclic peptides (**1-3**) based on the antibacterial agent gramicidin S was synthesized, each containing an azobenzene moiety for reversible switching between a *trans* isomer possessing an ill-defined conformation, and a *cis* isomer containing a well-defined secondary structure. Each peptide was assayed against *S. aureus*, with photoisomerization from *trans*-enriched to *cis*-enriched PSS resulting in significant differences in biological activity. Specifically, peptides **2a** and **2b** showed a fourfold difference in the minimum inhibitory concentration (MIC) values against *S. aureus*, between their respective *cis*-enriched and *trans*-enriched PSS, with the well-defined *cis*-enriched PSS found to be more active. These results confirmed that the secondary structure of the peptide and, hence, antibacterial activity can be regulated through photochemical control of the azobenzene photoswitch. Replacement of the hydrophobic valine and leucine residues with basic arginine residues gave peptides **3a** and **3b**, which were devoid of activity. Collectively, these results show that both well-defined secondary structure and amphiphilicity are essential for antibacterial activity against *S. aureus*. Furthermore, our findings suggest it is possible that amphiphilicity is more important for membrane penetration, where no conformational molecular recognition is required, unlike for most protein-protein interactions, for example, where well-defined secondary structure is crucial. This photopharmacological approach may offer benefits for the design of future antibiotics that possess significant therapeutic value, but are limited by factors such as bioavailability. This important strategy provides an opportunity to turn antibacterial activity ‘on’ and ‘off’ to allow potential future point-of-care applications.

2.5 Acknowledgements

This work was supported by the Australian Research Council (CE140100003). We also acknowledge the Australian National Fabrication Facility for providing the analytical facilities used in this work. The computational aspects of this work were supported by an award under the National Computational Merit Allocation Scheme for JY on the National Computing Infrastructure (NCI) National Facility at the Australian National University.

2.6 References

- (1) Legrand, B.; Mathieu, L.; Lebrun, A.; Andriamanarivo, S.; Lisowski, V.; Masurier, N.; Zirah, S.; Kang, Y. K.; Martinez, J.; Maillard, L. T., Thiazole-Based γ -Building Blocks as Reverse-Turn Mimetic to Design a Gramicidin S Analogue: Conformational and Biological Evaluation. *Chem. Eur. J.* **2014**, *20* (22), 6713–6720.
- (2) Llamas-Saiz, A. L.; Grotenbreg, G. M.; Overhand, M.; van Raaij, M. J., Double-stranded helical twisted [β]-sheet channels in crystals of gramicidin S grown in the presence of trifluoroacetic and hydrochloric acids. *Acta Crystallogr. D* **2007**, *63* (3), 401–407.
- (3) Jelokhani-Niaraki, M.; Hodges, R. S.; Meissner, J. E.; Hassenstein, U. E.; Wheaton, L., Interaction of gramicidin S and its aromatic amino-acid analog with phospholipid membranes. *Biophys. J.* **2008**, *95* (7), 3306–3321.
- (4) Kamysz, E.; Mickiewicz, B.; Kamysz, W.; Bielińska, S.; Rodziewicz-Motowidło, S.; Ciarkowski, J., Synthesis, biological activity and solution structure of new analogues of the antimicrobial Gramicidin S. *J. Pept. Sci.* **2011**, *17* (3), 211–217.
- (5) Nagamurthi, G.; Rambhav, S., Gramicidin-S: Structure-activity relationship. *J. Biosci.* **1985**, *7* (3), 323–329.
- (6) Prenner, E. J.; Kiricsi, M.; Jelokhani-Niaraki, M.; Lewis, R. N. A. H.; Hodges, R. S.; McElhaney, R. N., Structure-activity relationships of diastereomeric lysine ring size analogs of the antimicrobial peptide gramicidin S: mechanism of action and discrimination between bacterial and animal cell membranes. *J. Biol. Chem.* **2005**, *280* (3), 2002–2011.
- (7) Swierstra, J.; Kapoerchan, V.; Knijnenburg, A.; van Belkum, A.; Overhand, M., Structure, toxicity and antibiotic activity of gramicidin S and derivatives. *Eur. J. Clin. Microbiol. Infect. Dis.* **2016**, *35* (5), 763–769.
- (8) Tamaki, M.; Akabori, S.; Muramatsu, I., Properties of synthetic analogs of gramicidin S containing L-serine or L-glutamic acid residue in place of L-ornithine residue. *Int. J. Pept. Prot. Res.* **1996**, *47* (5), 369–375.
- (9) Tennessen, J. A., Molecular evolution of animal antimicrobial peptides: widespread moderate positive selection. *J. Evol. Biol.* **2005**, *18* (6), 1387–1394.
- (10) Kawai, M.; Yamamura, H.; Tanaka, R.; Umamoto, H.; Ohmizo, C.; Higuchi, S.; Katsu, T., Proline residue-modified polycationic analogs of gramicidin S with high antibacterial

- activity against both Gram-positive and Gram-negative bacteria and low hemolytic activity. *J. Pept. Res.* **2005**, *65* (1), 98–104.
- (11) Mogi, T.; Kita, K., Gramicidin S and polymyxins: the revival of cationic cyclic peptide antibiotics. *Cell. Mol. Life Sci.* **2009**, *66* (23), 3821–3826.
- (12) van der Knaap, M.; Lageveen, L. T.; Busscher, H. J.; Mars-Groenendijk, R.; Noort, D.; Otero, J. M.; Llamas-Saiz, A. L.; van Raaij, M. J.; van der Marel, G. A.; Overkleeft, H. S.; Overhand, M., Evaluation of Readily Accessible Azoles as Mimics of the Aromatic Ring of D-Phenylalanine in the Turn Region of Gramicidin S. *ChemMedChem* **2011**, *6* (5), 840–847.
- (13) Falciatore, A.; Bowler, C., The Evolution and Function of Blue and Red Light Photoreceptors. In *Current Topics in Developmental Biology*, Academic Press: 2005; Vol. 68, pp 317–350.
- (14) Lerch, M. M.; Hansen, M. J.; van Dam, G. M.; Szymanski, W.; Feringa, B. L., Emerging Targets in Photopharmacology. *Angew. Chem. Int. Ed.* **2016**, *55* (37), 10978–10999.
- (15) Broichhagen, J.; Trauner, D., The *in vivo* chemistry of photoswitched tethered ligands. *Curr. Opin. Chem. Biol.* **2014**, *21*, 121–127.
- (16) Koçer, A.; Walko, M.; Meijberg, W.; Feringa, B. L., A Light-Actuated Nanovalve Derived from a Channel Protein. *Science* **2005**, *309* (5735), 755–758.
- (17) Blanco, B.; Palasis, K. A.; Adwal, A.; Callen, D. F.; Abell, A. D., Azobenzene-containing photoswitchable proteasome inhibitors with selective activity and cellular toxicity. *Bioorg. Med. Chem.* **2017**, *25* (19), 5050–5054.
- (18) Harvey, A. J.; Abell, A. D., α -Ketoester-based photobiological switches: synthesis, peptide chain extension and assay against α -chymotrypsin. *Bioorg. Med. Chem. Lett.* **2001**, *11* (18), 2441–2444.
- (19) Karlsson, C.; Blom, M.; Johansson, M.; Jansson, A. M.; Scifo, E.; Karlén, A.; Govender, T.; Gogoll, A., Phototriggerable peptidomimetics for the inhibition of *Mycobacterium tuberculosis* ribonucleotide reductase by targeting protein–protein binding. *Org. Biomol. Chem.* **2015**, *13* (9), 2612–2621.
- (20) Pearson, D.; Abell, A. D., Structural Optimization of Photoswitch Ligands for Surface Attachment of α -Chymotrypsin and Regulation of Its Surface Binding. *Chem. Eur. J.* **2010**, *16* (23), 6983–6992.
- (21) Pearson, D.; Alexander, N.; Abell, A. D., Improved Photocontrol of α -Chymotrypsin Activity: Peptidomimetic Trifluoromethylketone Photoswitch Enzyme Inhibitors. *Chem. Eur. J.* **2008**, *14* (24), 7358–7365.

- (22) Reisinger, B.; Kuzmanovic, N.; Löffler, P.; Merkl, R.; König, B.; Sterner, R., Exploiting Protein Symmetry To Design Light-Controllable Enzyme Inhibitors. *Angew. Chem. Int. Ed.* **2014**, *53* (2), 595–598.
- (23) Borowiak, M.; Nahaboo, W.; Reynders, M.; Nekolla, K.; Jalinot, P.; Hasserodt, J.; Rehberg, M.; Delattre, M.; Zahler, S.; Vollmar, A.; Trauner, D.; Thorn-Seshold, O., Photoswitchable Inhibitors of Microtubule Dynamics Optically Control Mitosis and Cell Death. *Cell* **2015**, *162* (2), 403–411.
- (24) Engdahl, A. J.; Torres, E. A.; Lock, S. E.; Engdahl, T. B.; Mertz, P. S.; Streu, C. N., Synthesis, Characterization, and Bioactivity of the Photoisomerizable Tubulin Polymerization Inhibitor azo-Combretastatin A4. *Org. Lett.* **2015**, *17* (18), 4546–4549.
- (25) Velema, W. A.; van der Berg, J. P.; Hansen, M. J.; Szymanski, W.; Driessen, A. J. M.; Feringa, B. L., Optical control of antibacterial activity. *Nat. Chem.* **2013**, *5* (11), 924–928.
- (26) Wegener, M.; Hansen, M. J.; Driessen, A. J. M.; Szymanski, W.; Feringa, B. L., Photocontrol of Antibacterial Activity: Shifting from UV to Red Light Activation. *J. Am. Chem. Soc.* **2017**, *139* (49), 17979–17986.
- (27) Babii, O.; Afonin, S.; Berditsch, M.; Reißer, S.; Mykhailiuk, P. K.; Kubyshkin, V. S.; Steinbrecher, T.; Ulrich, A. S.; Komarov, I. V., Controlling Biological Activity with Light: Diarylethene-Containing Cyclic Peptidomimetics. *Angew. Chem. Int. Ed.* **2014**, *53* (13), 3392–3395.
- (28) Fujino, T.; Arzhantsev, S. Y.; Tahara, T., Femtosecond Time-Resolved Fluorescence Study of Photoisomerization of trans-Azobenzene. *J. Phys. Chem. A* **2001**, *105* (35), 8123–8129.
- (29) Kumar, G. S.; Neckers, D. C., Photochemistry of azobenzene-containing polymers. *Chem. Rev.* **1989**, *89* (8), 1915–1925.
- (30) Lednev, I. K.; Ye, T. Q.; Matousek, P.; Towrie, M.; Foggi, P.; Neuwahl, F. V. R.; Umapathy, S.; Hester, R. E.; Moore, J. N., Femtosecond time-resolved UV-visible absorption spectroscopy of trans-azobenzene: dependence on excitation wavelength. *Chem. Phys. Lett.* **1998**, *290* (1), 68–74.
- (31) Mahimwalla, Z.; Yager, K. G.; Mamiya, J.-i.; Shishido, A.; Priimagi, A.; Barrett, C. J., Azobenzene photomechanics: prospects and potential applications. *Polym. Bull.* **2012**, *69* (8), 967–1006.
- (32) Renner, C.; Moroder, L., Azobenzene as Conformational Switch in Model Peptides. *ChemBioChem* **2006**, *7* (6), 869–878.

- (33) Podewin, T.; Rampp, M. S.; Turkanovic, I.; Karaghiosoff, K. L.; Zinth, W.; Hoffmann-Röder, A., Photocontrolled chignolin-derived β -hairpin peptidomimetics. *ChemComm.* **2015**, *51* (19), 4001–4004.
- (34) Wang, C.-C.; Lai, W.-C.; Chuang, W.-J., Type I and II β -turns prediction using NMR chemical shifts. *J. Biomol. NMR* **2014**, *59* (3), 175–184.
- (35) Priewisch, B.; Rück-Braun, K., Efficient Preparation of Nitrosoarenes for the Synthesis of Azobenzenes. *J. Org. Chem.* **2005**, *70* (6), 2350–2352.
- (36) Freyer, W.; Brete, D.; Schmidt, R.; Gahl, C.; Carley, R.; Weinelt, M., Switching behavior and optical absorbance of azobenzene-functionalized alkanethiols in different environments. *J. Photochem. Photobiol. A* **2009**, *204* (2), 102–109.
- (37) Szymański, W.; Beierle, J. M.; Kistemaker, H. A. V.; Velema, W. A.; Feringa, B. L., Reversible Photocontrol of Biological Systems by the Incorporation of Molecular Photoswitches. *Chem. Rev.* **2013**, *113* (8), 6114–6178.
- (38) Ludwig, E.; Strunskus, T.; Hellmann, S.; Nefedov, A.; Wöll, C.; Kipp, L.; Rosnagel, K., Electronic structure, adsorption geometry, and photoswitchability of azobenzene layers adsorbed on layered crystals. *Phys. Chem. Chem. Phys.* **2013**, *15* (46), 20272–20280.
- (39) Rosler, K.-H. A.; Wright, J.; Fox, K. M.; Waters, R. M.; Callery, P. S., A Nuclear Magnetic Resonance (NMR) Method for the Determination of the *cis/trans* Isomeric Content of Chlorprothixene. *Pharm. Res.* **1989**, *6* (8), 706–708.
- (40) Phillips, S. T.; Rezac, M.; Abel, U.; Kossenjans, M.; Bartlett, P. A., “@-Tides”: The 1,2-Dihydro-3(6H)-pyridinone Unit as a β -Strand Mimic. *J. Am. Chem. Soc.* **2002**, *124* (1), 58–66.
- (41) Ramachandran, G. N.; Sasisekharan, V., Conformation of Polypeptides and Proteins. In *Advances in Protein Chemistry*, Anfinsen, C. B.; Anson, M. L.; Edsall, J. T.; Richards, F. M., Eds. Academic Press: 1968; Vol. 23, pp 283–437.
- (42) Gibbs, A. C.; Kondejewski, L. H.; Gronwald, W.; Nip, A. M.; Hodges, R. S.; Sykes, B. D.; Wishart, D. S., Unusual β -sheet periodicity in small cyclic peptides. *Nat. Struct. Mol. Biol.* **1998**, *5* (4), 284–288.
- (43) Lewis, P. N.; Momany, F. A.; Scheraga, H. A., Folding of polypeptide chains in proteins: a proposed mechanism for folding. *Proc. Natl. Acad. Sci. USA* **1971**, *68* (9), 2293–2297.
- (44) Berditsch, M.; Jäger, T.; Stempel, N.; Schwartz, T.; Overhage, J.; Ulrich, A. S., Synergistic effect of membrane-active peptides polymyxin B and gramicidin S on multidrug-

resistant strains and biofilms of *Pseudomonas aeruginosa*. *Antimicrob. Agents Chemother.* **2015**, 59 (9), 5288–5296.

(45) Pantos, A.; Tsogas, I.; Paleos, C. M., Guanidinium group: A versatile moiety inducing transport and multicompartmentalization in complementary membranes. *BBA-Biomembranes* **2008**, 1778 (4), 811–823.

2.7 Supplementary Information

2.7.1 Materials

Fmoc-D-Phe-OH, hydroxybenzotriazole (HOBt) and *N*-(3-dimethylaminopropyl)-*N'*-ethylcarbodiimide hydrochloride (EDC.HCl) were purchased from GL Biochem (Shanghai) Ltd., China. Dichloromethane (CH₂Cl₂), *N,N*-dimethylformamide (DMF), piperidine and methanol (MeOH) were purchased from Merck, Australia. 4-aminobenzylamine, 3-aminobenzoic acid, Fmoc-Glu(tBu)-OH, trifluoroacetic acid (TFA), acetonitrile and diisopropylethylamine (DIPEA) were purchased from Sigma–Aldrich, Australia. Toluene, dimethylsulfoxide (DMSO), and acetic acid were purchased from Chem Supply, Australia. 1-[Bis(dimethylamino)methylene]-1*H*-1,2,3-triazolo[4,5-*b*]pyridinium 3-oxid (HATU), 2-Chlorotriyl chloride resin, Fmoc-L-Pro-OH, Fmoc-L-Orn(Boc)-OH, Fmoc-L-Leu-OH, Fmoc-L-Val-OH, and Fmoc-Arg(Pbf)-OH were purchased from Chem-Impex International, Inc., USA. All solvents and reagents were used without purification unless noted.

2.7.2 Methods

2.7.2.1 High Performance Liquid Chromatography (HPLC)

The synthetic cyclic peptides **1-3** were analyzed and purified by reverse phase high performance liquid chromatography (RP-HPLC), using a Gilson purification system equipped with a UV-Vis absorbance detector and a Supelco Analytical C₁₈ column (Discovery BIO Wide Pore C5-5, 250 x 10 mm, 5 μm). Aqueous solvent A: Water:TFA (100:0.1 v/v) and organic solvent B: ACN:TFA (100:0.08 v/v) were used during the purification process.

2.7.2.2 Mass Spectrometry

High resolution mass spectral data were obtained using an Agilent 6230 TOF LC/MS mass spectrometer. Mass spectra were obtained over a range of $100 < m/z < 2000$.

2.7.2.3 UV-Vis Spectrophotometry

All UV-Vis spectra were obtained at $30 \pm 0.5^\circ\text{C}$ on the Varian Cary 5000 UV-Vis spectrophotometer. All measurements were performed using quartz cuvettes with a concentration of approximately $100 \mu\text{g/mL}$ of **1-3** in DMSO. For conversion from a *trans* to a *cis* conformation, **1-3** were irradiated for 2 hours, under a UV lamp (UVP[®] MRL-58, 352 nm) prior to each measurement. For conversion from the *cis* to *trans* isomer, visible light (405 nm) was used. The absorbances for the respective conformations of **1-3** were measured between 200-800 nm.

2.7.2.4 NMR Spectroscopy

¹H NMR spectrum of the azobenzene photoswitch was recorded in DMSO-d₆ solution using an Agilent DD2 500MHz spectrometer. ¹H NMR spectra of the cyclic peptides were recorded on an Agilent DD2 600MHz NMR spectrometer. Chemical shifts are reported in ppm (δ) using TMS (0.00 ppm) as the internal standard. Signals are recorded as s (singlet), d (doublet), t (triplet) or m (multiplet).

2.7.2.5 Molecular Modelling

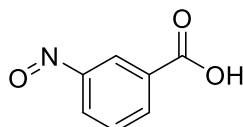
The lowest energy structures for *cis* and *trans* isomers of peptides **1-3** and a natural gramicidin S were determined in collaboration using Gaussian 09¹ package on the National Computing Infrastructure (NCI) National Facility, e.g. Raijin supercomputer. The initial geometries of peptides **1-3** and gramicidin S were constructed through GaussView 5.0 program. The geometry of each structure was optimized in the gas phase using the density functional theory (DFT) with

the B3LYP density function and basis sets of increasing size from STO-3G up to 6-31G** for all atoms.

2.7.3 Experimental

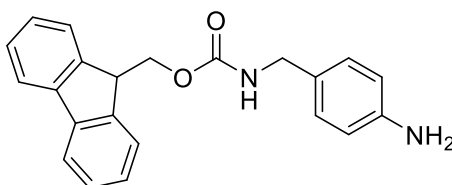
2.7.3.1 Synthesis of Azobenzene Photoswitch

3-nitrosobenzoic acid



To a solution of 3-aminobenzoic acid (5.0 g, 36.5 mmol) in dichloromethane (100 mL), a solution of oxone (22.4 g, 73.0 mmol) in water (400 mL) was added dropwise, and the mixture was stirred vigorously for 4h at rt. The mixture was filtered and dried overnight under vacuum to yield a yellow solid (5.0 g, 90%). ¹H NMR (500 MHz, DMSO-d₆): δ 8.41-8.39 (m, 1H), 8.36-8.35 (m, 1H), 8.20-8.17 (m, 1H), 7.89 (t, *J* = 7.8 Hz, 1H).

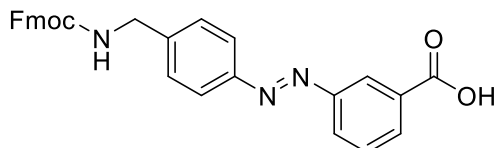
(9*H*-fluoren-9-yl) methyl 4-aminobenzylcarbamate



To a mixture of 4-aminobenzylamine (2.0 g, 16.4 mmol) in water (32 mL) and tetrahydrofuran (12 mL), 5% NaHCO₃ (1.5 mL) was added, and the mixture was stirred for 10 min at rt. *N*-(9-fluorenylmethoxycarbonyloxy)succinimide (5.5 g, 16.4 mmol) was suspended in tetrahydrofuran (20 mL) and the suspension was added dropwise, and the mixture stirred for 24h at rt. Water (500 mL) was added to the mixture and the product was precipitated as a pale

yellow solid. The precipitate was filtered and dried in vacuo to give a yellow solid (4.8 g, 84%). $^1\text{H NMR}$ (500 MHz, DMSO- d_6): δ 7.88 (d, $J = 7.5$ Hz, 1H), 7.69 (d, $J = 7.5$ Hz, 1H), 7.63 (t, $J = 6.0$ Hz, 1H), 7.41 (t, $J = 7.3$ Hz, 1H), 7.32 (t, $J = 7.5$ Hz, 1H), 6.88 (d, $J = 8.2$ Hz, 1H), 6.49 (d, $J = 8.3$ Hz, 1H), 4.30 (d, $J = 7.0$ Hz, 1H), 4.21 (d, $J = 6.7$ Hz, 1H), 3.99 (d, $J = 6.0$ Hz, 1H).

Azobenzene Photoswitch



To a solution of 3-nitrosobenzoic acid (2.3 g, 15.4 mmol) in DMSO (50 mL), glacial acetic acid (50 mL) was added, and the mixture was stirred for 10 min at rt. (9H-fluoren-9-yl) methyl 4-aminobenzylcarbamate (2.6 g, 7.7 mmol) was added to the reaction mixture and stirred overnight under N_2 at rt. The mixture was filtered under suction to reveal an orange solid. The remaining product in the filtrate was extracted by CH_2Cl_2 (50 mL), and the mixture was washed with water (2 x 50 mL) to remove acetic acid/DMSO. The organic layer was removed under N_2 to obtain an orange solid. The two orange solids were combined and dried in vacuo. The crude product was purified by column chromatography (9:1 CH_2Cl_2 /methanol) to give an orange solid (2.3 g, 63%). R.f (9:1 CH_2Cl_2 /methanol) = 0.4. $^1\text{H NMR}$ (500 MHz, DMSO- d_6): δ 13.30 (s, 1H), 8.38 (s, 1H), 8.16-8.11 (m, 2H), 7.95 (t, $J = 6.1$ Hz, 1H), 7.90 (d, $J = 6.9$ Hz, 4H), 7.76-7.71 (m, 3H), 7.45-7.40 (m, 4H), 7.34 (t, $J = 7.4$ Hz, 2H), 4.40 (d, $J = 6.7$ Hz, 2H), 4.29 (d, $J = 6.0$ Hz, 2H), 4.25 (t, $J = 6.5$ Hz, 1H). HRMS: (m/z) calc for $\text{C}_{29}\text{H}_{23}\text{N}_3\text{O}_4$: 478.1722 $[\text{M}+\text{H}]^+$, found: 478.1759.

2.7.3.2 Solid Phase Peptide Synthesis (SPPS) of Linear Peptides

Standard Fmoc-based SPPS and commercially available reagents were used for the synthesis of the linear peptides. 2-Chlorotrityl chloride resin preloaded with Fmoc-D-Phe-OH (0.58 mmol/g, 1.0 g, 1 equiv.) was used to synthesize the linear precursors. The unreacted active sites on the resin were capped with 17:2:1 CH₂Cl₂/MeOH/DIPEA (2 x 25 mL) for 30 min before washing the resin with CH₂Cl₂ (x3), DMF (x3) and CH₂Cl₂ (x3). *N*-Fmoc deprotection was carried out by treating the resin with 25% piperidine/DMF (25 mL) for 30 min before washing with CH₂Cl₂ (x3), DMF (x3) followed by CH₂Cl₂ (x3). Couplings of the amino acids and azobenzene photoswitch were performed using the following molar ratios of reagents: Fmoc-amino acids and Fmoc-azobenzene photoswitch (2 equiv.) dissolved in DMF (20 mL), 1-[Bis(dimethylamino)methylene]-1*H*-1,2,3-triazolo[4,5-*b*]pyridinium 3-oxid hexafluorophosphate (HATU)/DMF (0.5 M, 2 equiv.) and DIPEA (8 equiv.). The resin was washed with CH₂Cl₂ (x3), DMF (x3) followed by CH₂Cl₂ (x3), and the coupling procedures were repeated. The coupling time in all cases was 2h. Deprotection and coupling procedures were repeated alternatively until the sequence was completed. After the peptide sequences were completed and deprotected, the resin was washed with CH₂Cl₂ (x3), DMF (x3) followed by CH₂Cl₂ (x3) and dried under vacuum. The linear precursors were cleaved from the resin using 1.5% TFA in CH₂Cl₂ (2 x 20 mL) while maintaining the side chain protection of ornithine/arginine/glutamic acid residues. The reagents were left to stand for 15 min with stirring before filtering the peptide solution. The volatile products from the filtrate were removed by N₂ flow, and the linear peptides were placed under vacuum for 4h, to yield a crude orange solid.

2.7.3.3 Cyclization of Linear Peptides

Respective solutions of crude linear peptides in methanol (22 mg/mL) were irradiated by UV light ($\lambda = 352$ nm) for 4h, to convert the azobenzene into its *cis* isomer prior to cyclization. The solvent was removed in vacuo, and the residue was placed under vacuum for 30 min. The linear peptides were each dissolved in dry DMF (0.03 mmol/mL) and cyclized using the following reagents: HOBt (5 equiv.), EDC.HCl (5 equiv.) and DIPEA (10 equiv.) in dry DMF (63 mL).

The mixture was kept away from visible light using an aluminium foil cover and stirred overnight under N₂ conditions at rt. DMF was then removed by N₂ flow. The crude cyclic peptides were washed with toluene (3 x 20 mL) and methanol (3 x 30 mL) to remove residual DMF, and the solvent was removed in vacuo. The cyclic peptides were then dissolved in CH₂Cl₂ (60 mL), and the solutions were washed with saturated NaHCO₃ (4 x 60 mL) and brine (2 x 60 mL). The organic layer was dried over MgSO₄, and the solvent was removed in vacuo. The residue was dried under vacuum for 4h to yield an orange solid.

2.7.3.4 Deprotection of Side Chain Protecting Groups

The Boc protecting groups on the side chains of all ornithine residues were removed by treatment with 50% TFA/CH₂Cl₂ (v/v, 10 mL) for 1h. The volatiles were removed by a stream of N₂ to give gramicidin S and peptides **1** and **2a**, as orange solids. The Pbf protecting groups on the side chains of all arginine residues were removed by treatment with TFA/TIPS/H₂O (95:2.5:2.5, 10 mL) for 1h. The volatiles were removed by a stream of N₂ to give peptides **2b** and **3a-3b**, as orange solids. The tBu protecting groups on the side chains of both glutamic acid residues were removed by treatment with TFA/CH₂Cl₂ (9:1, v/v, 10 mL) for 1h. The volatiles were removed by a stream of N₂ to give peptide **2c** as an orange solid. All crude products were purified by RP-HPLC. Fraction collection was set for peak-based collection at 220 nm and 320 nm for gramicidin S and peptides **1-3** respectively. The identity of the pure products was confirmed by mass spectrometry.

2.7.3.5 Photoisomerization of Peptides 1-3

Peptides **1-3** were dissolved in DMSO at a concentration of 100 µg/mL and exposed to visible light of 405 nm for 2h to yield the *trans*-enriched PSS. The *trans*-enriched PSS of **1-3** were irradiated by UV light of 352 nm for 2h, to convert to the respective *cis*-enriched PSS.

2.7.3.6 Half-Life Analysis of Peptides 1-3

The half-life of peptides **1-3** was determined by UV-Vis spectrophotometry.² Prior to irradiation, peptides **1-3** in their thermally stable *trans*-enriched PSS were dissolved in DMSO, and the wavelengths of maximum absorbance (λ_{\max}) were measured using a Synergy H4 Hybrid Multi-Mode Microplate Reader. The peptides were then irradiated under UV light (352 nm) for 2h to convert the samples to their *cis*-enriched PSS, and the λ_{\max} were determined. The samples were irradiated under UV (352 nm) for a further 30 min to achieve the maximum attainable *cis*-enriched PSS, which was confirmed when no further increase was observed in the absorbance. Each peptide in its *cis*-enriched PSS was stored in the dark, to switch the samples back to their respective *trans*-enriched PSS by thermal relaxation. The absorbance for each peptide was measured every 10 min to monitor the change in the absorbance at 328 nm, which is characteristic of the *trans*-enriched PSS. The measurements were conducted over a period of 62h. The absorbance at 328 nm increased gradually over 62h for all peptides, which indicated the *cis-trans* thermal back isomerization. The absorbance curves at 328 nm gradually reached a plateau when the peptides reached their maximum attainable *trans*-enriched PSS. The average of the triplicates was calculated to obtain the average half-life for each sample. The half-life for each peptide was calculated by analyzing the increase in the UV-Vis absorbance curves² at 328 nm, using curve fitting in the GraphPad Prism 7.03 software.

2.7.3.7 Molecular Modelling

The lowest energy structures for the *cis* and *trans* isomers of peptides **1-3** were determined in the gas phase using the NWChem 6.6 package,³ with tight convergence criteria using a hybrid B3LYP functional with 6-31G** basis set for all atoms. The initial geometries of peptides **1-3** were constructed through the GaussView 5.0 package by modifying the corresponding gramicidin S unit comprised in the X-ray crystal structure (entry code 2019361, Crystallography Open Database <http://www.crystallography.net>), as reported.⁴ The azobenzene moiety in either *cis* or *trans* conformation was incorporated into the cyclic structure, to replace the corner residues (proline and D-phenylalanine). Conformational analyses including dihedral angles,

overall molecular lengths, and intramolecular hydrogen bond lengths, were conducted using the Chimera 1.11 software.⁵

2.7.3.8 Biological Assays (Antibacterial Susceptibility Evaluation)

Antibacterial activity was determined by the microdilution broth method as recommended by the CLSI (Clinical and Laboratory Standards Institute, Document M07-A8, 2009, Wayne, PA.) using cation-adjusted Mueller-Hinton broth (Trek Diagnostics Systems, U.K.). Serial two-fold dilutions of each peptide were made using DMSO as the diluent. Trays were inoculated with 5×10^4 CFU of *S. aureus* ATCC 49975 in a volume of 100 μ L (final concentration of DMSO was 3.2% (v/v)) and incubated at 37 °C for 16-20h. Growth of the bacterium was quantified by measuring the absorbance at 620 nm.

2.7.4 UV-Vis Spectrum for Peptides 1-3

The UV-Vis spectra for the *cis*-enriched and *trans*-enriched PSS of peptides **1-3** were recorded in Figure S2.1.

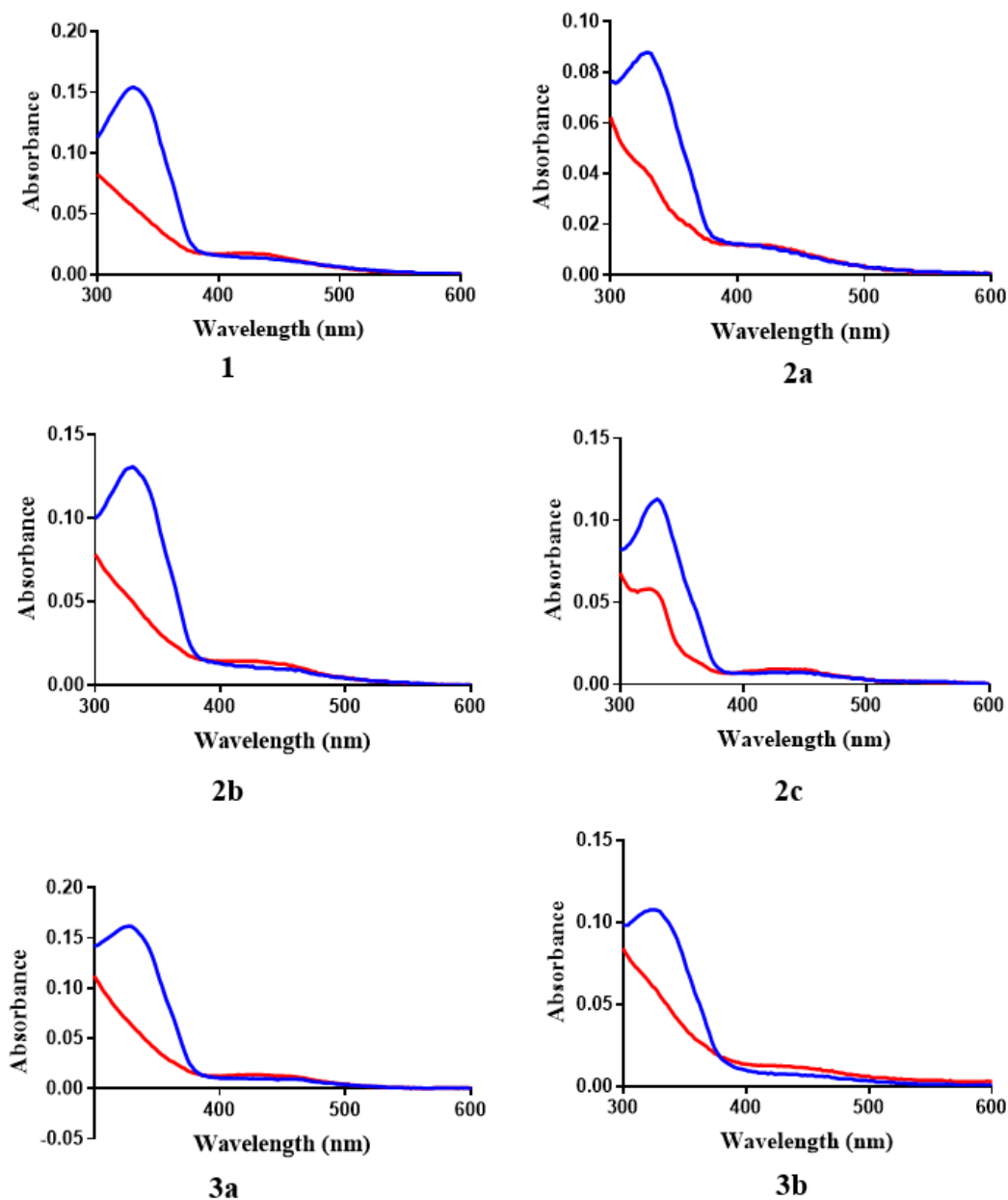


Figure S2.1. UV-Vis spectra for the *trans*-enriched PSS (blue) and *cis*-enriched PSS (red) after 2 hours of irradiation under visible light (405 nm) and UV light (352 nm) respectively. The *trans*-enriched PSS show a maximum absorbance in the 320 nm region, whereas the *cis*-enriched PSS have a higher absorbance at 428 nm, and an absorbance of much lower intensity at 320 nm.

2.7.5 ^1H NMR Spectroscopy

The ^1H NMR spectrum for the azobenzene photoswitch was recorded in the relaxed *trans* conformation on an Agilent DD2 500 MHz NMR spectrometer, while the ^1H NMR spectra for the gramicidin S and peptides **1-3** were recorded on an Agilent DD2 600 MHz NMR spectrometer. Prior irradiation, peptides **1-3** predominantly in the *trans*-enriched PSS were dissolved in methanol- d_6 or DMSO- d_6 and the NMR spectra were recorded. Subsequently, the *trans*-enriched PSS were irradiated under UV (352 nm) for the conversion into their corresponding *cis*-enriched PSS and the NMR spectra were again recorded. The $^3J_{\text{NHC}\alpha}$ for the *cis*-enriched PSS of peptides **1-3** were determined based on the amide NH shifts. The ratios of peak integrations for peptides **1-3** revealed the photoisomerization yield of the *cis*-enriched and *trans*-enriched PSS of each peptide. The connectivity of the peptides was determined by 2D NMR, ie. TOCSY and ROESY.

Table S2.1. $^3J_{\text{NHC}\alpha}$ values, ratios of peak integrations and photoisomerization yield for **1-3**.

| Peptide | Enriched-PSS | NH shifts, δ (ppm) | Ratio of peak integrations (<i>trans:cis</i>) | Photoisomerization Yield (%) |
|-----------|--------------|---------------------------|---|------------------------------|
| 1 | <i>cis</i> | 8.33 (t, $J=1.9$ Hz, 1H) | 0.23 : 2.15 | 90 |
| | | 8.11-8.08 (m, 1H) | | |
| | | 8.02-7.99 (d, 8.3 Hz, 3H) | | |
| | | 7.75 (d, 8.3 Hz, 1H) | | |
| | | 7.69 (t, $J=7.8$ Hz, 1H) | | |
| | <i>trans</i> | ND | 2.44 : 0.48 | 84 |
| 2a | <i>cis</i> | 8.41 (d, $J=6.5$ Hz, 1H) | 0.23 : 2.17 | 90 |
| | | 8.37 (t, $J=6.1$ Hz, 1H) | | |
| | | 8.27 (t, $J=8.1$ Hz, 2H) | | |
| | | 7.93 (d, $J=8.8$ Hz, 1H) | | |
| | | 7.83 (d, $J=8.4$ Hz, 1H) | | |
| | <i>trans</i> | ND | 2.06 : 0.27 | 88 |
| 2b | <i>cis</i> | 8.49 (d, $J=8.2$ Hz, 1H) | 0.96 : 2.37 | 71 |
| | | 8.36-8.31 (m, 1H) | | |
| | | 8.24 (d, $J=7.8$ Hz, 2H) | | |
| | | 7.91 (d, $J=8.6$ Hz, 2H) | | |
| | | 7.73 (d, $J=8.5$ Hz, 1H) | | |
| | <i>trans</i> | ND | 2.14 : 0.70 | 75 |

| | | | | |
|--------------|------------|--------------------------|-------------|----|
| 2c | <i>cis</i> | 8.26 (t, $J=8.0$ Hz, 2H) | 0.24 : 2.27 | 90 |
| | | 8.12 (d, $J=8.2$ Hz, 1H) | | |
| | | 8.02 (d, $J=7.3$ Hz, 2H) | | |
| | | 7.84 (d, $J=8.7$ Hz, 1H) | | |
| | | 7.67 (d, $J=8.5$ Hz, 1H) | | |
| <i>trans</i> | ND | 2.07 : 0.36 | 85 | |
| 3a | <i>cis</i> | 8.64-8.56 (m, 1H) | 0.40 : 2.15 | 84 |
| | | 8.40-8.33 (m, 1H) | | |
| | | 8.31-8.24 (m, 3H) | | |
| | | 8.11 (d, $J=5.8$ Hz, 1H) | | |
| | | 7.78 (d, $J=8.1$ Hz, 1H) | | |
| <i>trans</i> | ND | 2.14 : 1.11 | 66 | |
| 3b | <i>cis</i> | 8.56 (d, $J=6.3$ Hz, 1H) | 1.07 : 1.93 | 64 |
| | | 8.43 (d, $J=8.7$ Hz, 1H) | | |
| | | 8.14-8.10 (m, 1H) | | |
| | | 8.05 (d, $J=7.9$ Hz, 1H) | | |
| | | 7.98-7.88 (m, 2H) | | |
| | | 7.82 (d, $J=8.1$ Hz, 1H) | | |
| <i>trans</i> | ND | 2.20 : 1.08 | 67 | |

2.7.5.1 ^1H NMR Spectra

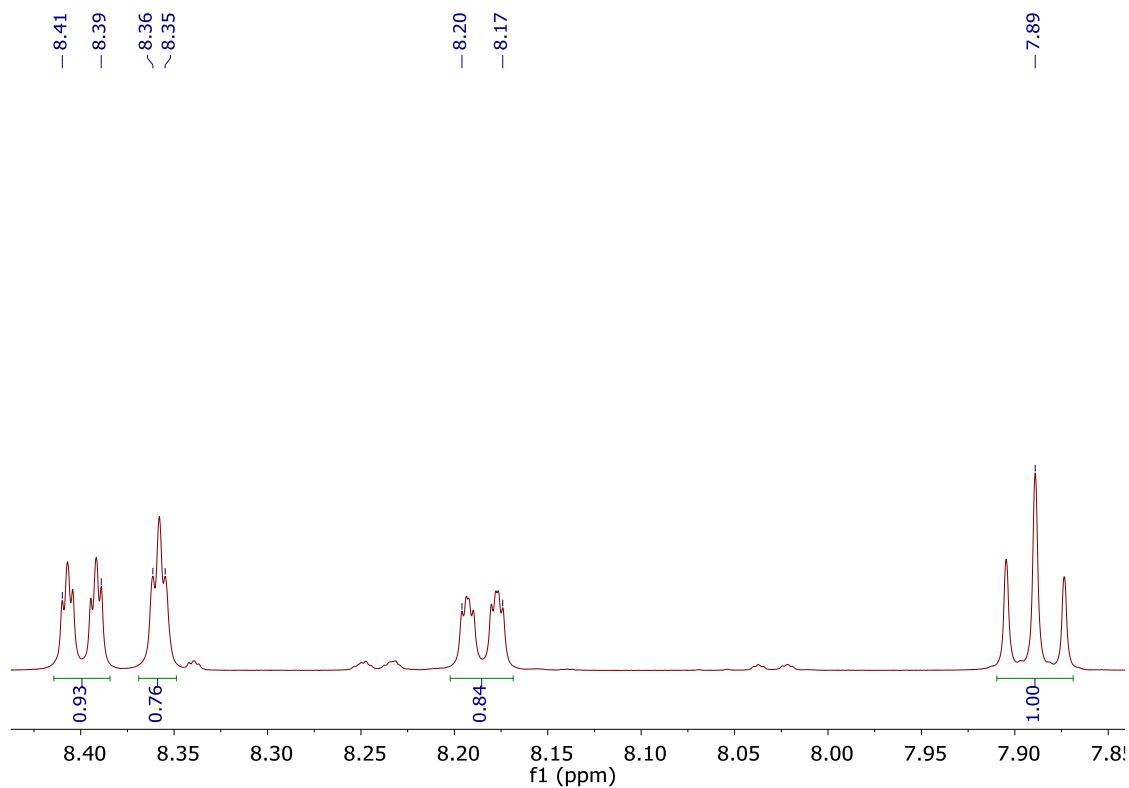


Figure S2.2a. ^1H NMR spectrum of 3-nitrosobenzoic acid.

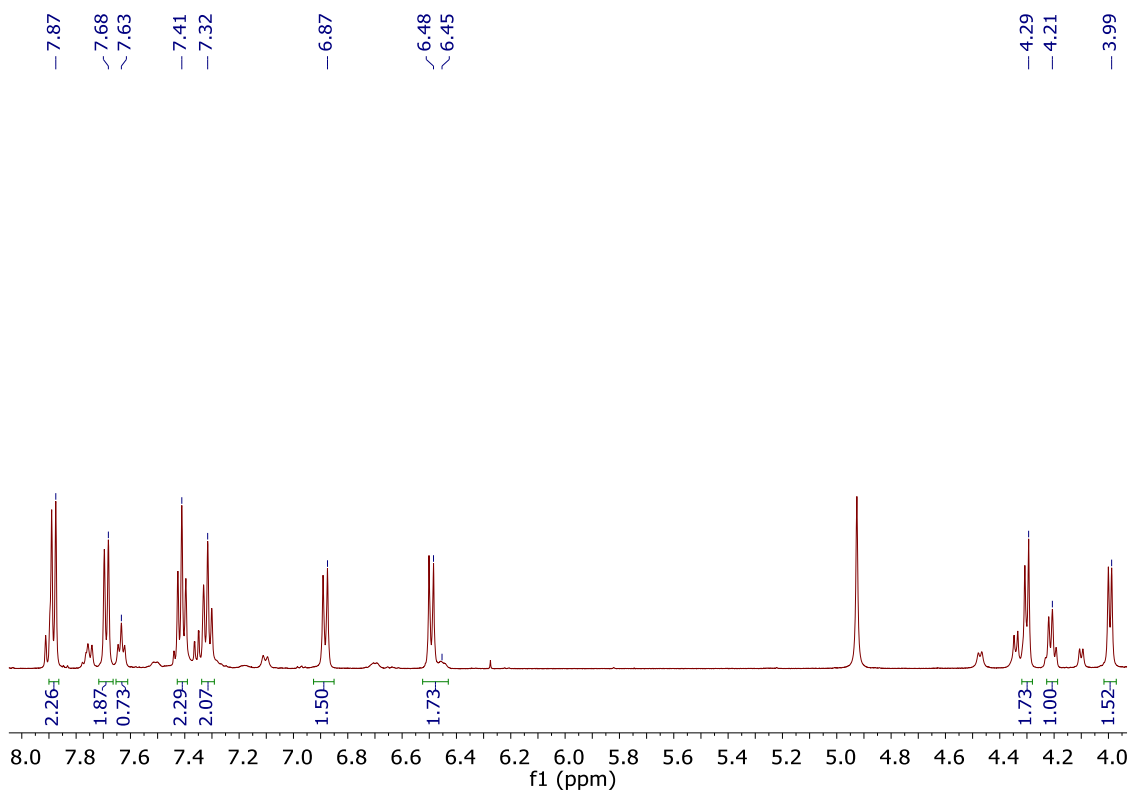


Figure S2.2b. ^1H NMR spectrum of (9H-fluoren-9-yl) methyl 4-aminobenzylcarbamate.

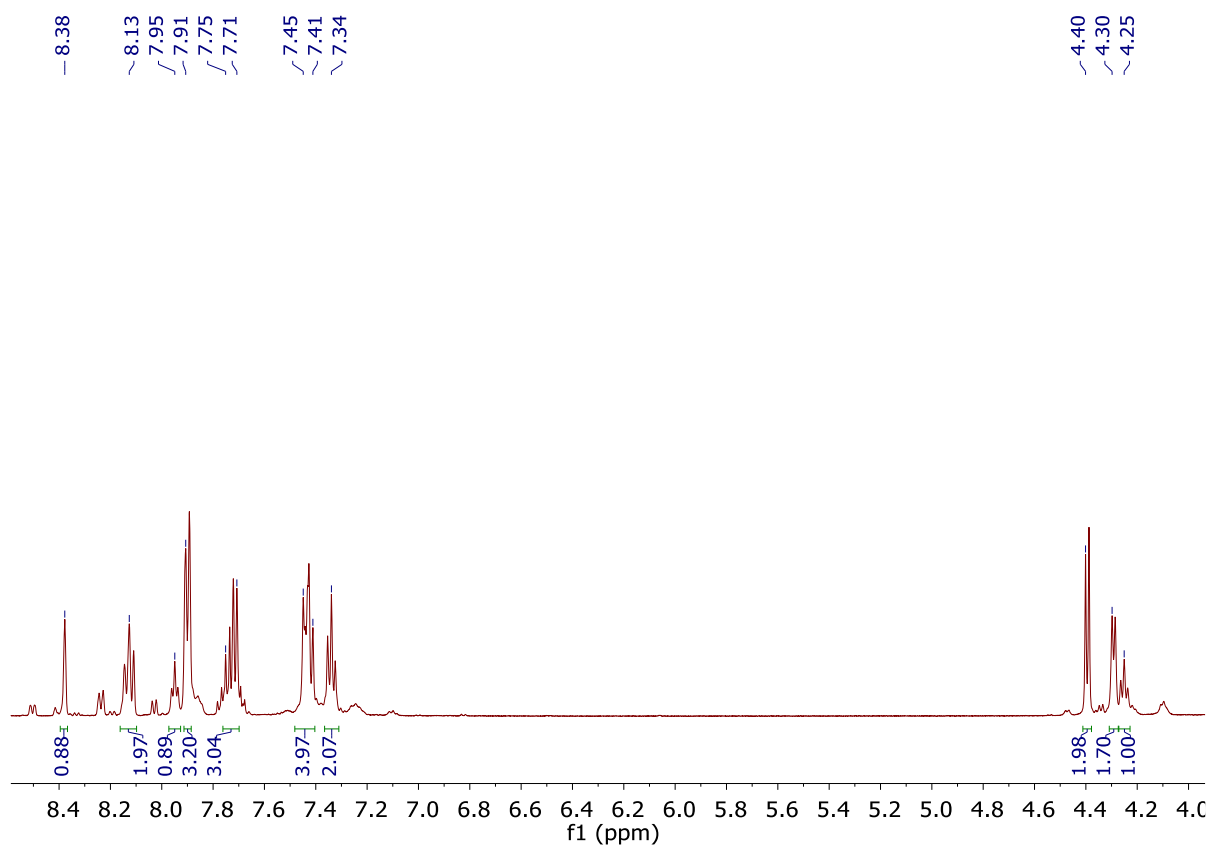


Figure S2.2c. ^1H NMR spectrum of azobenzene photoswitch.

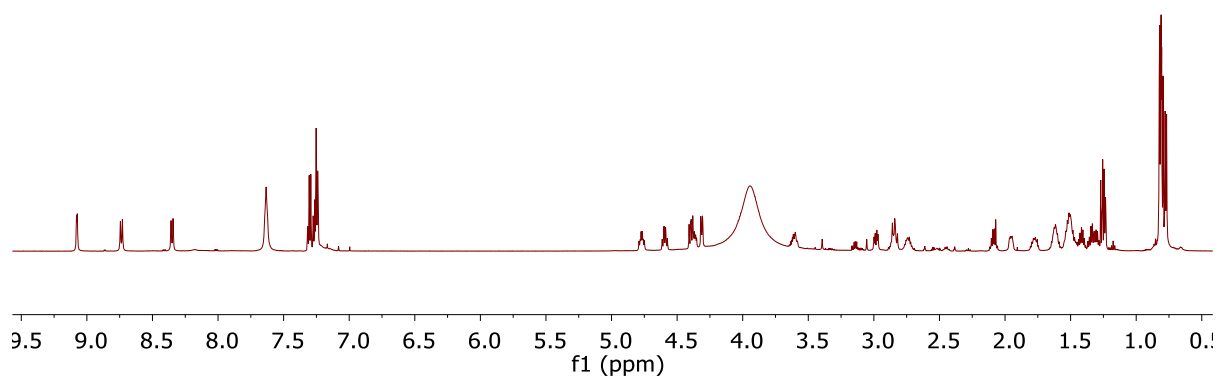


Figure S2.3. ^1H NMR spectrum of gramicidin S.

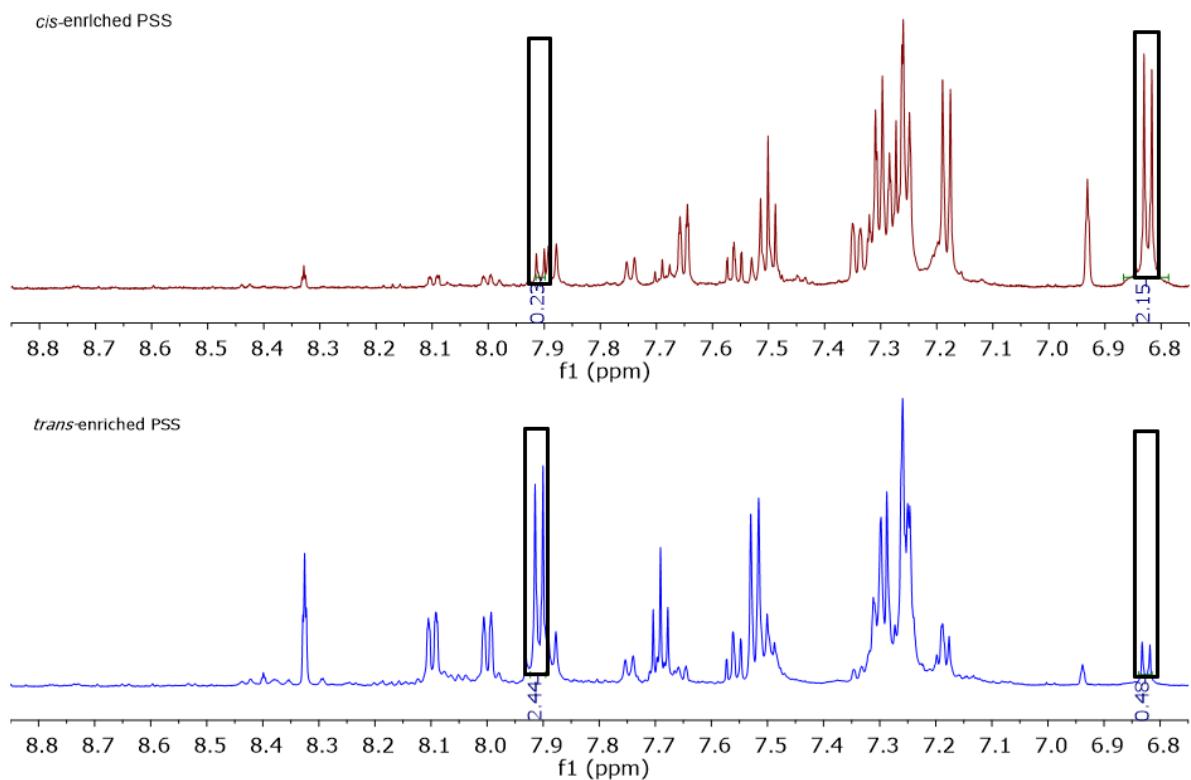


Figure S2.4a. ^1H NMR spectrum of *cis*- (red) and *trans*-enriched (blue) PSSs of peptide **1**. Boxed areas at δ 7.91 and δ 6.83 show the ratio between the *cis*- and *trans*-enriched PSSs.

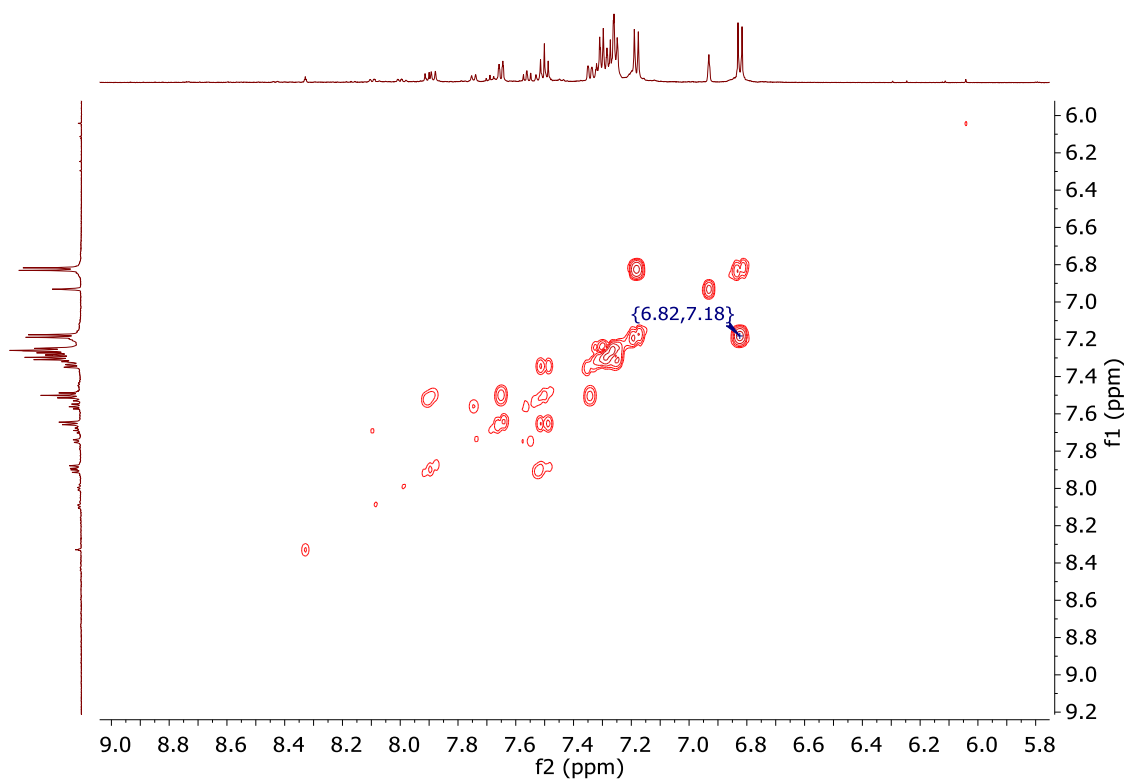


Figure S2.4b. COSY spectrum of the *cis*-enriched PSS of peptide **1**.

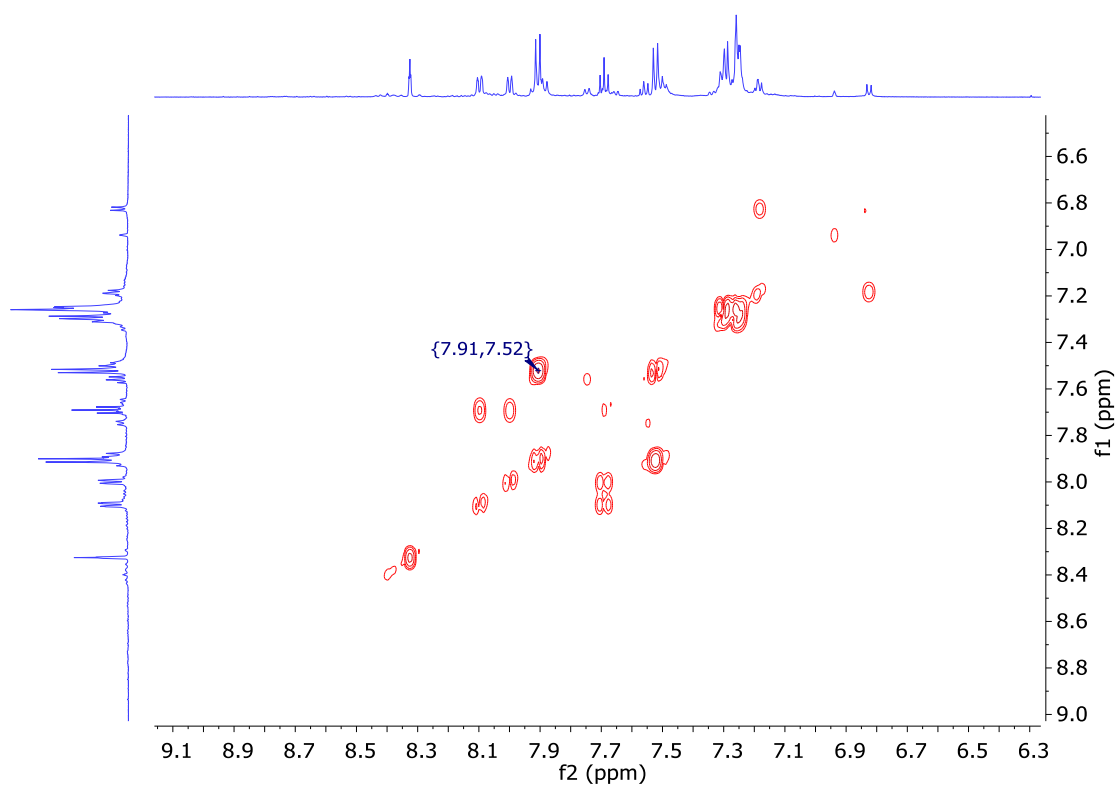


Figure S2.4c. COSY spectrum of the *trans*-enriched PSS of peptide **1**.

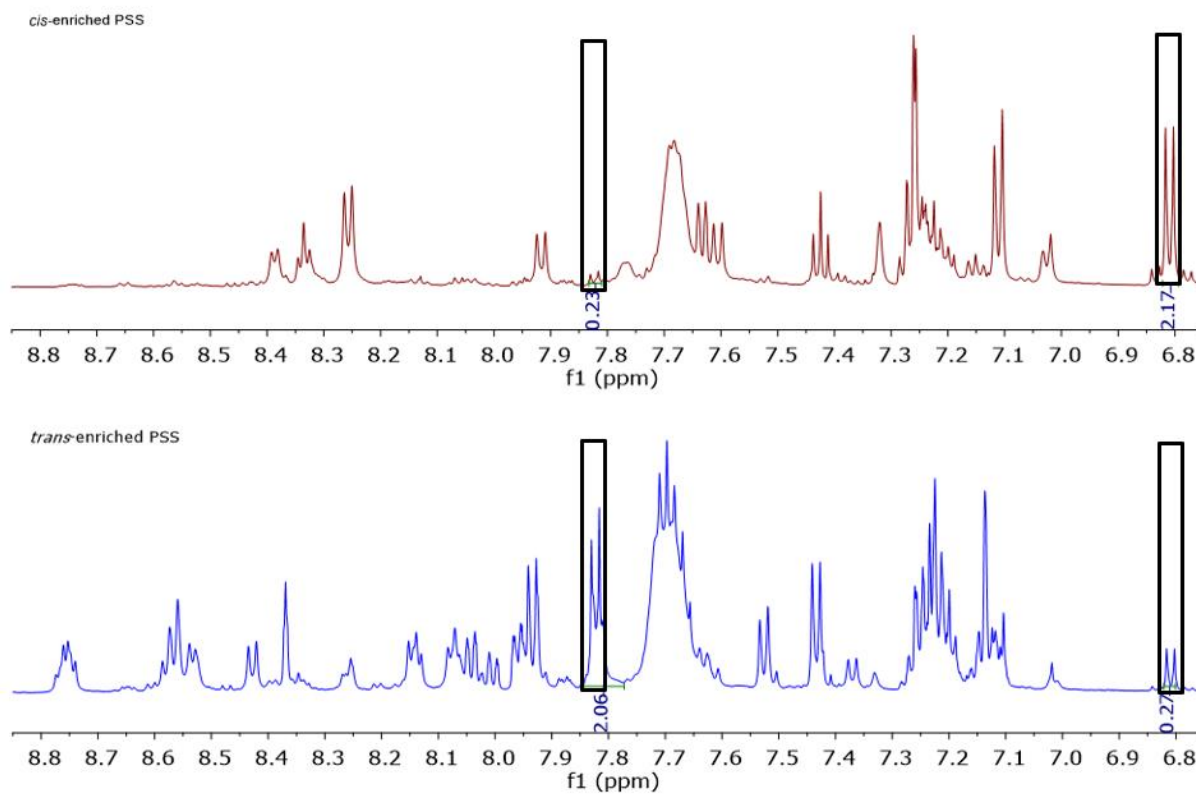


Figure S2.5a. ¹H NMR spectrum of *cis*- (red) and *trans*-enriched (blue) PSSs of peptide **2a**. Boxed areas at δ 7.83 and δ 6.81 show the ratio between the *cis*- and *trans*-enriched PSSs.

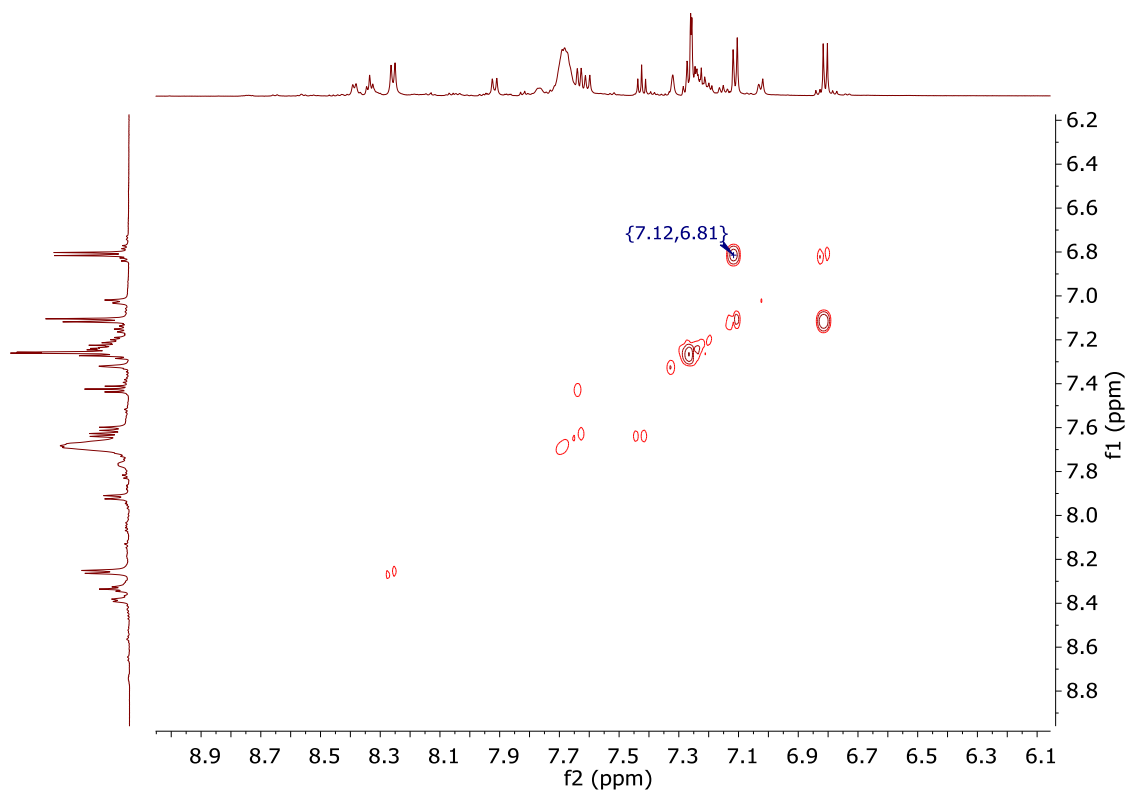


Figure S2.5b. COSY spectrum of the *cis*-enriched PSS of peptide **2a**.

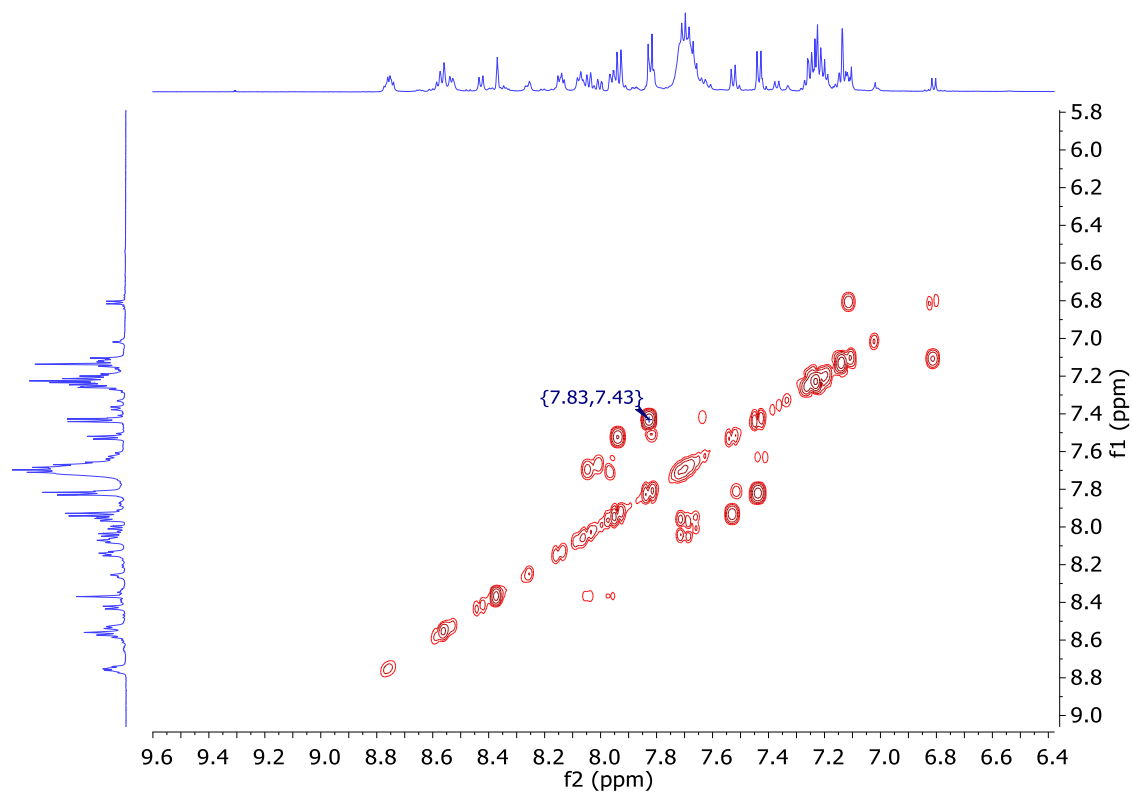


Figure S2.5c. COSY spectrum of the *trans*-enriched PSS of peptide **2a**.

2.7.6 Half-life Analysis

The absorbance at 328 nm increased gradually over 62h for peptides **1-3**, which indicated the *cis-trans* thermal back isomerization.² The absorbance curves at 328 nm gradually reached a plateau when peptides **1-3** were at their maximum attainable *trans*-enriched PSS. The half-life for each peptide was calculated by analyzing the increase in the UV-Vis absorbance curves at 328 nm, using curve fitting for non-linear regression of one-phase association.

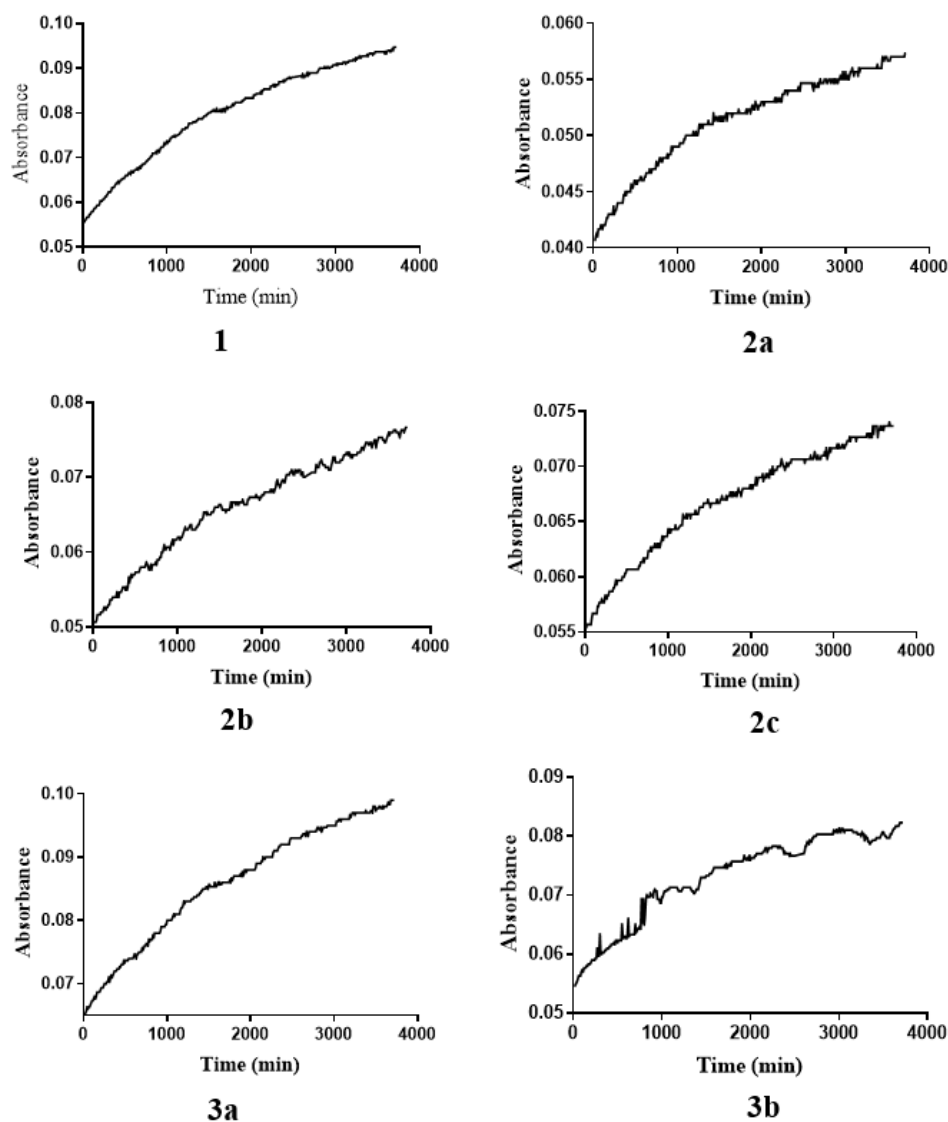


Figure S2.6. The absorbance curves of peptides **1-3** at their respective λ_{\max} when left in the dark for 62h. The gradual increase in the absorbance at 328 nm indicates the *cis-trans* thermal back isomerization of the peptide samples.

2.7.7 Molecular Modelling

Key structural differences between the *cis*-enriched and *trans*-enriched isomers of peptides **1-3** are summarized in Table S2.2-S2.3.

Table S2.2. Structural analysis of gramicidin S and the *cis*-enriched and *trans*-enriched isomers of peptides **1-3**.

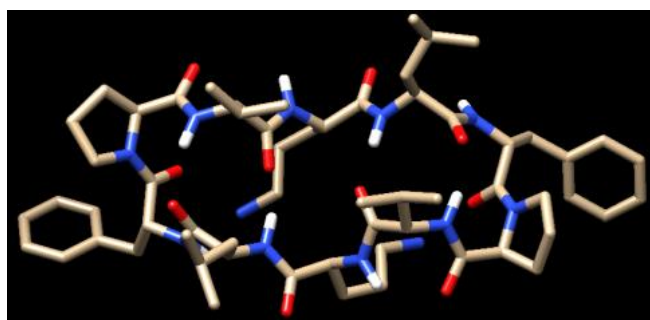
| Peptide | Enriched PSS | Average distance between backbone (Å) | Length of hydrogen bond (Å) | Number of hydrogen bonds | Number of residues conforming to β -sheet criteria | Distance between $C_{\alpha}(i)$ and $C_{\alpha}(i+3)$ (Å) | Presence of β -turn |
|--------------|--------------|---------------------------------------|-----------------------------|--------------------------|--|--|---------------------------|
| Gramicidin S | - | 4.6 | 2.1 | 4 | 5 | 5.3 | Present |
| | | | 2.0 | | | | |
| | | | 2.1 | | | | |
| | | | 2.2 | | | | |
| 1 | <i>cis</i> | 4.9 | 2.5 | 4 | 2 | 6 | Present |
| | | | 2.2 | | | | |
| | | | 2.0 | | | | |
| | <i>trans</i> | 9.6 | - | 0 | 1 | 7.2 | Absent |
| 2a | <i>cis</i> | 4.8 | 1.9 | 3 | 4 | 5.7 | Present |
| | | | 1.9 | | | | |
| | <i>trans</i> | 8.4 | - | 0 | 1 | 7.8 | Absent |
| 2b | <i>cis</i> | 4.9 | 1.9 | 3 | 3 | 5.8 | Present |
| | | | 2.0 | | | | |
| | <i>trans</i> | 8.9 | - | 0 | 0 | 8 | Absent |
| 2c | <i>cis</i> | 4.8 | 1.9 | 3 | 3 | 5.7 | Present |
| | | | 1.9 | | | | |
| | <i>trans</i> | 7.7 | - | 0 | 2 | 7.3 | Absent |
| 3a | <i>cis</i> | 4.9 | 1.9 | 3 | 2 | 5.8 | Present |
| | | | 2.0 | | | | |
| | <i>trans</i> | 9 | - | 0 | 0 | 8.4 | Absent |
| 3b | <i>cis</i> | 4.9 | 1.9 | 3 | 2 | 5.8 | Present |
| | | | 2.0 | | | | |
| | <i>trans</i> | 9 | - | 0 | 0 | 8.4 | Absent |

Table S2.3. Dihedral angles for gramicidin S and the *cis*-enriched and *trans*-enriched isomers of peptides 1-3.

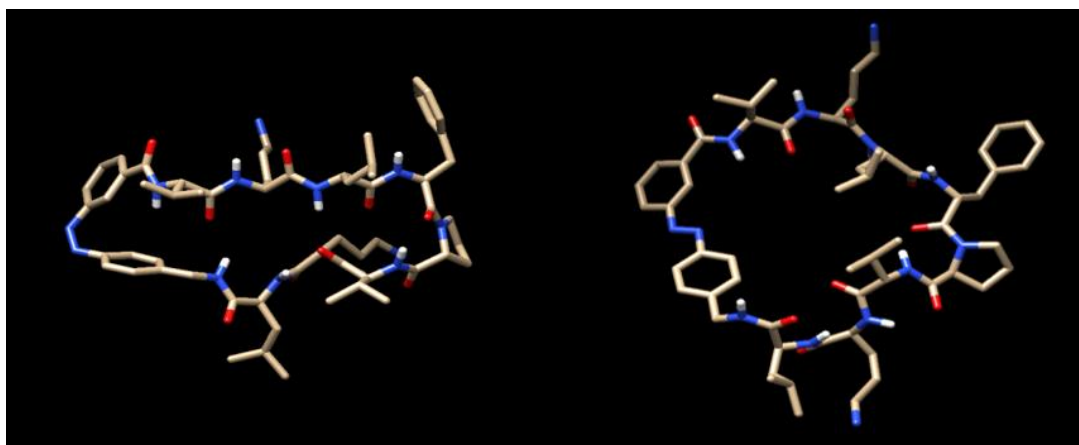
| Peptide | Enriched PSS | C α | Dihedral Angles (°) | | | β -Sheet Content (%) |
|--------------|--------------|-----------------------|---------------------|--------|----------|----------------------------|
| | | | ϕ | ψ | ω | |
| Gramicidin S | - | Pro | -83.7 | -1.9 | -179.9 | 50 |
| | | Val | -86.6 | 139.3 | 166.2 | |
| | | Orn | -135.2 | 134.5 | 173.3 | |
| | | Leu (<i>i</i>) | -136.8 | 107.3 | -174.4 | |
| | | D-Phe (<i>i</i> + 1) | 52 | -126.4 | -175.3 | |
| | | Pro (<i>i</i> + 2) | -80.3 | 5.1 | -179.6 | |
| | | Val (<i>i</i> + 3) | -108.4 | 126 | 169.2 | |
| | | Orn | -112.9 | 135.4 | 177.9 | |
| | | Leu | -141.1 | 103.2 | -173.2 | |
| | | D-Phe | 53.5 | -128.8 | -176.2 | |
| 1 | <i>cis</i> | Val | -121 | 146.9 | 173.5 | 25 |
| | | Orn | -79.3 | 156 | 175.6 | |
| | | Leu (<i>i</i>) | -143.4 | -161.6 | -177.9 | |
| | | D-Phe (<i>i</i> + 1) | -78.8 | -118.3 | -174.1 | |
| | | Pro (<i>i</i> + 2) | -61.8 | -38 | 168.6 | |
| | | Val (<i>i</i> + 3) | -81.7 | 87.6 | -159.3 | |
| | | Orn | -71.6 | -27.5 | 171.3 | |
| | <i>trans</i> | Leu | -117.7 | 125.7 | 179.8 | 13 |
| | | Val | -132.6 | 146.5 | 171.9 | |
| | | Orn | -58.2 | 139.1 | -171 | |
| | | Leu (<i>i</i>) | -166.1 | 157.6 | 168.2 | |
| | | D-Phe (<i>i</i> + 1) | -70 | -163 | -160.7 | |
| | | Pro (<i>i</i> + 2) | -84.9 | 48.7 | 174.2 | |
| | | Val (<i>i</i> + 3) | -85.4 | 82.9 | -160.2 | |
| Orn | -77.6 | -13.6 | 166.6 | | | |
| Leu | 24.9 | 148.8 | -14.7 | | | |

| | | | | | | |
|----|--------------|-----------------------|--------|--------|--------|----|
| 2a | <i>cis</i> | Val | -119.1 | 132.3 | 177.9 | 43 |
| | | Orn | -150.6 | 160.7 | 166.2 | |
| | | Leu (<i>i</i>) | -120.9 | -115.8 | 172.4 | |
| | | D-Phe (<i>i</i> + 1) | -100.8 | 109.7 | 177.8 | |
| | | Pro (<i>i</i> + 2) | 79 | -62.1 | 177.4 | |
| | | Val (<i>i</i> + 3) | -59.4 | 130.7 | -176.3 | |
| | | Orn | -153.1 | 154.6 | 176.8 | |
| | <i>trans</i> | Val | -134.2 | 38.1 | -169.3 | 14 |
| | | Orn | -82.6 | 66.4 | -173.6 | |
| | | Leu (<i>i</i>) | -74.9 | -22.9 | -177.7 | |
| | | D-Phe (<i>i</i> + 1) | -155.7 | 140.9 | 159.8 | |
| | | Pro (<i>i</i> + 2) | 82.4 | -56.2 | -167.2 | |
| | | Val (<i>i</i> + 3) | -81.4 | 73 | 173.4 | |
| | | Orn | -67.4 | 146.8 | -171.6 | |
| 2b | <i>cis</i> | Val | -110.9 | 129.7 | -179.8 | 43 |
| | | Arg | -159.3 | 161.6 | 155.9 | |
| | | Leu (<i>i</i>) | -107.7 | -104.5 | 160.6 | |
| | | D-Phe (<i>i</i> + 1) | -127 | 147.5 | -179.2 | |
| | | Pro (<i>i</i> + 2) | 76.2 | -69.8 | 177.5 | |
| | | Val (<i>i</i> + 3) | -74 | 123.8 | -173.8 | |
| | | Arg | -157.9 | 150.8 | 176.9 | |
| | <i>trans</i> | Val | -121.5 | 88.7 | -165 | 0 |
| | | Arg | -84.7 | 62.1 | -174.5 | |
| | | Leu (<i>i</i>) | -84 | -44.1 | -174 | |
| | | D-Phe (<i>i</i> + 1) | -172.3 | 151 | 156.4 | |
| | | Pro (<i>i</i> + 2) | 82 | -51.7 | -165.3 | |
| | | Val (<i>i</i> + 3) | -79.9 | 73.4 | 174.8 | |
| | | Arg | -70.8 | 133.4 | -172.2 | |
| 2c | <i>cis</i> | Val | -115 | 128.8 | 179.3 | 43 |
| | | Glu | -150.9 | 162.3 | 161.3 | |
| | | Leu (<i>i</i>) | -108.2 | -110.6 | 169.1 | |
| | | D-Phe (<i>i</i> + 1) | -108.8 | 115.1 | 177.5 | |
| | | Pro (<i>i</i> + 2) | 78.9 | -63.6 | 176.9 | |
| | | Val (<i>i</i> + 3) | -59.3 | 125.4 | -172.1 | |
| | | Glu | -153.9 | 155 | 171.5 | |
| | <i>trans</i> | Val | -132.2 | 39.5 | -169 | 29 |
| | | Glu | -81.1 | 60 | -170.9 | |
| | | Leu (<i>i</i>) | -89.1 | -24 | -176.5 | |
| | | D-Phe (<i>i</i> + 1) | -156.9 | 134 | 168.4 | |
| | | Pro (<i>i</i> + 2) | 80.4 | -67.9 | -178.3 | |
| | | Val (<i>i</i> + 3) | -80.4 | 80 | -177.9 | |
| | | Glu | -104.9 | 129.4 | -174.2 | |

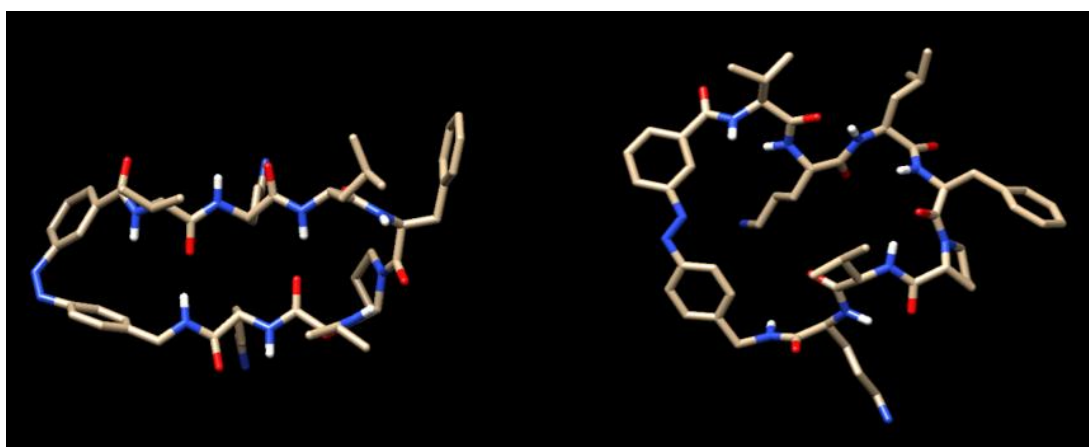
| | | | | | | |
|--------------|-----------------------|-----------------------|--------|--------|--------|----|
| 3a | <i>cis</i> | Val | -112.8 | 130.1 | 179.4 | 29 |
| | | Arg | -153.3 | 160.5 | 155.8 | |
| | | Leu (<i>i</i>) | -106.8 | -105.3 | 161 | |
| | | D-Phe (<i>i</i> + 1) | -126.5 | 146.2 | -179 | |
| | | Pro (<i>i</i> + 2) | 75.2 | -69.8 | 178.3 | |
| | | Arg (<i>i</i> + 3) | -74.4 | 130.2 | -172 | |
| | <i>trans</i> | Arg | -162 | 152.8 | 177.4 | 0 |
| | | Val | -84.5 | 67.6 | -160.2 | |
| | | Arg | -87.2 | 60.9 | -171.5 | |
| | | Leu (<i>i</i>) | -100.5 | -27.8 | -171.7 | |
| | | D-Phe (<i>i</i> + 1) | -165.7 | 143.2 | 152.9 | |
| | | Pro (<i>i</i> + 2) | 79.1 | -58.2 | -154.9 | |
| 3b | <i>cis</i> | Arg (<i>i</i> + 3) | -85.3 | 70 | 175.4 | 29 |
| | | Arg | -57.3 | 135.8 | -171.2 | |
| | | Val | -113 | 130.1 | 179.7 | |
| | | Arg | -153.8 | 161.1 | 155 | |
| | | Arg (<i>i</i>) | -107.4 | -104.3 | 161.9 | |
| | | D-Phe (<i>i</i> + 1) | -127.5 | 146.2 | -178.9 | |
| | <i>trans</i> | Pro (<i>i</i> + 2) | 75.1 | -70.2 | 178.4 | 0 |
| | | Arg (<i>i</i> + 3) | -74.9 | 129.9 | -171.7 | |
| | | Arg | -162 | 153.1 | 177.4 | |
| | | Val | -84.6 | 66.9 | -159.7 | |
| | | Arg | -87.5 | 60.9 | -171.6 | |
| | | Arg (<i>i</i>) | -104.3 | -23.6 | -172.3 | |
| <i>trans</i> | D-Phe (<i>i</i> + 1) | -165.9 | 142.4 | 152.9 | 0 | |
| | Pro (<i>i</i> + 2) | 78.8 | -58.6 | -154.8 | | |
| | Arg (<i>i</i> + 3) | -85.4 | 69.9 | 175.6 | | |
| | Arg | -57.6 | 135.6 | -171.3 | | |



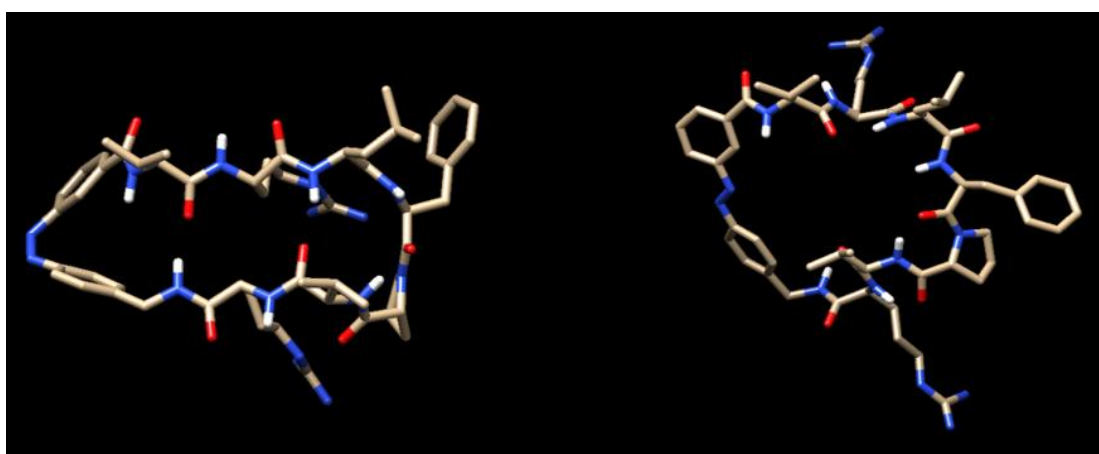
Gramicidin S



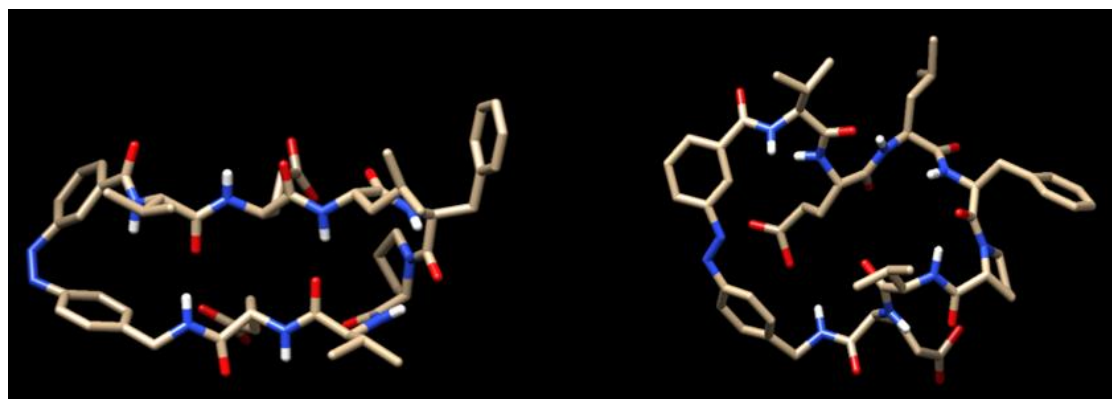
1



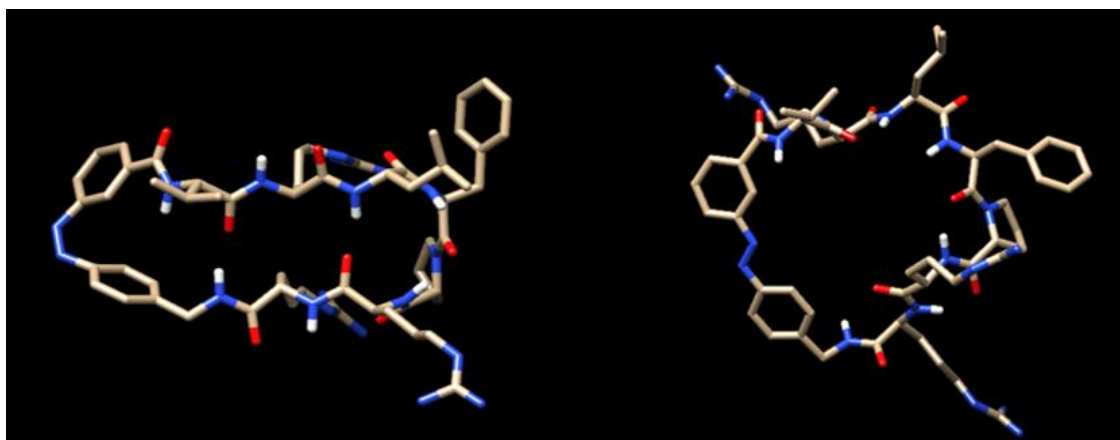
2a



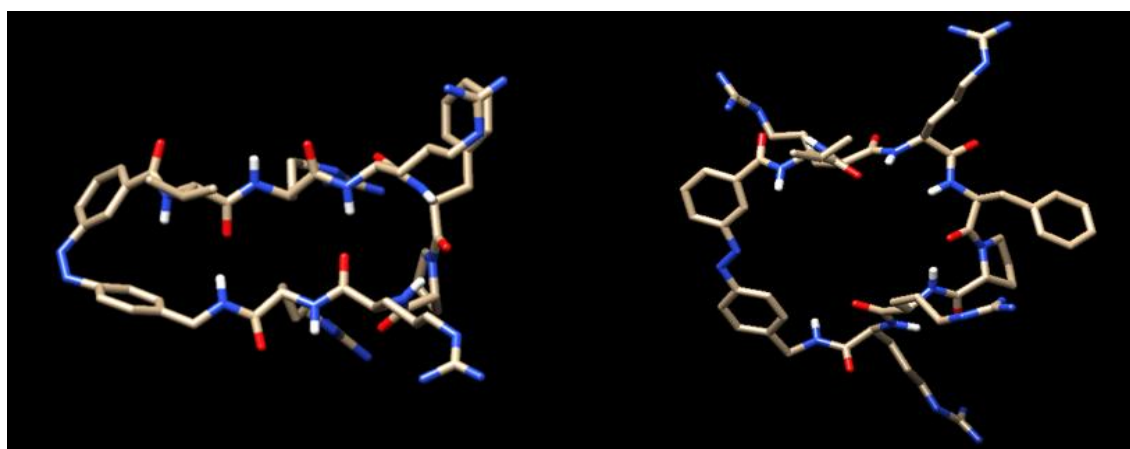
2b



2c



3a



3b

Figure S2.7. Modelling images of gramicidin S and its mimetics **1-3** in the *cis* conformation (left) and the *trans* conformation (right).


2.7.8 References

- (1) Frisch, M. J.; Trucks, G. W.; Schlegel, H. B.; Scuseria, G. E.; Robb, M. A.; Cheeseman, J. R.; Scalmani, G.; Barone, V.; Mennucci, B.; Petersson, G. A.; Nakatsuji, H.; Li, X.; Caricato, M.; Hratchian, H. P.; Izmaylov, A. F.; Bloino, J.; Zheng, G.; Sonnenberg, J. L.; Hada, M.; Ehara, M.; Toyota, K.; Fukuda, R.; Hasegawa, J.; Ishida, M.; Nakajima, T.; Honda, Y.; Kitao, O.; Nakai, H.; Vreven, T.; Montgomery, J., J. A.; Peralta, J. E.; Ogliaro, F.; Bearpark, M.; Heyd, J. J.; Brothers, E.; Kudin, K. N.; Staroverov, V. N.; Keith, T.; Kobayashi, R.; Normand, J.; Raghavachari, K.; Rendell, A.; Burant, J. C.; Iyengar, S. S.; Tomasi, J.; Cossi, M.; Rega, N.; Millam, J. M.; Klene, M.; Knox, J. E.; Cross, J. B.; Bakken, V.; Adamo, C.; Jaramillo, J.; Gomperts, R.; Stratmann, R. E.; Yazyev, O.; Austin, A. J.; Cammi, R.; Pomelli, C.; Ochterski, J. W.; Martin, R. L.; Morokuma, K.; Zakrzewski, V. G.; Voth, G. A.; Salvador, P.; Dannenberg, J. J.; Dapprich, S.; Daniels, A. D.; Farkas, O.; Foresman, J. B.; Ortiz, J. V.; Cioslowski, J.; Fox, D. J. *Gaussian 09, Revision B.01*, Gaussian, Inc., Wallingford CT, 2010.
- (2) Desponds, A.; Freitag, R., Synthesis and Characterization of Photoresponsive N-Isopropylacrylamide Cotelomers. *Langmuir* **2003**, *19* (15), 6261–6270.
- (3) Valiev, M.; Bylaska, E. J.; Govind, N.; Kowalski, K.; Straatsma, T. P.; Van Dam, H. J. J.; Wang, D.; Nieplocha, J.; Apra, E.; Windus, T. L.; de Jong, W. A., NWChem: A comprehensive and scalable open-source solution for large scale molecular simulations. *Comput. Phys. Commun.* **2010**, *181* (9), 1477–1489.
- (4) Llamas-Saiz, A. L.; Grotenbreg, G. M.; Overhand, M.; van Raaij, M. J., Double-stranded helical twisted [beta]-sheet channels in crystals of gramicidin S grown in the presence of trifluoroacetic and hydrochloric acids. *Acta Crystallogr. D* **2007**, *63* (3), 401–407.
- (5) Pettersen, E. F.; Goddard, T. D.; Huang, C. C.; Couch, G. S.; Greenblatt, D. M.; Meng, E. C.; Ferrin, T. E., UCSF Chimera—A visualization system for exploratory research and analysis. *J. Comput. Chem.* **2004**, *25* (13), 1605–1612.



CHAPTER 3

Short photoswitchable
antibacterial peptides



Foreword

This chapter extends our photopharmacological studies into antibacterial activity and reports on the design and synthesis of three short photoswitchable tetrapeptides (**1-3**) that specifically target *Staphylococcus aureus* (*S. aureus*). An azobenzene photoswitch was either incorporated into the side chain (peptides **1** and **2**) or the C-terminus (peptide **3**), to allow reversible switching between *cis*-enriched and *trans*-enriched photostationary states (PSS) when irradiated with light of a specific wavelength. Each PSS of peptides **1-3** was assayed against *S. aureus*, which revealed a contribution to antibacterial activity from several factors, such as hydrophobicity, net positive charge, azobenzene position, secondary structure, and amphiphilicity. Collectively, this work provides important fundamental insights for the design and synthesis of future antibacterial compounds.

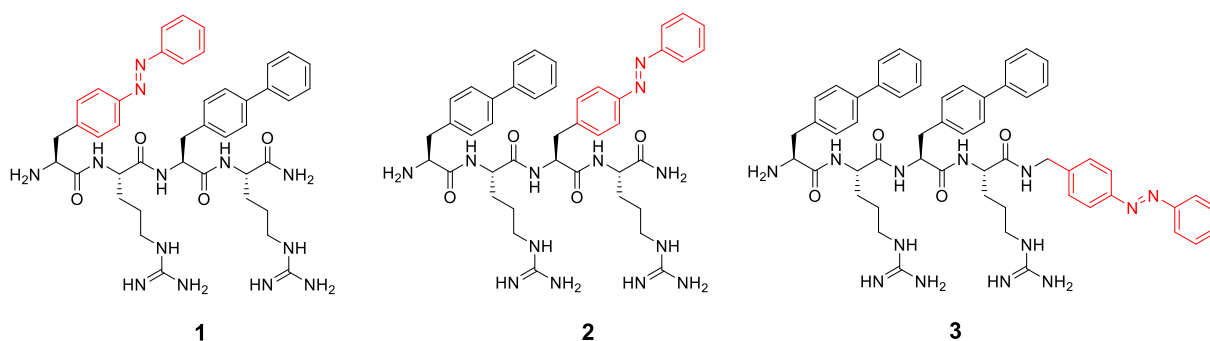


Figure 3.0. Three short photoswitchable peptides **1-3**, with an azobenzene photoswitch incorporated either at the side chain or C-terminus, to allow reversible switching between the *cis*-enriched and *trans*-enriched PSS.

Statement of Authorship

| | |
|---------------------|---|
| Title of Paper | Short photoswitchable antibacterial peptides |
| Publication Status | <input checked="" type="checkbox"/> Published <input type="checkbox"/> Accepted for Publication <input type="checkbox"/> Submitted for Publication <input type="checkbox"/> Unpublished and Unsubmitted work written in manuscript style |
| Publication Details | Yeoh, Y. Q.; Horsley, J. R.; Yu, J.; Polyak, S. W.; Jovcevski, B.; Abell, A. D., Short Photoswitchable Antibacterial Peptides. <i>ChemMedChem</i> 2020, 15 (16), 1505–1508. |

Principal Author

| | | | |
|--------------------------------------|--|------|-----------|
| Name of Principal Author (Candidate) | Yuan Qi Yeoh | | |
| Contribution to the Paper | Performed synthesis and characterization for all compounds and wrote manuscript. | | |
| Overall percentage (%) | 70 | | |
| Certification: | This paper reports on original research I conducted during the period of my Higher Degree by Research candidature and is not subject to any obligations or contractual agreements with a third party that would constrain its inclusion in this thesis. I am the primary author of this paper. | | |
| Signature | | Date | 22/6/2020 |

Co-Author Contributions

By signing the Statement of Authorship, each author certifies that:

- the candidate's stated contribution to the publication is accurate (as detailed above);
- permission is granted for the candidate to include the publication in the thesis; and
- the sum of all co-author contributions is equal to 100% less the candidate's stated contribution.

| | | | |
|---------------------------|---|------|-----------|
| Name of Co-Author | John R. Horsley | | |
| Contribution to the Paper | Helped in data interpretation and revised manuscript. A corresponding author. | | |
| Signature | | Date | 22/6/2020 |

| | | | |
|---------------------------|--|------|------------|
| Name of Co-Author | Jingxian Yu | | |
| Contribution to the Paper | Performed DFT calculations and revised manuscript. | | |
| Signature | | Date | 22/06/2020 |

| | | | |
|---------------------------|--|------|-----------|
| Name of Co-Author | Steven W. Polyak | | |
| Contribution to the Paper | Performed antibacterial assays and revised manuscript. | | |
| Signature | | Date | 15/6/2020 |

| | | | |
|---------------------------|--|------|-----------|
| Name of Co-Author | Blagojce Jovcevski | | |
| Contribution to the Paper | Performed antibacterial assays and revised manuscript. | | |
| Signature | | Date | 15/6/2020 |

| | | | |
|---------------------------|--|------|-----------|
| Name of Co-Author | Andrew D. Abell | | |
| Contribution to the Paper | Supervised development of work and revised manuscript. A corresponding author. | | |
| Signature | | Date | 22/6/2020 |

Short photoswitchable antibacterial peptides

Yuan Qi Yeoh^a, John R. Horsley^{a*}, Jingxian Yu^a, Steven W. Polyak^{b,1}, Blagojce Jovcevski^c,
and Andrew D. Abell^{a*}

^a*ARC Centre of Excellence for Nanoscale BioPhotonics (CNBP), Department of Chemistry, The University of Adelaide, SA 5005, Australia.*

^b*School of Biological Sciences, Department of Molecular and Cellular Biology, The University of Adelaide, SA 5005, Australia.*

^c*Adelaide Proteomics Centre, Department of Chemistry, School of Physical Sciences, The University of Adelaide, North Terrace, Adelaide SA 5005, Australia.*

¹*Present address: School of Pharmacy and Medical Sciences, University of South Australia, City East Campus (P4-10), North Terrace, Adelaide, SA 5000, Australia.*

Publication

Yeoh, Y. Q.; Horsley, J. R.; Yu, J.; Polyak, S. W.; Jovcevski, B.; Abell, A. D., Short Photoswitchable Antibacterial Peptides. *ChemMedChem* **2020**, *15* (16), 1505–1508.

3.1 Abstract

Three photoswitchable tetrapeptides, based on a known synthetic antibacterial, were designed and synthesized to determine activity against *Staphylococcus aureus* (*S. aureus*). Each peptide contains an azobenzene photoswitch incorporated into either the N-terminal side chain (**1**), C-terminal side chain (**2**), or the C-terminus (**3**), to allow reversible switching between *cis*-enriched and *trans*-enriched photostationary states (PSS). Biological assays revealed the C-terminal azobenzene (**3**) possessed the most potent antibacterial activity, with an MIC of 1 $\mu\text{g/mL}$. In this study, net positive charge, hydrophobicity, position of the azobenzene, secondary structure, and amphiphilicity were all found to contribute to antibacterial activity, with each of these factors likely facilitating the peptide to disrupt the negatively charged bacterial lipid membrane. Hence, these short photoswitchable antibacterial tetrapeptides provide insights for the future design and synthesis of antibiotics targeting *S. aureus*.

3.2 Introduction

Photopharmacology is an emerging strategy to modulate the bioactivity of a compound using a reversible molecular switch (photoswitch) to provide localized treatment of an associated disease.¹⁻² This approach offers an opportunity to mitigate off-target side effects,²⁻⁴ and in the context of an antibiotic, the development of resistance.² This typically involves incorporating a photoswitch, such as an azobenzene, into a compound, such as a peptide, to induce a change in physical and chemical properties upon photoisomerization with light of a specific wavelength.⁵ The use of light in this context can be fine-tuned with high spatiotemporal precision,^{1, 6-7} allowing delivery of a bioactive compound. An azobenzene can be interconverted between the *cis* and *trans* isomers on irradiation with UV and visible light respectively, resulting in a significant change in configuration and dipole moment.⁸⁻⁹ Moreover, an azobenzene photoswitch provides a high photoisomerization yield, fast isomerization, low rate of photobleaching, and relative ease of synthesis.^{7, 10-12} We have previously reported photoswitching of an azobenzene-containing cyclic peptide based on a natural antibiotic, gramicidin S,¹³ along with the use of an azobenzene to regulate biosensors,¹⁴ protease inhibitors,¹⁵⁻¹⁶ and smart membranes.¹⁷ Herein, we present the design, synthesis, and evaluation against *S. aureus* of three photoswitchable tetrapeptides (**1-3**, Figure 3.1). An azobenzene photoswitch was incorporated into either the side chain (peptides **1** and **2**) or the C-terminus (peptide **3**) to explore the optimum position for photoswitching between *trans*-enriched and *cis*-enriched PSS.

3.3 Results and Discussion

The design of peptides **1-3** (Figure 3.1) is based upon a known compound by Lau et al.,¹⁸ (compound **23**, NH₂-BRBR-CONH₂, where B = *p*-phenyl-phenylalanine) which was reported to have antibacterial activity against methicillin-resistant *S. aureus* (MRSA, Minimal inhibitory concentration (MIC) 5 µg/ml).¹⁸ Peptides **1** and **2** each contain a *p*-phenylazophenylalanine azobenzene photoswitch, which closely mimics the structure of the biphenyl side chains of compound **23**.¹⁸ Specifically, the N-terminal biphenyl of compound **23**¹⁸ was replaced with an azobenzene photoswitch in peptide **1**, while the C-terminal biphenyl was replaced with an azobenzene in peptide **2**. Peptide **3** has the same azobenzene photoswitch directly attached to the C-terminus. The rational positioning of the azobenzene photoswitch into each of peptides **1-3** allows retention of the overall positive charge (+3) in each case. The free amines located at the N-terminus and both side chains of each arginine residue remain available for protonation, and are crucial for antibacterial activity of compound **23** and other peptides targeting Gram-positive bacteria¹⁸⁻¹⁹ through the establishment of electrostatic interactions for binding to the negatively charged bacterial membrane.²⁰⁻²² The design of peptides **1-3** exploits the knowledge that the azobenzene photoswitch induces a change in dipole moment upon photoisomerization,^{8-9, 23} which in turn affects the amphiphilicity²⁴⁻²⁵ that is crucial to antibacterial activity.^{13, 26} Each peptide was synthesized using standard Fmoc solid phase peptide synthesis (SPPS) as outlined in the Experimental section, and purified by RP-HPLC. The component azobenzene photoswitch was synthesized using an existing methodology.¹⁵

Samples of peptides **1-3** were separately irradiated with visible light (405 nm) for 2h to yield the associated *trans*-enriched PSS, and the UV-Vis absorbance for each was reported (Figure S3.4). The *trans*-enriched PSS for each of peptides **1-3** showed an intense absorption band, with a maximum absorbance at 328 nm due to the symmetry-allowed $\pi \rightarrow \pi^*$ transition. Each peptide was then exposed to UV light (352 nm) for 2h to give the associated *cis*-enriched PSS, and the absorbance spectra reported (Figure S3.4). The *cis*-enriched PSS for each of peptides **1-3** exhibited a weak absorption at 428 nm resulting from the forbidden $n \rightarrow \pi^*$ transition, with a significantly reduced absorption at 328 nm. These absorbance values concur with literature, where both isomers of the azobenzene are known to give distinct but slightly overlapping absorption spectra.^{6, 27-28}

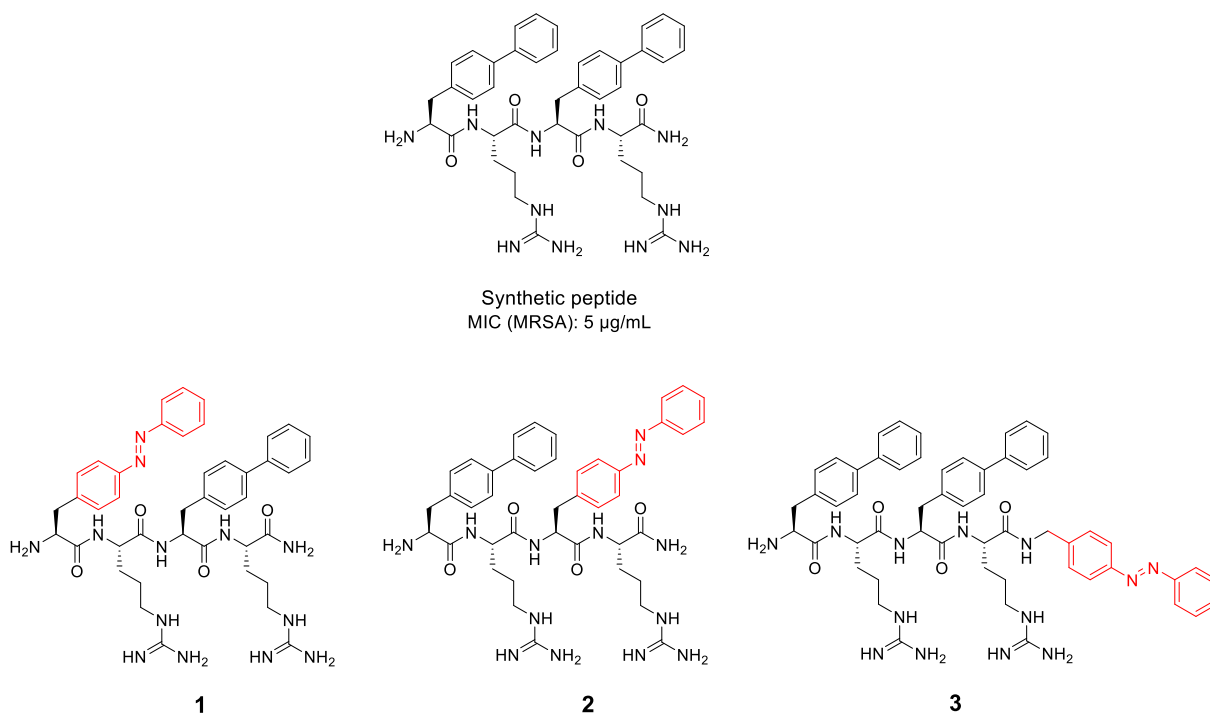


Figure 3.1. Chemical structures for compound **23**¹⁸ and peptide mimetics **1-3** (*trans* conformations are shown). The azobenzene photoswitch is highlighted in red.

The maximum attainable amount for each PSS (photoisomerization yield) of peptides **1-3** was determined by ¹H NMR analysis, particularly comparison of resonances corresponding to the *para*-substituted phenyl ring in the azobenzene photoswitch.¹³ Specifically, the resonances at δ 7.85 ppm and δ 6.78 ppm for peptide **1**, δ 7.81 ppm and δ 6.74 ppm for peptide **2**, and δ 7.85 ppm and δ 6.76 ppm for peptide **3** were used to calculate these ratios (Figures S3.11-S3.13). Relatively high photoisomerization yields for each PSS were observed, with *trans*-enriched PSS of 100%, 88%, and 85%, and *cis*-enriched PSS of 86%, 86%, and 91% for peptides **1-3** respectively (Table 3.1). Detailed ¹H NMR spectroscopy also confirmed the structural conformation of each peptide. Interestingly, ³J_{NH-C α H} coupling constants between 7.5-10 Hz²⁹ were observed for both *cis*-enriched and *trans*-enriched PSS of peptides **1-3**, indicating the presence of a β -strand geometry for each (Table S3.2). To further define secondary structure, the *cis* and *trans* isomers of peptides **1-3** were analyzed by density functional theory (DFT). Calculated dihedral angles for both *cis* and *trans* isomers of peptides **1-3** were consistent with a β -strand conformation³⁰ (Table S3.1, Figure S3.7), as per the ¹H NMR data. Collectively, these findings indicate that the incorporation of an azobenzene photoswitch into either the side chain

or the C-terminus of the peptides does not result in a significant change in secondary structure upon photoisomerization. Thus, any differences in antibacterial activity are likely attributable to other factors, such as the azobenzene position and amphiphilicity, and these are discussed later.

Half-lives for the *cis*-enriched PSS of each peptide were determined by measuring the kinetics of *cis-trans* thermal back isomerization, as detailed in the Supplementary Information. Briefly, samples of peptides **1-3** were each irradiated under UV light (352 nm) for 2.5h to provide the maximum attainable *cis*-enriched PSS. Each peptide in its *cis*-enriched PSS was then stored in the dark to switch to the respective *trans*-enriched PSS by thermal relaxation. The absorbance for each was measured every 10 min to monitor the change in absorbance at 328 nm, which is characteristic of the *trans*-enriched PSS. The half-life for each peptide was then calculated by extrapolating the curve, and the data analyzed using GraphPad Prism 8 software.³¹ The *cis*-enriched PSS for each of peptides **1-3** possess comparable half-lives of 43.4h, 44.6h, and 40.8h respectively, thus affording sufficient time for antibacterial assaying against *S. aureus* (24h).

Table 3.1. Photoisomerization yields and half-lives of peptide mimetics **1-3**, in their respective photostationary states (PSS).

| Peptide | Photoisomerization yield (%) | | Half-life for <i>cis</i> -enriched PSS (h) |
|----------|------------------------------|--------------------------|--|
| | <i>trans</i> -enriched PSS | <i>cis</i> -enriched PSS | |
| 1 | 100 | 86 | 43.4 |
| 2 | 88 | 86 | 44.6 |
| 3 | 85 | 91 | 40.8 |

The two photostationary states of peptides **1-3** were assayed against *S. aureus* ATCC 49775 (see 3.7.3.10 Biological Assays), as model compound **23**¹⁸ is active against this bacterial species. Each peptide was dissolved in DMSO at a concentration of 8 mg/mL, and irradiated separately using either UV (352 nm) or Vis (405 nm) light for 2h to obtain the respective *cis*-enriched and

trans-enriched PSS, which were then subjected to antimicrobial susceptibility assays.³² Peptide **1**, containing an azobenzene moiety to mimic the N-terminal biphenyl side chain of synthetic tetrapeptide (compound **23**¹⁸), displayed a modest antibacterial activity with MICs of 16 $\mu\text{g/mL}$ and 64 $\mu\text{g/mL}$ for the *trans*-enriched and *cis*-enriched PSS respectively (Table 3.2). Replacement of the C-terminal biphenyl side chain moiety with an azobenzene photoswitch, as in peptide **2**, increased antibacterial activity with MICs of 8 $\mu\text{g/mL}$ and 32 $\mu\text{g/mL}$ for the *trans*-enriched and *cis*-enriched PSS, respectively. As peptides **1** and **2** both possess an identical amino acid composition and similar secondary structure, these disparate antibacterial properties likely reflect the influence of the position of the azobenzene photoswitch. However, a four-fold difference in the MIC values between the *cis*-enriched and *trans*-enriched PSS of peptides **1** and **2** was observed (Table 3.2), suggesting that in addition to the specific location of the azobenzene moiety, the intrinsic properties of the photoswitch contribute to antibacterial activity. This four-fold disparity is likely due to a change in overall amphiphilicity,¹³ as the azobenzene photoswitch induces a considerable change in the dipole moment upon photoisomerization.⁸⁻⁹ As the *trans*-enriched PSS of peptides **1** and **2** most closely resemble the structure of the synthetic tetrapeptide (compound **23**¹⁸), it was not surprising that these were more active in suppressing the growth of *S. aureus* than their *cis*-enriched counterparts. Notably, the *trans*-enriched PSS of peptide **3** exhibited far superior antibacterial activity over peptides **1** and **2**, with a particularly potent MIC of 1 $\mu\text{g/mL}$ against *S. aureus*, again demonstrating the significance of the position of the azobenzene photoswitch. The *cis*-enriched PSS of peptide **3** was found to be insoluble in the assay medium, which further supports a change in hydrophobicity and overall amphiphilicity upon photoisomerization. Furthermore, the additional aromatic groups in peptide **3** increased the hydrophobicity of the compound in comparison to peptides **1** and **2**, as evidenced by the longer retention time observed by RP-HPLC (Figure S3.3). Placement of the azobenzene photoswitch at the C-terminus of peptide **3** provides increased hydrophobicity without altering the net positive charge, thus affording optimum amphiphilicity. These properties are clearly advantageous for the designed peptide to disrupt the bacterial lipid membrane, thereby providing a practical insight into the possible mechanism for antibacterial activity.

Table 3.2. Minimum inhibitory concentration (MIC) for the *trans*-enriched and *cis*-enriched PSS of peptide mimetics **1-3** against *S. aureus* ATCC 49775. The MIC for the *cis*-enriched PSS of peptide **3** was not determined due to its insolubility in the assay medium. (* ND – not determined)

| Peptide mimetics | Minimum Inhibitory Concentration (MIC) ($\mu\text{g/mL}$) | |
|------------------|---|--------------------------|
| | <i>trans</i> -enriched PSS | <i>cis</i> -enriched PSS |
| 1 | 16 | 64 |
| 2 | 8 | 32 |
| 3 | 1 | ND* |

3.4 Conclusion

In summary, three short photoswitchable antibacterial peptides, based on a known synthetic tetrapeptide, were designed and synthesized to investigate antibacterial activity against *S. aureus*. Each peptide (**1-3**) contains an azobenzene photoswitch incorporated either on a side chain (**1-2**) or the C-terminus (**3**), to allow reversible switching between the *cis*-enriched and *trans*-enriched PSS. Biological testing against *S. aureus* revealed a four-fold difference in the antibacterial activity between the *cis*-enriched and *trans*-enriched PSS of peptides **1** and **2**, revealing a change in overall amphiphilicity brought about by a change in dipole moment upon photoisomerization. A two-fold difference in the antibacterial activity between peptides **1** and **2** was also observed, and attributed to the positioning of the azobenzene photoswitch, as both peptides contain an identical amino acid composition and similar secondary structure as defined by the earlier ^1H NMR analysis and modelling. In each case, the *trans*-enriched PSS was more potent than its *cis*-enriched counterpart, as it most closely mimics the structure of the biphenyl side chain of the known antibacterial. The *trans*-enriched PSS of peptide **3** exhibited the most potent antibacterial activity, with an MIC of $1 \mu\text{g/mL}$ against *S. aureus*. The position of the azobenzene photoswitch is also conspicuous in **3**, as it allows an increase in hydrophobicity within the peptide without disrupting the net positive charge. Hydrophobicity and an overall positive charge are clearly desirable properties to enable the peptide to disrupt the negatively charged bacterial lipid membrane of *S. aureus*. Furthermore, as each *cis*-enriched and *trans*-

enriched PSS for each peptide was found to contain a β -strand geometry, it is likely that this well-defined secondary structure provides the fundamental framework to stabilize the amino acid residues responsible for maintaining amphiphilicity. Hence, an overall positive charge, hydrophobicity, azobenzene position, and amphiphilicity were all found to be crucial in promoting antibacterial activity.

3.5 Acknowledgements

This work was supported by the Australian Research Council (CE140100003). We also acknowledge the Australian National Fabrication Facility for providing the analytical facilities used in this work. The computational aspects of this work were supported by an award under the National Computational Merit Allocation Scheme for JY on the National Computing Infrastructure (NCI) National Facility at the Australian National University. SWP was supported by the National Health and Medical Research Council of Australia (GN1147538).

3.6 References

1. Hüll, K.; Morstein, J.; Trauner, D., *In Vivo* Photopharmacology. *Chem. Rev.* **2018**, *118* (21), 10710–10747.
2. Velema, W. A.; Szymanski, W.; Feringa, B. L., Photopharmacology: Beyond Proof of Principle. *J. Am. Chem. Soc.* **2014**, *136* (6), 2178–2191.
3. Lerch, M. M.; Hansen, M. J.; van Dam, G. M.; Szymanski, W.; Feringa, B. L., Emerging Targets in Photopharmacology. *Angew. Chem. Int. Ed.* **2016**, *55* (37), 10978–10999.
4. Wegener, M.; Hansen, M. J.; Driessen, A. J. M.; Szymanski, W.; Feringa, B. L., Photocontrol of Antibacterial Activity: Shifting from UV to Red Light Activation. *J. Am. Chem. Soc.* **2017**, *139* (49), 17979–17986.
5. Feliciano, M.; Vytla, D.; Medeiros, K. A.; Chambers, J. J., The GABA(A) receptor as a target for photochromic molecules. *Bioorg. Med. Chem.* **2010**, *18* (22), 7731–7738.
6. Beharry, A. A.; Woolley, G. A., Azobenzene photoswitches for biomolecules. *Chem. Soc. Rev.* **2011**, *40* (8), 4422–4437.
7. Szymański, W.; Beierle, J. M.; Kistemaker, H. A. V.; Velema, W. A.; Feringa, B. L., Reversible Photocontrol of Biological Systems by the Incorporation of Molecular Photoswitches. *Chem. Rev.* **2013**, *113* (8), 6114–6178.
8. Fliegl, H.; Köhn, A.; Hättig, C.; Ahlrichs, R., *Ab Initio* Calculation of the Vibrational and Electronic Spectra of *trans*- and *cis*-Azobenzene. *J. Am. Chem. Soc.* **2003**, *125* (32), 9821–9827.
9. Merino, E.; Ribagorda, M., Control over molecular motion using the *cis-trans* photoisomerization of the azo group. *Beilstein J. Org. Chem.* **2012**, *8*, 1071–1090.
10. Lubbe, A. S.; Szymanski, W.; Feringa, B. L., Recent developments in reversible photoregulation of oligonucleotide structure and function. *Chem. Soc. Rev.* **2017**, *46* (4), 1052–1079.
11. Mahimwalla, Z.; Yager, K. G.; Mamiya, J.-i.; Shishido, A.; Priimagi, A.; Barrett, C. J., Azobenzene photomechanics: prospects and potential applications. *Polym. Bull.* **2012**, *69* (8), 967–1006.
12. Maier, M. S.; Hüll, K.; Reynders, M.; Matsuura, B. S.; Leippe, P.; Ko, T.; Schäffer, L.; Trauner, D., Oxidative Approach Enables Efficient Access to Cyclic Azobenzenes. *J. Am. Chem. Soc.* **2019**, *141* (43), 17295–17304.

13. Yeoh, Y. Q.; Yu, J.; Polyak, S. W.; Horsley, J. R.; Abell, A. D., Photopharmacological Control of Cyclic Antimicrobial Peptides. *ChemBioChem* **2018**, *19* (24), 2591–2597.
14. Horsley, J. R.; Yu, J.; Wegener, K. L.; Hoppmann, C.; Rück-Braun, K.; Abell, A. D., Photoswitchable peptide-based ‘on-off’ biosensor for electrochemical detection and control of protein-protein interactions. *Biosens. Bioelectron.* **2018**, *118*, 188–194.
15. Blanco, B.; Palasis, K. A.; Adwal, A.; Callen, D. F.; Abell, A. D., Azobenzene-containing photoswitchable proteasome inhibitors with selective activity and cellular toxicity. *Bioorg. Med. Chem.* **2017**, *25* (19), 5050–5054.
16. Pearson, D.; Abell, A. D., Structural Optimization of Photoswitch Ligands for Surface Attachment of α -Chymotrypsin and Regulation of Its Surface Binding. *Chem. Eur. J.* **2010**, *16* (23), 6983–6992.
17. Kumeria, T.; Yu, J.; Alsawat, M.; Kurkuri, M. D.; Santos, A.; Abell, A. D.; Losic, D., Photoswitchable Membranes Based on Peptide-Modified Nanoporous Anodic Alumina: Toward Smart Membranes for On-Demand Molecular Transport. *Adv. Mater.* **2015**, *27* (19), 3019–3024.
18. Lau, Q. Y.; Ng, F. M.; Cheong, J. W. D.; Yap, Y. Y. A.; Tan, Y. Y. F.; Jureen, R.; Hill, J.; Chia, C. S. B., Discovery of an ultra-short linear antibacterial tetrapeptide with anti-MRSA activity from a structure–activity relationship study. *Eur. J. Med. Chem.* **2015**, *105*, 138–144.
19. Yeoh, Y. Q.; Horsley, J. R.; Polyak, S. W.; Abell, A. D., A hypoxia-activated antibacterial prodrug. *Bioorg. Med. Chem. Lett.* **2020**, *30* (11), 127140.
20. Bradshaw, J. P., Cationic Antimicrobial Peptides. *BioDrugs* **2003**, *17* (4), 233–240.
21. Kohn, E. M.; Shirley, D. J.; Arotzky, L.; Picciano, A. M.; Ridgway, Z.; Urban, M. W.; Carone, B. R.; Caputo, G. A., Role of Cationic Side Chains in the Antimicrobial Activity of C18G. *Molecules* **2018**, *23* (2), 329.
22. Tennesen, J. A., Molecular evolution of animal antimicrobial peptides: widespread moderate positive selection. *J. Evol. Biol.* **2005**, *18* (6), 1387–1394.
23. Wagner-Wysiecka, E.; Łukasik, N.; Biernat, J. F.; Luboch, E., Azo group(s) in selected macrocyclic compounds. *J. Incl. Phenom. Macro.* **2018**, *90* (3), 189–257.
24. Eisenberg, D.; Weiss, R. M.; Terwilliger, T. C.; Wilcox, W., Hydrophobic moments and protein structure. *Faraday Symp. Chem. Soc.* **1982**, *17*, 109–120.
25. Park, J. Y.; Umashankar, M.; Huh, D. S., Effect of UV illumination on the fabrication of honeycomb-patterned film in the photo-responsive poly(methylmethacrylate/azobenzene) copolymer. *Macromol. Res.* **2016**, *24* (4), 350–358.

26. Babii, O.; Afonin, S.; Berditsch, M.; Reißer, S.; Mykhailiuk, P. K.; Kubyshkin, V. S.; Steinbrecher, T.; Ulrich, A. S.; Komarov, I. V., Controlling Biological Activity with Light: Diarylethene-Containing Cyclic Peptidomimetics. *Angew. Chem. Int. Ed.* **2014**, *53* (13), 3392–3395.
27. Albert, L.; Vázquez, O., Photoswitchable peptides for spatiotemporal control of biological functions. *ChemComm* **2019**, *55* (69), 10192–10213.
28. Bandara, H. M. D.; Burdette, S. C., Photoisomerization in different classes of azobenzene. *Chem. Soc. Rev.* **2012**, *41* (5), 1809–1825.
29. Fernando, S. R. L.; Kozlov, G. V.; Ogawa, M. Y., Distance Dependence of Electron Transfer along Artificial β -Strands at 298 and 77 K. *Inorg. Chem.* **1998**, *37* (8), 1900–1905.
30. Abell, A. D.; Alexander, N. A.; Aitken, S. G.; Chen, H.; Coxon, J. M.; Jones, M. A.; McNabb, S. B.; Muscroft-Taylor, A., Synthesis of Macrocyclic β -Strand Templates by Ring Closing Metathesis. *J. Org. Chem.* **2009**, *74* (11), 4354–4356.
31. Desponds, A.; Freitag, R., Synthesis and Characterization of Photoresponsive N-Isopropylacrylamide Cotelomers. *Langmuir* **2003**, *19* (15), 6261–6270.
32. Lee, K. J.; Tieu, W.; Blanco-Rodriguez, B.; Paparella, A. S.; Yu, J.; Hayes, A.; Feng, J.; Marshall, A. C.; Noll, B.; Milne, R.; Cini, D.; Wilce, M. C. J.; Booker, G. W.; Bruning, J. B.; Polyak, S. W.; Abell, A. D., Sulfonamide-Based Inhibitors of Biotin Protein Ligase as New Antibiotic Leads. *ACS Chem. Biol.* **2019**, *14* (9), 1990–1997.

3.7 Supplementary Information

3.7.1 Materials

Dichloromethane (CH₂Cl₂), *N,N*-dimethylformamide (DMF), methanol (MeOH), and piperidine were purchased from Merck, Australia. Nitrosobenzene, 1-propanephosphonic anhydride solution (T3P), trifluoroacetic acid (TFA), *N*-methylmorpholine, triisopropylsilane (TIPS), 1,4-dioxane and diisopropylethylamine (DIPEA) were purchased from Sigma-Aldrich, Australia. Magnesium sulphate (MgSO₄), hydrochloric acid (HCl), ethyl acetate and acetic acid were purchased from Chem Supply, Australia. 1-[Bis(dimethylamino)methylene]-1*H*-1,2,3-triazolo[4,5-*b*]pyridinium 3-oxid hexafluorophosphate (HATU), Fmoc-4-amino-L-phenylalanine, and Boc-*L*-Ala(4,4'-biphenyl)-OH, Fmoc-Arg(Pbf)-OH, and 2-Chlorotrityl chloride resin were purchased from Chem-Impex International, Inc., USA. Sieber amide resin was purchased from GL Biochem (Shanghai) Ltd. Acetonitrile was purchased from Thermo Fisher Scientific, Inc., Australia. All solvents and reagents were used without purification unless noted.

3.7.2 Methods

High Performance Liquid Chromatography (HPLC)

The peptide mimetics **1-3** were analyzed and purified by reverse phase high performance liquid chromatography (RP-HPLC), using a Gilson purification system equipped with a UV-Vis absorbance detector and a Supelco Analytical C₁₈ column (Discovery BIO Wide Pore C5-5, 250 x 10 mm, 5 μm). Aqueous solvent A: Water:TFA (100:0.1 v/v) and organic solvent B: ACN:TFA (100:0.08 v/v) were used during the purification process.

Mass Spectrometry

High resolution mass spectral data were obtained using an Agilent 6230 TOF LC/MS mass spectrometer. Mass spectra were obtained over a range of $100 < m/z < 2000$.

UV-Vis Spectrophotometry

All UV-Vis spectra were obtained at $25 \pm 0.5^\circ\text{C}$ on the Synergy H4 Hybrid Multi-Mode Microplate Reader. All measurements were performed in a 96-well plate with a concentration of approximately $100 \mu\text{g/mL}$ of **1-3** in DMSO. For conversion from a *trans* to a *cis* conformation, **1-3** were irradiated for 1h, under a UV lamp (UVP[®] MRL-58, 8 W, 352 nm) prior to measurement. For conversion from the *cis* to *trans* conformation, visible light (405 nm) was used. The absorbances for the respective conformations of **1-3** were measured between 200 – 800 nm.

NMR Spectroscopy

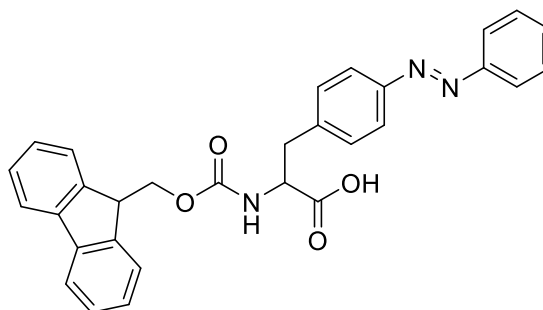
¹H NMR spectrum of the azobenzene photoswitch was recorded in DMSO-d₆ solution using an Agilent DD2 500MHz spectrometer. ¹H NMR spectra of the peptide mimetics **1-3** were recorded on an Agilent DD2 600MHz NMR spectrometer. Chemical shifts are reported in ppm (δ) using TMS (0.00 ppm) as the internal standard. Signals are recorded as s (singlet), d (doublet), t (triplet) or m (multiplet).

Molecular Modelling

The lowest energy conformation for *cis* and *trans* isomers of peptides **1-3** were determined in collaboration using Gaussian 09¹ package on the National Computing Infrastructure (NCI) National Facility, e.g. Raijin supercomputer. The initial geometries of peptides **1-3** were constructed through GaussView 5.0 program. The geometry of each structure was optimized in the gas phase using the density functional theory (DFT) with the B3LYP density function and basis sets of increasing size from STO-3G up to 6-31G** for all atoms.

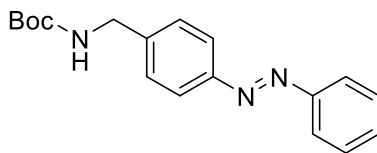
3.7.3 Experimental

3.7.3.1 Synthesis of (*E*)-2-(((9H-fluoren-9-yl)methoxy)carbonyl)amino)-3-(4-(phenyldiazenyl)phenyl)propanoic acid



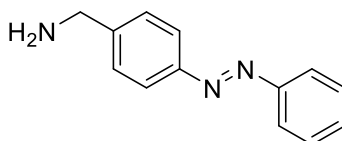
To a stirring solution of nitrosobenzene (1.1 g, 10.3 mmol) in glacial acetic acid (85 mL), Fmoc-4-amino-*L*-phenylalanine (4.6 g, 11.3 mmol) was added, and the mixture was refluxed at 40 °C for 24h. Water (100 mL) was added to the mixture, and the precipitate was filtered and dried under vacuum. The crude product was purified by column (8:2 CH₂Cl₂/MeOH) to give an orange solid (4.89 g, 97%). ¹H NMR (500 MHz, DMSO-*d*₆): δ 7.87 (d, *J* = 7.8 Hz, 4H), 7.82 (d, *J* = 8.3 Hz, 2H), 7.76 (d, *J* = 8.5 Hz, 1H), 7.64-7.54 (m, 5H), 7.50 (d, *J* = 8.1 Hz, 2H), 7.41-7.36 (m, 2H), 7.31-7.26 (m, 2H), 4.28-4.24 (m, 1H), 4.22 (d, *J* = 7.0 Hz, 2H), 4.17 (t, *J* = 6.4 Hz, 1H), 3.20 (dd, *J* = 13.7, 4.3 Hz, 1H), 2.99 (dd, *J* = 13.6, 10.8 Hz, 1H). HRMS: *m/z*_{calc} for C₃₀H₂₅N₃O₄ = 492.1918 [M+H⁺], *m/z*_{found} = 492.1917.

3.7.3.2 Synthesis of *tert*-butyl (*E*)-(4-(phenyldiazenyl)benzyl)carbamate



To a stirring solution of nitrosobenzene (1.0 g, 9.3 mmol) in glacial acetic acid (50 mL), Boc-*L*-Ala(4,4'-biphenyl)-OH (2.1 g, 9.4 mmol) was added, and the mixture was stirred at rt for 24h. Water (50 mL) was added to the mixture, and the precipitate was filtered and dried under vacuum to give an orange solid (2.8 g, 97%). ¹H NMR (500 MHz, DMSO-*d*₆): δ 7.89-7.85 (m, 4H), 7.62-7.54 (m, 3H), 7.50-7.44 (m, 3H), 4.23 (d, *J* = 6.0 Hz, 2H), 1.41 (s, 9H). HRMS: *m/z*_{calc} for C₁₈H₂₁N₃O₂ = 312.1707 [M+H⁺], *m/z*_{found} = 312.1705.

3.7.3.3 Deprotection of *tert*-butyl (*E*)-(4-(phenyldiazenyl)benzyl)carbamate to yield (*E*)-(4-(phenyldiazenyl)phenyl)methanamine



(*E*)-2-((((9H-fluoren-9-yl)methoxy)carbonyl)amino)-3-(4-(phenyldiazenyl)phenyl)propanoic acid was dissolved in a mixture of 1M HCl/dioxane, and the mixture was stirred at rt for 1h. The solvent was removed under N₂ flow, and the residue was purified by column (7:3 CH₂Cl₂/MeOH) to give a quantitative yield of an orange solid. ¹H NMR (500 MHz, DMSO-*d*₆): δ 8.32 (br s, 2H), 7.96-7.94 (m, 2H), 7.92-7.90 (m, 2H), 7.69-7.67 (m, 2H), 7.64-7.57 (m, 3H), 4.16 (s, 2H). HRMS: *m/z*_{calc} for C₁₃H₁₃N₃ = 212.1182 [M+H]⁺, *m/z*_{found} = 212.1185.

3.7.3.4 Solid Phase Peptide Synthesis (SPPS)

Peptides 1-2

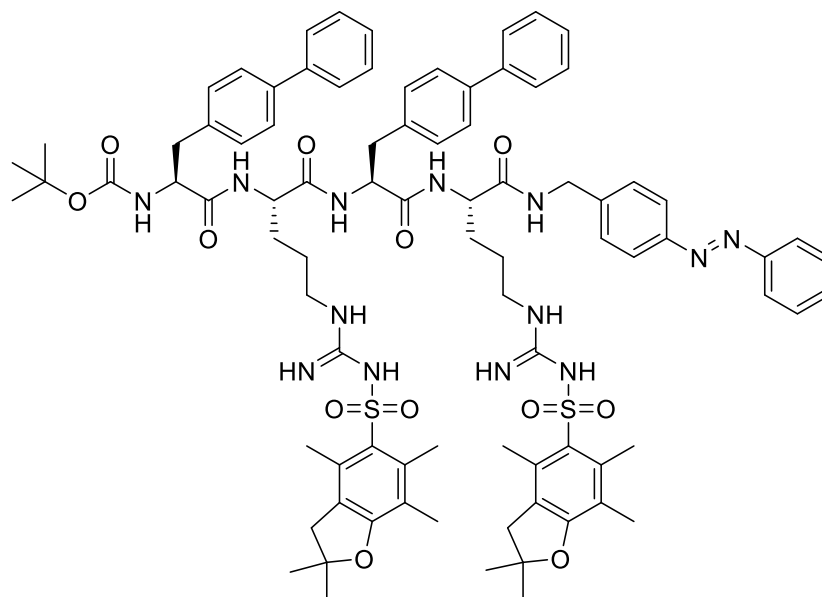
Standard Fmoc-based SPPS and commercially available reagents were used for the synthesis of peptides **1-2** using the Sieber amide resin with a loading of (0.4 mmol/g, 1.0 g, 1 equiv.). The resin was swelled in DMF (25 mL) for 1h before the deprotection of Fmoc using 25% piperidine/DMF (2 x 25 mL) for 30 min. The resin was then washed with CH₂Cl₂ (x3), DMF (x3), and CH₂Cl₂ (x3). The unreacted active sites on the resin were capped with 3:2 acetic anhydride/pyridine (2 x 25 mL), and the capping solution was allowed to stand for 30 min before washing the resin with CH₂Cl₂ (x3), DMF (x3) and CH₂Cl₂ (x3). Couplings of the amino acids and azobenzene photoswitch on the Sieber amide resin were performed using the following molar ratios of reagents: Fmoc-amino acids and Fmoc-azobenzene photoswitch (2 equiv.) dissolved in 20% *N*-methylmorpholine/DMF (20 mL), and HATU (2 equiv.). *N*-Fmoc deprotection was carried out by treating the resin with 25% piperidine/DMF (25 mL) for 30 min before washing with CH₂Cl₂ (x3), DMF (x3) followed by CH₂Cl₂ (x3). Coupling and deprotection procedures were repeated alternatively until the sequence was completed. The linear peptides **1-2**, together with Pbf protecting groups on the side chain of arginine residues were cleaved from the resin using TFA/TIPS/CH₂Cl₂ (95:2.5:2.5, 20 mL). The reagents were left to stand for 1h with stirring before filtering the peptide solution. The volatile products from the filtrate were removed by N₂ flow, and the linear peptides **1-2** were placed under vacuum for 1h, to yield an orange solid. All crude products were purified by RP-HPLC to give an orange solid. HRMS: Peptide **1**: m/z_{calc} for C₄₂H₅₃N₁₃O₄ = 804.4419 [M+H]⁺, m/z_{found} =804.4416. Peptide **2**: m/z_{calc} for C₄₂H₅₃N₁₃O₄ = 804.4419 [M+H]⁺, m/z_{found} =804.4416.

Linear precursor for peptide 3

Standard Fmoc-based SPPS and commercially available reagents were used for the synthesis of the precursor for peptide **3** using the 2-Chlorotrityl chloride resin. Resin preloaded with Fmoc-Arg-OH (0.4 mmol/g, 1.0 g, 1 equiv.) was used to synthesize the linear precursor. The unreacted active sites on the resin were capped with a solution of 17:2:1 CH₂Cl₂/MeOH/DIPEA (2 x 25

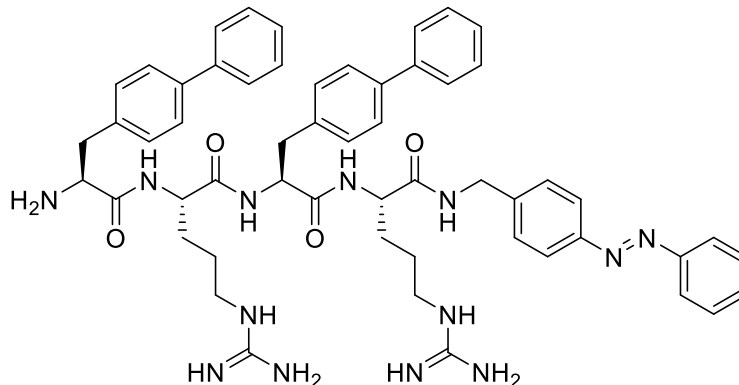
mL). The capping solution was allowed to stand for 30 min before washing the resin with CH₂Cl₂ (x3), DMF (x3), and CH₂Cl₂ (x3). *N*-Fmoc deprotection was carried out by treating the resin with 25% piperidine/DMF (25 mL) for 30 min before washing with CH₂Cl₂ (x3), DMF (x3), followed by CH₂Cl₂ (x3). For the couplings of the amino acids, the following molar ratios of reagents were used: Fmoc-amino acid/Boc-amino acid (2 equiv.) dissolved in DMF (20 mL), 0.5 M HATU/DMF, and DIPEA (8 equiv.). The resin was washed with CH₂Cl₂ (x3), DMF (x3), followed by CH₂Cl₂ (x3), and the coupling procedures were repeated. The coupling time in all cases was 2h. Deprotection and coupling procedures were repeated alternatively until the sequence was completed. After the peptide sequences were completed and deprotected, the resin was washed with CH₂Cl₂ (x3), DMF (x3), followed by CH₂Cl₂ (x3), and dried under vacuum. For the cleavage of the linear precursor from the resin, a solution of 1.5% TFA/CH₂Cl₂ (2 x 20 mL) was used while maintaining the *N*-terminus Boc protecting group and the side chain protections of arginine residues. The reagents were left to stand for 15 min with stirring before filtering the peptide solution. The volatile products from the filtrate were removed by N₂ flow, and the linear precursor was placed under vacuum for 1h, to yield a yellow solid.

3.7.3.5 Coupling of linear precursor of peptide 3 and (*E*)-(4-(phenyldiazenyl)phenyl)methanamine



To a stirring solution of the linear precursor of peptide **3** (0.8 g, 0.6 mmol), DIPEA (1.1 mL, 6.0 mmol), and T3P[®] (50% in ethyl acetate, 0.4 g, 1.2 mmol) in ethyl acetate (20 mL), (*E*)-(4-(phenyldiazenyl)phenyl)methanamine (0.1 g, 0.6 mmol) was added, and the mixture was stirred for 24h at rt. The solvent was removed in vacuo to give an orange precipitate. HRMS: m/z_{calc} for $\text{C}_{86}\text{H}_{103}\text{N}_{13}\text{O}_{12}\text{S}_2 = 1574.7364$ $[\text{M}+\text{H}]^+$, $m/z_{\text{found}} = 1574.7356$.

3.7.3.6 Deprotection of Boc and Pbf Protecting Groups to yield peptide 3



All protecting groups were deprotected using 95% TFA/CH₂Cl₂ (10 mL) for 1h at rt. The solvents were removed in vacuo, and the residue was purified by RP-HPLC to give an orange solid. HRMS: m/z_{calc} for C₅₅H₆₃N₁₃O₄ = 970.5199 [M+H]⁺, m/z_{found} = 970.5239.

3.7.3.7 Photoisomerization of Peptides 1-3

Peptides **1-3** were dissolved in DMSO at a concentration of 100 μg/mL and exposed to visible light of 405 nm for 2h to yield the *trans*-enriched PSS. The *trans*-enriched PSS of **1-3** were irradiated by UV light of 352 nm for 2h, to convert to the respective *cis*-enriched PSS.

3.7.3.8 Half-Life Analysis of Peptides 1-3

The half-life of peptides **1-3** was determined by measuring the kinetics of *cis-trans* thermal back isomerization, characterized using UV-Vis spectrophotometry. Prior to irradiation, peptides **1-3** in their thermally stable *trans*-enriched PSS were dissolved in DMSO, and the wavelengths of maximum absorbance (λ_{max}) were measured using a Synergy H4 Hybrid Multi-Mode Microplate Reader. The peptides were then irradiated under UV light (352 nm) for 2h to convert the samples to their *cis*-enriched PSS, and the λ_{max} were determined. The samples were irradiated under UV (352 nm) for a further 30 min to achieve the maximum attainable *cis*-

enriched PSS, which was confirmed when no further increase was observed in the absorbance at the λ_{max} . Each peptide in its *cis*-enriched PSS was then stored in the dark to switch to the respective *trans*-enriched PSS by thermal relaxation. The absorbance for each peptide was measured every 10 min to monitor the change in the absorbance at 328 nm, which is characteristic of the *trans*-enriched PSS. The measurements were conducted over a period of 64h. The half-life for each peptide was then calculated by extrapolating the curve, and the data analyzed using GraphPad Prism 8 software.²

3.7.3.9 Molecular Modelling

The lowest energy structures for the *cis* and *trans* isomers of peptides **1-3** were determined in the gas phase using the NWChem 6.6 package,³ with tight convergence criteria using a hybrid B3LYP functional with 6-31G** basis set for all atoms. The initial geometries of peptides **1-3** were constructed through the GaussView 5.0 package. Conformational analyses of the dihedral angles were conducted using the Chimera 1.14 software.⁴

3.7.3.10 Biological Assays (Antibacterial Susceptibility Evaluation)

Antibacterial activity was determined by the microdilution broth method as recommended by the CLSI (Clinical and Laboratory Standards Institute, Document M07-A8, 2009, Wayne, PA.) using cation-adjusted Mueller-Hinton broth (Trek Diagnostics Systems, U.K.). Serial two-fold dilutions of each peptide were made using DMSO as the diluent. Specifically, the concentration range for the antibacterial peptides in the assays was an 8-point two-fold dilution series, starting at 128 $\mu\text{g/ml}$ (i.e. 128, 64, 32, 16, 8, 4, 2, 1 $\mu\text{g/ml}$). Trays were inoculated with 5×10^4 CFU of *Staphylococcus aureus* ATCC 49975 in a volume of 100 μL (final concentration of DMSO was 3.2% (v/v)) and incubated at 37 °C for 24h. Growth of the bacterium was quantified by measuring the absorbance at 620 nm.

3.7.4 HPLC Chromatograms

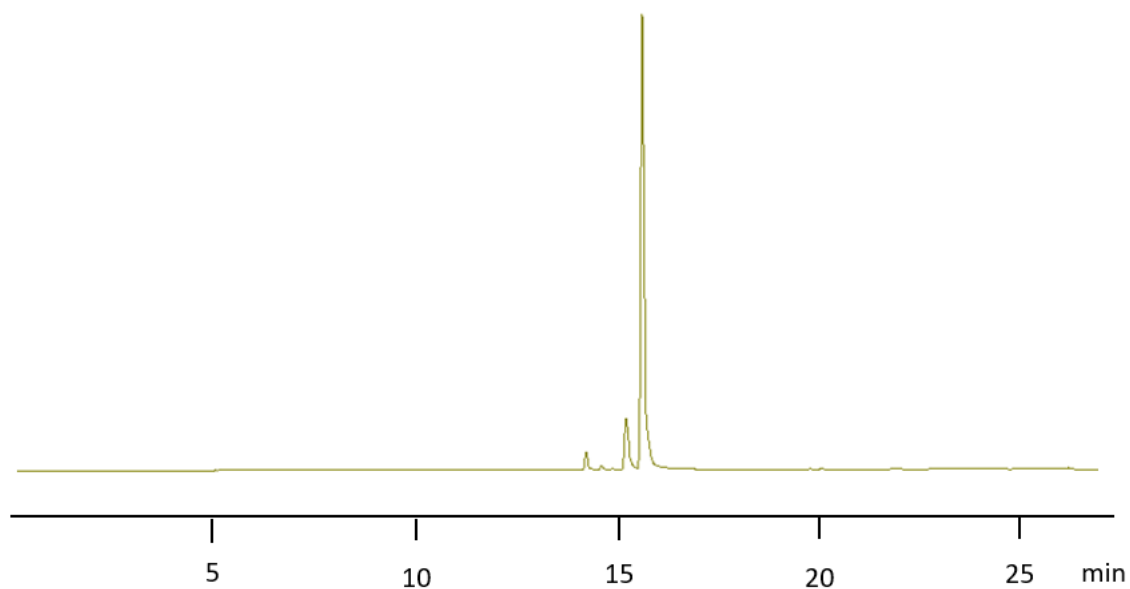


Figure S3.1. HPLC chromatogram for peptide **1**, visualized at 320 nm. The retention time for peptide **1** was found to be 15.8 min.

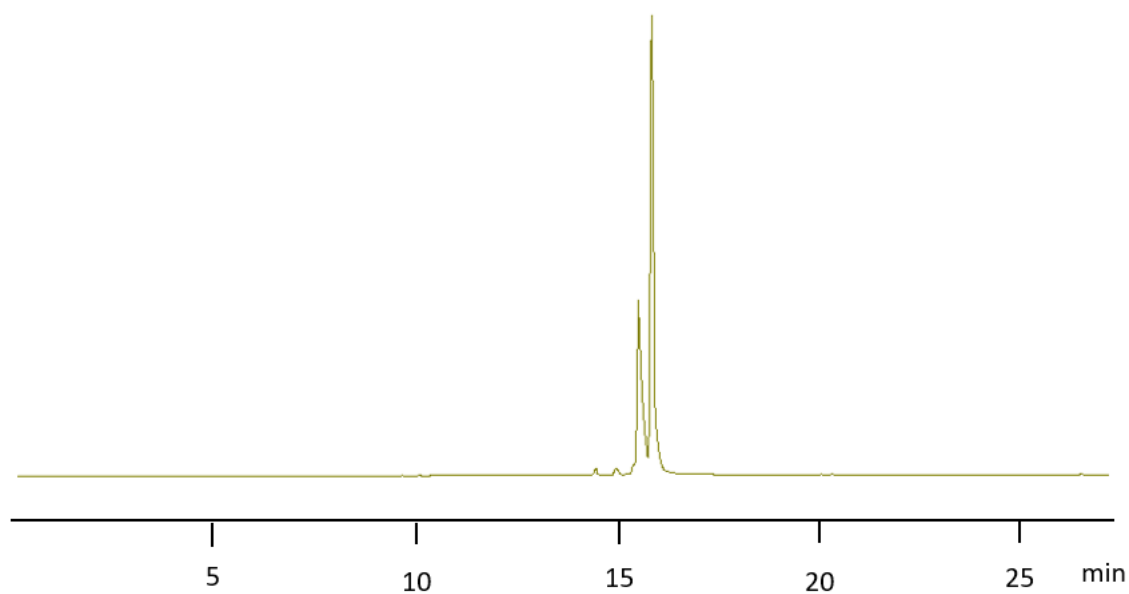


Figure S3.2. HPLC chromatogram for peptide **2**, visualized at 320 nm. The retention time for peptide **2** was found to be 15.8 min.

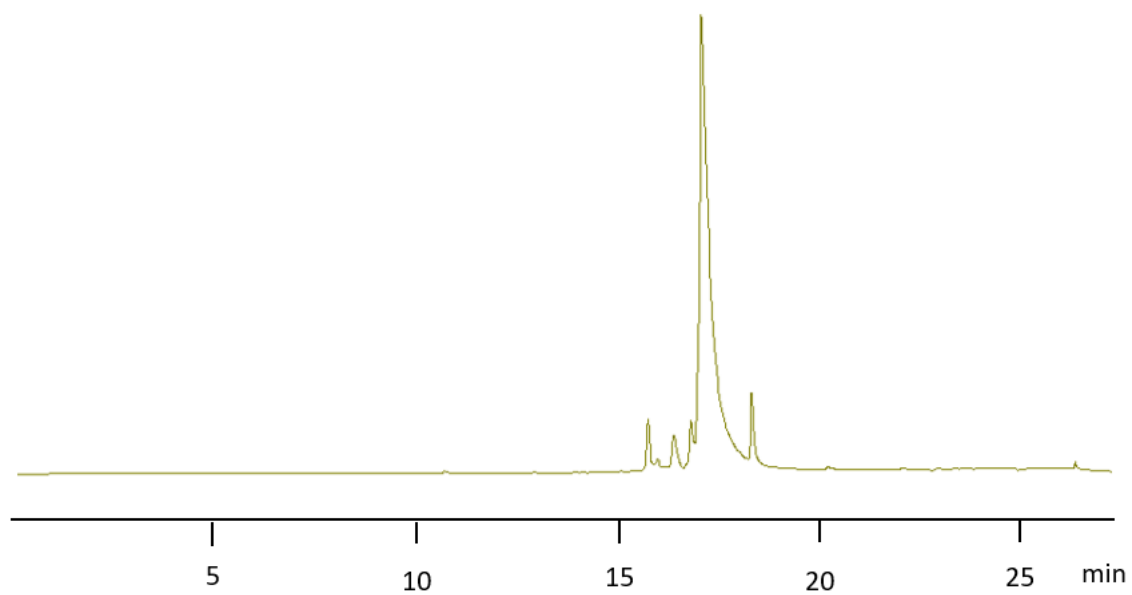
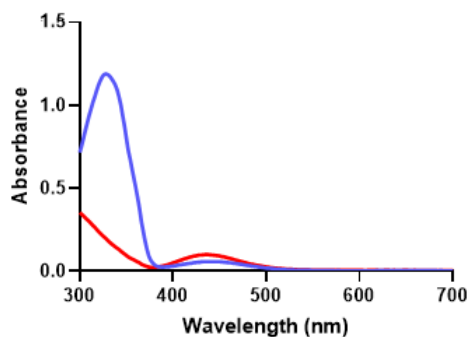
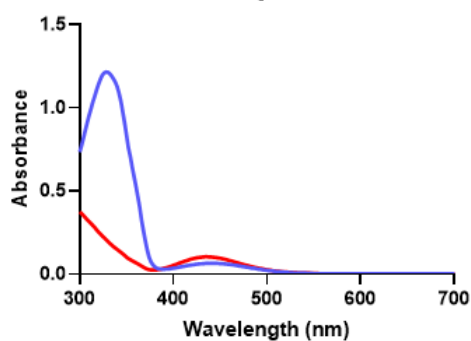


Figure S3.3. HPLC chromatogram for peptide **3**, visualized at 320 nm. The retention time for peptide **3** was found to be 17.0 min.

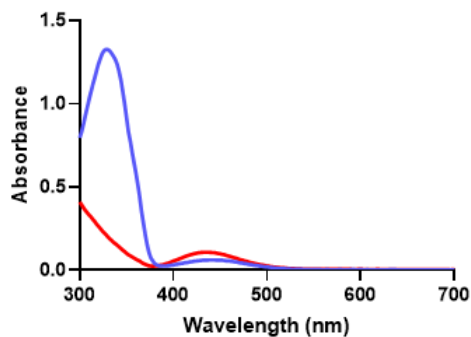
3.7.5 UV-Vis Spectra



1

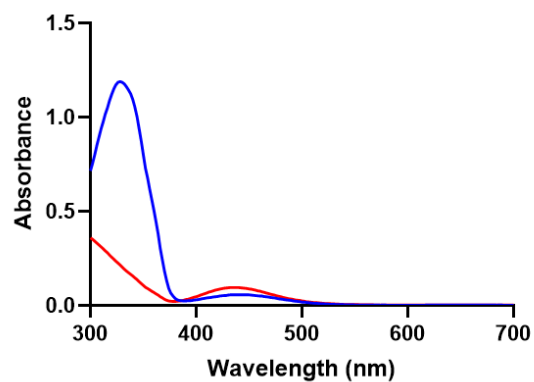


2

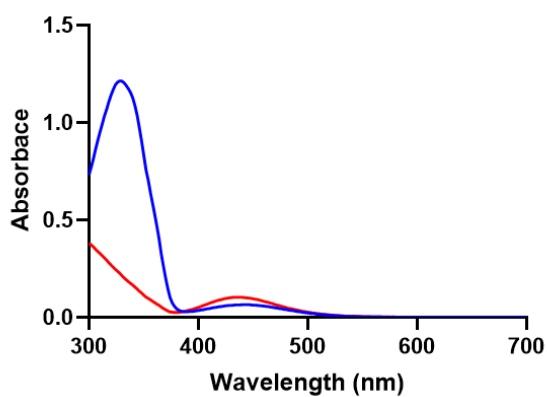


3

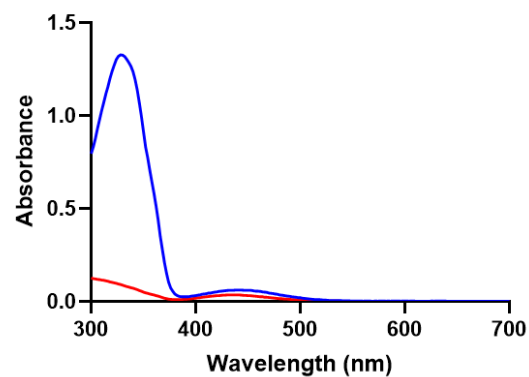
Figure S3.4. UV-Vis spectra for peptides **1-3** in the *trans*-enriched PSS (blue) and *cis*-enriched PSS (red) after 2 hours of irradiation under Vis (405 nm) and UV (352 nm) respectively. The *trans*-enriched PSS shows a maximum absorbance at 328 nm, while the *cis*-enriched PSS shows a higher absorbance at 428 nm, and a much lower absorbance at 328 nm.



1



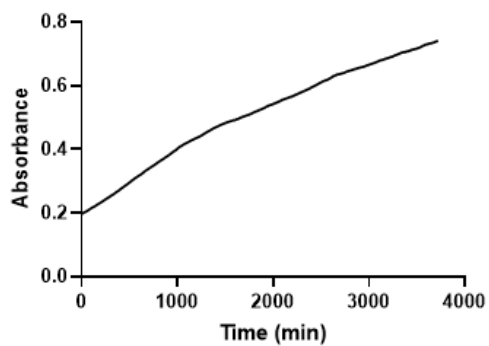
2



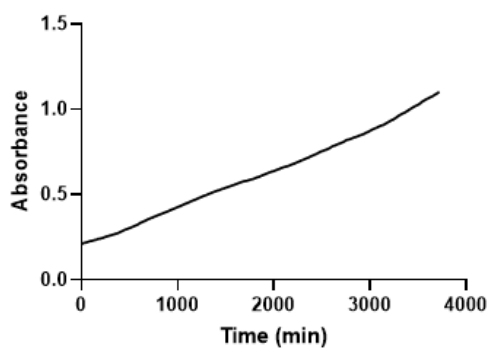
3

Figure S3.5. UV-Vis spectra for peptides **1-3** before (blue) and after (red) UV irradiation for 15 min. The high intensity of absorbance at 328 nm shows that peptides **1-3** existed predominantly in the *trans* conformation prior to UV irradiation. The absorbance at 328 nm decreases drastically upon UV exposure for 15 min, indicating successful photoconversion of the peptides into the *cis* conformation.

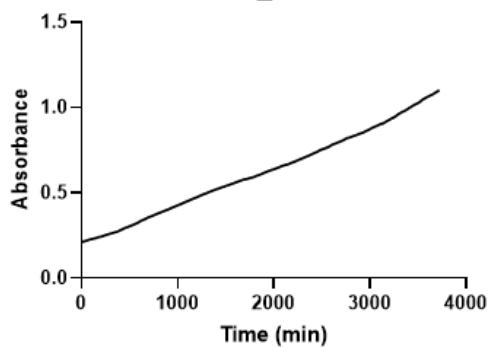
3.7.6 Half-Life Analysis



1



2



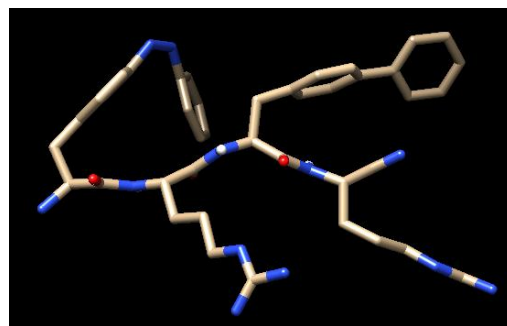
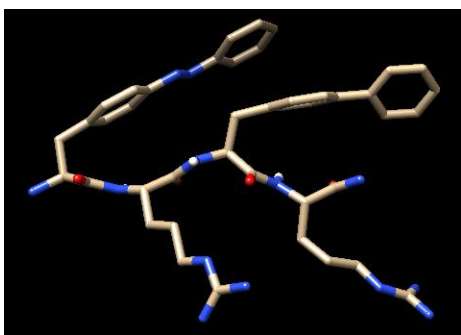
3

Figure S3.6. The absorbance curves of peptides **1-3** at their respective λ_{\max} when left in the dark for 64h. The gradual increase in the absorbance at 328 nm indicates the *cis-trans* thermal back isomerization of the peptide samples.

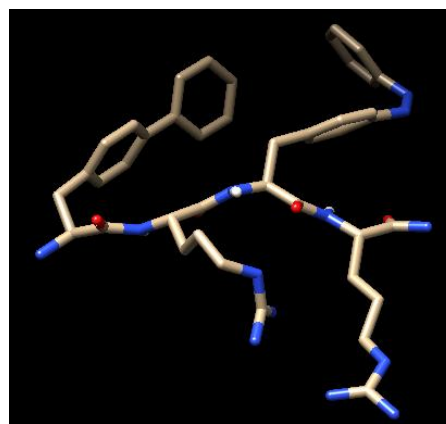
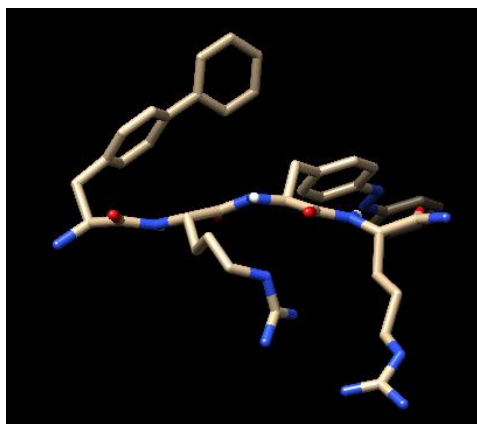
3.7.7 Molecular Modelling

Table S3.1. Phi (ϕ) and psi (ψ) dihedral angles for the *trans* and *cis* isomers of peptides **1-3**. A typical β -strand is characterized with $-160^\circ < \phi < -100^\circ$ and $90^\circ < \psi < 160^\circ$.⁵

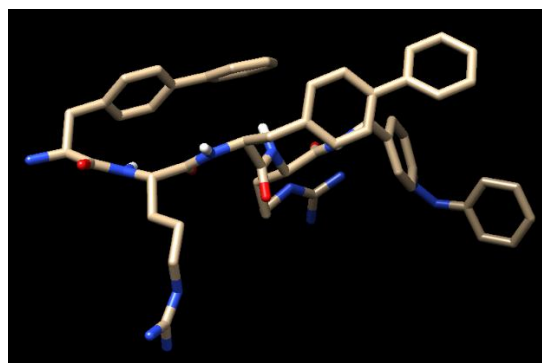
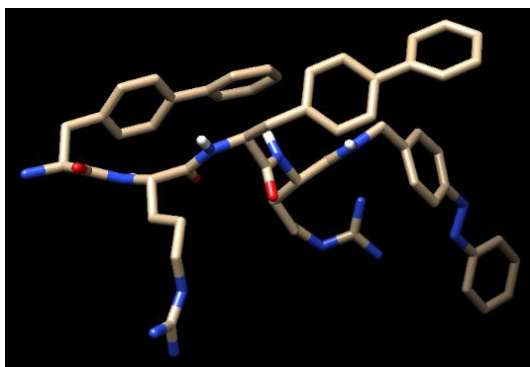
| Peptide | Isomer | Ca | Dihedral angle ($^\circ$) | | β -strand content (%) |
|----------|--------------|--------------------------------|-----------------------------|--------|-----------------------------|
| | | | ϕ | ψ | |
| 1 | <i>trans</i> | Azobenzene | - | 136.8 | 100 |
| | | Arginine | -142.2 | 149.6 | |
| | | <i>p</i> -phenyl-phenylalanine | -108.1 | 141.5 | |
| | | Arginine | -138.1 | 132.0 | |
| | <i>cis</i> | Azobenzene | - | 130.6 | 100 |
| | | Arginine | -150.3 | 155.0 | |
| | | <i>p</i> -phenyl-phenylalanine | -119.2 | 144.0 | |
| | | Arginine | -142.7 | 134.7 | |
| 2 | <i>trans</i> | <i>p</i> -phenyl-phenylalanine | - | 137.6 | 71 |
| | | Arginine | -158.2 | 172.2 | |
| | | Azobenzene | -142.5 | 174.1 | |
| | | Arginine | -152.1 | 156.2 | |
| | <i>cis</i> | <i>p</i> -phenyl-phenylalanine | - | 142.1 | 86 |
| | | Arginine | -153.3 | 172.3 | |
| | | Azobenzene | -124.5 | 152.4 | |
| | | Arginine | -150.8 | 153.2 | |
| 3 | <i>trans</i> | <i>p</i> -phenyl-phenylalanine | - | 152.8 | 71 |
| | | Arginine | -149.2 | 146.9 | |
| | | <i>p</i> -phenyl-phenylalanine | -47.3 | 129.9 | |
| | | Arginine | -141.8 | 61.4 | |
| | <i>cis</i> | <i>p</i> -phenyl-phenylalanine | - | 152.7 | 71 |
| | | Arginine | -149.6 | 148.6 | |
| | | <i>p</i> -phenyl-phenylalanine | -46.3 | 129.7 | |
| | | Arginine | -142.1 | 54.5 | |



Peptide 1



Peptide 2



Peptide 3

Figure S3.7. Molecular models showing the presence of β -strand conformation for the *trans* (left) and *cis* (right) isomers of peptides 1-3.

3.7.8. ^1H NMR Spectroscopy

Table S3.2. $^3J_{\text{NH-C}\alpha\text{H}}$ values for the amide NH in peptides **1-3**. $^3J_{\text{NH-C}\alpha\text{H}}$ values of 7.5-10 Hz indicate the presence of β -strand.⁶⁻⁷

| Peptide | Enriched PSS | $^3J_{\text{NH-C}\alpha\text{H}}$ (Hz) | β -strand Content (%) |
|----------|--------------|---|-----------------------------|
| 1 | <i>trans</i> | 8.0 (Arg), 8.0 (Biphenylalanine), 8.3 (Arg) | 100 |
| | <i>cis</i> | 8.1 (Arg), 8.3 (Biphenylalanine), 10.7 (Arg) | 67 |
| 2 | <i>trans</i> | 8.0 (Arg), 7.9 (Azobenzene), 8.1 (Arg) | 100 |
| | <i>cis</i> | 7.9 (Arg), 7.9 (Azobenzene), 7.9 (Arg) | 100 |
| 3 | <i>trans</i> | 8.1 (Arg), 6.1 (Azobenzene), 8.1 (Arg), 7.2 (Biphenylalanine) | 50 |
| | <i>cis</i> | 8.1 (Arg), 6.1 (Azobenzene), 8.2 (Arg), 8.2 (Biphenylalanine) | 75 |

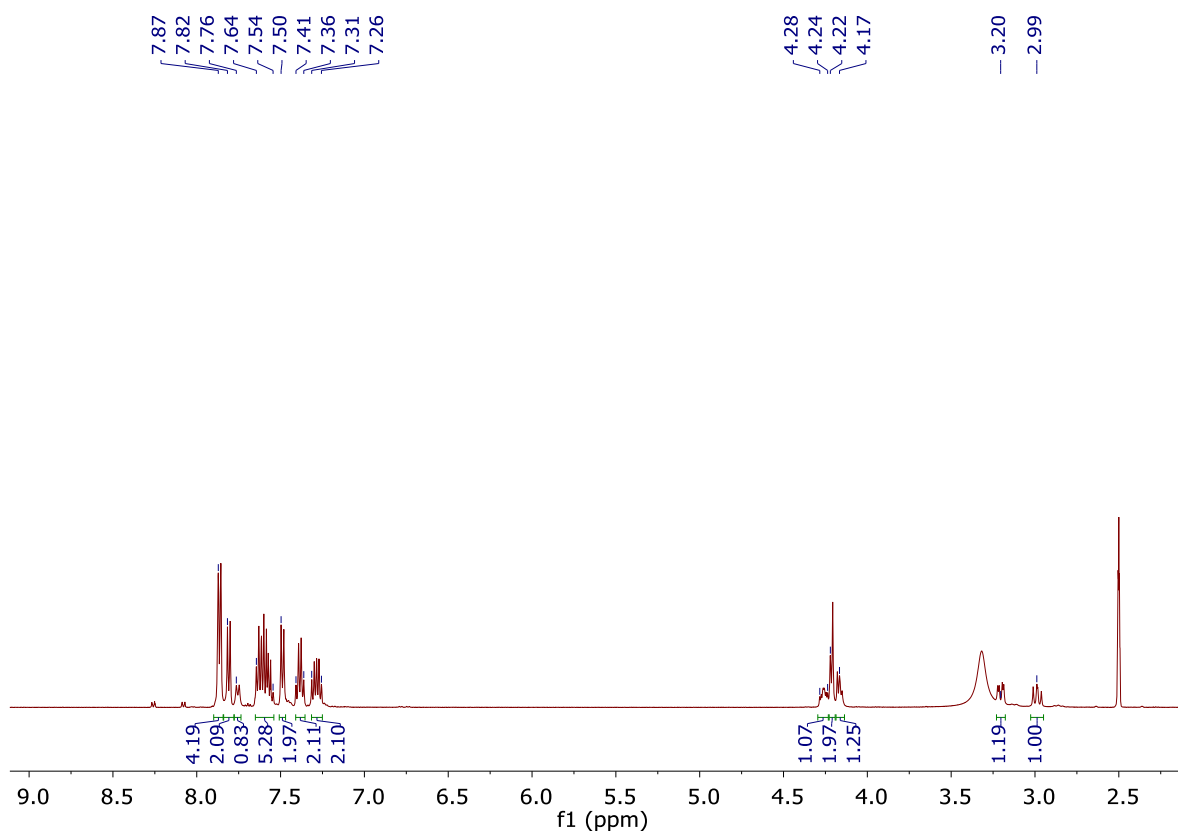


Figure S3.8. ^1H NMR spectrum for (*E*)-2-(((9H-fluoren-9-yl)methoxy)carbonyl)amino)-3-(4-(phenyldiazenyl)phenyl)propanoic acid.

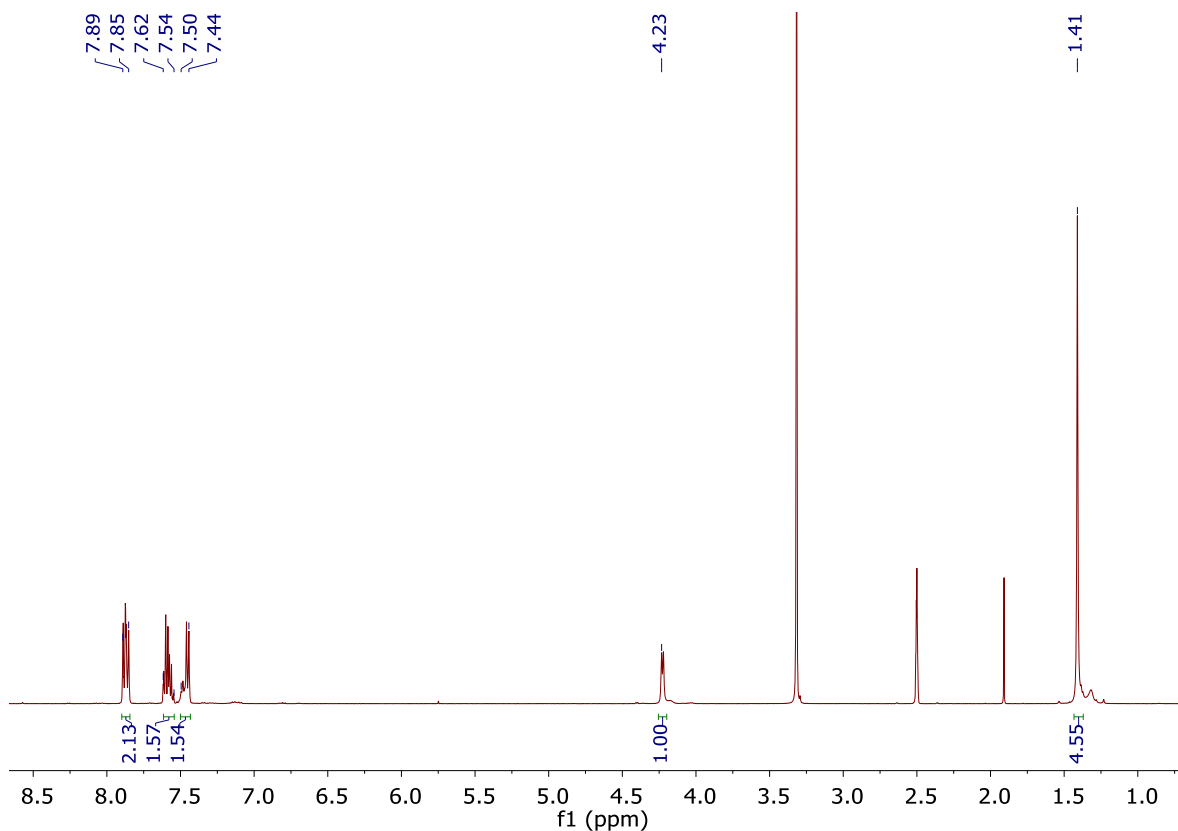


Figure S3.9. ^1H NMR spectrum for *tert*-butyl (*E*)-(4-(phenyldiazenyl)benzyl)carbamate.

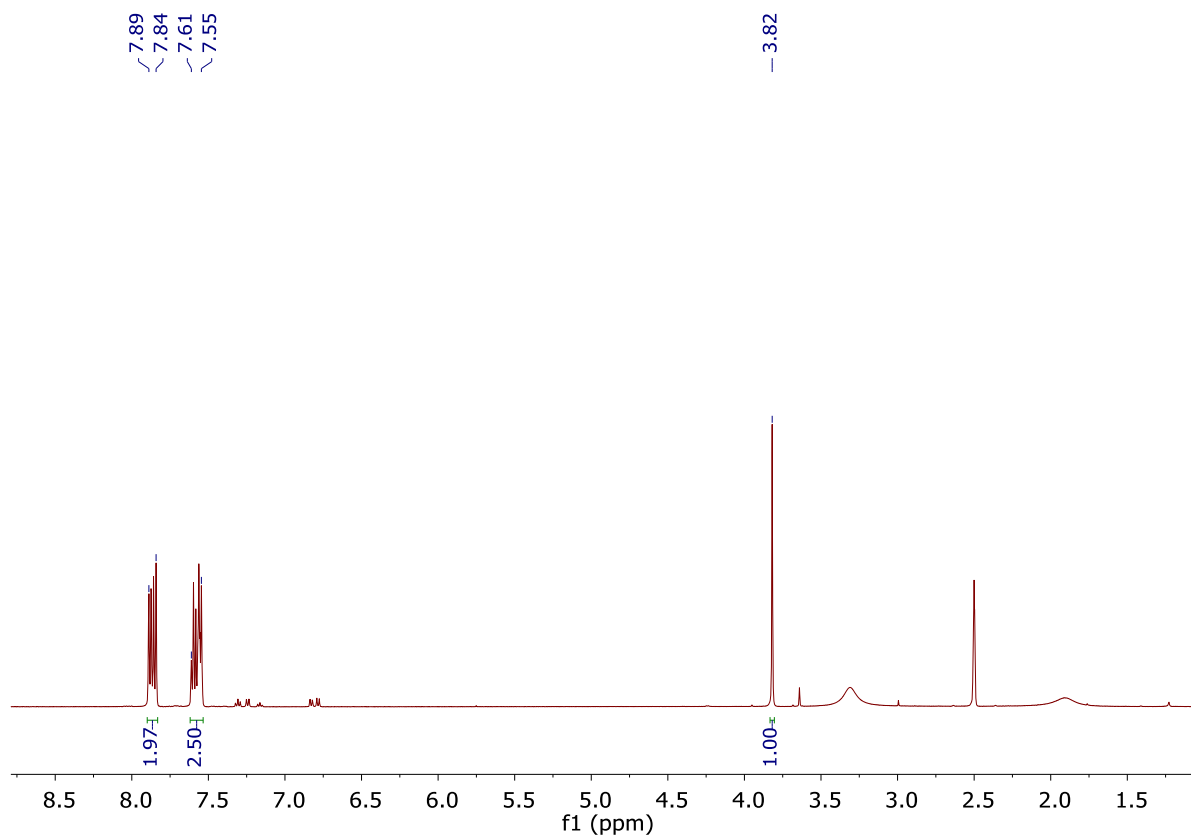


Figure S3.10. ^1H NMR spectrum for *(E)*-4-(phenyldiazenyl)benzyl carbamate.

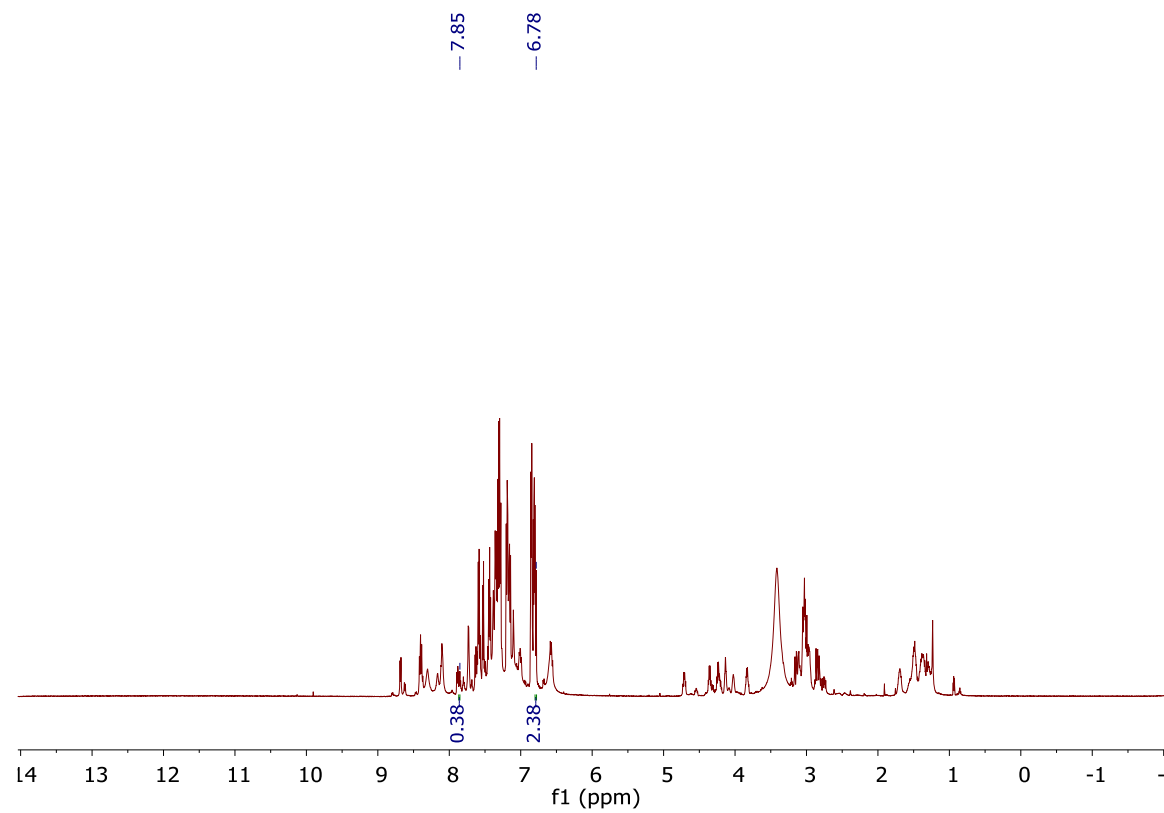
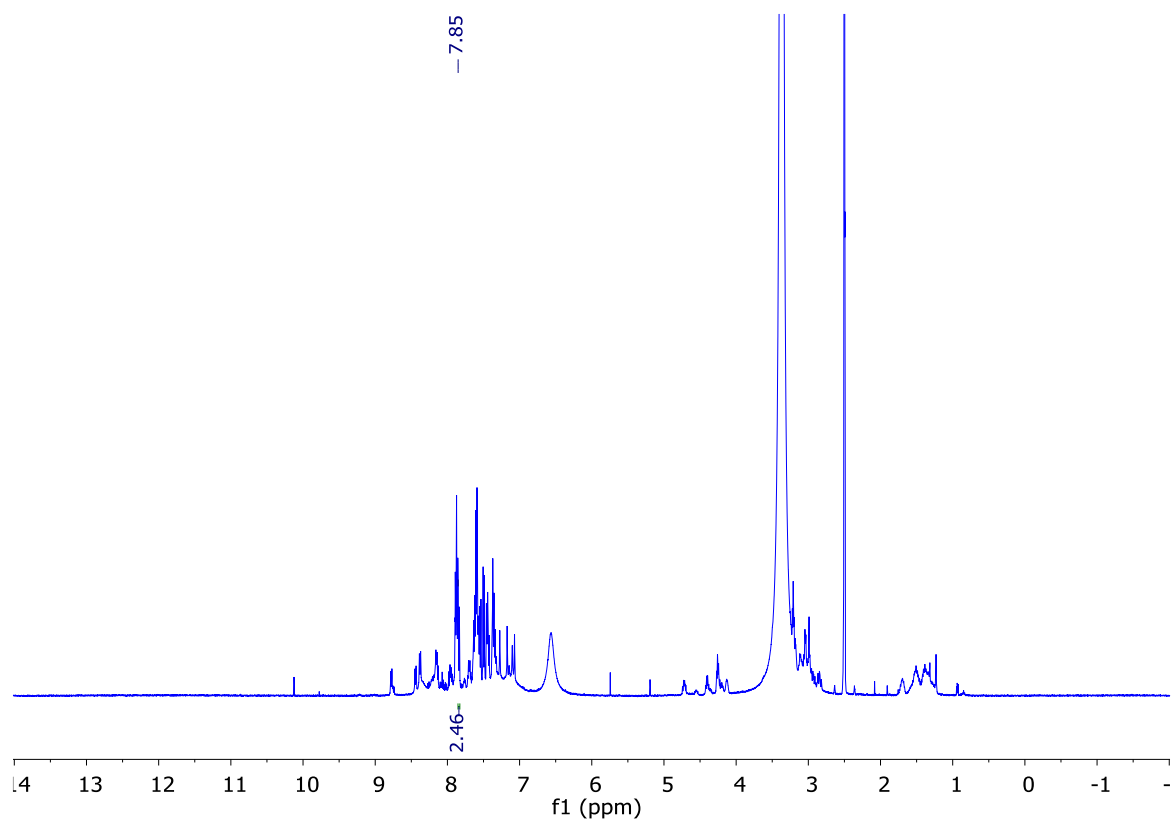


Figure S3.11. ¹H NMR spectra for the *trans*-enriched (blue) and *cis*-enriched (red) PSSs of peptide **1**.

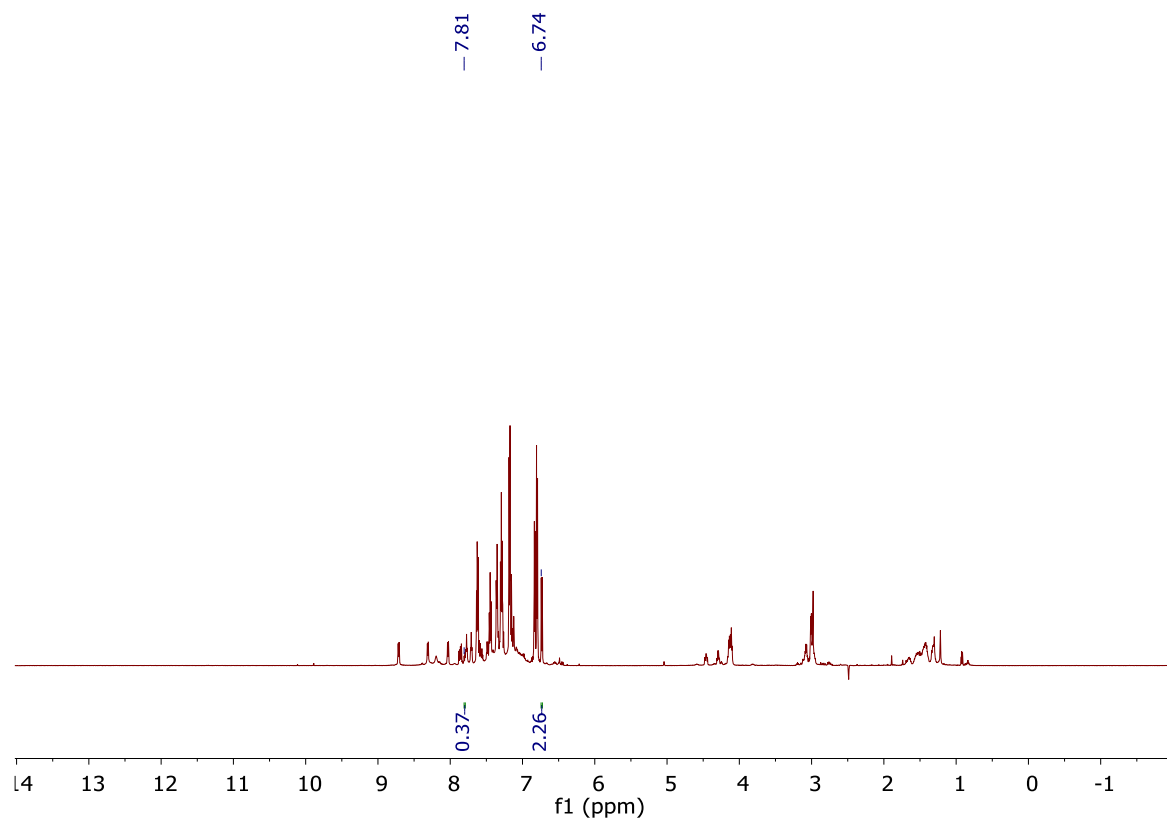
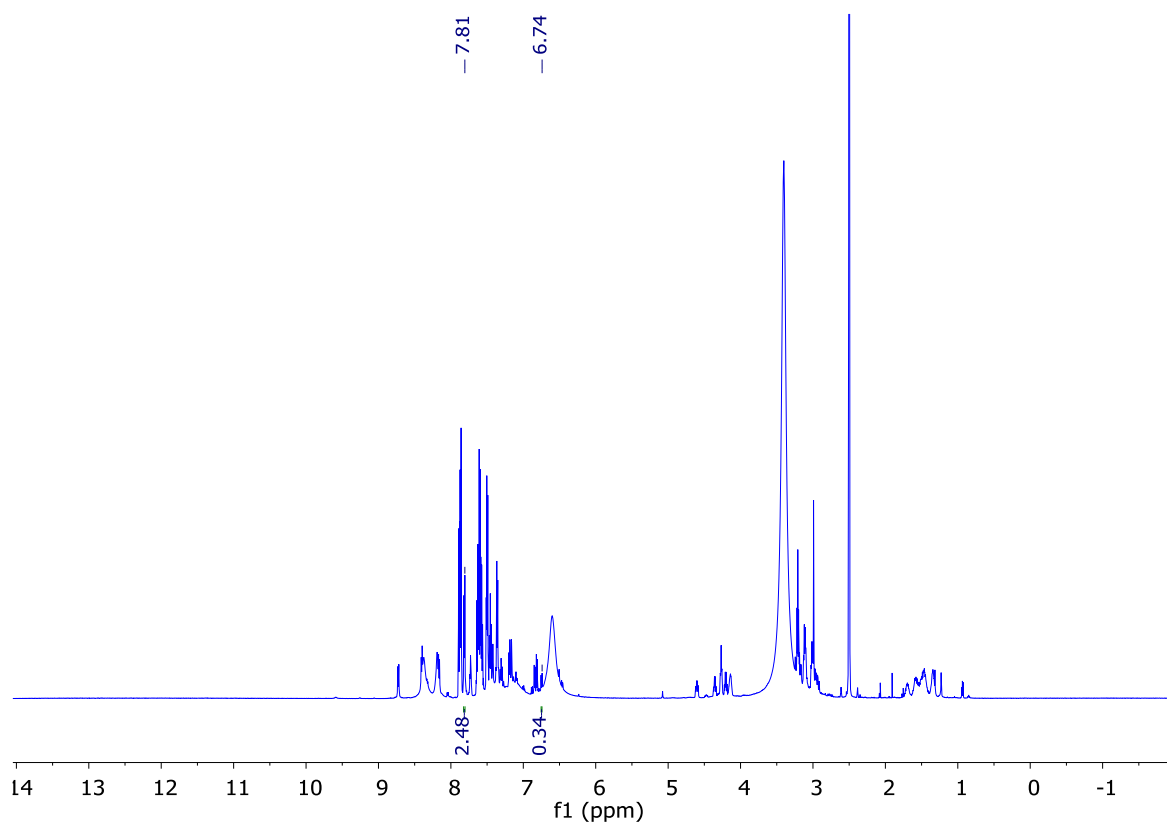


Figure S3.12. ¹H NMR spectra for the *trans*-enriched (blue) and *cis*-enriched (red) PSSs of peptide **2**.

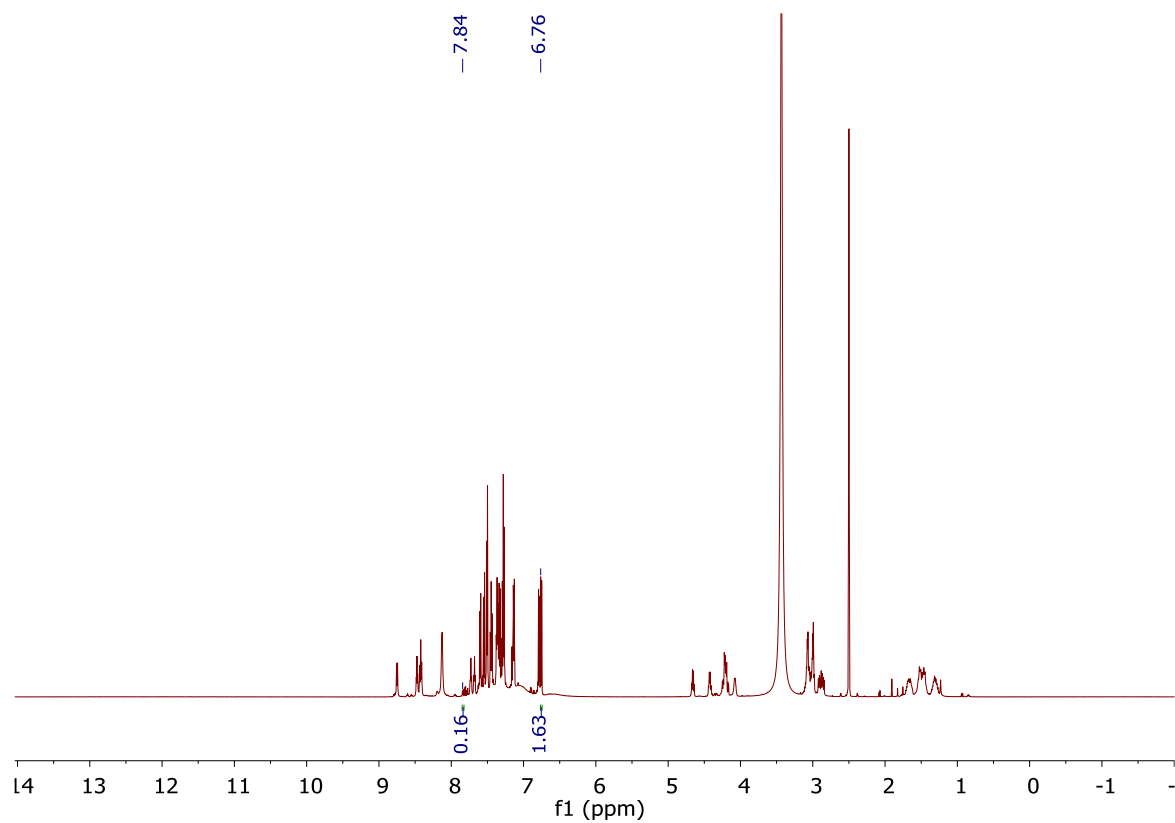
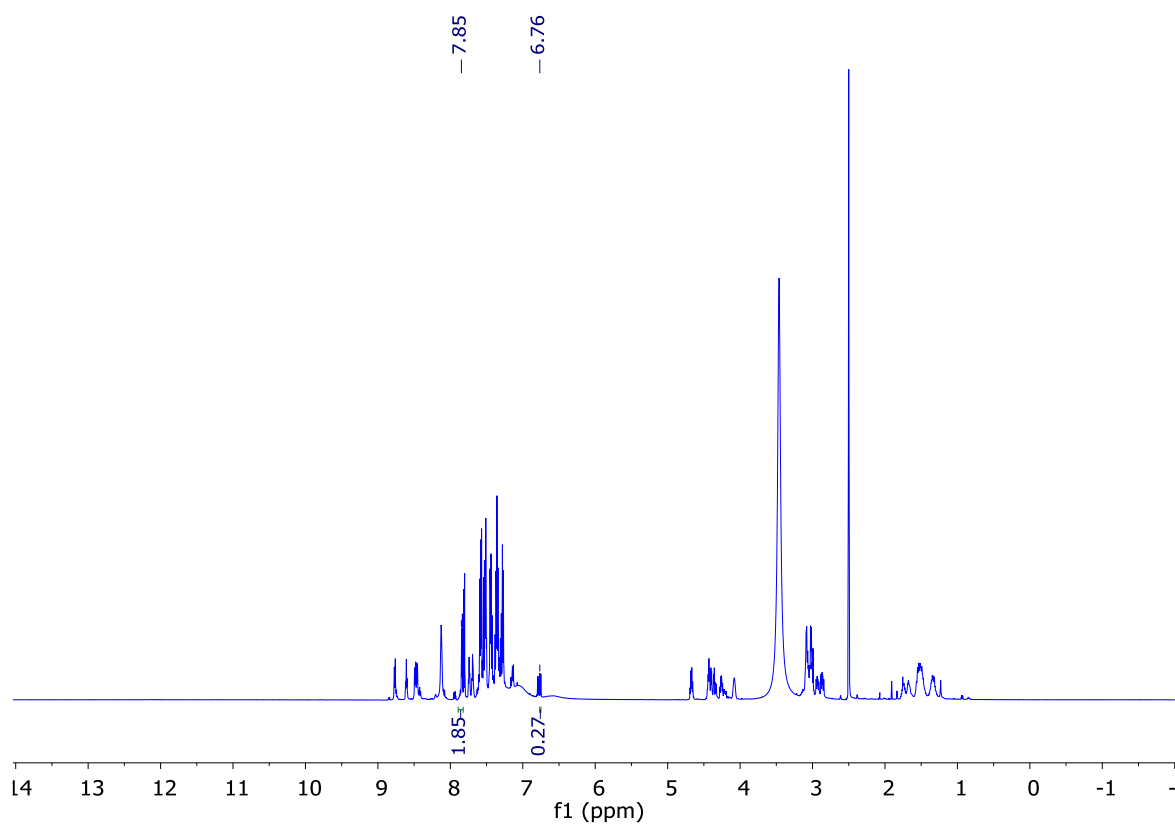


Figure S3.13. ¹H NMR spectra for the *trans*-enriched (blue) and *cis*-enriched (red) PSSs of peptide **3**.


3.7.9 References

1. Frisch, M. J.; Trucks, G. W.; Schlegel, H. B.; Scuseria, G. E.; Robb, M. A.; Cheeseman, J. R.; Scalmani, G.; Barone, V.; Mennucci, B.; Petersson, G. A.; Nakatsuji, H.; Li, X.; Caricato, M.; Hratchian, H. P.; Izmaylov, A. F.; Bloino, J.; Zheng, G.; Sonnenberg, J. L.; Hada, M.; Ehara, M.; Toyota, K.; Fukuda, R.; Hasegawa, J.; Ishida, M.; Nakajima, T.; Honda, Y.; Kitao, O.; Nakai, H.; Vreven, T.; Montgomery, J., J. A.; Peralta, J. E.; Ogliaro, F.; Bearpark, M.; Heyd, J. J.; Brothers, E.; Kudin, K. N.; Staroverov, V. N.; Keith, T.; Kobayashi, R.; Normand, J.; Raghavachari, K.; Rendell, A.; Burant, J. C.; Iyengar, S. S.; Tomasi, J.; Cossi, M.; Rega, N.; Millam, J. M.; Klene, M.; Knox, J. E.; Cross, J. B.; Bakken, V.; Adamo, C.; Jaramillo, J.; Gomperts, R.; Stratmann, R. E.; Yazyev, O.; Austin, A. J.; Cammi, R.; Pomelli, C.; Ochterski, J. W.; Martin, R. L.; Morokuma, K.; Zakrzewski, V. G.; Voth, G. A.; Salvador, P.; Dannenberg, J. J.; Dapprich, S.; Daniels, A. D.; Farkas, O.; Foresman, J. B.; Ortiz, J. V.; Cioslowski, J.; Fox, D. J. *Gaussian 09, Revision B.01*, Gaussian, Inc.: Wallingford CT, 2010.
2. Desponds, A.; Freitag, R., Synthesis and Characterization of Photoresponsive N-Isopropylacrylamide Cotelomers. *Langmuir* **2003**, *19* (15), 6261–6270.
3. Valiev, M.; Bylaska, E. J.; Govind, N.; Kowalski, K.; Straatsma, T. P.; Van Dam, H. J. J.; Wang, D.; Nieplocha, J.; Apra, E.; Windus, T. L.; de Jong, W. A., NWChem: A comprehensive and scalable open-source solution for large scale molecular simulations. *Comput. Phys. Commun.* **2010**, *181* (9), 1477–1489.
4. Pettersen, E. F.; Goddard, T. D.; Huang, C. C.; Couch, G. S.; Greenblatt, D. M.; Meng, E. C.; Ferrin, T. E., UCSF Chimera—A visualization system for exploratory research and analysis. *J. Comput. Chem.* **2004**, *25* (13), 1605–1612.
5. Abell, A. D.; Alexander, N. A.; Aitken, S. G.; Chen, H.; Coxon, J. M.; Jones, M. A.; McNabb, S. B.; Muscroft-Taylor, A., Synthesis of Macrocyclic β -Strand Templates by Ring Closing Metathesis. *J. Org. Chem.* **2009**, *74* (11), 4354–4356.
6. Fernando, S. R. L.; Kozlov, G. V.; Ogawa, M. Y., Distance Dependence of Electron Transfer along Artificial β -Strands at 298 and 77 K. *Inorg. Chem.* **1998**, *37* (8), 1900–1905.
7. Phillips, S. T.; Rezac, M.; Abel, U.; Kossenjans, M.; Bartlett, P. A., “@-Tides”: The 1,2-Dihydro-3(6H)-pyridinone Unit as a β -Strand Mimic. *J. Am. Chem. Soc.* **2002**, *124* (1), 58–66.



CHAPTER 4

A hypoxia-activated antibacterial
prodrug



Foreword

While Chapters 2 and 3 focus on a photopharmacological approach to control antibacterial activity, this chapter emphasizes an alternative strategy, specifically the design and synthesis of a hypoxia-activated prodrug to modulate antibacterial activity. Hypoxia is a condition resulting from oxygen deficiency found in certain bacterial-infected tissues. This unique microenvironmental feature allows for a hypoxia-activated prodrug strategy to regulate the activity of an antibiotic, such that the active agent is only released under reductive conditions that mimic hypoxia. This chapter reports a prodrug based on a known antibacterial compound to target *Staphylococcus aureus* (*S. aureus*) and *Escherichia coli* (*E. coli*) under such reductive conditions. Prodrug **2** was synthesized by masking the N-terminus and side chain amines of a component lysine residue as 4-nitrobenzyl carbamates, while activation to liberate the active antibacterial **1** was demonstrated on treatment with a model reductant, tin(II) chloride. Antibacterial susceptibility assays were performed to confirm the bioactivities of the prodrug and its corresponding active component.

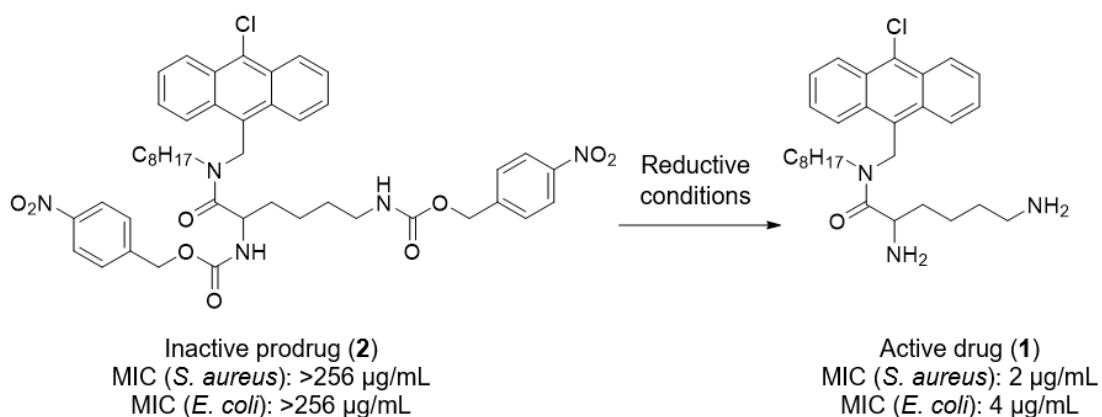


Figure 4.0. Reductive elimination of the 4-nitrobenzyl carbamate protecting groups in prodrug **2** to reveal the free amines in **1** for antibacterial activity against *S. aureus* and *E. coli*. This concept potentially allows for active control over the delivery of antibiotics that otherwise may pose limitations such as toxicity and bioavailability.

Statement of Authorship

| | |
|---------------------|---|
| Title of Paper | A hypoxia-activated antibacterial prodrug |
| Publication Status | <input checked="" type="checkbox"/> Published <input type="checkbox"/> Accepted for Publication <input type="checkbox"/> Submitted for Publication <input type="checkbox"/> Unpublished and Unsubmitted work written in manuscript style |
| Publication Details | Yeoh, Y. Q.; Horsley, J. R.; Polyak, S. W.; Abell, A. D., A hypoxia-activated antibacterial prodrug. <i>Bioorg. Med. Chem. Lett.</i> 2020, 30 (11), 127140. |

Principal Author

| | | | |
|--------------------------------------|--|------|-----------|
| Name of Principal Author (Candidate) | Yuan Qi Yeoh | | |
| Contribution to the Paper | Performed synthesis and characterization for all compounds and wrote manuscript. | | |
| Overall percentage (%) | 70 | | |
| Certification: | This paper reports on original research I conducted during the period of my Higher Degree by Research candidature and is not subject to any obligations or contractual agreements with a third party that would constrain its inclusion in this thesis. I am the primary author of this paper. | | |
| Signature | | Date | 15/6/2020 |

Co-Author Contributions

By signing the Statement of Authorship, each author certifies that:

- the candidate's stated contribution to the publication is accurate (as detailed above);
- permission is granted for the candidate to include the publication in the thesis; and
- the sum of all co-author contributions is equal to 100% less the candidate's stated contribution.

| | | | |
|---------------------------|---|------|---------|
| Name of Co-Author | John R. Horsley | | |
| Contribution to the Paper | Helped in data interpretation and revised manuscript. | | |
| Signature | | Date | 15/6/20 |

| | | | |
|---------------------------|--|------|---------|
| Name of Co-Author | Steven W. Polyak | | |
| Contribution to the Paper | Performed antimicrobial assays and revised manuscript. | | |
| Signature | | Date | 15/6/20 |

| | | | |
|---------------------------|--|------|-----------|
| Name of Co-Author | Andrew D. Abell | | |
| Contribution to the Paper | Supervised development of work and revised manuscript. A corresponding author. | | |
| Signature | | Date | 22/6/2020 |

A hypoxia-activated antibacterial prodrug

Yuan Qi Yeoh,^a John R. Horsley,^a Steven W. Polyak,^{b,1} and Andrew D. Abell^{a*}

^a*ARC Centre of Excellence for Nanoscale BioPhotonics (CNBP), Department of Chemistry, The University of Adelaide, SA 5005, Australia.*

^b*School of Biological Sciences, Department of Molecular and Cellular Biology, The University of Adelaide, SA 5005, Australia.*

¹*Present address: School of Pharmacy and Medical Sciences, University of South Australia, City East Campus (P4-10), North Terrace, Adelaide, SA 5000, Australia.*

Publication

Yeoh, Y. Q.; Horsley, J. R.; Polyak, S. W.; Abell, A. D., A hypoxia-activated antibacterial prodrug. *Bioorg. Med. Chem. Lett.* **2020**, *30* (11), 127140.

4.1 Abstract

A prodrug based on a known antibacterial compound is reported to target *Staphylococcus aureus* (*S. aureus*) and *Escherichia coli* (*E. coli*) under reductive conditions. The prodrug was prepared by masking the N-terminus and side chain amines of a component lysine residue as 4-nitrobenzyl carbamates. Activation to liberate the antibacterial was demonstrated on treatment with a model reductant, tin(II) chloride. The bioactivity of **1** was confirmed in antibacterial susceptibility assays, whereas prodrug **2** was inactive.

4.2 Introduction

Tissue hypoxia is a common microenvironmental hallmark associated with bacterial infection.¹ Animal studies have demonstrated that hypoxia is associated with a range of bacterial infections, with low levels of oxygen caused by reduced blood supply to the infected tissue.²⁻³ Hypoxia-activated prodrugs present as a strategy to regulate the activity of an antibiotic, such that the active agent is only released under conditions of low oxygen, as found in certain bacterial-infected tissues.⁴⁻⁵ This limits general exposure to the active agent, thereby mitigating possible undesirable side effects. Importantly, it can potentially improve the efficacy of treatment as the active antibacterial is delivered specifically to the site of infection and not to the healthy microflora. Improved drug delivery, such as this, can also suppress antibiotic resistance. Proof of concept studies have demonstrated that hypoxia-activated prodrugs can effectively target cancer tumors that likewise experience hypoxic environments.⁶⁻⁹ However, similar studies on bacterial-infected tissue are scarce.¹⁰ Such prodrugs typically mask a key functional group within the parent active drug with a protecting group that is susceptible to reduction under hypoxic conditions. This then allows for site-specific release of the active drug.¹¹

A number of protecting groups susceptible to cleavage under hypoxia¹²⁻¹³ have been employed in the design and development of prodrugs. In this conceptual study, we exploit the unique hypoxic environment associated with bacterial-infected tissue with the design and synthesis of antibacterial prodrug **2** (Figure 4.1) that is specifically activated under reductive conditions. The prodrug is based on the proven broad-spectrum antibacterial **1**¹⁴, which was chosen to provide the appropriate functionality to allow attachment of a group activated under hypoxic conditions to successfully target both Gram-positive bacteria, *S. aureus*, and Gram-negative *E. coli*. Furthermore, it is known to be nontoxic towards mammalian cells.¹⁴ Antibacterial **1** possesses a lysine residue with free amines at both the N-terminus and side chain that are essential for its bioactivity. Once protonated, these groups establish electrostatic interactions between the antibacterial agent and the negatively charged bacterial membrane.¹⁵⁻¹⁷ In this study, the amines were masked with nitrobenzylcarbonyl moieties in **2** to neutralize the electrostatic charge of the compound, thereby abolishing binding to the bacteria. Subsequent removal of the protecting groups under conditions that mimic hypoxia is proposed to restore the binding interaction and antibacterial activity. Previous studies utilized similar nitrobenzyl protecting groups to

synthesize numerous prodrugs, which were shown to be significantly less toxic than the active component *in vitro* and *in vivo*.¹⁸⁻²⁰ Reduction of prodrug **2** would likely occur in the hypoxic extracellular environment where it can target the bacterial membrane. The nitro group reduction strategy was purposely chosen here as it is well known to work in cellular and extracellular hypoxic environments.²¹⁻²³

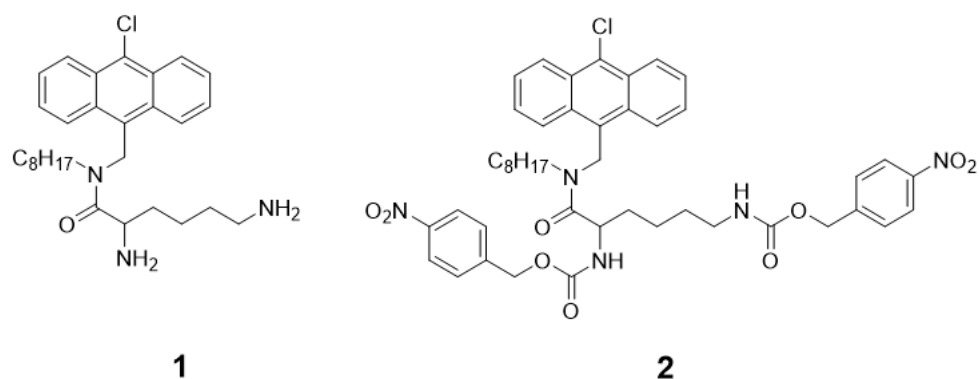
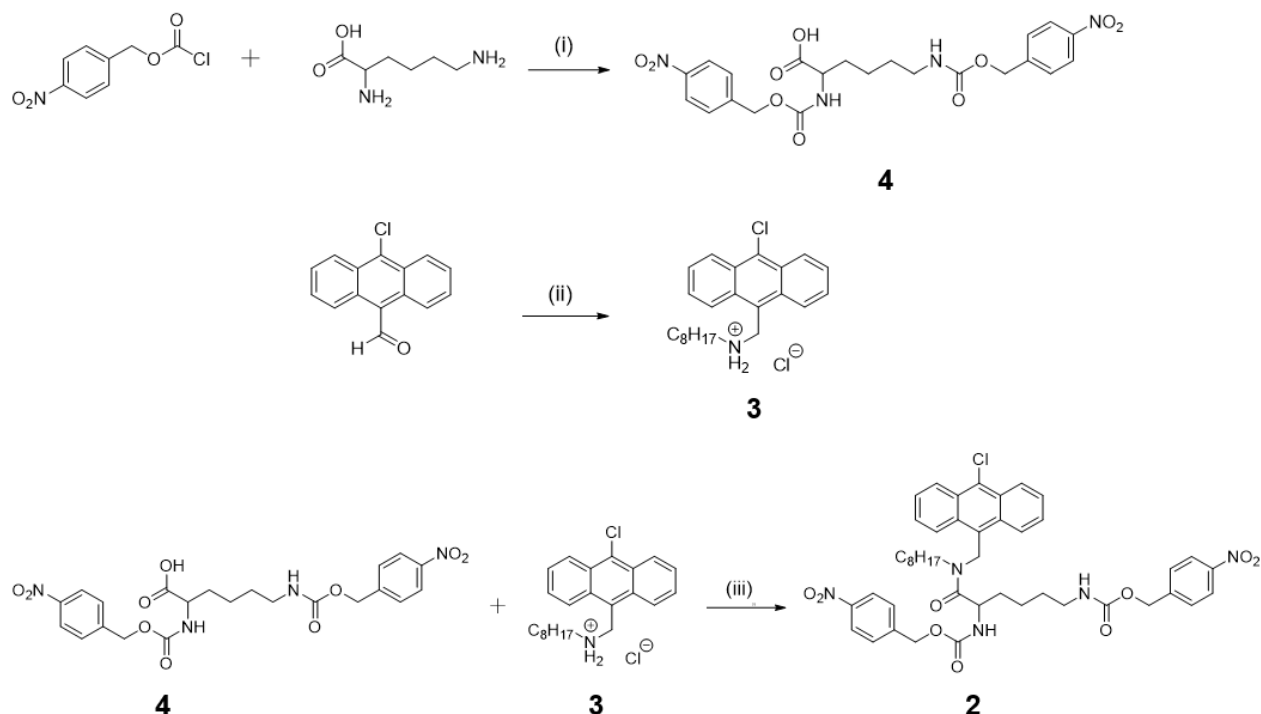


Figure 4.1. Structures of the active antibacterial **1**¹⁴ and inactive prodrug **2**.

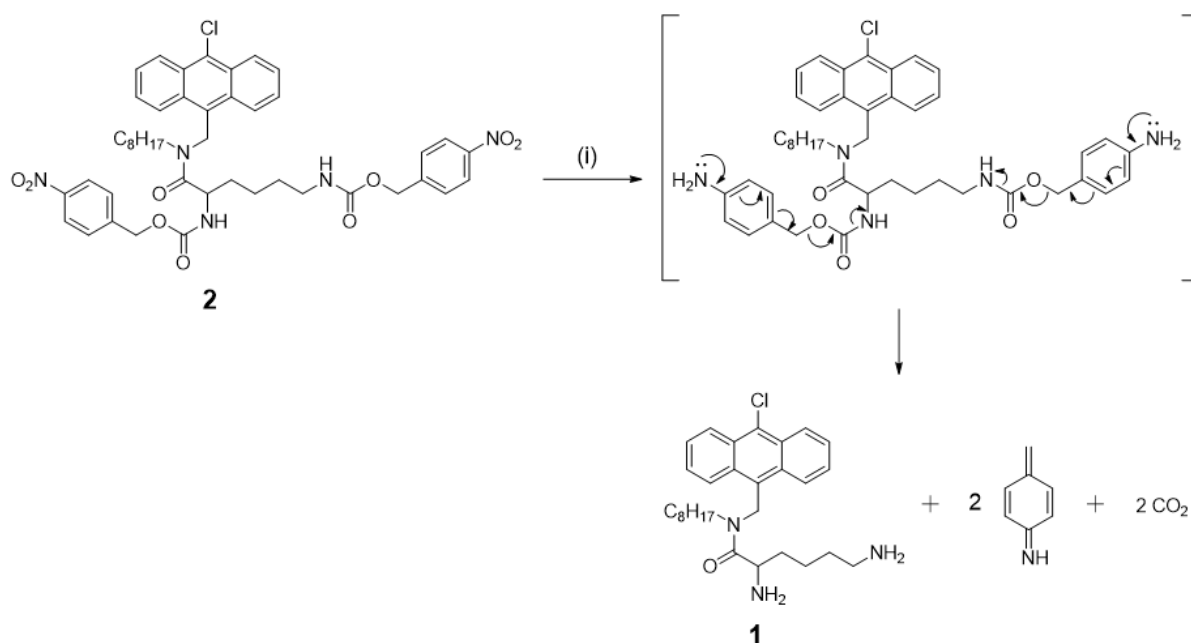
4.3 Results and Discussion

Prodrug **2** was synthesized using standard solution-based chemistry, as detailed in the Experimental section of the Supplementary Information. Briefly, lysine was reacted with two equivalents of 4-nitrobenzyl chloroformate in the presence of sodium bicarbonate/dioxane to give bis 4-nitrobenzylcarbonyl-protected **4** (Scheme 4.1). 10-Chloro-9-anthraldehyde was reacted with octylamine, and the resulting intermediate imine reduced and acidified to give **3**. Compounds **3** and **4** were then coupled using HBTU and DIPEA in DMF/CHCl₃ to give the desired prodrug **2**, which was purified using reverse-phase HPLC, and characterized by ¹H NMR.



Scheme 4.1. Synthesis of antibacterial prodrug **2**. Reagents (i) dioxane/Na₂CO₃, rt, 16h, (ii) C₈H₁₇NH₂, MeOH, 6h, then NaBH₄, MeOH, 18h, followed by 4M HCl, (iii) DIPEA, HBTU, DMF/CHCl₃ (5:3), rt, 24h.

We next demonstrated that the nitrobenzylcarbonyl protecting groups of prodrug **2** could be removed on reduction with tin(II) chloride as a mimic of hypoxia to reveal the active antibacterial agent **1** (Scheme 4.2). The product was then purified using reverse-phase HPLC, and characterized by ^1H NMR and high resolution mass spectrometry (HRMS). In addition, **1** gave a characteristic emission between 400-500 nm of some ten-fold greater intensity than **2** (Figure 4.2). This is consistent with quenching from the nitrobenzylcarbonyl groups due to intramolecular photoinduced electron transfer (PET).²⁴ Collectively, these results confirm the successful reduction and removal of the 4-nitrobenzylcarbonyl groups from the prodrug **2** to reveal the active antibacterial **1** under conditions that mimic environmental hypoxia.



Scheme 4.2. Reduction of antibacterial prodrug **2** to reveal the active antibacterial **1**¹⁴. Reagents (i) $\text{SnCl}_2 \cdot 2\text{H}_2\text{O}$ (20 eq.), dry CHCl_3 , dry MeOH, 50 °C, 22h.

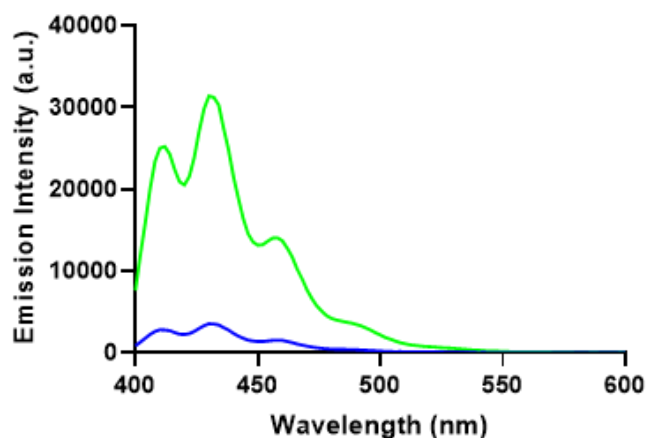


Figure 4.2. Emission spectra for the prodrug **2** (blue) and active antibacterial **1** (green), measured between 400-600 nm, with an excitation wavelength of 380 nm.

Prodrug **2** and active antibacterial **1** were separately assayed against Gram-positive *S. aureus* ATCC 49775 and Gram-negative *E. coli* K 12, in accordance with protocol²⁵ detailed in the Experimental section of the Supplementary Information. In brief, two-fold serial dilutions were made for each compound and separately inoculated with both bacteria at 37°C for 16-20 hours. The lowest concentration that inhibited bacterial growth was reported as the minimal inhibitory concentration (MIC). As expected, compound **1** was active against both bacteria and yielded MICs of 2 µg/mL and 4 µg/mL against *S. aureus* and *E. coli*, respectively, consistent with the potencies previously reported.¹⁴ In contrast, prodrug **2** was inactive against both species at the highest tested concentration (256 µg/mL, Table 4.1). These data confirm the importance of the free amines for antibacterial activity. Our goal was to demonstrate that liberation of the active antibacterial agent **1** from prodrug **2** can kill these bacteria, which was successfully achieved.

Table 4.1. Antibacterial activity of **1** and **2** against *S. aureus* and *E. coli*.

| Minimum inhibitory concentration, MIC (µg/mL) | Prodrug 2 | Active antibacterial 1 |
|---|------------------|-------------------------------|
| <i>S. aureus</i> ATCC 49775 | > 256 | 2 |
| <i>E. coli</i> K 12 | > 256 | 4 |

4.4 Conclusion

In summary, prodrug **2** has been synthesized and shown to be inactive against both *S. aureus* ATCC 49775 and *E. coli* K 12, with the active agent **1** revealed on chemical reduction. This study models a hypoxia-activated strategy to control antibacterial activity, and is potentially the first step towards a hypoxia-activated antibiotic to allow localized treatment, improved efficacy, and suppression of bacterial resistance. It is anticipated that this work will provide further opportunities for cellular studies with bioreductive prodrugs that target bacterial-infected tissue.

4.5 Acknowledgements

This work was supported by the Australian Research Council (CE140100003). We also acknowledge the Australian National Fabrication Facility for providing the analytical facilities used in this work. SWP was supported by the National Health and Medical Research Council of Australia (GN1147538).

4.6 References

- (1) Schaffer, K.; Taylor, C. T., The impact of hypoxia on bacterial infection. *FEBS J.* **2015**, 282 (12), 2260–2266.
- (2) Colgan, S. P.; Taylor, C. T., Hypoxia: an alarm signal during intestinal inflammation. *Nat. Rev. Gastroenterol. Hepatol.* **2010**, 7 (5), 281–287.
- (3) Worlitzsch, D.; Tarran, R.; Ulrich, M.; Schwab, U.; Cekici, A.; Meyer, K. C.; Birrer, P.; Bellon, G.; Berger, J.; Weiss, T.; Botzenhart, K.; Yankaskas, J. R.; Randell, S.; Boucher, R. C.; Döring, G., Effects of reduced mucus oxygen concentration in airway *Pseudomonas* infections of cystic fibrosis patients. *J. Clin. Invest.* **2002**, 109 (3), 317–325.
- (4) Yang, H.; Sha, W.; Liu, Z.; Tang, T.; Liu, H.; Qin, L.; Cui, Z.; Chen, J.; Liu, F.; Zheng, R.; Huang, X.; Wang, J.; Feng, Y.; Ge, B., Lysine acetylation of DosR regulates the hypoxia response of *Mycobacterium tuberculosis*. *Emerg. Microbes Infect.* **2018**, 7 (1), 34.
- (5) Fu, Q.; Yang, Y. J.; Li, C.; Zeng, Q. F.; Zhou, T.; Li, N.; Liu, Y.; Liu, S. K.; Liu, Z. J.; The CC and CXC chemokine receptors in channel catfish (*Ictalurus punctatus*) and their involvement in disease and hypoxia responses. *Dev. Comp. Immunol.* **2017**, 77, 241–251.
- (6) Albertella, M. R.; Loadman, P. M.; Jones, P. H.; Phillips, R. M.; Rarnpling, R.; Burnet, N.; Alcock, C.; Anthoney, A.; Vjaters, E.; Dunk, C. R.; Harris, P. A.; Wong, A.; Lalani, A. S.; Twelves, C. J., Hypoxia-selective targeting by the bioreductive prodrug AQ4N in patients with solid tumors: Results of a phase I study. *Clin. Cancer Res.* **2008**, 14 (4), 1096–1104.
- (7) Cazares-Körner, C.; Pires, I. M.; Swallow, I. D.; Grayer, S. C.; O'Connor, L. J.; Olcina, M. M.; Christlieb, M.; Conway, S. J.; Hammond, E. M., CH-01 is a Hypoxia-Activated Prodrug That Sensitizes Cells to Hypoxia/Reoxygenation Through Inhibition of Chk1 and Aurora A. *ACS Chem. Biol.* **2013**, 8 (7), 1451–1459.
- (8) Jameson, M. B.; Rischin, D.; Pegram, M.; Gutheil, J.; Patterson, A. V.; Denny, W. A.; Wilson, W. R., A phase I trial of PR-104, a nitrogen mustard prodrug activated by both hypoxia and aldo-keto reductase 1C3, in patients with solid tumors. *Cancer Chemother. Pharmacol.* **2010**, 65 (4), 791–801.
- (9) Wang, J.; Foehrenbacher, A.; Su, J.; Patel, R.; Hay, M. P.; Hicks, K. O.; Wilson, W. R., The 2-Nitroimidazole EF5 Is a Biomarker for Oxidoreductases That Activate the Bioreductive Prodrug CEN-209 under Hypoxia. *Clin. Cancer Res.* **2012**, 18 (6), 1684–1695.

- (10) Denny, W. A.; Palmer, B. D., The nitroimidazooxazines (PA-824 and analogs): structure-activity relationship and mechanistic studies. *Future Med. Chem.* **2010**, *2* (8), 1295–1304.
- (11) Testa, B., Prodrugs: bridging pharmacodynamic/pharmacokinetic gaps. *Curr. Opin. Chem. Biol.* **2009**, *13* (3), 338–344.
- (12) Eom, T.; Yoo, W.; Lee, Y. D.; Park, J. H.; Choe, Y.; Bang, J.; Kim, S.; Khan, A., An activatable anticancer polymer-drug conjugate based on the self-immolative azobenzene motif. *J. Mater. Chem. B.* **2017**, *5* (24), 4574–4578.
- (13) Teti, G.; Focaroli, S.; Salvatore, V.; Mazzotti, E.; Ingra, L.; Mazzotti, A.; Falconi, M., The Hypoxia-Mimetic Agent Cobalt Chloride Differently Affects Human Mesenchymal Stem Cells in Their Chondrogenic Potential. *Stem Cells Int.* **2018**, *2018*, 3237253.
- (14) Ghosh, C.; Manjunath, G. B.; Akkapeddi, P.; Yarlagadda, V.; Hoque, J.; Uppu, D. S. S. M.; Konai, M. M.; Halder, J., Small Molecular Antibacterial Peptoid Mimics: The Simpler the Better! *J. Med. Chem.* **2014**, *57* (4), 1428–1436.
- (15) Kohn, E. M.; Shirley, D. J.; Arotzky, L.; Picciano, A. M.; Ridgway, Z.; Urban, M. W.; Carone, B. R.; Caputo, G. A., Role of Cationic Side Chains in the Antimicrobial Activity of C18G. *Molecules* **2018**, *23* (2), 329.
- (16) Bradshaw, J. P., Cationic antimicrobial peptides - Issues for potential clinical use. *Biodrugs* **2003**, *17* (4) 233–240.
- (17) Tennesen, J. A., Molecular evolution of animal antimicrobial peptides: widespread moderate positive selection. *J. Evol. Biol.* **2005**, *18* (6), 1387–1394.
- (18) Grinda, M.; Clarhaut, J.; Renoux, B.; Tranoy-Opalinski, I.; Papot, S., A self-immolative dendritic glucuronide prodrug of doxorubicin. *MedChemComm* **2012**, *3* (1), 68–70.
- (19) Liang, D.; Wu, X.; Hasinoff, B. B.; Herbert, D. E.; Tranmer, G. K., Evaluation of Nitrobenzyl Derivatives of Camptothecin as Anti-Cancer Agents and Potential Hypoxia Targeting Prodrugs. *Molecules* **2018**, *23* (8), 2041.
- (20) Mauger, A. B.; Burke, P. J.; Somani, H. H.; Friedlos, F.; Knox, R. J., Self-Immolative Prodrugs: Candidates for Antibody-Directed Enzyme Prodrug Therapy in Conjunction with a Nitroreductase Enzyme. *J. Med. Chem.* **1994**, *37* (21), 3452–3458.
- (21) Xiao, W.; Sun, G.; Fan, T.; Liu, J.; Zhang, N.; Zhao, L.; Zhong, R., Reductive Activity and Mechanism of Hypoxia- Targeted AGT Inhibitors: An Experimental and Theoretical Investigation. *Int. J. Mol. Sci.* **2019**, *20* (24), 6308.

- (22) O'Connor, L. J.; Cazares-Körner, C.; Saha, J.; Evans, C. N. G.; Stratford, M. R. L.; Hammond, E. M.; Conway, S. J., Efficient synthesis of 2-nitroimidazole derivatives and the bioreductive clinical candidate Evofosfamide (TH-302). *Org. Chem. Front.* **2015**, *2* (9), 1026–1029.
- (23) Wang, J.; Guise, C. P.; Dachs, G. U.; Phung, Y.; Hsu, A.; Lambie, N. K.; Patterson, A. V.; Wilson, W. R., Identification of one-electron reductases that activate both the hypoxia prodrug SN30000 and diagnostic probe EF5. *Biochem. Pharmacol.* **2014**, *91* (4), 436–446.
- (24) Zhang, X. F., The effect of phenyl substitution on the fluorescence characteristics of fluorescein derivatives via intramolecular photoinduced electron transfer. *Photochem. Photobiol. Sci.* **2010**, *9*, 1261–1268.
- (25) Yeoh, Y. Q.; Yu, J.; Polyak, S. W.; Horsley, J. R.; Abell, A. D., Photopharmacological control of cyclic antimicrobial peptides. *ChemBioChem* **2018**, *19* (24), 2591–2597.

4.7 Supplementary Information

4.7.1 Materials

Dichloromethane (CH₂Cl₂), *N,N*-dimethylformamide (DMF), diethyl ether, ethyl acetate, and methanol (MeOH) were purchased from Merck, Australia. 4-nitrobenzyl chloroformate, 10-chloro-9-anthraldehyde, octylamine, sodium borohydride, dioxane, trifluoroacetic acid (TFA), and diisopropylethylamine (DIPEA) were purchased from Sigma–Aldrich, Australia. Sodium carbonate (Na₂CO₃), sodium chloride (NaCl), tin(II) chloride (SnCl₂.2H₂O), potassium hydrogen sulphate (KHSO₄), magnesium sulphate (MgSO₄), hexane, and dimethylsulfoxide (DMSO) were purchased from Chem Supply, Australia. *o*-(Benzotriazol-1-yl)-*N,N,N',N'*-tetramethyluronium hexafluorophosphate (HBTU), H-Lys-OH.HCl, and Boc-Lys(Boc)-OH, were purchased from Chem-Impex International, Inc., USA. Sodium azide and acetonitrile were purchased from Thermo Fisher Scientific, Inc., Australia. Chloroform (CHCl₃), and hydrochloric acid (HCl) were purchased from RCI Labscan, Ltd., Australia. All solvents and reagents were used without purification unless noted.

4.7.2 Methods

Reverse Phase High Performance Liquid Chromatography (RP-HPLC)

All samples were analyzed by reverse phase high performance liquid chromatography (RP-HPLC), using a HP 1100 LC system equipped with a UV-Vis absorbance detector and a Phenomenex Analytical C₁₈ column (Discovery BIO Wide Pore C5-5, 250 x 10 mm, 5 μm). Aqueous solvent A: Water:TFA (100:0.1 v/v) and organic solvent B: ACN:TFA (100:0.08 v/v) were used.

Purification of the samples were performed by RP-HPLC using a Gilson purification system equipped with a UV-Vis absorbance detector and a Supelco Analytical C₁₈ column (Discovery

BIO Wide Pore C5-5, 250 x 10 mm, 5 μm). Aqueous solvent A: Water:TFA (100:0.1 v/v) and organic solvent B: ACN:TFA (100:0.08 v/v) were used during the purification process.

Absorbance Measurements

The absorbance spectra were obtained at $25 \pm 0.5^\circ\text{C}$ on the BioTek™ Synergy™ H4 hybrid microplate reader. All measurements were performed in a 96-well plate with a concentration of approximately 100 $\mu\text{g}/\text{mL}$ of all samples in DMSO. The absorbances for all samples were measured between 200-800 nm.

Fluorescence Measurements

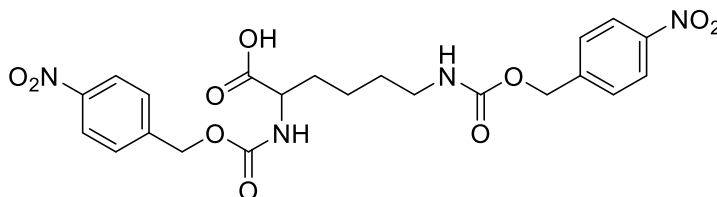
The fluorescence spectra were obtained at $25 \pm 0.5^\circ\text{C}$ on the BioTek™ Synergy™ H4 hybrid microplate reader. All measurements were performed in a 96-well plate with a concentration of approximately 100 $\mu\text{g}/\text{mL}$ of all samples in DMSO. The maximum absorbance wavelength, λ_{max} (380 nm) was used as the excitation wavelength for all fluorescence measurements, while the emission wavelength was set at 400-600 nm. The average of the triplicates was calculated to obtain the average emission intensity for each sample.

Antibacterial Susceptibility Evaluation

Antibacterial activity was determined by the microdilution broth method as recommended by the CLSI (Clinical and Laboratory Standards Institute, Document M07-A8, 2009, Wayne, Pa.) using cation-adjusted Mueller-Hinton broth (Trek Diagnostics Systems, U.K.). Serial two-fold dilutions of each sample were made using DMSO as the diluent. Trays were inoculated with 5×10^4 CFU of either *S. aureus* ATCC 49975 or *E. coli* K 12 in a volume of 100 μL (final concentration of DMSO was 3.2% (v/v)), and incubated at 37°C for 16-20 hours. Growth of the bacterium was quantified by measuring the absorbance at 620 nm.

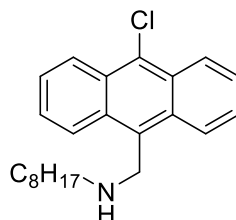
4.7.3 Experimental

4.7.3.1 Synthesis of *N*²,*N*⁶-bis(((4-nitrobenzyl)oxy)carbonyl)lysine (4)



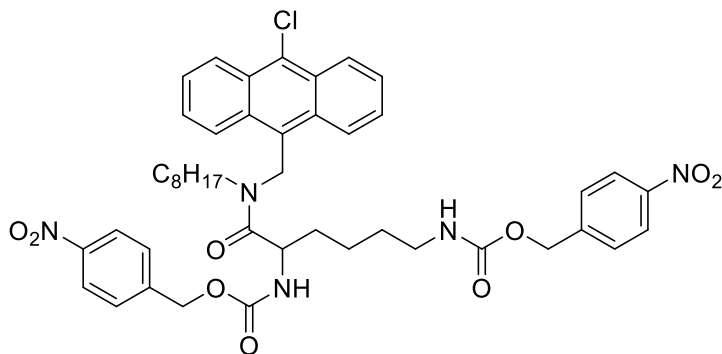
To a stirring solution of 4-nitrobenzyl chloroformate (4.0 g, 18.6 mmol) in dioxane (15 mL), a solution of sodium azide (1.4 g, 21.5 mmol) in water (5 mL) was added dropwise, and the mixture was stirred for 2h at rt. This solution was added dropwise to a stirring solution of H-Lys-OH.HCl (1.7 g, 9.3 mmol) in 1:1 dioxane/10% Na₂CO₃ (10 mL). The resulting mixture was maintained between pH 9-10 with the addition of 10% Na₂CO₃ and stirred overnight at rt. Water (50 mL) was added to the mixture and the suspension was washed with diethyl ether (3 x 50 mL). The aqueous layer was acidified with 1M HCl, and the precipitate was filtered and dried under suction to give a white solid (2.5 g, 53%). ¹H NMR (500 MHz, DMSO-d₆): δ 8.23 (d, *J*=8.7 Hz, 4H), 7.61-7.57 (m, 5H), 7.39 (t, *J*=5.4 Hz, 1H), 5.18 (d, *J*=13.1 Hz, 4H), 3.92-3.87 (m, 1H), 3.01-2.97 (m, 2H), 1.74-1.67 (m, 1H), 1.63-1.55 (m, 1H), 1.44-1.37 (m, 2H), 1.36-1.30 (m, 2H). *m/z*_{calc}: 505.1565, *m/z*_{found}: 505.1580 [M+H]⁺.

4.7.3.2 Synthesis of *N*-((10-chloroanthracen-9-yl)methyl)octan-1-aminium (3)



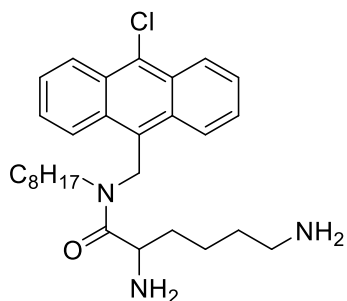
To a stirring solution of 10-chloro-9-anthraldehyde (2.0 g, 8.3 mmol) in 1:1 dry chloroform/dry methanol (80 mL), octylamine (1.07 g, 8.3 mmol) was added dropwise, and the mixture was stirred for 6h at rt. The resulting mixture was cooled to 0 °C before the addition of sodium borohydride (0.57 g, 15.0 mmol), and the mixture was warmed to rt with stirring overnight. The solvent was removed in vacuo, and the residue was dissolved in diethyl ether (60 mL). 2N NaOH (60 mL) was added, and the mixture was stirred vigorously for 15 mins at rt. The immiscible fractions were separated, and the organic layer was washed with water (2 x 80 mL) and brine (2 x 80 mL). The organic layer was dried over MgSO₄, and the solvent was removed in vacuo. 4N HCl (12 mL) was added to the residue, resulting in an instantaneous formation of a precipitate. The precipitate was filtered under suction and washed with hexane to give a yellow solid (2.2 g, 76%). ¹H NMR (500 MHz, CDCl₃): δ 9.99 (br s, 2H), 8.52 (d, *J*=8.7 Hz, 2H), 8.40 (d, *J*=8.9 Hz, 2H), 7.72-7.69 (m, 2H), 7.63-7.60 (m, 2H), 4.95 (br s, 2H), 2.64-2.58 (m, 2H), 1.77-1.71 (m, 2H), 1.18-1.09 (m, 10 H), 0.79 (t, *J*=7.1 Hz, 3H). *m/z*_{calc}: 354.1983, *m/z*_{found}: 354.1981 [M+H]⁺.

4.7.3.3 Synthesis of the antibacterial prodrug (2)



To a solution of N^2,N^6 -bis(((4-nitrobenzyl)oxy)carbonyl)lysine (1.3 g, 2.6 mmol) in 5:2 DMF/chloroform (30 mL), DIPEA (0.8 g, 6.4 mmol) and HATU (1.0 g, 2.6 mmol) were added and stirred for 10 mins at 0 °C. N -((10-chloroanthracen-9-yl)methyl)octan-1-aminium (0.9 g, 2.6 mmol) was added to the mixture and stirred for 30 mins at 0 °C. The mixture was warmed to rt and stirred overnight under N_2 . The solvent was removed in vacuo and the residue was dissolved in ethyl acetate (60 mL). The solution was washed with $KHSO_4$ (60 mL), water (3 x 60 mL) and brine (60 mL), and the organic layer was dried over $MgSO_4$. The solvent was removed in vacuo and the crude product was purified by RP-HPLC to give a yellow solid. 1H NMR (500 MHz, $CDCl_3$): δ 8.62 (d, $J=8.1$ Hz, 2H), 8.28 (d, $J=8.8$ Hz, 2H), 8.21-8.16 (m, 4H), 7.63-7.60 (m, 2H), 7.58-7.55 (m, 2H), 7.50 (d, $J=8.4$ Hz, 2H), 7.46 (d, $J=8.5$ Hz, 2H), 6.11 (d, $J=15.3$ Hz, 1H), 5.89 (d, $J=8.7$ Hz, 1H), 5.30-5.27 (m, 1H), 5.19-5.13 (m, 4H), 4.81 (t, $J=6.0$ Hz, 1H), 4.63-4.58 (m, 1H), 3.12-3.09 (m, 2H), 2.96-2.89 (m, 1H), 2.73-2.67 (m, 1H), 1.66-1.62 (m, 2H), 1.50-1.33 (m, 6H), 1.21-1.15 (m, 2H), 1.11-1.03 (m, 4H), 0.97-0.93 (m, 3H), 0.91-0.88 (m, 1H), 0.83 (t, $J=7.3$ Hz, 3H). m/z_{calc} : 840.3370, m/z_{found} : 840.3379 $[M+H]^+$.

4.7.3.4 Reduction of antibacterial prodrug (2) to give the active antibacterial (1)



To a stirring solution of the prodrug (0.3 g, 0.4 mmol) in dry chloroform (30 mL) and dry methanol (10 mL), $\text{SnCl}_2 \cdot 2\text{H}_2\text{O}$ (1.35 g, 6.0 mmol) was added, and the mixture was refluxed at 50 °C for 22h. The solvent was removed in vacuo and the residue was dissolved in chloroform (100 mL). The precipitate was filtered under suction, and the filtrate was washed with brine (4 x 100 mL). The organic layer was dried over MgSO_4 , and purified by RP-HPLC to give a yellow solid. ^1H NMR (500 MHz, CD_3OD): δ 8.63 (d, $J=8.5$ Hz, 2H), 8.45 (d, $J=8.7$ Hz, 2H), 7.72-7.65 (m, 4H), 6.16 (d, $J=15.3$ Hz, 1H), 5.50 (d, $J=15.3$ Hz, 1H), 4.29 (t, $J=6.2$ Hz, 1H), 3.05-2.98 (m, 1H), 2.76-2.73 (m, 2H), 2.70-2.63 (m, 1H), 1.87-1.78 (m, 2H), 1.60-1.53 (m, 2H), 1.50-1.40 (m, 2H), 1.39-1.30 (m, 2H), 1.24-1.17 (m, 2H), 1.11-1.05 (m, 2H), 1.02-0.96 (m, 3H), 0.94-0.90 (m, 2H), 0.86 (t, $J=7.3$ Hz, 3H), 0.82-0.78 (m, 1H). m/z_{calc} : 482.2933, m/z_{found} : 482.2931 $[\text{M}+\text{H}]^+$.

4.7.4 Spectroscopic Analysis

All samples were dissolved in DMSO at a concentration of 100 $\mu\text{g/mL}$, and the absorbance spectra were recorded using a BioTek™ Synergy™ H4 hybrid multimode microplate reader.

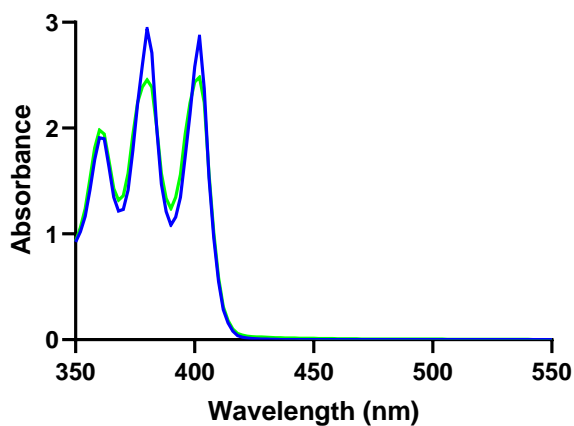
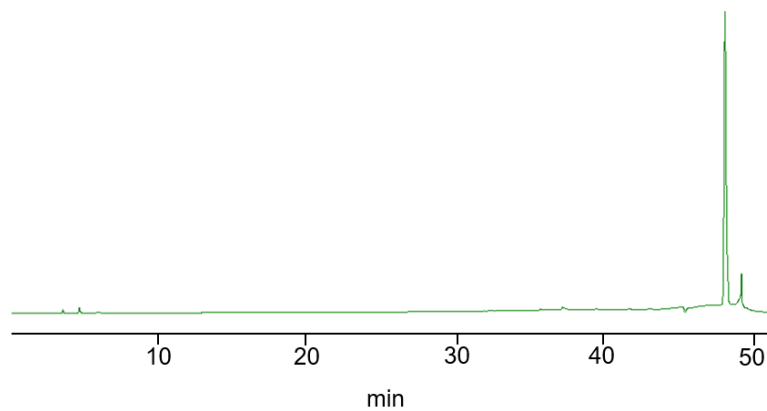


Figure S4.1. Absorbance spectra for the prodrug **2** (blue) and active antibacterial **1** (green). The maximum absorbance wavelength (λ_{max}) for both samples were determined to be 380 nm.

4.7.5 HPLC Chromatograms

(a)



(b)

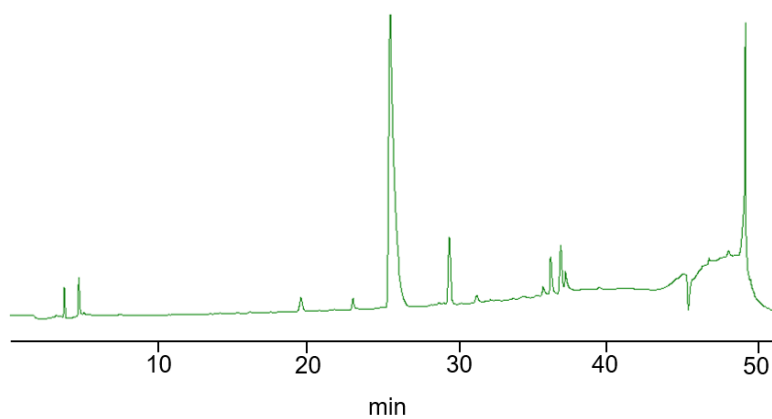


Figure S4.2. HPLC chromatograms of the samples visualized at 254 nm. (a) prodrug **2** and (b) active antibacterial **1**. The active antibacterial **1** showed a retention time of 25 mins, while the prodrug **2** showed a significant longer retention time (48 mins), indicating the large difference in polarity in the compounds.

4.7.6 ^1H NMR Spectra

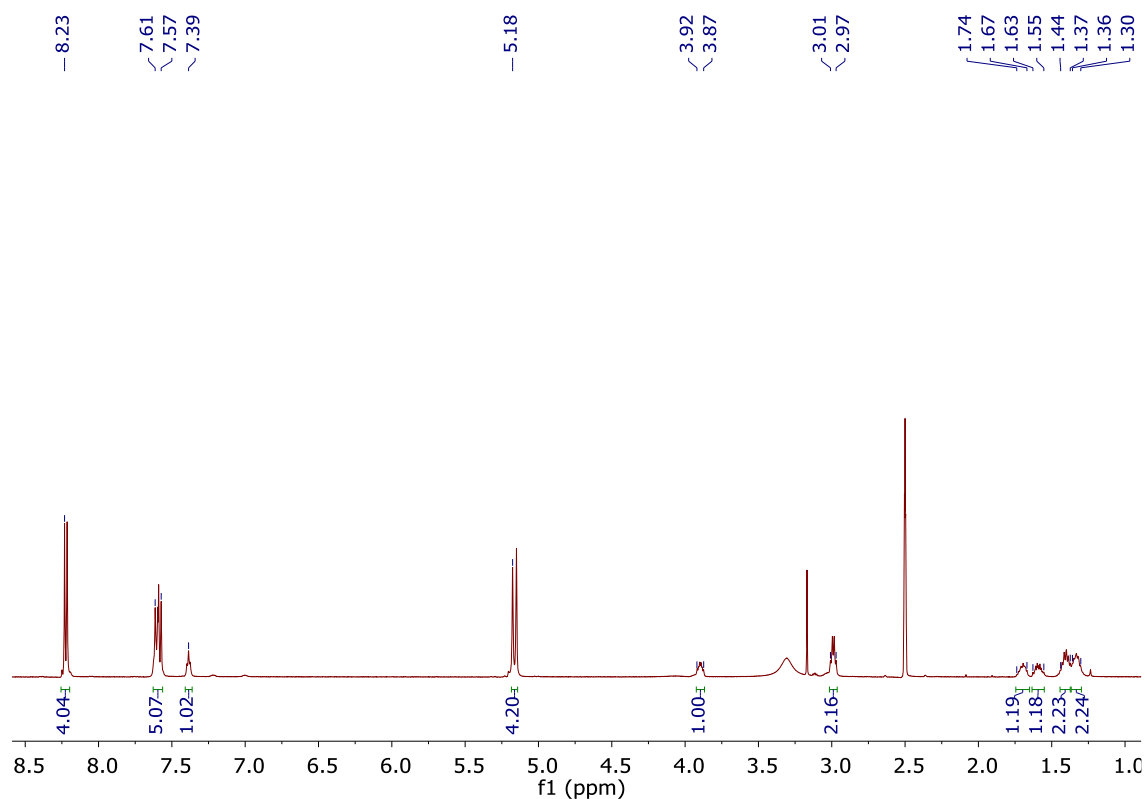


Figure S4.3. ^1H NMR spectrum for N^2,N^6 -bis(((4-nitrobenzyl)oxy)carbonyl)lysine (**4**) in DMSO-d_6 .

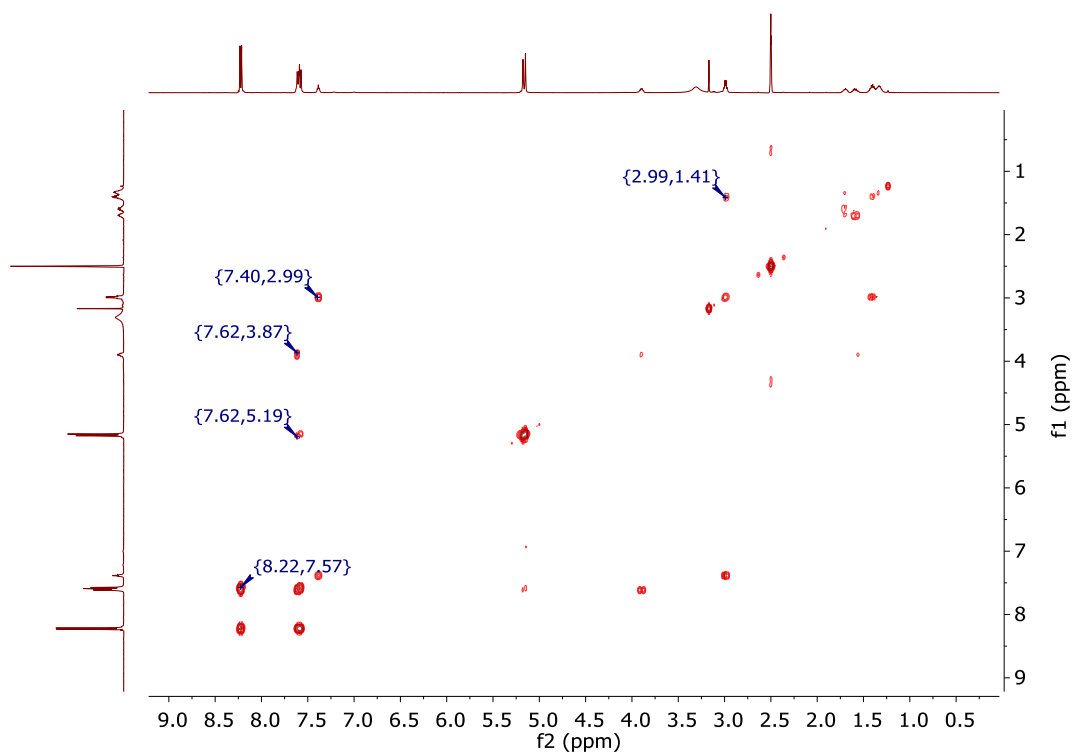


Figure S4.4. COSY spectrum for N^2,N^6 -bis(((4-nitrobenzyl)oxy)carbonyl)lysine (**4**) in DMSO-d_6 .

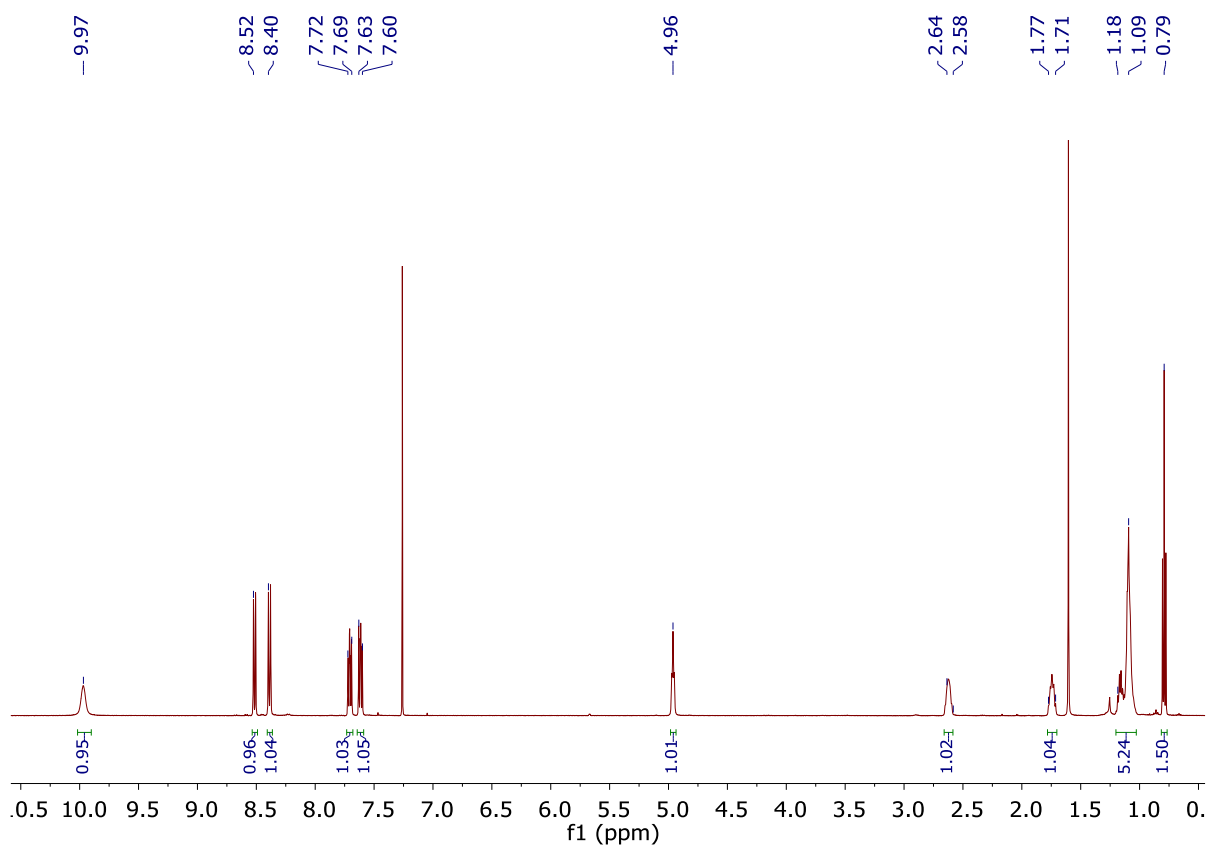


Figure S4.5. ^1H NMR spectrum for *N*-((10-chloroanthracen-9-yl)methyl)octan-1-amium (**3**) in CDCl_3 .

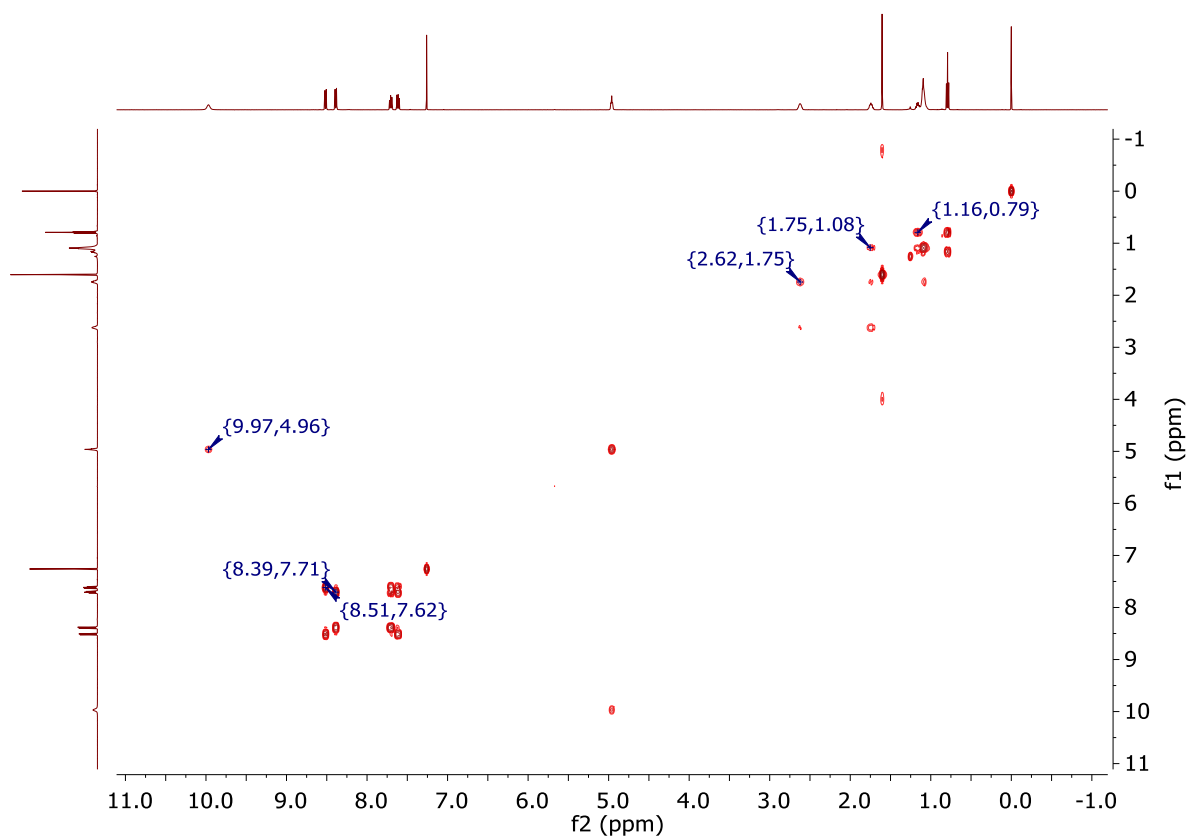


Figure S4.6. COSY spectrum for *N*-((10-chloroanthracen-9-yl)methyl)octan-1-amium (**3**) in CDCl_3 .

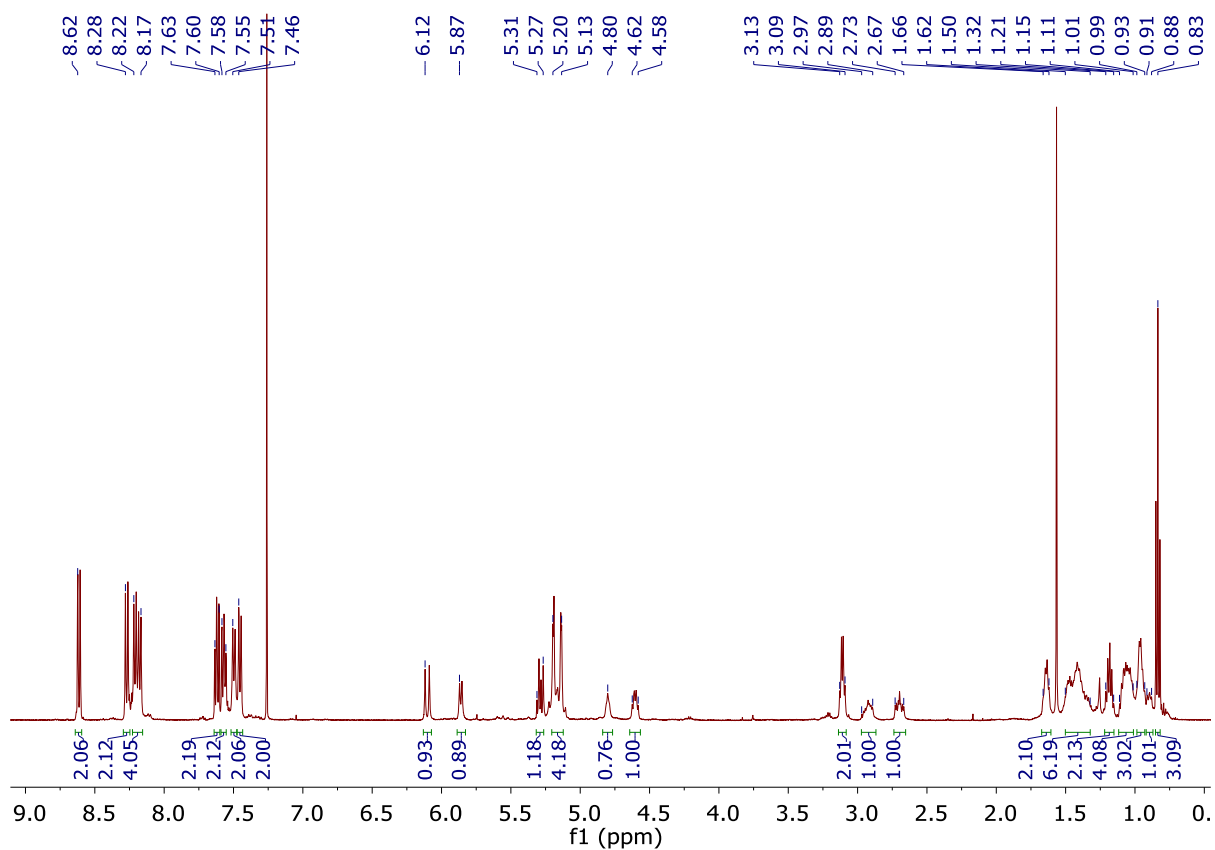


Figure S4.7. ^1H NMR spectrum for the antibacterial prodrug **2** in CDCl_3 .

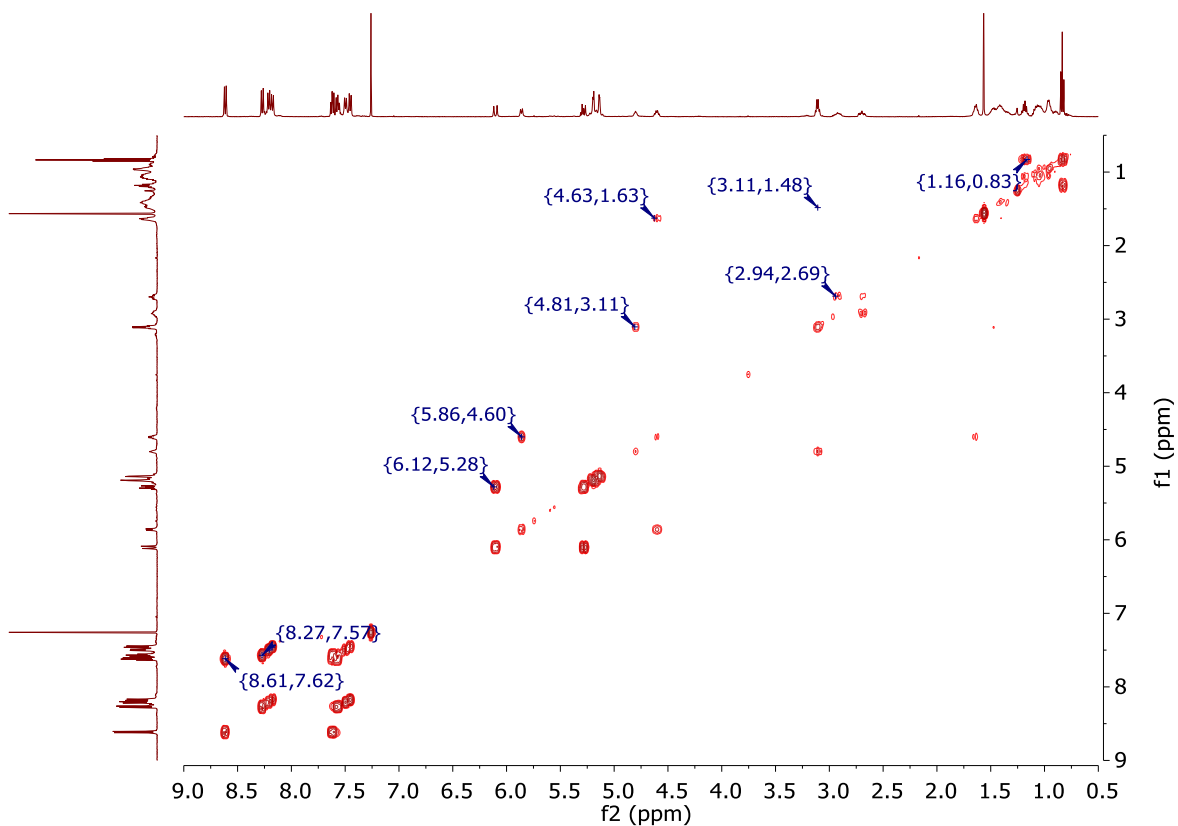


Figure S4.8. COSY spectrum for the antibacterial prodrug **2** in CDCl_3 .

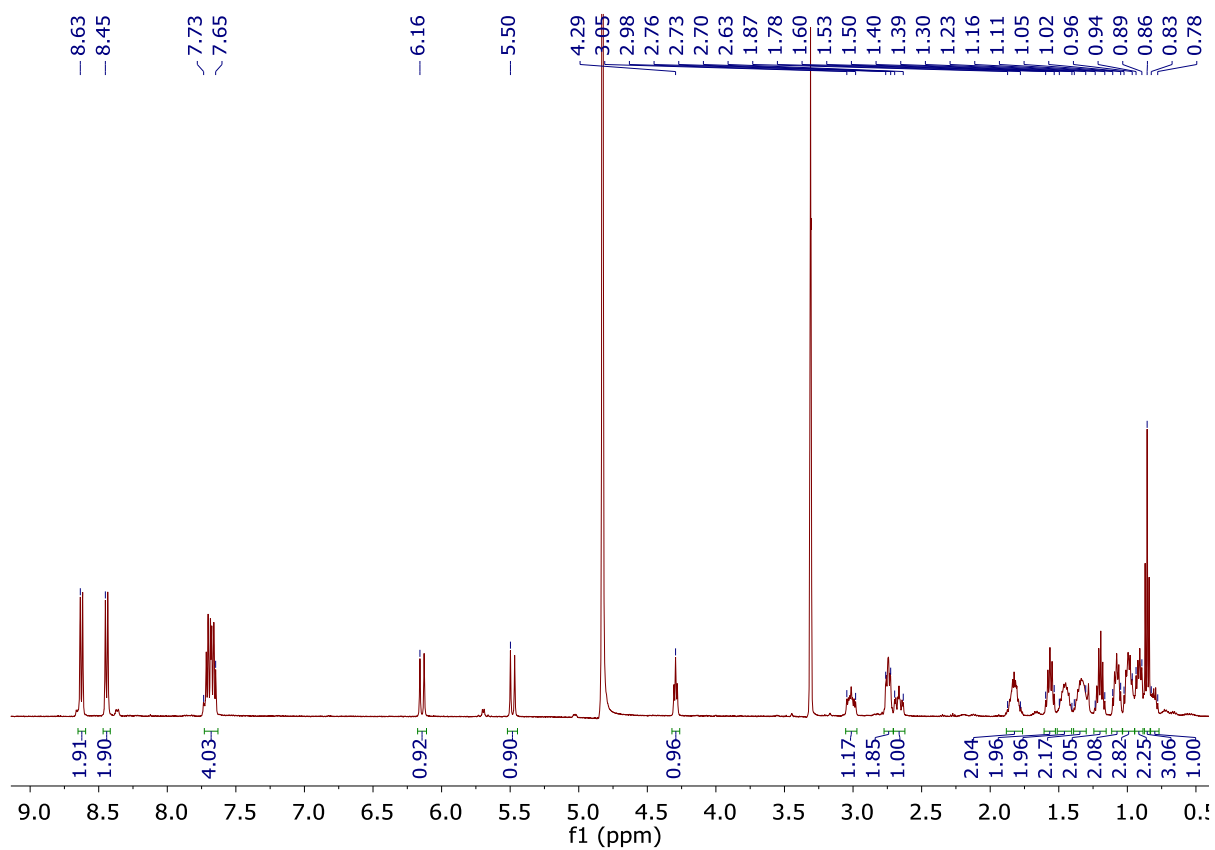



Figure S4.9. ¹H NMR spectrum for the active antibacterial **1** afforded from the reduction of prodrug **2** in CD₃OD.



CHAPTER 5

Unravelling structural dynamics
within a photoswitchable single-
peptide: A step towards multi-
modal bio-inspired nanodevices



Foreword

Previous chapters have focused on peptides containing a well-defined β -sheet secondary structure. This chapter looks at one of those photoswitchable peptides, namely **2a** from Chapter 2, hereafter referred to as peptide **1**, to investigate the relationship between structure and function. To understand how a protein function necessitates a comprehensive study of their inherent structural dynamic properties. A single-peptide junction device was constructed for this purpose, characterized by electrical conductance to probe the structural dynamic behavior of the photoswitchable peptide. The peptide contains an azobenzene photoswitch to interconvert between the *cis* and *trans* isomer upon irradiation using light of a specific wavelength, which induces distinct structural dynamic behavior for each isomer. Real-time conductance measurements were performed on each isomer, with molecular dynamics simulations and quantum transport calculations conducted to rationalize the associated structural dynamic properties corresponding to each conductance state. Modulating the conductance within each isomer of peptide **1** revealed structural dynamic behavior that may potentially extend to both intrinsically disordered proteins, and those containing a well-defined secondary structure.

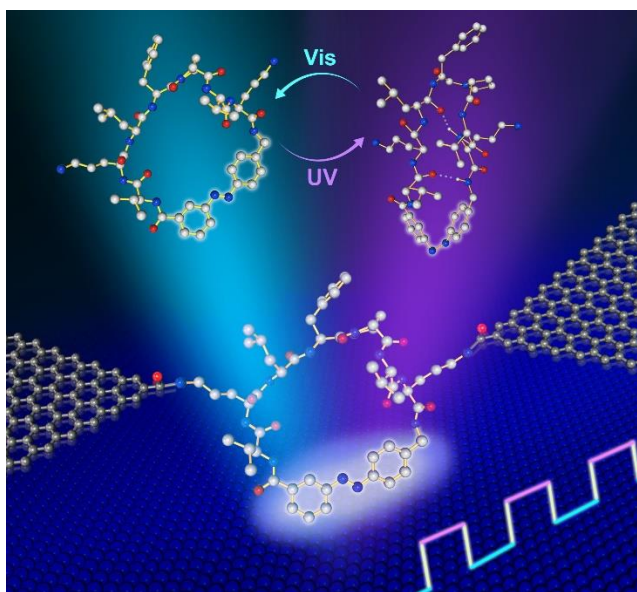


Figure 5.0. A single-molecule junction containing a single-peptide with an azobenzene photoswitch to interconvert between the *trans* (left) and *cis* (right) configurations upon photoisomerization using UV and visible light. Real-time electrical measurements revealed multi-modal conductance states within each isomer, providing insights into the structural dynamics, and demonstrated the capacity to modulate conductance for bio-inspired electronic nanodevices.

Statement of Authorship

| | |
|---------------------|--|
| Title of Paper | Unravelling structural dynamics within a photoswitchable single-peptide: A step towards multi-modal bio-inspired nanodevices |
| Publication Status | <input type="checkbox"/> Published <input checked="" type="checkbox"/> Accepted for Publication <input type="checkbox"/> Submitted for Publication <input type="checkbox"/> Unpublished and Unsubmitted work written in manuscript style |
| Publication Details | Chen, X.; Yeoh, Y. Q.; He, Y.; Zhou, C.; Horsley, J. R.; Abell, A. D.; Yu, J.; Guo, X., Unravelling structural dynamics within a photoswitchable single-peptide: A step towards multi-modal bio-inspired nanodevices. <i>Angew. Chem. Int. Ed.</i> 2020, 10.1002/anie.202004701. |

Principal Author

| | | | | |
|--------------------------------------|--|-----------|------|-----------|
| Name of Principal Author (Candidate) | Yuan Qi Yeoh | | | |
| Contribution to the Paper | Performed synthesis and characterization of the photoswitchable peptide. Helped in the device fabrication and characterization. Wrote manuscript. | | | |
| Overall percentage (%) | 40 | | | |
| Certification: | This paper reports on original research I conducted during the period of my Higher Degree by Research candidature and is not subject to any obligations or contractual agreements with a third party that would constrain its inclusion in this thesis. I am the primary author of this paper. | | | |
| Signature | <table border="1" style="width: 100%;"> <tr> <td style="width: 60%;"></td> <td style="width: 10%; text-align: center;">Date</td> <td style="width: 30%; text-align: center;">15/6/2020</td> </tr> </table> | | Date | 15/6/2020 |
| | Date | 15/6/2020 | | |

Co-Author Contributions

By signing the Statement of Authorship, each author certifies that:

- i. the candidate's stated contribution to the publication is accurate (as detailed above);
- ii. permission is granted for the candidate to include the publication in the thesis; and
- iii. the sum of all co-author contributions is equal to 100% less the candidate's stated contribution.

| | | | | |
|---------------------------|--|-----------|------|-----------|
| Name of Co-Author | Xinjiani Chen | | | |
| Contribution to the Paper | Fabricated and characterized the single-molecule nanodevice. Analyzed data and wrote manuscript. | | | |
| Signature | <table border="1" style="width: 100%;"> <tr> <td style="width: 60%;"></td> <td style="width: 10%; text-align: center;">Date</td> <td style="width: 30%; text-align: center;">15/6/2020</td> </tr> </table> | | Date | 15/6/2020 |
| | Date | 15/6/2020 | | |

| | | | | |
|---------------------------|--|-----------|------|-----------|
| Name of Co-Author | Yanbin He | | | |
| Contribution to the Paper | Performed molecular dynamics simulations, quantum transport calculations, and data analysis. Wrote manuscript. | | | |
| Signature | <table border="1" style="width: 100%;"> <tr> <td style="width: 60%;"></td> <td style="width: 10%; text-align: center;">Date</td> <td style="width: 30%; text-align: center;">15/6/2020</td> </tr> </table> | | Date | 15/6/2020 |
| | Date | 15/6/2020 | | |

| | | | |
|---------------------------|--|------|-----------|
| Name of Co-Author | Chenguang Zhou | | |
| Contribution to the Paper | Helped in the device fabrication and characterization. Wrote manuscript. | | |
| Signature | | Date | 15/6/2020 |

| | | | |
|---------------------------|-------------------------------------|------|---------|
| Name of Co-Author | John R. Horsley | | |
| Contribution to the Paper | Analyzed data and wrote manuscript. | | |
| Signature | | Date | 15/6/20 |

| | | | |
|---------------------------|---|------|-----------|
| Name of Co-Author | Andrew D. Abell | | |
| Contribution to the Paper | Revised manuscript. A corresponding author. | | |
| Signature | | Date | 22/6/2020 |

| | | | |
|---------------------------|---|------|-----------|
| Name of Co-Author | Jingxian Yu | | |
| Contribution to the Paper | Analyzed data and revised manuscript. A corresponding author. | | |
| Signature | | Date | 15/6/2020 |

| | | | |
|---------------------------|--|------|-----------|
| Name of Co-Author | Xuefeng Guo | | |
| Contribution to the Paper | Supervised development of work and revised manuscript. A corresponding author. | | |
| Signature | | Date | 2020/6/15 |

Unravelling structural dynamics within a photoswitchable single-peptide: A step towards multi-modal bio-inspired nanodevices

Xinjiani Chen^{a,1}, Yuan Qi Yeoh^{b,1}, Yanbin He^{b,c,1}, Chenguang Zhou^d, John R. Horsley^b, Andrew D. Abell^{b,*}, Jingxian Yu^{b,*} and Xuefeng Guo^{a,d,*}

^a*Peking-Tsinghua Center for Life Sciences, Academy for Advanced Interdisciplinary Studies, Peking University, Beijing 100871, P. R. China.*

^b*ARC Centre of Excellence for Nanoscale BioPhotonics (CNBP), Institute of Photonics and Advanced Sensing (IPAS), School of Physical Sciences, The University of Adelaide, North Terrace, Adelaide SA 5005, Australia.*

^c*Pharmaceutical Department, Changzhi Medical College, Changzhi 046000, P. R. China.*

^d*Beijing National Laboratory for Molecular Sciences, State Key Laboratory for Structural Chemistry of Unstable and Stable Species, College of Chemistry and Molecular Engineering, Peking University, Beijing 100871, P. R. China.*

¹*These authors contributed equally to this work.*

Publication

Chen, X.; Yeoh, Y. Q.; He, Y.; Zhou, C.; Horsley, J. R.; Abell, A. D.; Yu, J.; Guo, X., Unravelling structural dynamics within a photoswitchable single-peptide: A step towards multi-modal bio-inspired nanodevices. *Angew. Chem. Int. Ed.* **2020**, 10.1002/anie.202004701.

5.1 Abstract

Proteins are in continuous motion, with their structural dynamic behavior crucial to function. However, the majority of protein structures have been elucidated under equilibrium conditions. We aim to provide a better understanding of the dynamic behavior inherent to proteins by fabricating a label-free nanodevice comprising a single-peptide junction, to measure real-time conductance from which their structural dynamic behavior can be inferred. This device contains an azobenzene photoswitch for interconversion between a well-defined *cis*, and disordered *trans* isomer. Real-time conductance measurements revealed three distinct states for each isomer, with molecular dynamics simulations showing each state corresponds to a specific range of hydrogen bond lengths within the *cis* isomer, and specific dihedral angles in the *trans* isomer. We have provided hitherto undisclosed insights into the structural dynamic behavior of peptides, which may rationally extend to proteins, and demonstrated the capacity to modulate conductance, which advances the design and development of bio-inspired electronic nanodevices.

5.2 Introduction

All proteins are dynamic structures that are in continuous motion,¹ with atoms undergoing random thermal fluctuations and small conformational changes by virtue of their local environment.² In the majority of cases, their function is determined by well-defined secondary structures,³ such as helices and β -strands, but in a growing number of cases, cellular function has been shown to be defined by a disordered structure.⁴ The functional role of such intrinsically disordered proteins is acknowledged in areas such as transcriptional regulation, translation, and cellular signal transduction, where flexibility is required for such transient interactions,⁵ however our understanding of their structural dynamic properties is limited.⁶ These dynamic properties cannot be fully elucidated under equilibrium conditions,⁷ e.g. X-ray crystallography, that only provide a snapshot of the proteins frozen in crystal structures.⁸ To further our understanding of structured/unstructured proteins in motion, a sophisticated system is required to measure the physical properties from which their structural dynamic behavior can be inferred. This can be achieved using a functional, ultrasensitive device able to utilize simpler model peptides,⁹⁻¹⁰ with structural dynamic properties detected and measured in real-time with single-bond resolution. Model peptides present as ideal alternatives for this purpose due to the intrinsic complexity of proteins.¹¹

Hence, we propose to exploit a single-peptide with an in-built photoswitch (cyclic peptide **1**, Figure 5.1a) that allows reversible interconversion between two isomers to define their structural dynamic properties. We have previously shown that photoisomerization of this peptide triggers a significant geometric change between the well-defined *cis* isomer and disordered *trans* isomer.¹² By having both isomers in the one simple model, it is possible to study their respective structural dynamic behavior in a controlled setting at the most fundamental level, which provides an appropriate model for the two protein structures described above. For device fabrication, cyclic peptide **1** will be covalently attached to nanogapped graphene electrodes to form a graphene-molecule-graphene single-molecule junction (GMG-SMJ, Figure 5.1b). According to our established procedures,¹³⁻¹⁶ the single-molecule electronic detection method (e.g. field-effect transistor, FET) can then be used to probe the structural dynamic properties of each isomer of the peptide by transducing molecular information into quantized changes in conductance, with precise spatial control and high temporal resolution.¹⁷

This label-free technique is ideal for investigating the structural dynamic behavior of such a photoswitchable peptide, where alternative optical and mechanical detection methods can themselves induce undesirable structural changes within the molecule.¹⁸⁻¹⁹ When cyclic peptide **1** is bridged between the nanogapped electrodes, photoisomerization of the azobenzene photoswitch is expected to result in a significant difference in electronic conductance between the two isomers due to their distinctive structures. Real-time conductance measurements on the GMG-SMJ platform enable the structural dynamic behavior of both well-defined and intrinsically disordered peptides to be revealed and compared from within the one single-peptide, thus providing important fundamental insights into this dynamic phenomenon.

5.3 Results and Discussion

5.3.1 Peptide Design and Device Fabrication

We have previously reported the synthesis of cyclic peptide **1** (Figure 5.1a).¹² ¹H NMR spectroscopy and lowest energy density functional theory (DFT) calculations revealed the *cis* isomer of **1** adopts a β -sheet geometry with well-defined intramolecular hydrogen bonds, while the *trans* isomer is devoid of secondary structure.¹² Detailed GMG-SMJ device fabrication and peptide coupling procedures are provided in the Supplementary Information. Briefly, the free amines located on the two ornithine residues of cyclic peptide **1** were coupled to the carboxylic acid-functionalized nanogapped graphene point contacts (Figure 5.1b). The fixed gap device has significant advantages over conventional STM measurements,²⁰ particularly as the peptide forms stable, covalent linkages to the two electrodes. This device was then characterized electronically, where the successful formation of a single-molecule junction is confirmed by a typical *I-V* curve, and an open circuit represents no peptide coupling (Figure 5.1c). The real-time measurements were carried out with a fixed source-drain bias voltage of 0.2 V and a sampling rate of 57.6 kSa/s at room temperature under ambient conditions. The photoinduced folding and unfolding processes in an azobenzene-containing peptide are well known²¹⁻²² and occur on a picosecond timescale,²³ and thus are not the focus of this study.

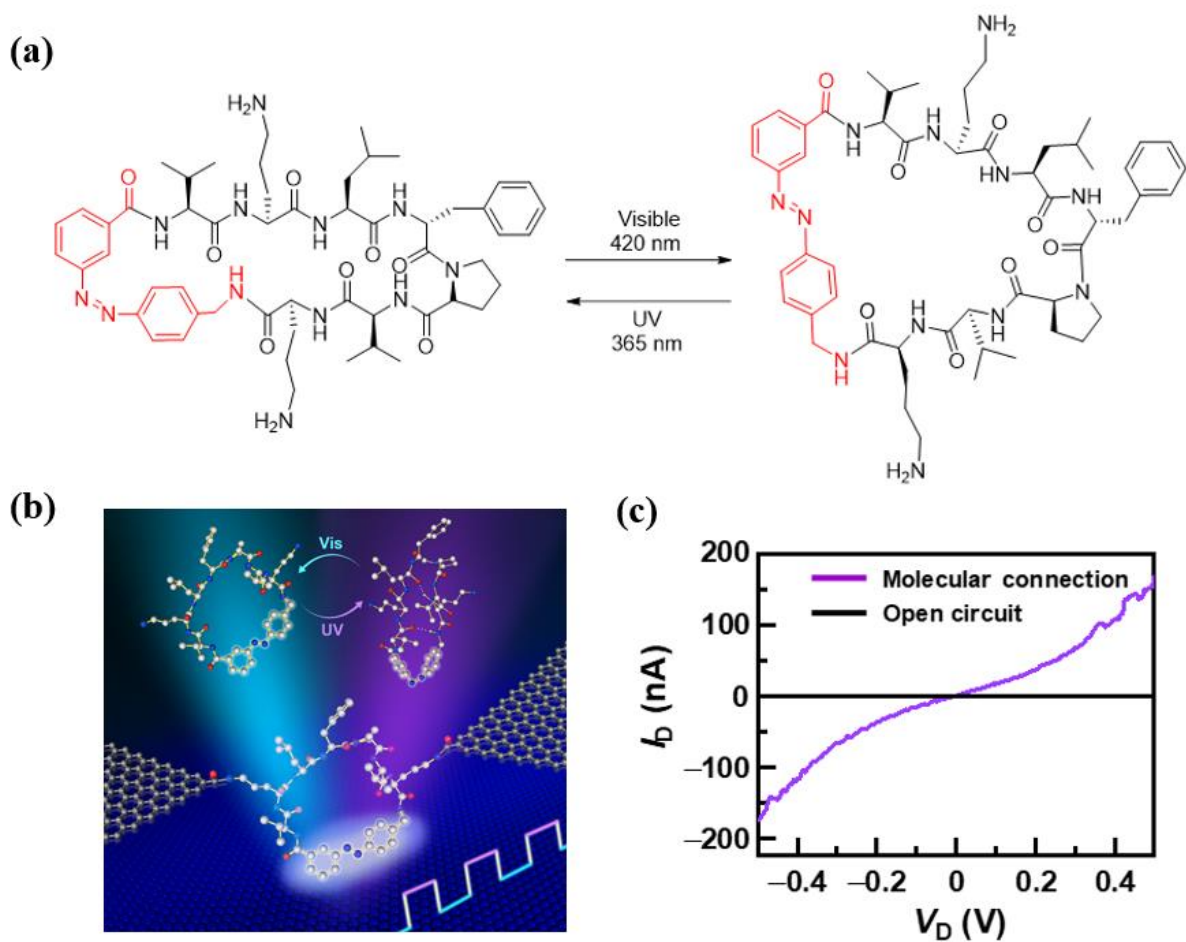


Figure 5.1. A graphene-molecule-graphene single-molecule junction (GMG-SMJ) containing a photoswitchable peptide. **(a)** Chemical structures of the *cis* (left) and *trans* (right) isomers of cyclic peptide **1** upon photoisomerization using light of a specific wavelength. The azobenzene photoswitch is highlighted in red. **(b)** Schematic representation of GMG-SMJ device. **(c)** Molecular connection test. Comparison of I - V curves for an open circuit (no connection, black) and molecular connection (purple), indicating the successful formation of the GMG-SMJ device.

5.3.2 Real-time conductance measurements for *cis* and *trans* isomers of cyclic peptide 1

To investigate the structural dynamics of cyclic peptide **1**, real-time conductance measurements were initially undertaken on the GMG-SMJ containing the *trans* isomer under dark conditions (Figure 5.2, *trans* 1). Within this conformation, a trimodal distribution was found, where the observed current fluctuated between three distinct states, as shown in Figures 5.3 and S5.4. A low conductance state (State 1) was found to be the most populated, while States 2 and 3 appeared like current spikes with moderate and high conductance, respectively. The resulting current-count histogram showed three Gaussian-type fitting peaks with occupancy rates of $90.9\% \pm 0.5\%$, $7.4\% \pm 0.4\%$, and $1.7\% \pm 0.6\%$, corresponding to States 1, 2, and 3, respectively, indicating that State 1 is dominant in the *trans* isomer (Figure 5.3a). Figure S5.6d clearly shows that the noise level emanating from the device itself was approximately 1 nA, however, the difference in current between each of the three conductance states was shown to be in the order of 10 nA. This is highlighted in Figure S5.4, which shows all three conductance states observed over different time periods. Hence, the lower occupancy rates for State 2 and State 3 for the *trans* isomer are not deemed to be random noise, as the observed current values can clearly be discriminated from the noise. Dwell times (τ) of each state were extracted using a hidden Markov model (Figure S5.7) with time intervals obtained from QuB software,²⁴ while the subsequent frequency analysis demonstrated typical single exponential functions. The corresponding dwell times of the low ($\tau_{\text{state 1}}$), moderate ($\tau_{\text{state 2}}$) and high ($\tau_{\text{state 3}}$) conductance states were 1.813 ± 0.083 ms, 0.073 ± 0.012 ms, and 0.094 ± 0.008 ms, respectively (Figure 5.3c). These data indicate that the *trans* isomer undergoes thermal fluctuations, resulting in these distinct variations in conductance.

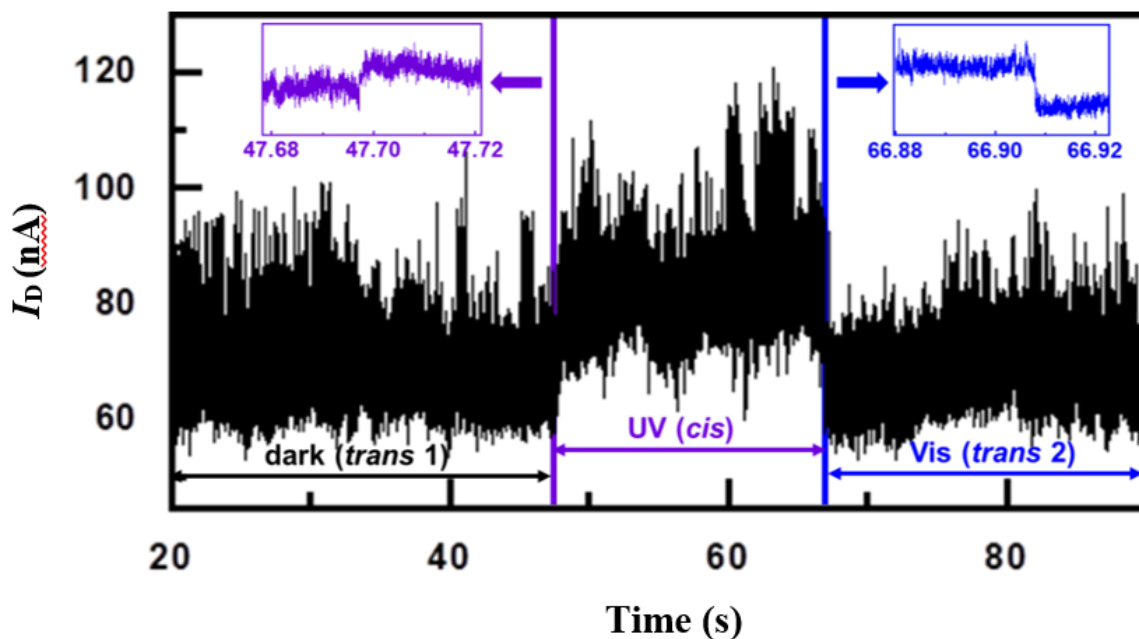


Figure 5.2. Real-time conductance measurements in a photoswitching cycle. Left: GMG-SMJ containing cyclic peptide **1** in its *trans* configuration (dark, *trans* 1), center: following UV irradiation (365 nm) to convert to the *cis* configuration (UV, *cis*), right: following Vis irradiation (420 nm) to convert to the *trans* configuration (Vis, *trans* 2). Insets: enlarged sections containing the relevant *I-t* curves upon UV irradiation (left, purple) and Vis irradiation (right, blue), showing instantaneous switching between isomers. $V_D = 0.2$ V, $V_G = 0$ V, and the sampling rate is 57.6 kSa/s.

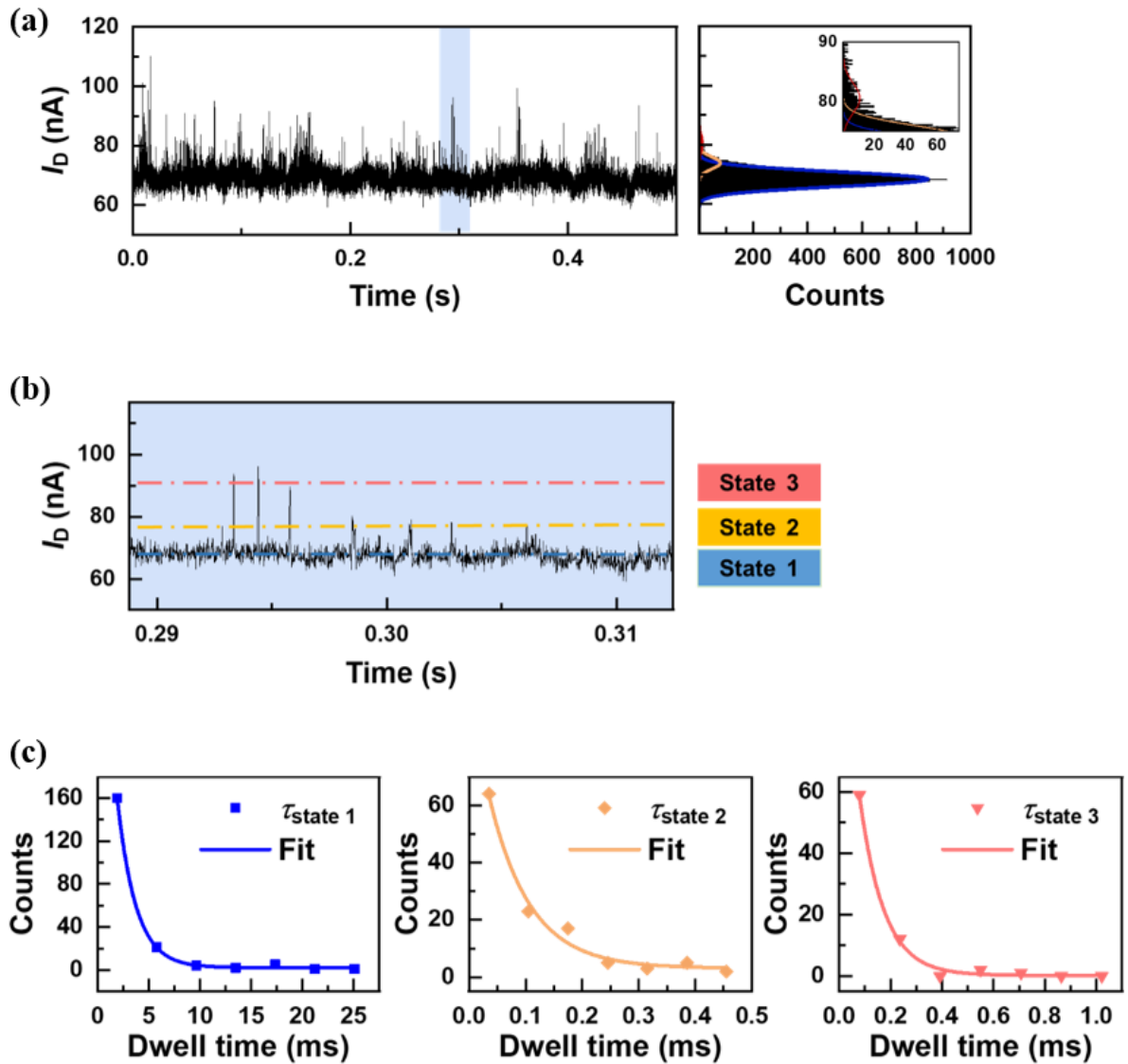


Figure 5.3. Real-time conductance measurements of GMG-SMJ (*trans* 1) under dark conditions with corresponding statistical analyses. **(a)** Representative I - t trajectories of the GMG-SMJ (*trans* 1) (left) with the corresponding histogram (right). Three conductance states are observed in the I - t trajectories. The analysis of the current-count histogram shows the highest occupancy rate for low conductance state (State 1, blue), then moderate conductance state (State 2, orange), and high conductance state (State 3, red). Inset: enlarged section for States 2 and 3. **(b)** Enlarged section of 5.3a showing conductance states 1-3. **(c)** Plots of time intervals for the low (left), moderate (center) and high (right) conductance states. Dwell times (τ) were extracted from the idealized fittings of I - t curves using QuB software as shown in the Supplementary Information (5.7.5 Kinetic analysis).

Upon irradiation using UV light (365 nm), the overall conductance increased instantaneously, indicating conversion to the *cis* isomer (Figure 5.2, purple inset). Detailed analysis of this dynamic process revealed that the real-time *I-t* measurements for the *cis* conformation also exhibited a trimodal current distribution, with occupancy rates of $14.3\% \pm 0.6\%$, $79.5\% \pm 0.7\%$, and $6.1\% \pm 2.4\%$ for the low, moderate, and high states, respectively (Figure 5.4). In contrast to the *trans* isomer, the most populated state in the *cis* isomer is the moderate conductance state (State 2). The dwell times of the three states were calculated to be $\tau_{\text{state 1}} 0.883 \pm 0.061$ ms, $\tau_{\text{state 2}} 1.067 \pm 0.086$ ms, and $\tau_{\text{state 3}} 0.063 \pm 0.002$ ms corresponding to the low, moderate and high conductance states, respectively (Figure 5.4c). The overall conductance, occupancy rates and dwell times found for the *cis* isomer are not comparable to those of the GMG-SMJ containing the *trans* isomer, indicating that these three conductance states are clearly not a consequence of photoconversion between the isomers. As the dwell times for each state were observed to occur on a submillisecond timescale, and photoisomerization of azobenzene is known to occur on a picosecond timescale,²⁵ the conductance changes could not solely originate from the azobenzene photoswitch. In addition, to demonstrate the reversible nature of the photoswitchable device, visible light (420 nm) was used to convert the peptide to the *trans* isomer (Figure 5.2, *trans* 2, blue inset). The conductance decreased instantaneously and essentially matched that of *trans* 1 (Figure S5.5). Covalent binding to the graphene electrodes did not appear to greatly affect the intrinsic properties of cyclic peptide **1**, with Figure S5.3 showing the ultrasensitive photoresponsive features that allow it to act as a light-triggered switch element. In support of the current fluctuations emanating from the photoresponse of the cyclic peptide and not from the graphene electrodes or the environment, control experiments on partially cleaved and totally cleaved graphene devices were carried out (Figure S5.6). Each control experiment exhibited only one Gaussian-type fitting peak for UV, visible light, and in dark conditions. The absence of current fluctuations from these controls indicates that UV/Vis light has no observable effect on the graphene device, and hence, does not influence our results. Overall, the high temporal resolution of real-time measurements demonstrates the presence of small structural perturbations within each conformation of cyclic peptide **1**. These perturbations within each isomer may result from a negligible free energy barrier or the absence thereof, brought about by subtle movement of the peptide backbone,²⁶ and could provide vital information on their structural dynamics. Furthermore, the increase in conductance following UV irradiation is attributed to the distinctive β -sheet secondary structure of the *cis* isomer, which is stabilized by intramolecular hydrogen bonds. In our previous study,²⁷ it was reported that the formation and

deformation of hydrogen bonds occur on a submillisecond timescale in GMG-SMJs. As we observed the conductance to fluctuate between the three states of the *cis* GMG-SMJ on a submillisecond timescale (Figure 5.4), we postulate they are a direct consequence of the dynamic structural fluctuations that affect intramolecular hydrogen bonding. However, detailed computational studies are required to support these notions, and will be discussed in the following section.

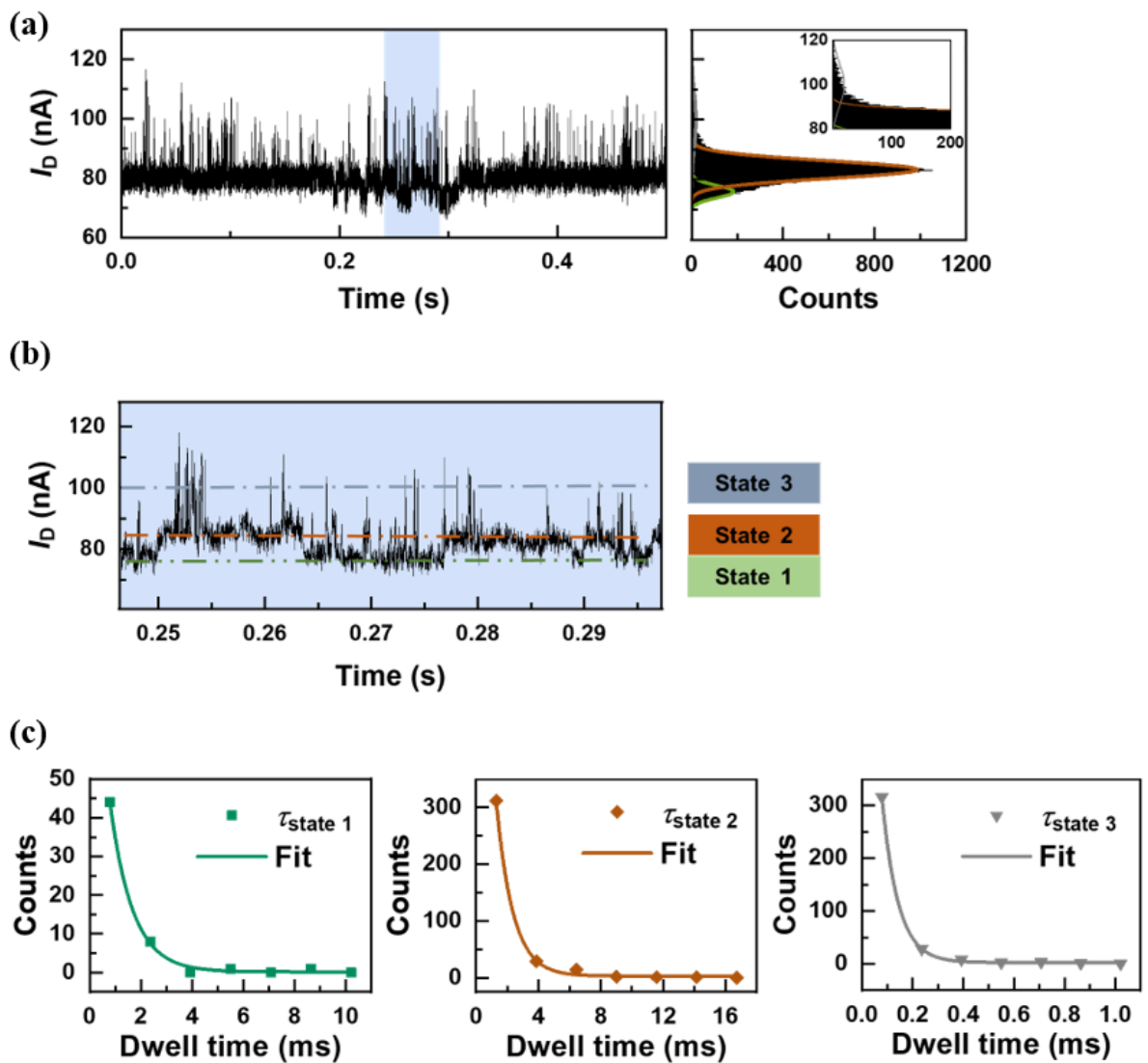


Figure 5.4. Real-time conductance measurements of GMG-SMJ (*cis*) under UV conditions with corresponding statistical analyses. **(a)** Representative $I-t$ trajectories of the GMG-SMJ (*cis*) (left) with the corresponding histogram (right). Three conductance states are observed in the $I-t$ trajectories. The analysis of the current-count histogram shows the highest occupancy rate for the moderate conductance state (State 2, orange), then low conductance state (State 1, green), and high conductance state (State 3, grey). Inset: enlarged section for State 3. **(b)** Enlarged section of 5.4a showing conductance states 1-3. **(c)** Plots of time intervals for the low (left), moderate (center) and high (right) conductance states. Dwell times (τ) were extracted from the idealized fittings of $I-t$ curves using QuB software as shown in the Supplementary Information (5.7.5 Kinetic analysis).

5.3.3 Molecular dynamics (MD) simulations of GMG-SMJ

MD simulations were conducted to gain further insights into the observed structural dynamics of the GMG-SMJ. The representative snapshots of the *cis* and *trans* GMG-SMJs (Figure S5.10) during the course of simulations were chosen by the hieragglo algorithm-based cluster analysis using the root-mean-square (RMS) of the carbon atoms in the peptide backbone and azobenzene moiety. This was undertaken as the average frame derived from an MD run is commonly ill-defined and does not represent an appropriate chemical structure. Quantum transport simulations using DFT in conjunction with non-equilibrium Green's function (NEGF) were then performed to elucidate the difference in electronic conductance between these *cis* and *trans* GMG-SMJ snapshots. It was found that the *cis* GMG-SMJ possessed a zero-bias transmission coefficient of $3.0 \times 10^{-12} G_0$ at the Fermi level (red curve, Figure S5.10a), approximately two orders of magnitude higher than the *trans* GMG-SMJ ($1.0 \times 10^{-14} G_0$, black curve). Importantly, this trend is consistent with experimental observations (Figures 5.2 and S5.3). It is worth mentioning that we cannot make a direct comparison between the calculated transmission and the measured conductance, as coherent charge transport²⁸⁻²⁹ and electrodes of finite cross section³⁰⁻³¹ were employed in the conductance calculations, while other incoherent processes³²⁻³⁴ such as hopping may contribute to the conductance measurements. The Molecular Projected Self-consistent Hamiltonian (MPSH) states of the *cis* GMG-SMJ (Figure S5.12) exhibit a HOMO-LUMO energy gap of ~ 0.612 eV, while an increased HOMO-LUMO energy gap of ~ 0.688 eV is given for the *trans* GMG-SMJ. Notably, the LUMO (Figure S5.12) in both GMG-SMJs is localized on one of the electrodes, while the HOMO is distributed on the molecule, residing on the azobenzene moiety for the *trans* isomer, and the peptide backbone for the *cis* isomer. This indicates different roles for azobenzene and the peptide backbone in determining transmission conductance of the *cis* and *trans* isomers. Further transmission eigenchannel analysis for the *cis* GMG-SMJ showed a continuous and well-spanned electron density distribution across the entire junction (Figure S5.10b), indicating a higher conductance than its *trans* counterpart. The higher conductance in the *cis* GMG-SMJ is defined by the overlapping atomic orbitals from the peptide backbone, azobenzene moiety, and intramolecular hydrogen bonding (Figure S5.10b). In contrast, the *trans* GMG-SMJ exhibited a discontinuous conduction channel (Figure S5.10c), with the electron density predominantly localized on the azobenzene moiety, thus resulting in an overall lower conductance. This result, together with the frontier

MPSH states, indicates that the π -conjugated *trans* azobenzene plane plays a critical role in formulating the GMG-SMJ transmission eigenchannel (Figure S5.10c).

Hence, the MD simulation for the *trans* GMG-SMJ was further analyzed by the cluster analysis method using the dihedral angle (φ) between the azobenzene and graphene planes. The dihedral angle is defined by six carbon atoms. Three of these were selected from the right-hand side electrode to determine the graphene plane, while the azobenzene plane is defined by the other three atoms; two from the moiety and one from the peptide/graphene contacting region indicated in Figures 5.5a-b. The corresponding histogram of dihedral angles is depicted in Figure 5.5c, and the representative snapshots for each cluster were subjected to quantum transport calculations. It was found that the computed conductance oscillated in a wave form following the change in the dihedral angle (Figure 5.5d). Clearly, three computed conductance states (States 1-3) were identified, which are consistent with the real-time experimental conductance measurements (Figure 5.3), where the *trans* isomer predominantly resides in the low conductance state (State 1), with a lower population evident for moderate and high conductance states. Specifically, the computed low conductance state (State 1, green dashed line, Figure 5.5d) spans a broad range of dihedral angles and has the highest occupancy rate of $\sim 47.6\%$ (Table S5.3), with $\varphi \approx 25^\circ$ being the predominant species (green band, Figure 5.5c). The computed transmission eigenchannel for the selected device snapshot (State 1, Figure 5.5e) displays a discontinuous conduction channel with much lower electron density. The moderate conductance state (State 2, orange band, Figure 5.5c) was found at $\varphi \approx -50^\circ$ and 40° , showing the second highest occupancy rate of $\sim 28.6\%$ (Table S5.3 and Figure 5.5f), while the high conductance state (State 3, blue dashed line) was found at $\varphi \approx 0^\circ$, with the lowest occupancy rate of $\sim 23.8\%$ (blue band, Figure 5.5c and Table S5.3). This dihedral angle ($\varphi \approx 0^\circ$) allows for a better π electron alignment between the *trans* azobenzene plane and graphene electrodes, thus promoting electronic coupling between the azobenzene and the electrodes. This is evidenced by the transmission eigenchannel (Figure 5.5g), which shows a well-spanned conductive channel with high electron density, predominantly localized on the azobenzene moiety. However, this conformation induces such a large distortion in each of the ornithine side chains, resulting in the lowest occupancy rate. The simulated conductance states and their corresponding occupancy rates concur with the real-time conductance measurements, providing clear theoretical evidence to interpret the experimental observations. Hence, these MD simulations revealed that φ is

crucial for modulating conductance within the three discrete states found in the *trans* GMG-SMJ. While the occupancy rate is predominantly in the low conductance state for the *trans* isomer, MD simulations have shown that it can also experience higher conductance, depending on the specific orientation of the peptide within the GMG-SMJ. Notably, such variations in the dihedral angles amount to modulation of the conductance within each discrete state. The oscillation of conductance observed in Figure 5.5d suggests that the inherent flexibility of the *trans* isomer efficiently provides direct access to each conductance state over a wide and diverse range, depending on the orientation of the peptide. This structural dynamic behavior may potentially extend to intrinsically disordered proteins, where such structural plasticity may influence transient interactions that are readily broken and reformed, such as cellular signaling.

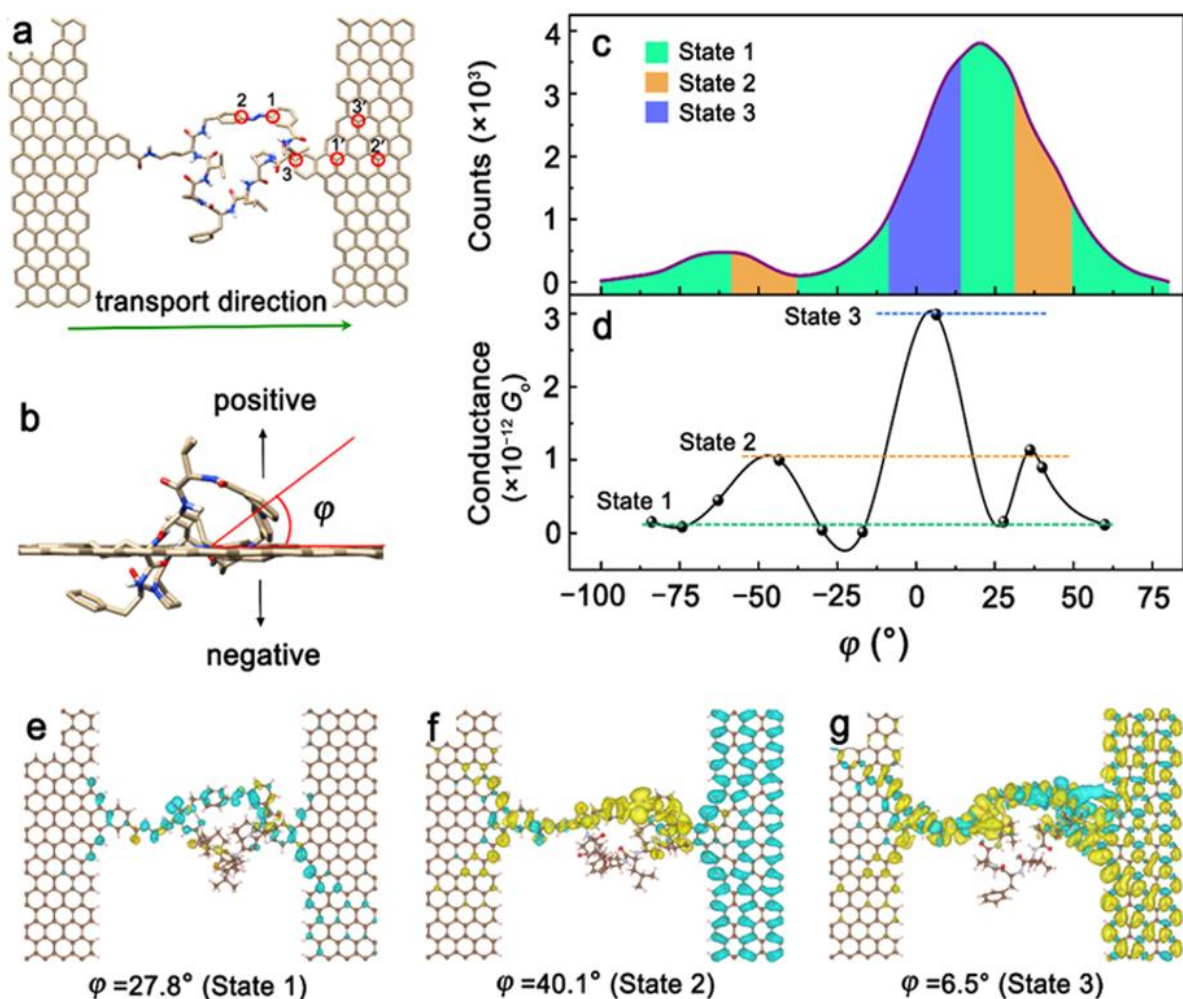


Figure 5.5. Conductance analyses for the *trans* GMG-SMJ MD simulation. (a) Top view and (b) side view of the dihedral angle (ϕ) between the azobenzene and graphene planes as defined by three atoms from each. (c) Histogram (curve) of dihedral angles over the course of MD simulation, and corresponding attribution (coloured bands) to the conductance states (green band = low conductance state, orange = moderate, blue = high). (d) Dependence of computed conductance on dihedral angles for the selected *trans* GMG-SMJ snapshots. (e–g) Computed eigenchannels of the selected GMG-SMJ snapshots with their respective dihedral angles indicated, representing the three conductance states.

MD simulations showed that the *cis* isomer adopts a well-defined β -sheet secondary structure maintained by two intramolecular hydrogen bonds. Hydrogen bonding has been shown to play a significant role in electronic transport within peptides.³⁵⁻³⁶ There are three possible factors affecting the conductance in the *cis* GMG-SMJ as evidenced in Figure S5.10b, namely (i) dihedral angle (ϕ) between the azobenzene moiety and electrode plane, (ii) hydrogen bond 1

distance (d_1), and (iii) hydrogen bond 2 distance (d_2) (Figure 5.6a). Hydrogen bond d_1 is defined by the CO (Leu) – NH (Orn) distance, while d_2 is defined by the CO (Val) – NH (Azo) distance. The *cis* GMG-SMJ MD trajectory was further analyzed by the cluster analysis method utilizing these three factors. In order to investigate one factor in isolation from the other two variables, representative snapshots were chosen for one, while keeping the other two parameters relatively constant. The subsequent quantum transport simulations revealed that changes in either φ or d_2 do not lead to a noticeable change in the computed conductance of the *cis* GMG-SMJ (Figure S5.13), whereas d_1 was found to be critical in determining conductance (Figure 5.6b). The computed conductance values are $4.5 \times 10^{-11} G_0$ and $4.4 \times 10^{-12} G_0$ for $d_1 = 1.76 \text{ \AA}$ and 1.85 \AA respectively, while a further drop in conductance to $10^{-13} G_0$ was experienced when d_1 is greater than 2.10 \AA (Figure 5.6b). The three distinct conductance states representative of d_1 shown in Figures 5.6d-f are: 1.76 \AA (high), 1.85 \AA (moderate), and 2.21 \AA (low). It was determined that the moderate conductance state (State 2) with d_1 between $1.80 - 2.10 \text{ \AA}$ was the predominant species (orange band, Figure 5.6c). Occupancy rates of $\sim 28.4\%$, $\sim 65.9\%$, and $\sim 5.7\%$ were found for the low, moderate, and high conductance state (States 1–3) respectively (Table S5.4 and Figure 5.6c), which also correspond with the experimental real-time measurements for the *cis* isomer (Figure 5.4). These three conductance states remarkably coincide with the fluctuations in d_1 as revealed by MD, thus confirming that d_1 is directly correlated to conductance. While the dihedral angle (φ) is crucial to the conductance in the *trans* isomer, virtually no change in conductance was found when φ is between -60 and 60 degrees in the *cis* isomer (Figure S5.13), suggesting that flexibility is not such a critical factor here. In contrast to the more flexible *trans* isomer, significant changes in conductance in the *cis* isomer can occur through the smallest of structural dynamic perturbations (sub-angstrom) within d_1 . Thus, the structural dynamic properties revealed in d_1 provide new opportunities to modulate conductance within the well-defined *cis* isomer.

Despite the snapshot $d_1 = 2.21 \text{ \AA}$ representing a strong hydrogen bond,³⁷ it lies in the low conductance state (State 1). It is noteworthy that Figure 5.6b shows two additional data points, $d_1 = 2.60 \text{ \AA}$ (moderate hydrogen bond strength) and $d_1 = 3.80 \text{ \AA}$ (weak hydrogen bond strength), that are also located in the low conductance state. However, when d_1 is less than 2.10 \AA , the conductance increased exponentially to State 2 (moderate) and State 3 (high). These results may provide support for further investigation into the definition and interpretation of hydrogen bond

strengths within a well-defined secondary structure. Collectively, this work goes beyond transducing the hydrogen bond dynamic process into real-time electronic signals, and indeed correlates the hydrogen bond lengths with their associated conductance states. These structural dynamic properties observed within d_1 of the *cis* isomer with single-bond resolution, provide crucial insights into the structural dynamic behavior of proteins that contain well-defined intramolecular hydrogen bonds needed to stabilize secondary structure.

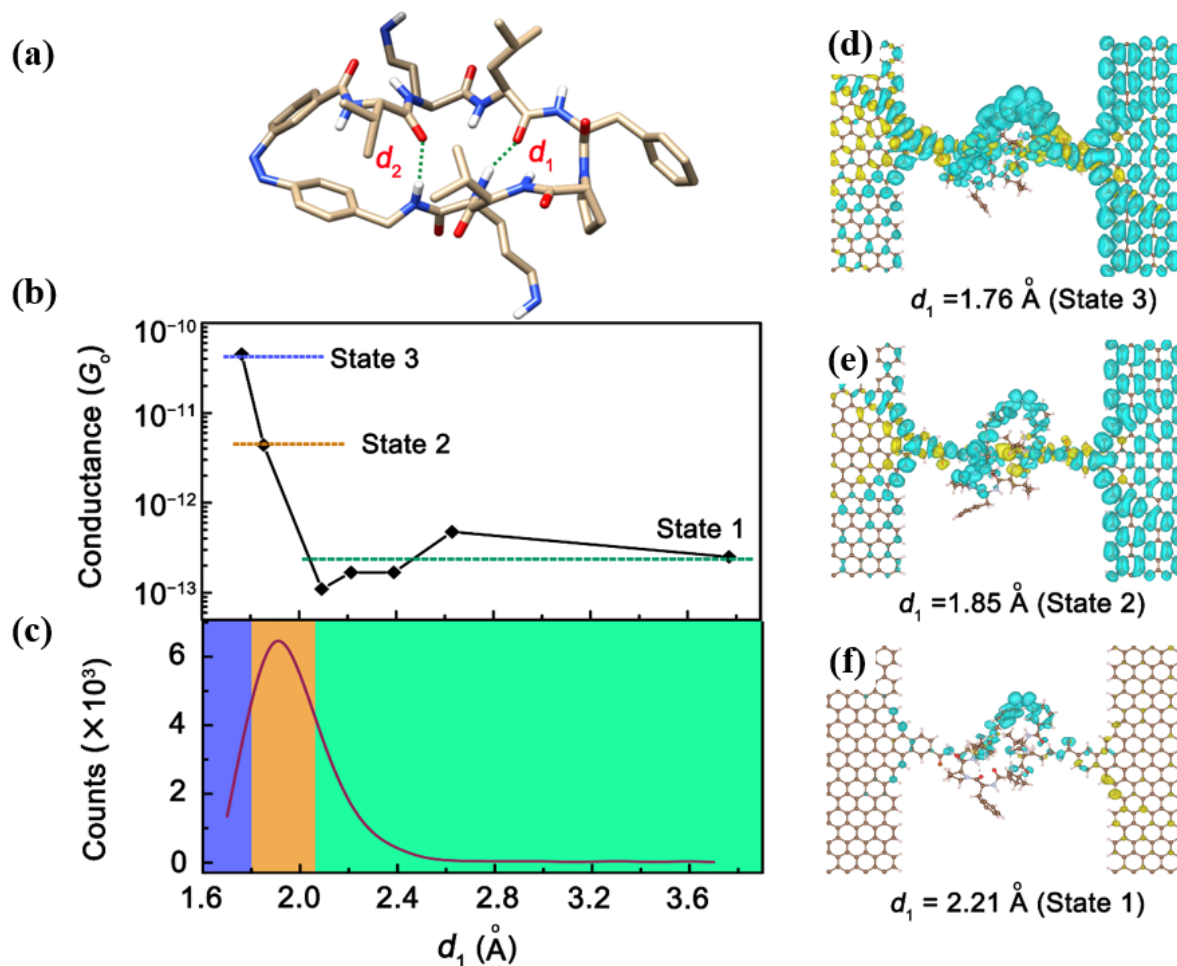


Figure 5.6. Conductance analyses for the *cis* GMG-SMJ MD simulation. **(a)** Image of hydrogen bond 1 (d_1) and hydrogen bond 2 (d_2). **(b)** Dependence of computed conductance on d_1 distance. **(c)** Histogram (curve) of d_1 over the course of MD simulation, and corresponding attribution (coloured bands) to the conductance states. **(d–f)** Computed eigenchannels of the selected snapshots representing the low conductance state (State 1), moderate (State 2), and high (State 3).

5.4 Conclusion

Conductance measurements on a GMG-SMJ containing the photoswitchable cyclic peptide **1** revealed two distinct conformations, with an overall higher conductance observed in the *cis* isomer than for its *trans* counterpart, which is consistent with our MD simulations. This single-molecule electronic device has established itself as a robust platform to unravel the structural dynamic properties of peptides at the molecular level. For the first time, we have unveiled three distinct conductance states which remarkably correlate to various unique structural dynamic properties within each isomer. Not only have we demonstrated modulation of conductance within this device using light, but also revealed that perturbations within both the well-defined and intrinsically disordered isomers of cyclic peptide **1** (structural dynamics) provide further capacity to manipulate conductance with precise spatial control and high temporal resolution. The *trans* isomer of cyclic peptide **1** was shown to possess a disordered configuration, while the *cis* isomer was found to contain a well-defined β -sheet secondary structure. Hence, by studying these two distinctly different isomers within the one single-peptide, we have been able to provide hitherto undisclosed fundamental insights into their unique structural dynamic behavior, which may rationally extend to both intrinsically disordered proteins and those containing a well-defined secondary structure. This capacity to modulate conductance within peptides paves the way for the future design of multi-modal nanodevices with practical applications in areas such as biosensing, where such bio-inspired molecular components offer a greener approach for the advancement of these technologies.

5.5 Acknowledgements

We acknowledge the National Key R&D Program of China (2017YFA0204901), the National Natural Science Foundation of China (21727806 and 21933001), the Natural Science Foundation of Beijing (Z181100004418003), the Australian Research Council (ARC) Discovery Project (DP180101581), the Centre of Excellence for Nanoscale BioPhotonics (CE140100003), Applied Basic Research Program of Shanxi Province (201701D221046), and Doctoral Scientific Research Foundation and Innovation Team Project of Changzhi Medical College (BS15014, CX201904) for financial support. We also acknowledge the Australian National Fabrication Facility for providing the analytical facilities used in this work. Computational aspects of this work were supported by an award under National Computational Merit Allocation Scheme for J.Y. on National Computing Infrastructure (NCI) at Australian National University and Pawsey Supercomputing Centre in Western Australia.

5.6 References

1. Vinson, V. J., Proteins in Motion. *Science* **2009**, *324* (5924), 197.
2. Radivojac, P.; Iakoucheva, L. M.; Oldfield, C. J.; Obradovic, Z.; Uversky, V. N.; Dunker, A. K., Intrinsic disorder and functional proteomics. *Biophys. J.* **2007**, *92* (5), 1439–1456.
3. Horsley, J. R.; Yu, J. X.; Wegener, K. L.; Hoppmann, C.; Ruck-Braun, K.; Abell, A. D., Photoswitchable peptide-based 'on-off' biosensor for electrochemical detection and control of protein-protein interactions. *Biosens. Bioelectron.* **2018**, *118*, 188–194.
4. Babu, M. M.; van der Lee, R.; de Groot, N. S.; Gsponer, J., Intrinsically disordered proteins: regulation and disease. *Curr. Opin. Struct. Biol.* **2011**, *21* (3), 432–440.
5. Dyson, H. J.; Wright, P. E., Intrinsically unstructured proteins and their functions. *Nat. Rev. Mol. Cell Bio.* **2005**, *6* (3), 197–208.
6. Nyqvist, I.; Dogan, J., Characterization of the dynamics and the conformational entropy in the binding between TAZ1 and CTAD-HIF-1 α . *Sci Rep-Uk* **2019**, *9* (1), 16557.
7. Samuni, U.; Friedman, J. M., Proteins in Motion. In *Protein-Ligand Interactions: Methods and Applications*, Nienhaus, G. U., Ed. Humana Press Inc: New Jersey, USA, 2005, pp 287–300.
8. Henzler-Wildman, K.; Kern, D., Dynamic personalities of proteins. *Nature* **2007**, *450* (7172), 964–972.
9. Guo, C.; Yu, X.; Refaely-Abramson, S.; Sepunaru, L.; Bendikov, T.; Pecht, I.; Kronik, L.; Vilan, A.; Sheves, M.; Cahen, D., Tuning electronic transport via hepta-alanine peptides junction by tryptophan doping. *Proc. Natl. Acad. Sci. USA* **2016**, *113* (39), 10785.
10. Xiao, X.; Xu, B.; Tao, N., Changes in the Conductance of Single Peptide Molecules upon Metal-Ion Binding. *Angew. Chem. Int. Ed.* **2004**, *43* (45), 6148–6152.
11. Yu, J. X.; Horsley, J. R.; Abell, A. D., Peptides as Bio-Inspired Electronic Materials: An Electrochemical and First-Principles Perspective. *Acc. Chem. Res.* **2018**, *51* (9), 2237–2246.
12. Yeoh, Y. Q.; Yu, J. X.; Polyak, S. W.; Horsley, J. R.; Abell, A. D., Photopharmacological control of cyclic antimicrobial peptides. *ChemBioChem* **2018**, *19* (24), 2591–2597.
13. Gu, C. H.; Hu, C.; Wei, Y.; Lin, D. Q.; Jia, C. C.; Li, M. Z.; Su, D. K.; Guan, J. X.; Xia, A. D.; Xie, L. H.; Nitzan, A.; Guo, H.; Guo, X. F., Label-free dynamic detection of single-molecule nucleophilic-substitution reactions. *Nano Lett.* **2018**, *18* (7), 4156–4162.

14. Jia, C. C.; Migliore, A.; Xin, N.; Huang, S. Y.; Wang, J. Y.; Yang, Q.; Wang, S. P.; Chen, H. L.; Wang, D. M.; Feng, B. Y.; Liu, Z. R.; Zhang, G. Y.; Qu, D. H.; Tian, H.; Ratner, M. A.; Xu, H. Q.; Nitzan, A.; Guo, X. F., Covalently bonded single-molecule junctions with stable and reversible photoswitched conductivity. *Science* **2016**, *352* (6292), 1443–1445.
15. Xin, N.; Li, X. X.; Jia, C. C.; Gong, Y.; Li, M. L.; Wang, S. P.; Zhang, G. Y.; Yang, J. L.; Guo, X. F., Tuning charge transport in aromatic-ring single-molecule junctions via ionic-liquid gating. *Angew. Chem. Int. Ed.* **2018**, *57* (43), 14026–14031.
16. Cao, Y.; Dong, S. H.; Liu, S.; He, L.; Gan, L.; Yu, X. M.; Steigerwald, M. L.; Wu, X. S.; Liu, Z. F.; Guo, X. F., Building High-Throughput Molecular Junctions Using Indented Graphene Point Contacts. *Angew. Chem. Int. Ed.* **2012**, *51* (49), 12228–12232.
17. Gu, C. H.; Jia, C. C.; Guo, X. F., Single-molecule electrical detection with real-time label-free capability and ultrasensitivity. *Small Methods* **2017**, *1* (5), 1700071.
18. Hedegaard, S. F.; Derbas, M. S.; Lind, T. K.; Kasimova, M. R.; Christensen, M. V.; Michaelsen, M. H.; Campbell, R. A.; Jorgensen, L.; Franzyk, H.; Cardenas, M.; Nielsen, H. M., Fluorophore labeling of a cell-penetrating peptide significantly alters the mode and degree of biomembrane interaction. *Sci Rep-Uk* **2018**, *8*, 6327.
19. Liu, J.; Huang, X.; Wang, F.; Hong, W., Quantum Interference Effects in Charge Transport through Single-Molecule Junctions: Detection, Manipulation, and Application. *Acc. Chem. Res.* **2019**, *52* (1), 151–160.
20. Zhang, B. T.; Song, W. S.; Pang, P.; Zhao, Y. N.; Zhang, P. M.; Csabai, I.; Vattay, G.; Lindsay, S., Observation of giant conductance fluctuations in a protein. *Nano Futures* **2017**, *1* (3), 035002.
21. Xia, S. H.; Cui, G.; Fang, W.H.; Thiel, W., How Photoisomerization Drives Peptide Folding and Unfolding: Insights from QM/MM and MM Dynamics Simulations. *Angew. Chem. Int. Ed.* **2016**, *55* (6), 2067–2072.
22. Zhang, F. Z.; Zarrine-Afsar, A.; Al-Abdul-Wahid, M. S.; Prosser, R. S.; Davidson, A. R.; Woolley, G. A., Structure-Based Approach to the Photocontrol of Protein Folding. *J. Am. Chem. Soc.* **2009**, *131* (6), 2283–2289.
23. Ihalainen, J. A.; Bredenbeck, J.; Pfister, R.; Helbing, J.; Chi, L.; van Stokkum, I. H. M.; Woolley, G. A.; Hamm, P., Folding and unfolding of a photoswitchable peptide from picoseconds to microseconds. *Proc. Natl. Acad. Sci. USA* **2007**, *104* (13), 5383–5388.
24. Nicolai, C.; Sachs, F., Solving ion channel kinetics with the QuB software. *Biophys. Rev. Lett.* **2013**, *8*, 191–211.

25. Bandara, H. M. D.; Burdette, S. C., *Chem. Soc. Rev.* **2012**, *41*, 1809–1825.
26. Schlag, E. W.; Sheu, S.-Y.; Yang, D.-Y.; Selzle, H. L.; Lin, S. H., Distal Charge Transport in Peptides. *Angew. Chem. Int. Ed.* **2007**, *46* (18), 3196–3210.
27. Zhou, C.; Li, X. X.; Gong, Z. L.; Jia, C. C.; Lin, Y. W.; Gu, C. H.; He, G.; Zhong, Y. W.; Yang, J. L.; Guo, X. F., Direct observation of single-molecule hydrogen-bond dynamics with single-bond resolution. *Nat. Commun.* **2018**, *9*, 807.
28. Imry, Y.; Landauer, R., Conductance viewed as transmission. *Rev. Mod. Phys.* **1999**, *71* (2), S306–S312.
29. Papior, N.; Lorente, N.; Frederiksen, T.; García, A.; Brandbyge, M., Improvements on non-equilibrium and transport Green function techniques: The next-generation transiesta. *Comput. Phys. Commun.* **2017**, *212*, 8–24.
30. Li, Z. H.; Smeu, M.; Afsari, S.; Xing, Y. J.; Ratner, M. A.; Borguet, E., Single-Molecule Sensing of Environmental pH-an STM Break Junction and NEGF-DFT Approach. *Angew. Chem. Int. Ed.* **2014**, *53* (4), 1098–1102.
31. Horsley, J. R.; Yu, J.; Abell, A. D., The Correlation of Electrochemical Measurements and Molecular Junction Conductance Simulations in β -Strand Peptides. *Chem. Eur. J.* **2015**, *21* (15), 5926–5933.
32. Berritta, M.; Manrique, D. Z.; Lambert, C. J., Interplay between quantum interference and conformational fluctuations in single-molecule break junctions. *Nanoscale* **2015**, *7* (3), 1096–1101.
33. Schosser, W. M.; Zotti, L. A.; Cuevas, J. C.; Pauly, F., Doping hepta-alanine with tryptophan: A theoretical study of its effect on the electrical conductance of peptide-based single-molecule junctions. *J. Chem. Phys.* **2019**, *150* (17), 174705.
34. Yu, J.; Horsley, J. R.; Abell, A. D., Exploiting the interplay of quantum interference and backbone rigidity on electronic transport in peptides: a step towards bio-inspired quantum interferometers. *Mol. Syst. Des. Eng.* **2017**, *2* (1), 67–77.
35. Arikuma, Y.; Takeda, K.; Morita, T.; Ohmae, M.; Kimura, S., Linker Effects on Monolayer Formation and Long-Range Electron Transfer in Helical Peptide Monolayers. *J. Phys. Chem. B* **2009**, *113* (18), 6256–6266.
36. Shah, A.; Adhikari, B.; Martic, S.; Munir, A.; Shahzad, S.; Ahmad, K.; Kraatz, H.-B., Electron transfer in peptides. *Chem. Soc. Rev.* **2015**, *44* (4), 1015–1027.
37. MacLeod, J. M.; Rosei, F., *Directed Assembly of Nanostructures. Comprehensive Nanoscience and Technology*. Academic Press, Cambridge: 2011.

5.7 Supplementary Information

5.7.1 Device fabrication and molecular connection

The high-quality single-layered graphene was grown by chemical vapor deposition (CVD) on copper foils. The graphene films were then transferred onto the SiO₂/Si wafers (300 nm silicon oxide) by wet etching. The source/drain metal electrode (8 nm Cr/60 nm Au) arrays were patterned by three steps of lithography and two steps of thermal evaporation. The nanogapped graphene electrode arrays were constructed by the electron beam lithography (EBL), followed by oxygen plasma etching to functionalize the graphene point contacts with carboxylic acid groups (Figure S5.1). For the molecular linkage, the cyclic peptide (1.0 mg, 0.98 μmol) was coupled onto the carboxylic acid groups on the graphene point contacts via amide bond using 1-ethyl-3-(3-dimethylaminopropyl) carbodiimide (EDCI) (10 mg, 52 μmol), a well-known carbodiimide dehydrating/activating agent, in pyridine (10 mL) for 48h in the dark. After reaction, the device was removed from the solution, rinsed with deionized water and acetone for several times, and dried under a N₂ stream.

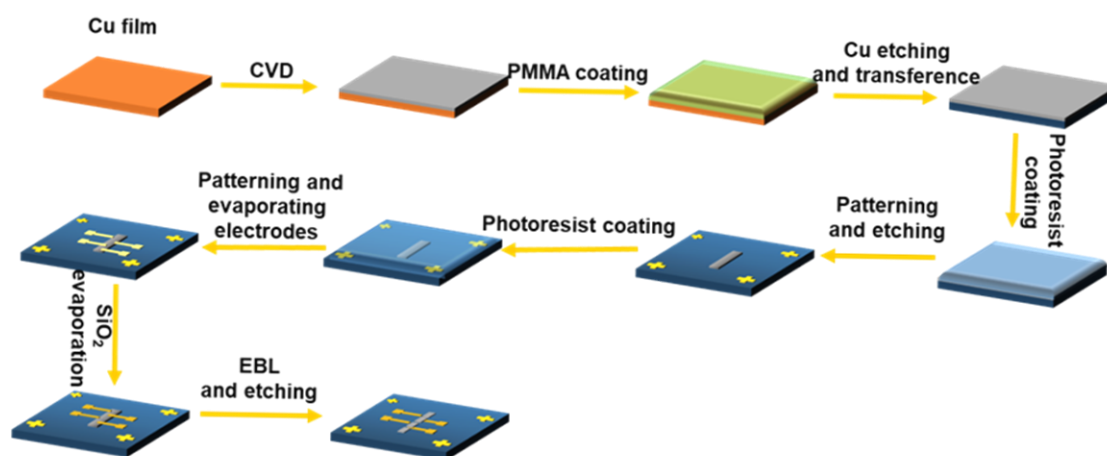


Figure S5.1. Schematic diagram for the device fabrication procedure.

5.7.2 Probability analysis of single-molecule connection

A theoretical analysis was performed to predict the number of junctions contributing to the charge transport, as shown in previous studies.¹⁻² The probability of connected devices with n -rejoined junctions, G_n was calculated using a binomial distribution as shown in (1) and optimized connection yields, $Y_{\text{connection}}$ as shown in (2):

$$G_n = \frac{m!}{n!(m-n)!} p^n (1-p)^{m-n} \quad n = 0, 1, 2, \dots, m \quad (1)$$

$$Y_{\text{connection}} = 1 - G_0 = 1 - \frac{m!}{0!(m-0)!} p^0 (1-p)^m \quad (2)$$

where m is the number of graphene contacts (169 in current pattern) and p is the probability of successful connection for each junction.

The device is conductive if there are one or more molecules connected to the junction. Peptide coupling to the nanogapped point contacts under optimized conditions yielded successful connection rate of ~2%, which meant that G_0 was 0.98. Thus, the ratio of single-molecule junction devices to the overall reconnected devices was expressed as $G_1/2\%$, which was estimated to be 98.99%. This indicated that there was only one molecule in the junction that contributed to the conductivity in most cases.

5.7.3 Experimental Results

5.7.3.1 Electrical measurements of single-molecule junctions

I - V measurements were carried out by utilizing an Agilent 4155C semiconductor characterization system with a scanning interval of 0.05 V per step. The real-time measurements of the device were carried out by a Karl Suss (PM5) manual probe station. The electrical signals were collected and exhibited by an HF2LI Lock-In Amplifier, a DL 1211 Current Amplifier, and a NIDAQ card, with a sampling rate of 57.6kSa/s and a bias voltage of 0.2 V. Each measurement was performed at room temperature under ambient conditions. The test system was equipped with an electric shield to ensure that any possible external disturbance would not affect the conductance properties of the device.

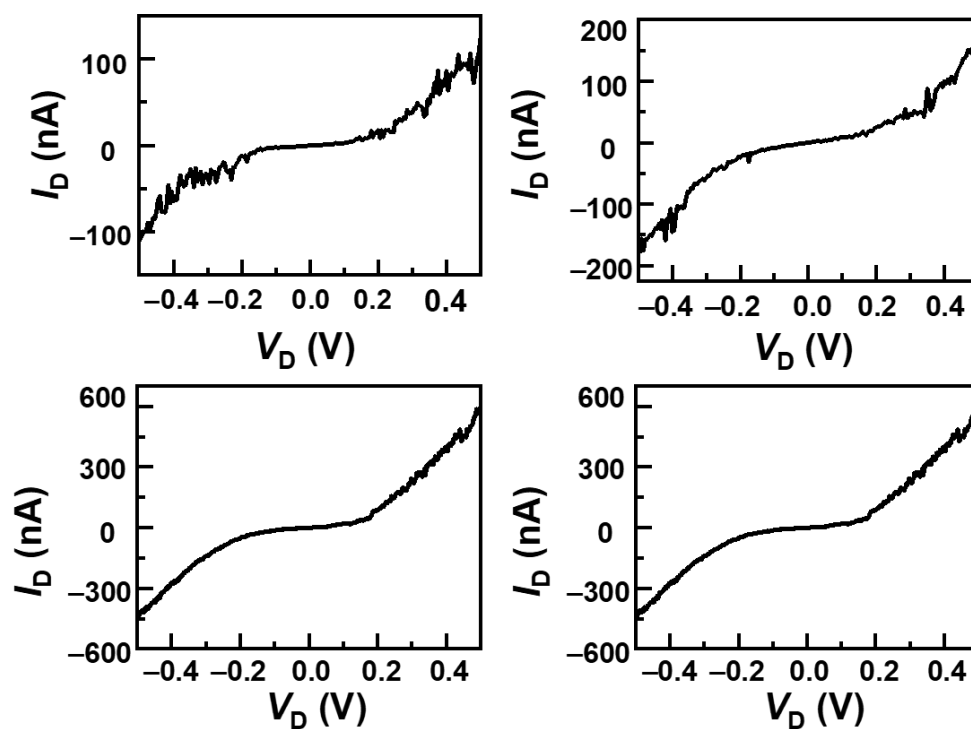


Figure S5.2. I - V curves of four different graphene-molecule-graphene single-molecule junctions (GMG-SMJs). The gate voltage was 0 V.

5.7.3.2 Reproducibility of the photoswitching process in single-molecule junctions

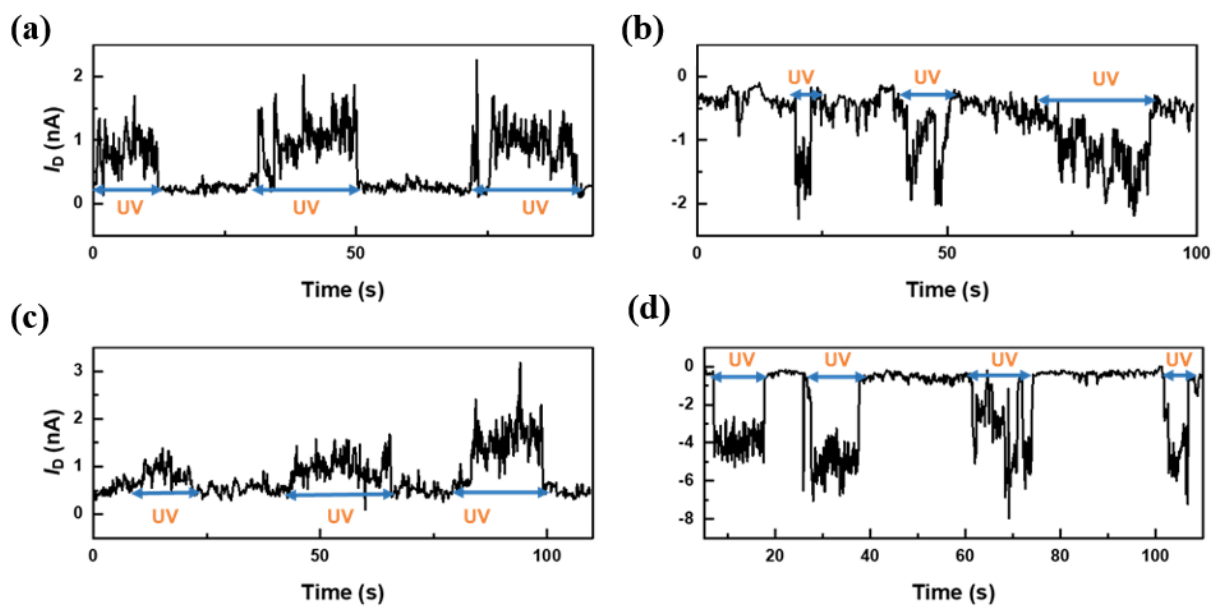
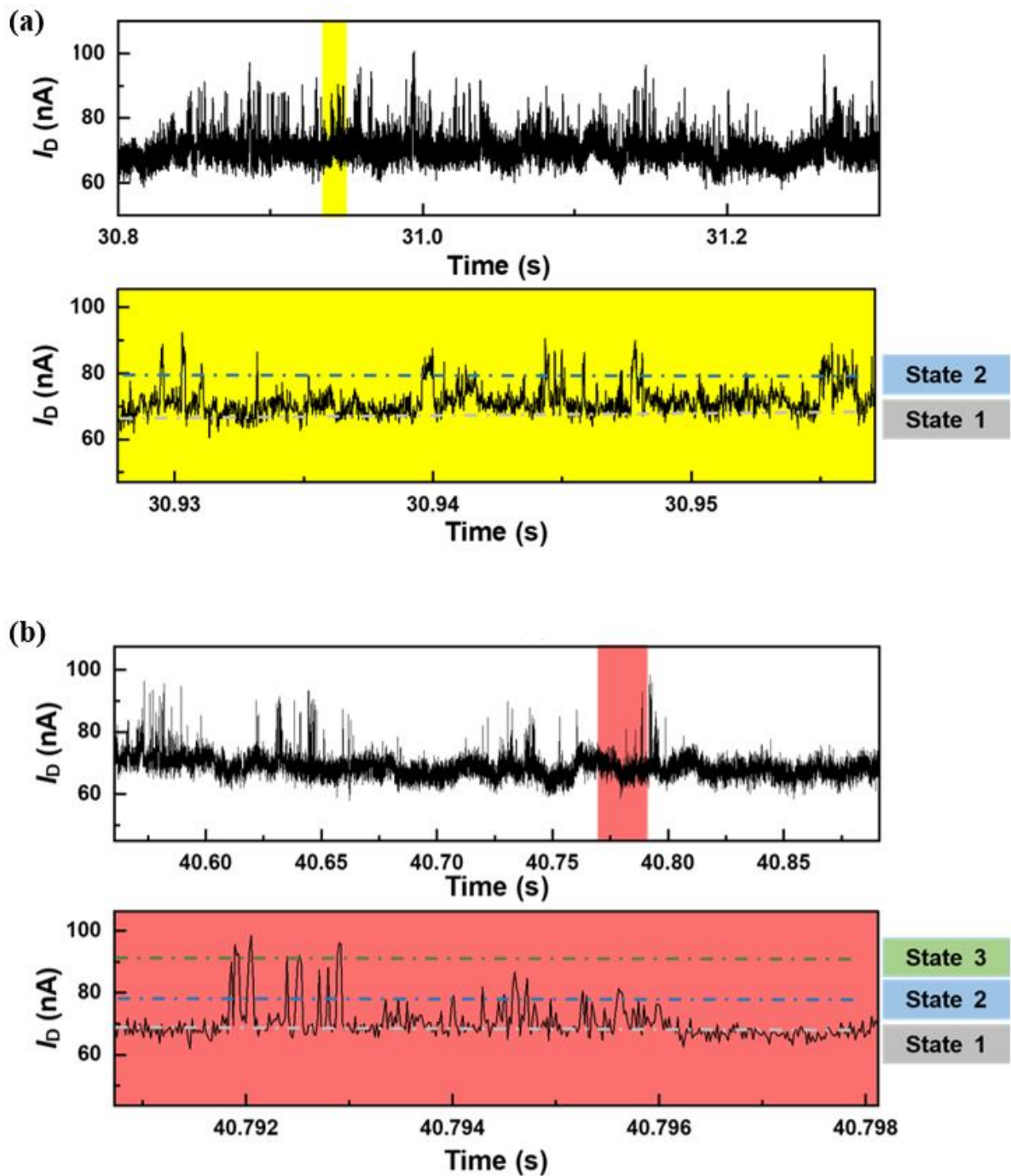


Figure S5.3. Conductance measurements of the photoswitching process of single-molecule junctions at different bias voltages, demonstrating the reproducibility of the photoswitching process. (a) $V_D = 0.1$ V, (b) $V_D = -0.1$ V, (c) $V_D = 0.2$ V, (d) $V_D = -0.2$ V. The gate voltage was 0 V. Measurements were carried out using Agilent 4155C semiconductor characterization system with a lower sampling rate of 2 ms.

5.7.3.3 Real-time electrical measurements of GMG-SMJ's at different time periods



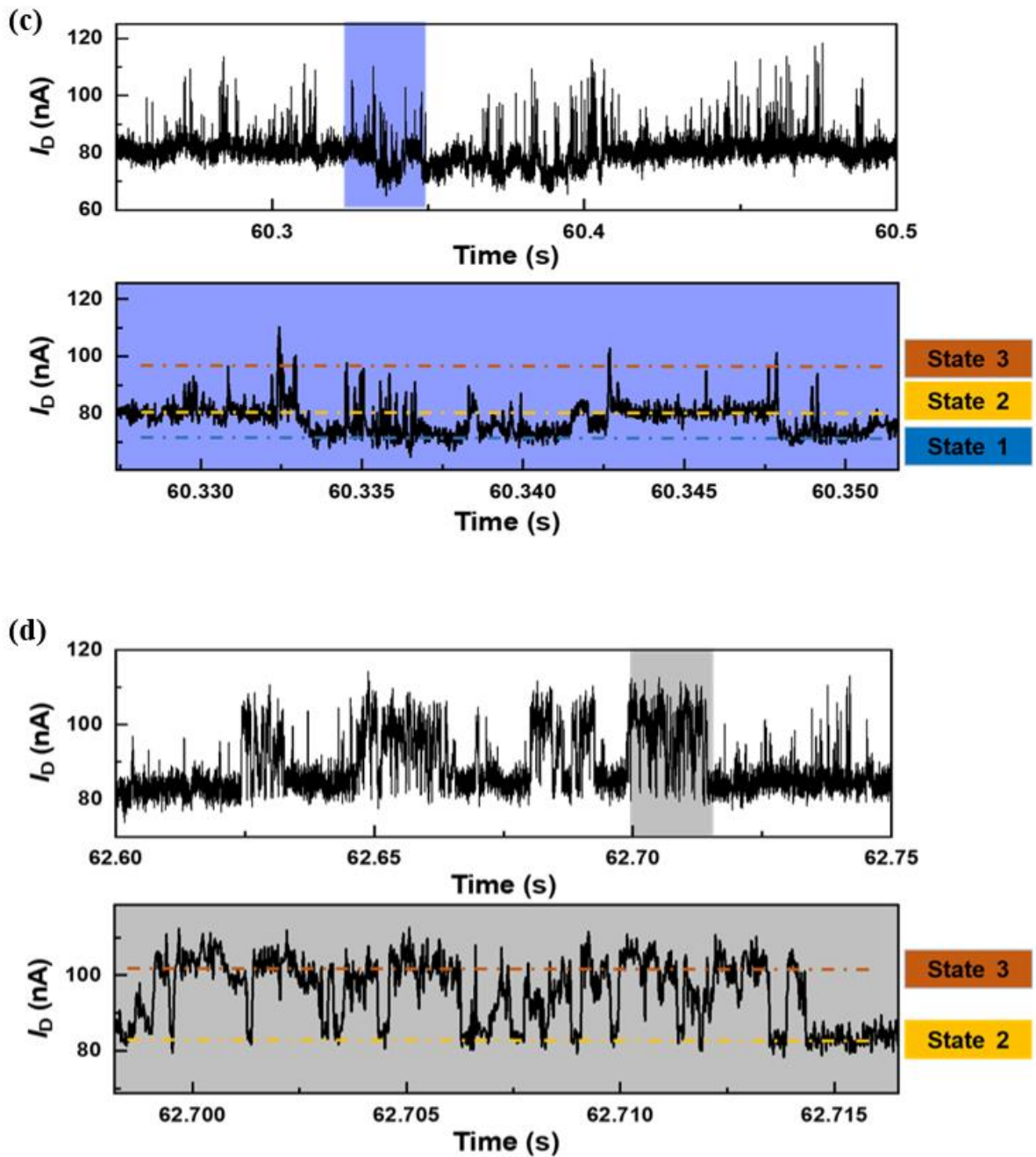


Figure S5.4. Real-time conductance measurements of GMG-SMJJs at different time periods. Figures a-d show another set of data from the same device in Figure 5.3. (a) $I-t$ curves under dark condition, where States 1-2 were observed, (b) $I-t$ curves under dark condition, where all three states (States 1-3) were observed, (c) $I-t$ curves under UV condition, where all three states (States 1-3) were observed, (d) $I-t$ curves under UV condition, where States 2-3 were observed. $V_D = 0.2$ V.

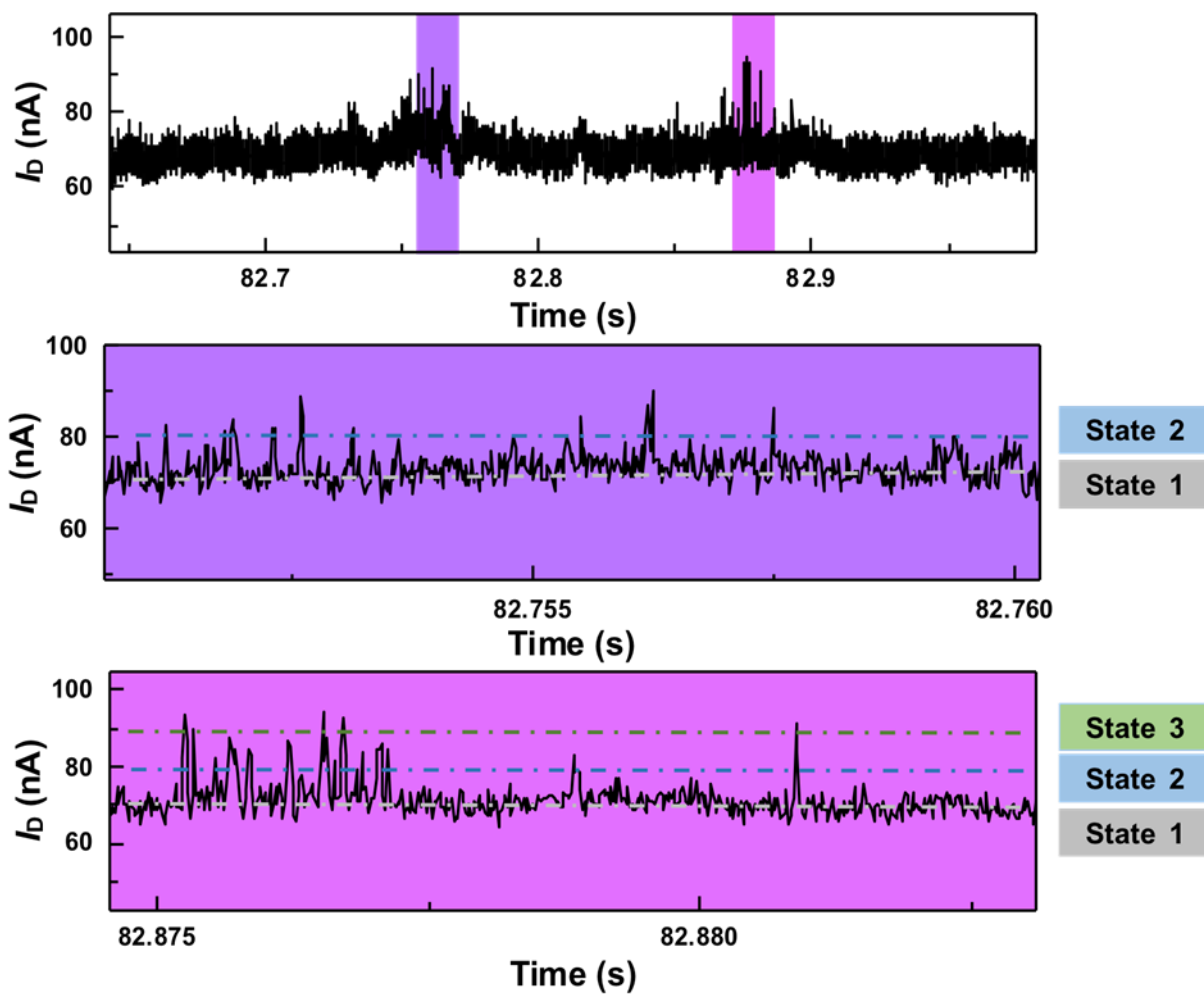


Figure S5.5. Real-time conductance measurements of cyclic peptide **1** under visible light irradiation after UV exposure.

5.7.4 Electrical measurements of control experiments

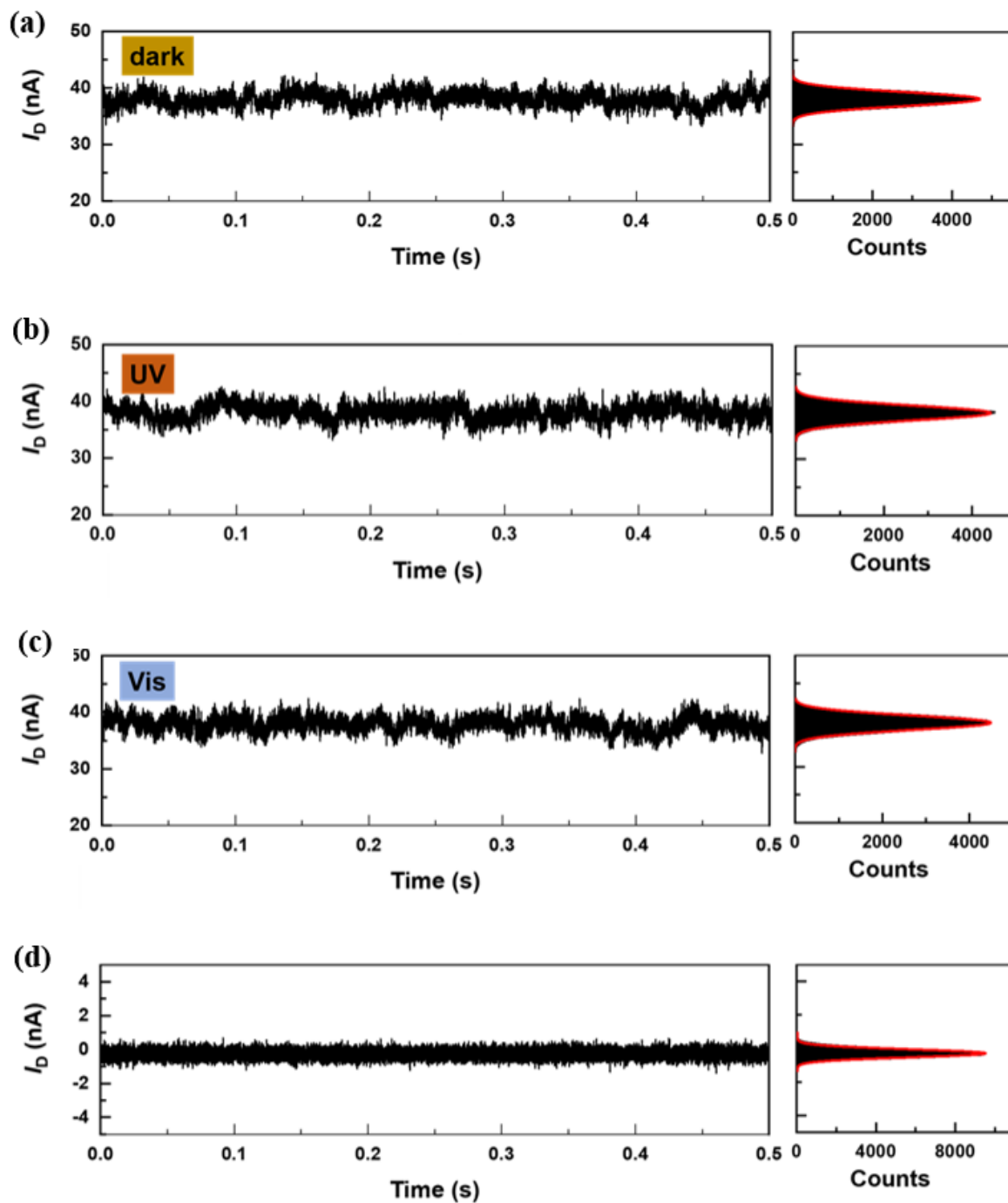


Figure S5.6. Control experiments under different conditions. **(a-c)** I - t curves of a partially cleaved graphene ribbon device under dark conditions, UV, and visible light, respectively. **(d)** I - t curves of a totally cleaved graphene ribbon device, showing the noise level that originates from the equipment and the environment. $V_D = 0.2$ V.

5.7.5 Kinetic Analysis

Dwell times (τ) were extracted from the idealized fittings of the original $I-t$ curves through the QuB software (Figure S5.7). Three states were distinguished for each isomer. In general, an elementary single-molecule reaction follows a single-step Poisson process that is stochastic, memory-free, and independent. Thus, the distributions of the dwell times of events can be fitted with a single exponential function:

$$P(\tau) = \frac{1}{\langle \tau \rangle} \exp\left(-\frac{\tau}{\langle \tau \rangle}\right)$$

where $\langle \tau \rangle$ is the mean dwell time and can be calculated through the exponential fitting parameter.

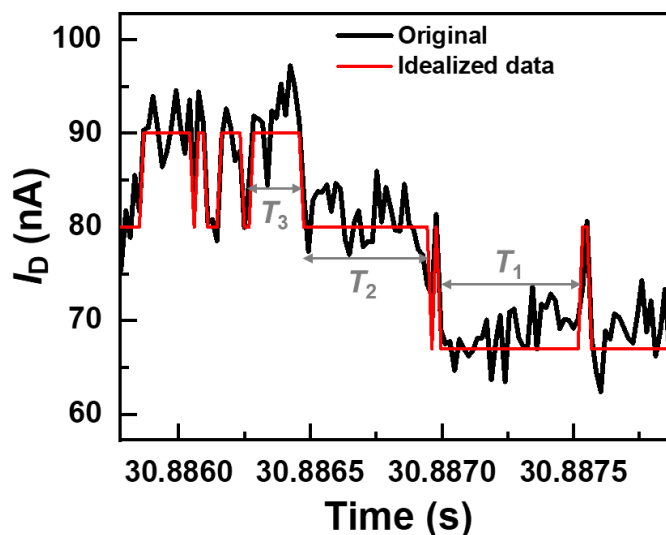


Figure S5.7. Kinetic analysis model. $I-t$ curve (black) of the GMG-SMJ and the idealized fit (red) obtained from a segmental k -means method based on the hidden Markov model analysis using the QuB software.

5.7.6 Molecular Dynamics (MD) Simulations of GMG-SMJs

5.7.6.1 GMG-SMJ junction model

Each graphene electrode consists of 128 carbon atoms arranged in a 16×8 array (Figure S5.8). The contact point extends out from the middle edge, and is comprised of 11 carbon atoms (Figure S5.9b). The two electrodes are aligned in the same plane, with critical distances indicated in Figure S5.8. Cyclic peptide **1** in either of the two photoisomeric states was bridged between the nanogapped graphene electrodes via amide bonds. All inner edge carbon atoms were saturated with H atoms.

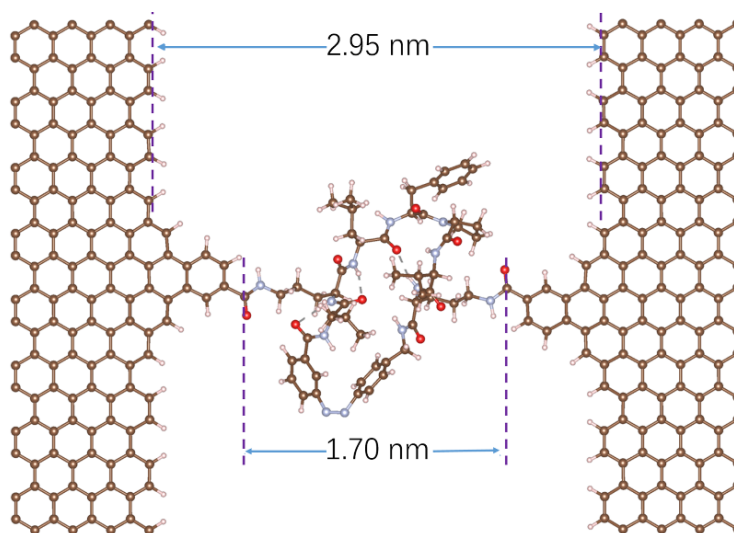


Figure S5.8. GMG-SMJ junction model constructed for MD simulations, where brown spheres denote carbon, red = oxygen, silver = nitrogen, and pale pink = hydrogen.

5.7.6.2 Force field parameters

The AMBER ff14SB and GAFF 2 force field parameters were adopted for all MD simulations. The partial atomic charges of ornithine (ORN) was derived by Pendley,³ and downloaded via the AMBER parameter database (<http://research.bmh.manchester.ac.uk/bryce/amber/>). The partial atomic charges of the azobenzene (AZO, Figure S5.9a) residue were determined with the restrained electrostatic potential (RESP) approach⁴ by fitting the electrostatic potential grids of both the *trans* and *cis* isomers using the RESP program implemented in the AMBER package. The derived partial atomic charges and their associated atom types are listed in Table S5.1, and the GAFF parameters are included in Table S5.2. In relation to the graphene electrodes (Figure S5.9b), the atoms in the shade region were set as a zero atomic charge, and fixed at a force constant of 500 kcal/mol/Å³. The partial atomic charges, types and GAFF parameters of the atoms situated in the peptide/electrode contacting region are included in Tables S5.1 and S5.2.

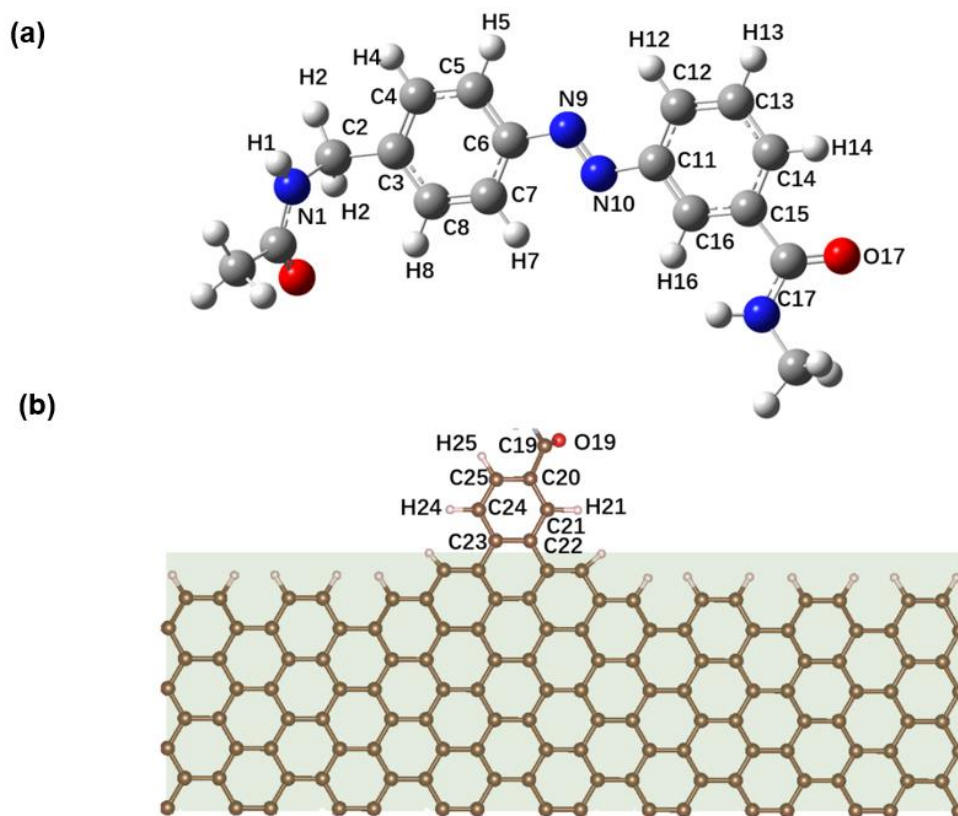


Figure S5.9. (a) Chemical structure of the azobenzene residue adopted for the determination of partial atomic charges. (b) Graphene electrode and key atoms pertaining to the contacting region.

Table S5.1. Atom type and partial atomic charge adopted for the azobenzene residue and electrode atoms.

| Atom name | Atom type | Charge | Atom name | Atom type | Charge |
|------------|-----------|---------|-----------|-----------|---------|
| Azobenzene | | | | | |
| N1 | n | -0.4157 | N9 | ne | -0.3711 |
| H1 | hn | 0.2719 | N10 | nf | -0.3008 |
| C2 | c3 | 0.0024 | C11 | ca | 0.6492 |
| H2 | h1 | 0.0691 | C12 | ca | -0.3691 |
| C3 | ca | 0.0241 | H12 | ha | 0.1852 |
| C4 | ca | -0.1137 | C13 | ca | -0.0808 |
| H4 | ha | 0.1743 | H13 | ha | 0.1542 |
| C5 | ca | -0.4849 | C14 | ca | -0.2258 |
| H5 | ha | 0.2193 | H14 | ha | 0.1723 |
| C6 | ca | 0.7532 | C15 | ca | 0.0537 |
| C7 | ca | -0.4849 | C16 | ca | -0.4323 |
| H7 | ha | 0.2193 | H16 | ha | 0.1718 |
| C8 | ca | -0.1137 | C17 | c | 0.5973 |
| H8 | ha | 0.1743 | O17 | o | -0.5679 |
| Electrode | | | | | |
| C19 | c | 0.5973 | C23 | ca | 0.1034 |
| O19 | o | -0.5679 | C24 | ca | -0.3798 |
| C20 | ca | 0.3412 | H24 | ha | 0.1754 |
| C21 | ca | -0.3154 | C25 | ca | -0.3459 |
| H21 | ha | 0.1654 | H25 | ha | 0.1695 |
| C22 | ca | 0.0568 | | | |

Table S5.2. GAFF parameters adopted for the azobenzene residue and electrode atoms.

| Bond | k_b (kcal/mol) | Distance (Å) |
|------------|------------------|--------------|
| Azobenzene | | |
| c3-hc | 330.6 | 1.097 |
| c-c3 | 313.0 | 1.524 |
| c-o | 637.7 | 1.218 |
| c-n | 427.6 | 1.379 |
| hn-n | 403.2 | 1.013 |
| c3-n | 328.7 | 1.462 |
| c3-h1 | 330.6 | 1.097 |
| Electrode | | |
| ca-ca | 378.6 | 1.398 |
| ca-ha | 395.7 | 1.086 |
| c-ca | 272.7 | 1.491 |

| Angle | k_θ (kcal/mol/radian ²) | Degree (°) |
|------------|--|------------|
| Azobenzene | | |
| hc-c3-hc | 39.40 | 107.58 |
| c-c3-hc | 26.93 | 108.77 |
| c3-c-o | 67.40 | 123.20 |
| c3-c-n | 66.79 | 115.18 |
| c-n-hn | 48.33 | 117.55 |
| c-n-c3 | 63.39 | 120.69 |
| n-c-o | 74.22 | 123.05 |
| ca-c-n | 67.68 | 115.25 |
| h1-c3-n | 49.84 | 108.88 |
| c3-n-hn | 45.80 | 117.68 |
| h1-c3-h1 | 39.24 | 108.46 |
| Electrode | | |
| ca-ca-ca | 68.8 | 120.02 |
| ca-ca-ha | 48.7 | 119.88 |
| c-ca-ca | 66.4 | 120.33 |

| Dihedral angle | Redundancy (IDIVF) | Vn/2 (kcal/mol) | Phase (°) | Periodicity |
|----------------|-----------------------|-----------------|-----------|-------------|
| Azobenzene | | | | |
| hc-c3-c-o | 1 | 0.80 | 0.000 | -1.000 |
| hc-c3-c-o | 1 | 0.00 | 0.000 | -2.000 |
| hc-c3-c-o | 1 | 0.08 | 180.00 | 3.000 |
| n-c-c3-hc | 6 | 0.00 | 180.00 | 2.000 |
| c3-c-n-hn | 4 | 10 | 180.00 | 2.000 |
| c3-c-n-c3 | 1 | 0.00 | 0.00 | -2.000 |
| c3-c-n-c3 | 1 | 1.50 | 180.00 | 1.000 |
| o-c-n-hn | 1 | 2.50 | 180.00 | -2.000 |
| o-c-n-hn | 1 | 2.00 | 0.00 | 1.000 |
| o-c-n-c3 | 4 | 10.00 | 180.00 | 2.00 |
| h-n-c-ca | 4 | 10.00 | 180.00 | 2.00 |
| c3-n-c-ca | 4 | 10.00 | 180.00 | 2.00 |
| hc-c3-n-c | 6 | 0.00 | 0.00 | 2.00 |
| hn-n-c-o | 1 | 2.50 | 180.00 | -2.00 |
| hn-n-c-o | 1 | 2.00 | 0.00 | 1.00 |
| c3-n-c-o | 4 | 10.00 | 180.00 | 2.00 |
| hc-c3-n-hn | 6 | 0.00 | 0.00 | 2.00 |
| Electrode | | | | |
| X -ca-ca-X | 4 | 14.5 | 180.00 | 2.00 |

5.7.6.3 MD simulation protocols and data analysis

MD simulations for the GMG-SMJ junctions were performed with the non-periodic condition in the canonical (NVT) ensemble using the Sander algorithm, as implemented in the Amber package (Ver 16-17.03).⁵ After energy minimization using the steepest descent (5000 steps) and conjugate gradient (5000 steps) method, each system was warmed up to room temperature (300 K) in 20 ps, and then allowed to equilibrate for 500 ps. In the production runs, the MD trajectory was written for every 100 steps, resulting in 6×10^4 frames (6 ns) for the subsequent cluster analyses. The following settings were activated throughout the heating and production phases. The temperatures were maintained using the weak coupling algorithm ($n_{\text{tc}} = 1$), with a time step of 1 fs. The SHAKE algorithm was used to constrain bonds involving hydrogen atoms. The cluster analyses were performed for the production trajectories using the CPPTRAJ software,⁶ and the Chimera software⁷ was chosen to visualize MD snapshots.

In order to correlate structural dynamics and conductance of the GMG-SMJ junctions, the MD trajectory for either of the two isomers was first subjected to the cluster analysis based on the root-mean-square (RMS) value of the carbon atoms in the azobenzene and peptide backbone using the hieragglo algorithm with an epsilon value of 2. The representative snapshots for each isomer were chosen to compute the transmission spectra (Figure S5.10), because the average frame derived from a MD run is commonly ill-defined and does not represent an appropriate chemical structure. Subsequently, the MD trajectory for the *trans* isomer was classified into eleven clusters based on the dihedral angle (Figure 5.5a) using the hieragglo algorithm with an epsilon value of 10. The corresponding histogram is depicted as a function of dihedral angle (Figure 5.5c), and the representative snapshots for each cluster were subjected to transport conductance calculations (Figure 5.5d). Similarly, the MD trajectory for the *cis* isomer was classified into eleven clusters based on either the dihedral angle (Figure 5.5a) or the two intramolecular hydrogen bonds (namely d_1 and d_2 , Figure 5.6a) using the hieragglo algorithm with an epsilon value of 10. No definitive correlation of conductance was found with the dihedral angle or d_2 (Figure S5.13). The corresponding histogram as a function of d_1 is depicted in Figure 5.6c, and the representative snapshots for each cluster were subject to compute transport conductance (Figure 5.6b).

5.7.7 Computational Results

5.7.7.1 Quantum transport calculations

Transmission coefficients $T(E)$ of each selected GMG-SMJ molecular junction snapshot were conducted with the non-equilibrium Green's function approach combined with density functional theory (NEGF-DFT), as implemented in the TRANSIESTA package.⁸ The entire junction device was fitted into a cuboid box, with a space from the graphene plane to the bottom of 6.0 Å, and 24.0 Å to the top. The transport direction was defined as the z axis, with periodic boundary conditions employed in the xy directions. A GGA/PBE functional⁹ and norm-conserving Troullier-Martins pseudopotentials¹⁰ were employed. The valence electronic orbitals of the cyclic peptide and the electrode contact points were described using double- ζ polarized (DZP) basis sets, while the single-zeta polarized (SZP) was chosen for the other C atoms in the electrodes. The Brillouin zone was sampled as a Monkhorst-Pack grid using $1 \times 1 \times 50$ k-points and a cut-off energy of 250 Ry was used. Eigenchannels were computed using the Inelastica package,¹¹ and visualized using the VESTA program.¹²

5.7.7.2 Transmission channels and eigenchannels

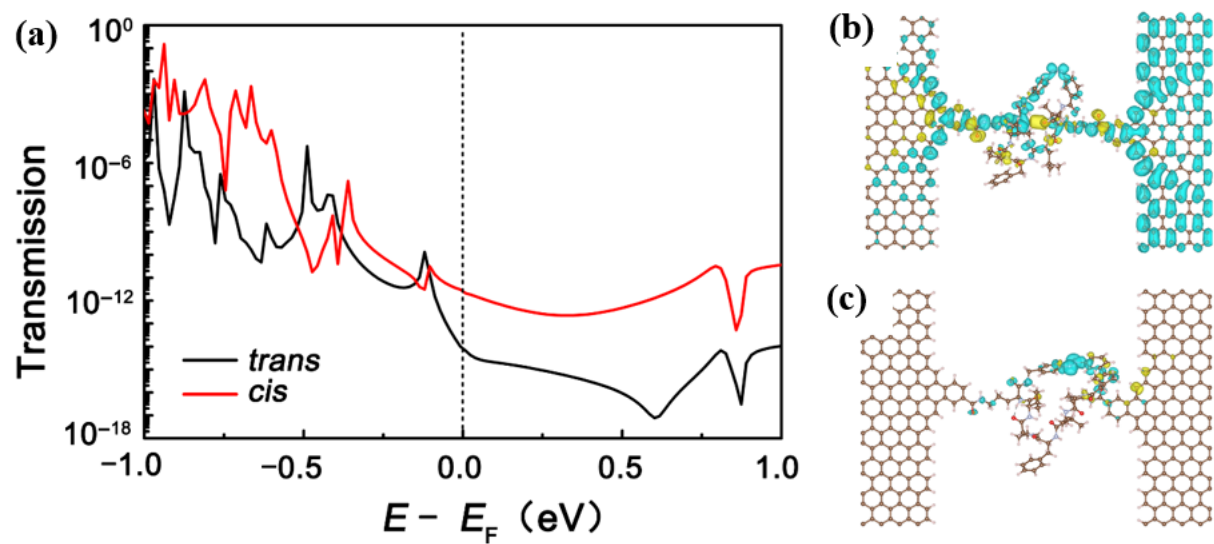


Figure S5.10. Transmission spectra and eigenchannels of the representative *cis* and *trans* GMG-SMJ snapshots. (a) Zero-bias transmission spectra of the *cis* (red) and *trans* (black) GMG-SMJs. Transmission eigenchannels for (b) *cis* and (c) *trans* GMG-SMJs.

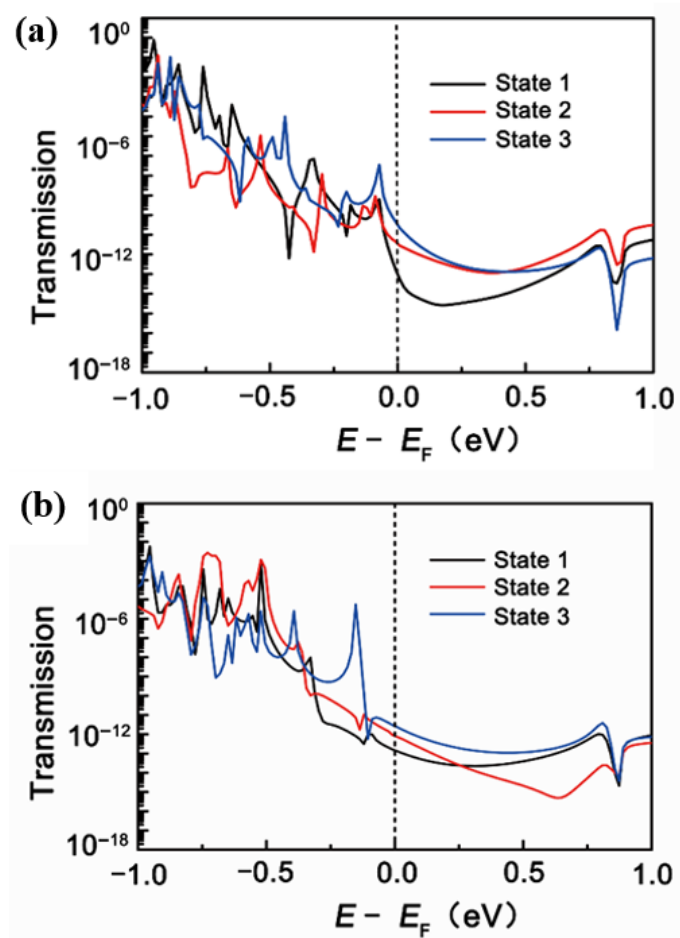


Figure S5.11. Transmission spectra of the representative three conductance states for (a) *cis* and (b) *trans* GMG-SMJ snapshots.

5.7.7.3 Molecular projected self-consistent Hamiltonian (MPSH) states of the *trans* and *cis* GMG-SMJs

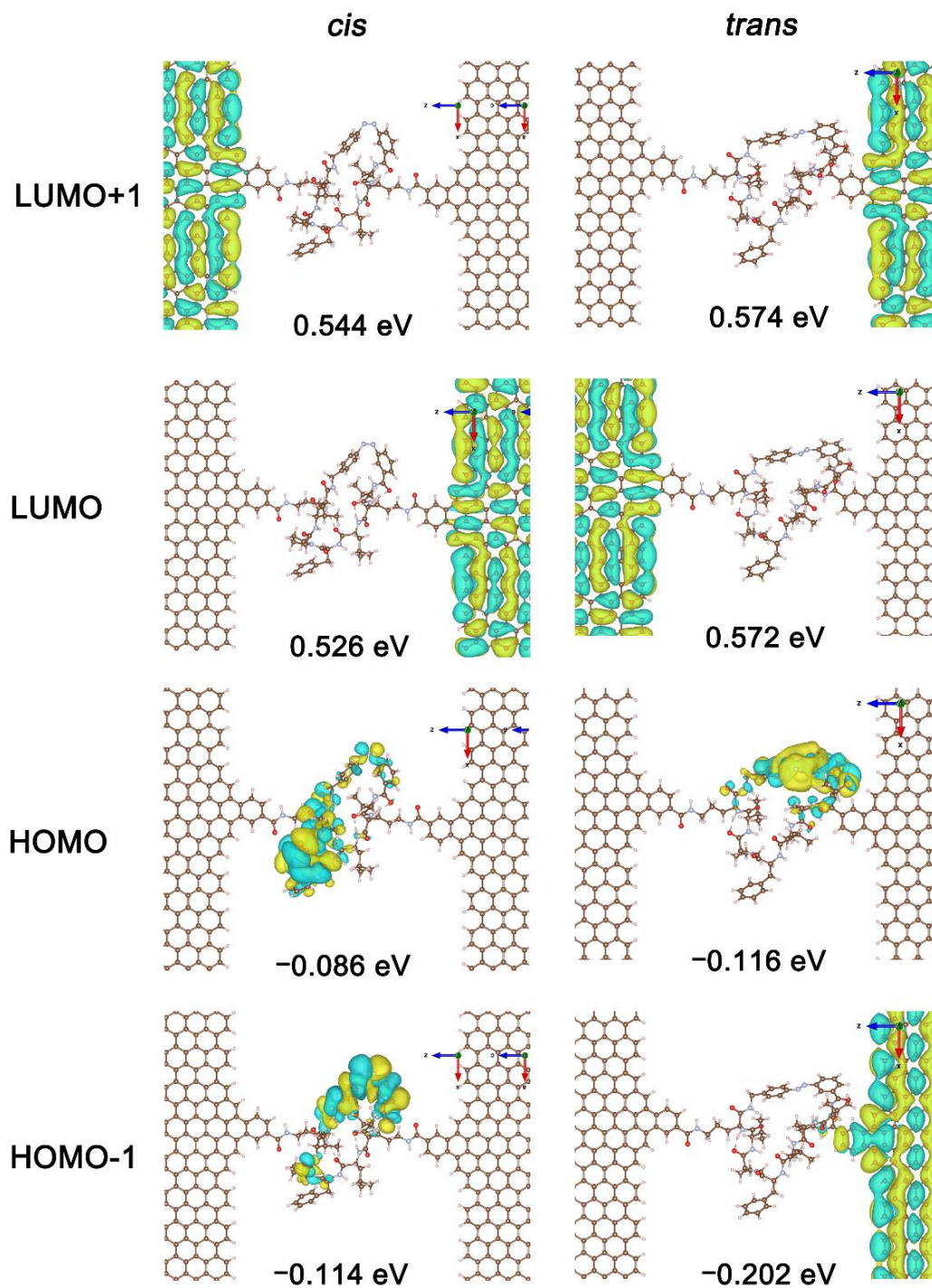


Figure S5.12. MPSH states of the highest occupied molecular orbitals (HOMOs) and lowest unoccupied molecular orbitals (LUMOs) for the *cis* (left) and *trans* (right) GMG-SMJs.

Table S5.3. Statistical analysis of the dihedral angle between azobenzene and electrode plane for the *trans* GMG-SMJ.

| Dihedral angle (°) | Conductance state | Occupancy rate (%) |
|--------------------|-------------------|--------------------|
| < -60 | | |
| -40 to -5 | State 1 | 47.6 |
| 15 to 35 | | |
| > 50 | | |
| -60 to -40 | State 2 | 28.6 |
| 35 to 50 | | |
| -5 to 15 | State 3 | 23.8 |

5.7.7.4 Dependence of computed conductance of *cis* GMG-SMJ snapshots on the dihedral angle (φ) and the distance of H-bond 2 (d_2)

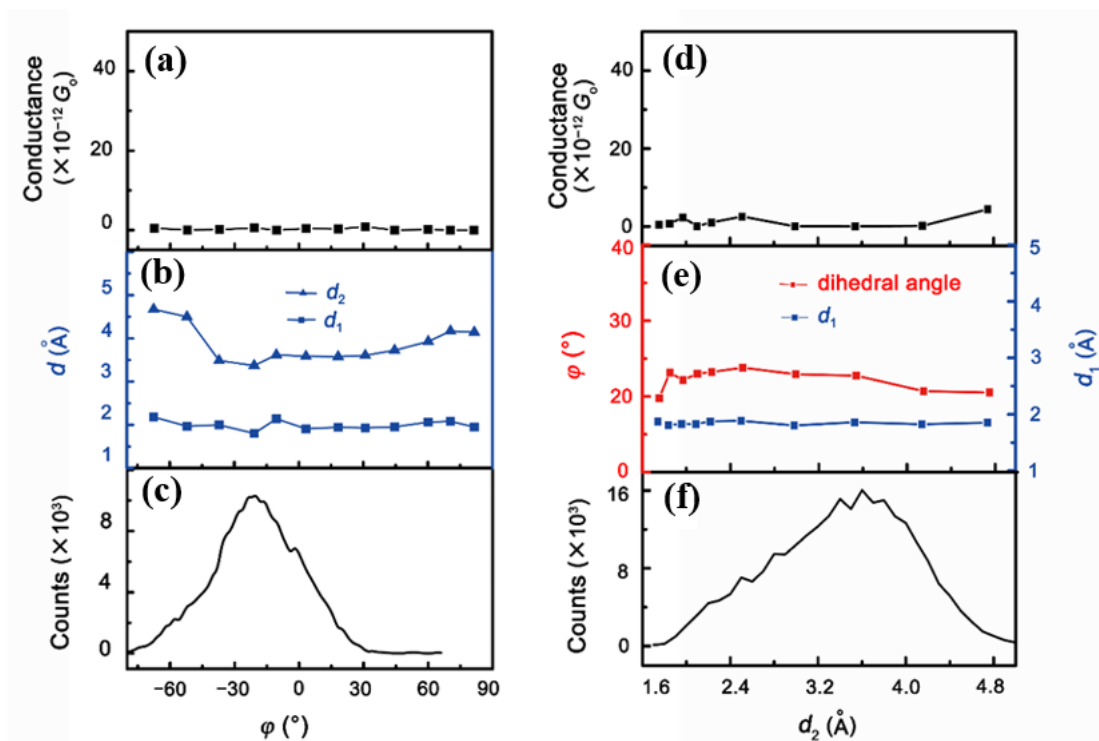


Figure S5.13. Conductance analysis for the MD simulations of *cis* GMG-SMJ snapshots. **(a)** Dependence of computed conductance on dihedral angle (φ). **(b)** The corresponding H-bond 1 distance (d_1) and H-bond 2 distance (d_2) for the selected GMG-SMJ snapshots. **(c)** Distribution of the φ over the course of simulations. **(d)** Dependence of computed conductance on d_2 . **(e)** The corresponding φ and d_1 for the selected GMG-SMJ snapshots. **(f)** Distribution of d_2 over the course of simulations.

Table S5.4. Statistical analysis of H-bond 1 distance (d_1) for the *cis* GMG-SMJ.

| Distance (Å) | Conductance state | Occupancy rate (%) |
|--------------|-------------------|--------------------|
| < 1.80 | State 3 | 5.7 |
| 1.80 to 2.10 | State 2 | 65.9 |
| > 2.10 | State 1 | 28.4 |

5.7.8 References

1. Cao, Y.; Dong, S. H.; Liu, S.; He, L.; Gan, L.; Yu, X. M.; Steigerwald, M. L.; Wu, X. S.; Liu, Z. F.; Guo, X. F., Building High-Throughput Molecular Junctions Using Indented Graphene Point Contacts. *Angew. Chem. Int. Ed.* **2012**, *51* (49), 12228–12232.
2. Jia, C. C.; Wang, J. Y.; Yao, C. J.; Cao, Y.; Zhong, Y. W.; Liu, Z. R.; Liu, Z. F.; Guo, X. F., Conductance switching and mechanisms in single-molecule junctions. *Angew. Chem. Int. Ed.* **2013**, *52* (33), 8666–8670.
3. Pendley, S. S.; Yu, Y. B.; Cheatham, T. E., Molecular dynamics guided study of salt bridge length dependence in both fluorinated and non-fluorinated parallel dimeric coiled-coils. *Proteins* **2009**, *74* (3), 612–629.
4. Cornell, W. D.; Cieplak, P.; Bayly, C. I.; Kollman, P. A., Application of RESP charges to calculate conformational energies, hydrogen bond energies, and free energies of solvation. *J. Am. Chem. Soc.* **1993**, *115* (21), 9620–9631.
5. Case, D. A.; Cheatham, T. E.; Darden, T.; Gohlke, H.; Luo, R.; Merz, K. M., Jr.; Onufriev, A.; Simmerling, C.; Wang, B.; Woods, R. J., The Amber biomolecular simulation programs. *J. Comput. Chem.* **2005**, *26* (16), 1668–1688.
6. Roe, D. R.; Cheatham, T. E., PTRAJ and CPPTRAJ: Software for Processing and Analysis of Molecular Dynamics Trajectory Data. *J. Chem. Theory Comput.* **2013**, *9* (7), 3084–3095.
7. Pettersen, E. F.; Goddard, T. D.; Huang, C. C.; Couch, G. S.; Greenblatt, D. M.; Meng, E. C.; Ferrin, T. E., UCSF Chimera—A visualization system for exploratory research and analysis. *J. Comput. Chem.* **2004**, *25* (13), 1605–1612.
8. Papior, N.; Lorente, N.; Frederiksen, T.; García, A.; Brandbyge, M., Improvements on non-equilibrium and transport Green function techniques: The next-generation transiesta. *Comput. Phys. Commun.* **2017**, *212*, 8–24.
9. Perdew, J. P.; Burke, K.; Ernzerhof, M., Generalized Gradient Approximation Made Simple. *Phys. Rev. Lett.* **1996**, *77* (18), 3865–3868.
10. Troullier, N.; Martins, J. L., Efficient pseudopotentials for plane-wave calculations. *Phys. Rev. B* **1991**, *43* (3), 1993–2006.

11. Frederiksen, T.; Paulsson, M.; Brandbyge, M.; Jauho, A.-P., Inelastic transport theory from first principles: Methodology and application to nanoscale devices. *Phys. Rev. B* **2007**, *75* (20), 205413.
12. Momma, K.; Izumi, F., VESTA 3 for three-dimensional visualization of crystal, volumetric and morphology data. *J. Appl. Crystallogr.* **2011**, *44* (6), 1272–1276.



CHAPTER 6

Conclusion and further studies



6.1 Conclusion

The research presented in this thesis provided a thorough investigation of the relationship between structure and function using model peptides, due to the complex nature of proteins. We have demonstrated that an ability to control structure will allow for the modulation of antibacterial properties using a photopharmacological approach and hypoxia-activated prodrug strategy. The regulation of peptide activity offers an opportunity to mitigate off-target side effects, and in the context of an antibiotic, the development of resistance. Moreover, we unravelled the intrinsic dynamic properties corresponding to specific structural changes within each isomer of a photoswitchable cyclic peptide using the electrically characterized single-molecule junction technique. This research deepens our understanding of the structure and the intrinsic dynamic behavior of peptides, with these fundamental properties potentially extending to proteins.

6.2 Further studies

In chapters 2-3, the regulation of antibacterial activity through the photochemical control of an azobenzene photoswitch was demonstrated. However, cytotoxicity tests on human cells and pharmacokinetics studies are required to fully evaluate the efficacy of the peptide mimetics to function as potential antibiotics *in vivo*. Numerous challenges associated with light delivery must be overcome to exploit the full potential of photopharmacology. Light does not penetrate tissue efficiently due to melanin pigmentation of the skin and the absorption of biomolecules, such as heme and flavoproteins.¹ Nevertheless, recent advancements in biomedical engineering research have proposed innovative methods to allow subdermal light delivery using optoelectronic implants and optical fibers (Figure 6.1).² Future work on chapters 2-3 may involve attachment of the photoswitchable antibacterial peptides onto optical fibers, where light from an external source can be transmitted through the fibers to enable photoswitching between two peptide conformations to modulate the antibacterial activity. Moreover, the intensity and wavelength of light, location, and time of irradiation can then be tuned with spatiotemporal

precision. These new technologies can potentially improve precision sensing, diagnosis, and point-of-care treatment for bacterial infections.

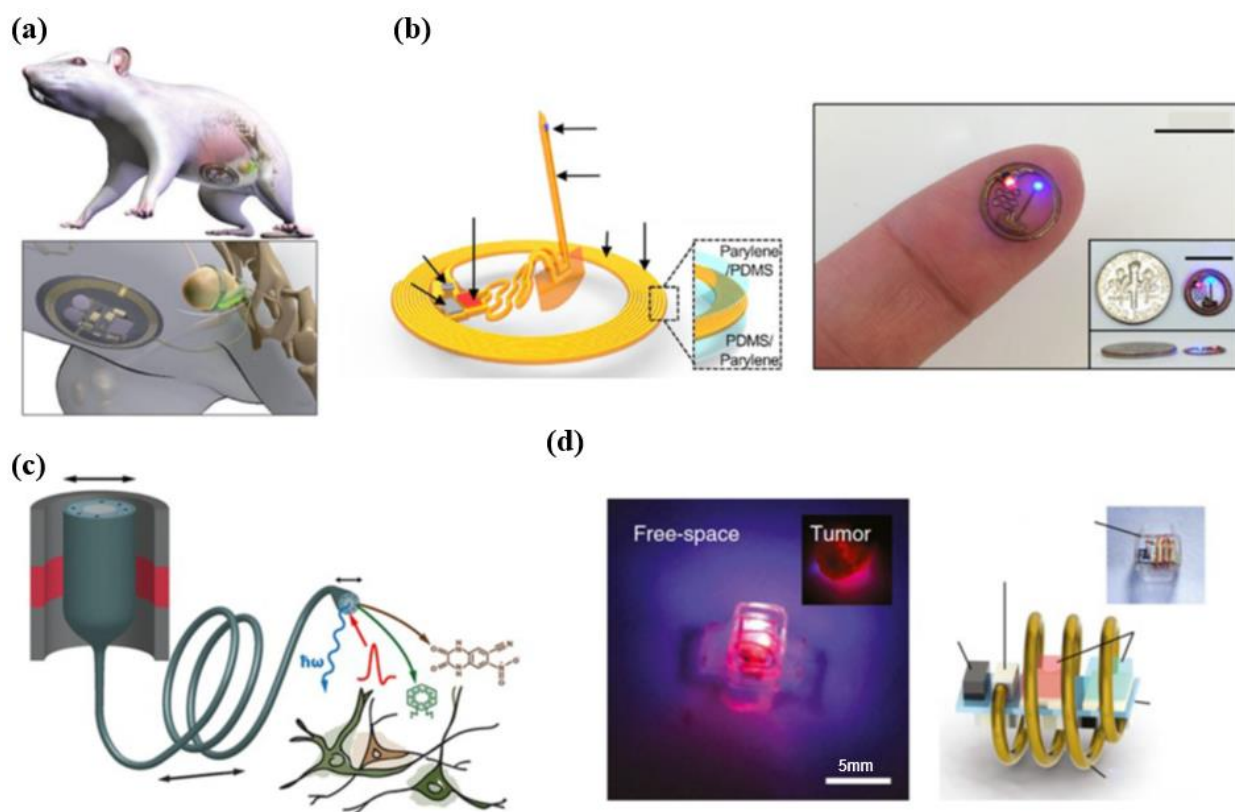


Figure 6.1. New technologies for light delivery. **(a)** A wireless optoelectronic implant to control bladder function in rats. **(b)** A microscale injectable light-emitting diode to allow subdermal light delivery in the brains of mice. **(c)** Multifunctional optical fibers to probe neuronal activity. **(d)** A wireless photonic device that emits light for photodynamic therapy of tumors. (Figure adapted from Morstein et al.¹)

Chapter 4 successfully demonstrated the liberation of an active antibacterial agent on reduction under conditions that mimic hypoxia, however, the activation of the prodrug under tissue hypoxia remains to be done. Moreover, the dose-limiting toxicity and mechanism of activation of the bioreductive prodrug need to be investigated to examine the clinical relevance of the hypoxia-activated prodrug strategy for bacterial-infected tissue.

Chapter 5 provided a step towards multi-modal bio-inspired nanodevices by unravelling the structural dynamic behavior of a photoswitchable cyclic peptide that can be interconverted

between a well-defined *cis* isomer and an ill-defined *trans* isomer. Our photoresponsive single-molecule device offers the capacity to modulate conductance, which paves the way for the realization of photocontrollable bio-inspired molecular electronic components. Future work on this research could focus on improving device stability and optimizing the device fabrication to probe the fundamental molecular properties, such as molecular structure, dynamics, and reactivity. This bottom-up approach is required to solve the challenge of miniaturizing components in conventional silicon electronics.³

6.3 References

1. Morstein, J.; Trauner, D., New players in phototherapy: photopharmacology and bio-integrated optoelectronics. *Curr. Opin. Chem. Biol.* **2019**, *50*, 145–151.
2. Canales, A.; Park, S.; Kiliyas, A.; Anikeeva, P., Multifunctional Fibers as Tools for Neuroscience and Neuroengineering. *Acc. Chem. Res.* **2018**, *51* (4), 829–838.
3. Jeong, H.; Kim, D.; Xiang, D.; Lee, T., High-Yield Functional Molecular Electronic Devices. *ACS Nano* **2017**, *11* (7), 6511–6548.